

# Assembling covalent organic framework films as hole transport layers for inverted perovskite solar cells



## Dissertation

Zur Erlangung des akademischen Grades

Doktor der Naturwissenschaften

(Dr. rer. nat.)

Eingereicht an der Fakultät für Mathematik und Naturwissenschaften

der Bergischen Universität Wuppertal

von

Yazhou Xu

geb. in Yichun, China

Wuppertal 2023



This work was carried out during the period from March 2016 to March 2023 in the Department of Chemistry, Macromolecular Chemistry group, Bergische Universität Wuppertal, under the supervision of Prof. Dr. Ullrich Scherf.



## **Abstract**

In the first part of this work, a series of hole transport layer molecules were designed and synthesized with trisphenylbenzene, trisphenylamine and trithiophenebenzene as core and diphenylamine, carbazole, di(4-methoxy-phenyl)amine and di(4-methoxy)carbazole as terminals to investigate relations between structural features and optoelectronic physicochemical properties, as well as the photovoltaic performance of these small molecules as hole transport materials in dopant-free inverted (p-i-n) perovskite solar cells. The best photovoltaic performance of perovskite solar cells presented here are devices with TPA-NC-TPAOMe as hole transport layer, which show up to 12.76% of photoelectric conversion efficiency, 66.31% of fill factor, 0.94 V of open-circuit voltage and 20.47 mA/cm<sup>2</sup> of short circuit current density.

In the second part of this work, a series of covalent organic frameworks based on the cores of the first part are designed and synthesized as films directly on top of ITO substrates, which serve as hole transport layer in perovskite solar cells. The main goal was to design polymers with suitable hole mobilities in dopants-free invert (p-i-n) perovskite solar cells, which can skip solution processing to overcome solubility issues of general hole transport layers using polymeric materials. The best photovoltaic performances were shown by perovskite solar cells using TPA-NC-T1 as hole transport layer, showing 2.48% of photoelectric conversion efficiency, 17.21% of fill factor, 0.99 V of open-circuit voltage and 14.74 mA/cm<sup>2</sup> of short circuit current density.

## **Zusammenfassung**

Im ersten Teil dieser Arbeit wurde eine Reihe von Modellverbindungen mit Triphenylbenzol-, Triphenylamin- und Trithiophenbenzoleinheiten als Kernbausteine und Diphenylamin, Carbazol, Di(4-methoxyphenyl)amin und Di(4-methoxy)carbazol als Verbindungsbausteine hergestellt um die Einflüsse von Struktureinheiten auf die optoelektronischen, physikochemischen Eigenschaften und die Leistungsfähigkeit in photovoltaischen Bauteilen basierend auf kleinen Molekülen als Lochleiter in undotierten, invertierten (p-i-n) Perovskitsolarzellen zu untersuchen. Die leistungsfähigsten Bauteile in diesem Kapitel nutzten die Modellverbindung TPA-NC-TPAOMe als Lochleiter und zeigten Leistungsumwandlungseffizienzen von bis zu 12,76 %, 66,31 % Füllfaktor, eine Leerlaufspannung von 0,94 V und eine Kurzschlussstromdichte von - 20,47 mA/cm<sup>2</sup>.

Im zweiten Teil dieser Arbeit wurden analog unterschiedliche kovalente organische Gerüststrukturen (*covalent organic frameworks*, COFs) mit den zuvor evaluierten Kern- und Verbindungsbausteinen direkt auf ITO Substrat hergestellt um als Lochleiter für Perovskitsolarzellen zu dienen. Das Hauptteil dieses Kapitels war es, Polymere mit geeigneten Ladungsträgermobilitäten herzustellen, um diese im Anschluss ohne die Notwendigkeit von Lösungsmittelauftragung einzusetzen und damit einen Vorteil gegenüber anderen, in organischen Lösungsmitteln löslichen Polymeren zu schaffen. Die leistungsfähigsten Bauteile in diesem Kapitel nutzten das Polymer TPA-NC-T1 als Lochleiter und zeigten Leistungsumwandlungseffizienzen von bis zu 2,48 %, 17,21 % Füllfaktor, eine Leerlaufspannung von 0,99 V und eine Kurzschlussstromdichte von -14,74 mA/cm<sup>2</sup>.

## Contents

1	Introduction.....	1
1.1	General introduction into porous materials.....	1
1.2	Covalent organic frameworks.....	4
1.2.1	Design principle.....	6
1.2.2	Properties and characterization of COFs.....	9
1.2.3	Synthesis.....	10
1.2.4	Linkages and reaction conditions.....	11
1.2.5	Reaction mechanisms.....	14
1.2.6	Functional Exploration and Applications.....	15
1.3	Motivation and Objectives.....	20
1.4	References.....	20
2	Triphenylamine-based hole transport materials for p-i-n perovskite solar cells.....	27
2.1	Introduction.....	27
2.2	Results and Discussions.....	32
2.2.1	Synthesis.....	32
2.2.2	Optoelectronic properties.....	45
2.2.3	Photovoltaic performance of perovskite solar cells (PSC).....	51
2.3	Conclusion.....	77
2.4	Experimental Section.....	78
2.4.1	Device Preparation.....	78

2.4.2	Synthesis of molecules.....	79
2.5	References .....	99
3	COF films as hole transport layers in p-i-n Perovskite solar cells.....	101
3.1	Introduction .....	101
3.2	Results and Discussions .....	103
3.2.1	Synthesis and naming of COFs.....	103
3.2.2	Optical and electrochemical properties.....	104
3.2.3	Perovskite layer forming on top of COF films .....	111
3.2.4	Photovoltaic performance of perovskite solar cells .....	113
3.3	Conclusion.....	119
3.4	Experimental Section .....	120
3.4.1	Synthesis of molecules.....	120
3.4.2	Synthesis of COF powders.....	122
3.4.3	Synthesis of COF films on ITO .....	127
3.4.4	Device Preparation.....	128
3.5	References .....	129
4	Summary .....	130



# 1 Introduction

## 1.1 General introduction into porous materials

A porous solid is defined as “a solid with pores, which are cavities, channels or interstices” by International Union of Pure and Applied Chemistry (IUPAC). The structure of these inner pores can be “opened”, “closed” or “interconnected”.<sup>1</sup> Porous solids are composed of either inorganic or organic materials, or even designed as inorganic/organic hybrid materials. Nearly all the man-made porous solids or even some natural materials, such as natural zeolites, possess empty spaces or voids/pores with sizes ranging from nanometer- to centimeter-scale.<sup>2</sup> Due to the cavities, the surface area of the porous materials is significantly higher than for non-porous materials. Porosity is a property to describe materials' permeability to gases and liquids, which always strongly depends on intrinsic void structure inside materials.<sup>3</sup> Porous materials are a class of very important materials in both scientific and industry research fields. Because of elevated surface areas, porous materials can not only be used as matrices for gas storage and separation,<sup>4</sup> but also as catalyst scaffolds in heterogenous catalysis or photo-redox catalysis.<sup>5, 6</sup> Over the last decade, numerous new porous materials or composite materials based on porous materials have been under investigation.<sup>7</sup> In the near future, there might be an “explosion” on porous materials development in both fields of science and technology based on the progress gained.<sup>8, 9</sup>

Porous materials can be classified into three classes based on their mean diameter of the pore, which are microporous materials (diameter < 2 nm), mesoporous materials (2 nm < diameter < 50 nm) and macroporous materials (diameter > 50 nm) according to the IUPAC.<sup>3</sup> Also, based on their different chemical composition, porous materials can be roughly divided into two classes which are inorganic porous materials and organic porous materials. Activated carbon, mesoporous silicates and zeolites are the most representative inorganic porous materials which are widely used in industry field because of their low price and high surface area.<sup>10</sup> Activated carbon and zeolites dominate the global industrial market for the application of water treatment, gas storage, molecule separation and catalysis platform. Activated carbon is a porous inorganic material, in which up to 90% of it are composed of elementary carbon. It became a promising absorbent solid because of high porous density, large surface area and considerable stability.<sup>11, 12</sup> Similar with activated

carbon, zeolites are another very important class of porous inorganic materials with high degree of porosity and large surface area, which are constructed by the non-tunable, three dimensional framework structure.<sup>13</sup> Superior to activated carbon, zeolites can be designed with a hierarchically porous structure, which can improve the utilizability significantly.<sup>14, 15, 16</sup> Due to these remarkable properties, zeolites became widely used as absorbent in water treatment, as separator in gas separations, as promising carriers for drug delivery and as catalysts or catalysts platforms in chemical industry.<sup>17, 18, 19, 20</sup> However, inorganic porous materials display several disadvantages related to their hydrophilicity, sorption kinetics, processability and designability.<sup>21</sup> Especially the lack of chemical methods for precise functionalization limit further development of porous inorganic materials.<sup>22</sup>

Porous organic materials can be classified into porous organic frameworks and porous organic cages and polymers. Most porous organic materials are actually extended networks or frameworks with continued structure which constructed by repeating units, for example, metal organic frameworks (MOFs)<sup>23</sup>, covalent organic frameworks (COFs)<sup>24</sup> and conjugated microporous polymers (CMPs)<sup>25</sup>. Based on definition of *polymer* by IUPAC, these networks or frameworks can be classified as polymeric.<sup>26</sup> COFs and MOFs are three dimensional networks assembled by simple building blocks. Pores are formed in between the space-demanding building blocks (extrinsic porosity). In contrast, to most porous organic frameworks, porous organic cages and polymers create free volume inside a distinct molecule due to their structures (intrinsic porosity). In these materials, rigidity and robustness of the molecular arrangement create cavities of precise size and shape which has been utilized for precise separations. Recently, Liu *et al.* reported the separation of hydrogen isotopes using a barely porous organic cage enabled by the uniform cavity of ca. 2 Å inside a cage molecule. Porous organic materials tend to aggregate to solids due to presence of covalent or coordinative interactions. However, in 2015 Giri *et al.* even presented examples of permanently porous liquids.<sup>27, 28</sup> Although intrinsically porous organic cages and polymers do not possess comparable porosity or surface area as high as those of porous organic frameworks, they show interesting properties such as uniform pore sizes, solubility, carrier mobility or ion conductivity and the opportunity for potential functionalization.<sup>29</sup> Chen *et al* incorporated a cationic skeleton into COF leading to a significantly Li<sup>+</sup> conductivity.<sup>30</sup> Solubility must always be taken into account, considering that many devices fabrication processes need solution-processability,

such as spin-coating or drop-casting. Most networks or frameworks are insoluble in water or common organic solvents, while soluble polymers or molecules can be easily processed into films. However, in the last years large efforts have been put into the processing of insoluble frameworks like COFs.<sup>31</sup> Moreover, these materials have superior properties for the utilization in optoelectronic and energy materials.<sup>32</sup> Therefore, in the following section the focus will be placed on covalent organic frameworks.<sup>33</sup>

Porous organic polymers can be further distinguished by the nature of the chemical bonds that are present. Hydrogen bonded organic frameworks (HOFs) are typically non-covalently linked porous organic polymers. HOFs are porous crystalline networks constructed by hydrogen bonds, with mostly weak and flexible interactions. The most common porous organic polymers are covalent porous organic materials, for example, CMPs, COFs, covalent triazine frameworks (CTFs), porous aromatic frameworks (PAFs), hyper crosslinked polymers (HCPs) and polymers of intrinsic microporosity (PIMs), in which the repeat units or building blocks are linked exclusively by covalent bonds. PIMs are normally one dimensional porous organic polymers assembled by twisted polymer chains or backbones.<sup>34</sup> HCPs are another type of porous organic materials with high surface area as promising candidates for gas separation and storage, especially for hydrogen storage.<sup>35</sup> Different from PIMs, the porous structure of HCPs are built through extensive crosslinking reactions which prevent the polymer chains from collapsing into a dense, non-porous state.<sup>36</sup> PAFs are important porous organic polymers with rigid and extend framework structure, in which different aromatic building units are linked through carbon-carbon type covalent bonds. PAFs, also known as porous polymer networks (PPNs), are a special type of CMPs, because similar with CMPs, most linkers are extended  $\pi$ -conjugated molecules.<sup>37</sup> In contrast to CMPs PAFs, e.g., are composed around non- $\pi$ -conjugated tetrahedral tetraphenylmethane units, including derivatives containing other central atoms (such as Si and Ge) or tetrakisphenyladamantane and spirobifluorene cores<sup>38, 39, 40</sup>. CTFs could also be considered as another type of CMPs because they contain extended  $\pi$ -conjugated system, e.g. porous organic polymers with aromatic C=N linkage (triazine unit).<sup>41</sup> MOFs, also known as porous coordination polymers (PCPs), are crystalline porous organic networks generated from metal-containing nodes (metal ions or clusters, identical to the secondary building units (SBUs)) and organic units through coordinated bond formation.<sup>23, 42, 43</sup> CMPs are a class of amorphous porous 3D polymers, which are normally synthesized by the

irreversible reaction of two or more different monomers, such as Sonogashira-Hagihara coupling, Suzuki-Miyaura coupling, Yamamoto type coupling, Heck coupling.<sup>3</sup> CMPs are extended  $\pi$ -conjugated frameworks, distinguished from the other polymers that are non  $\pi$ -conjugated.<sup>25</sup> CMPs can be considered as a unique type of PAFs, in PAFs the core molecule always brake the  $\pi$ -conjugation, such as in tetraphenylmethane and spirobifluorene. CTFs can be viewed as a subclass of CMPs because of the same porous framework structure with full extended  $\pi$ -conjugated system but with triazine as linker unit. The classification of porous materials is shown as a route diagram in figure 1.

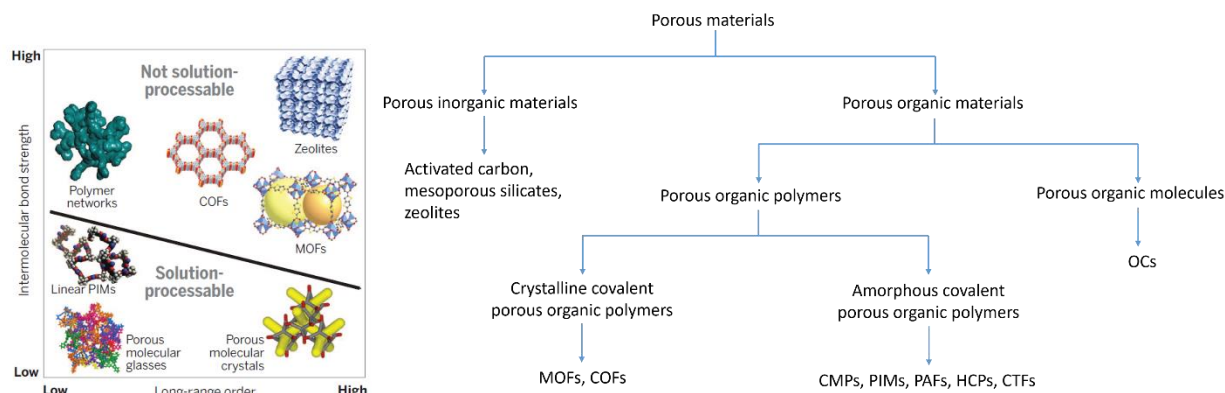


Figure 1. Classification of porous materials.<sup>33</sup>

## 1.2 Covalent organic frameworks

COFs have gained interests in material science since their first synthesis in Yaghi's lab in 2005.<sup>44</sup> COFs are a type of crystalline porous organic polymer network, in which various molecules are linked to form periodically ordered skeletons by strong and dynamic covalent bonds through reversible (equilibrium) reactions.<sup>8, 24, 45</sup> These covalent bonds include imines,<sup>46</sup> boronic esters,<sup>44</sup> triazines<sup>47</sup> and C=C connections<sup>48</sup>. Different from other porous organic polymers, a significant feature of COFs is their low density, permanent porosity and high surface area due to the light element composition and highly ordered crystalline structures.<sup>49</sup> In addition, COF structures are predesignable, synthetically controllable, and functionally manageable.<sup>24</sup> All these unique

advantages make COFs promising candidates in various applications, such as molecule adsorption and separation,<sup>50</sup> optoelectronics,<sup>51, 52</sup> heterogeneous catalysis,<sup>53</sup> photo-redox catalysis,<sup>54</sup> catalyst platforms,<sup>55</sup> photovoltaic devices,<sup>56, 57, 58</sup> sensing<sup>59</sup> and energy storage<sup>60, 61</sup>. The development of design principles, synthetic strategies, structure analysis and structure functionalization have much improved explorations of new COFs structures and their applications.<sup>7, 49, 62</sup> COFs can be separated into three dimensional (3D) COFs and two dimensional COFs (2D). Till now, 2D COFs attracted more attention than 3D COFs due to several disadvantages of 3D COFs. Firstly, 3D COFs often cause crystallization issues, leading to harsher reaction conditions than in 2D COFs.<sup>63</sup> Besides, 3D COFs are relatively less stable than 2D COFs due to crystallization issues and absence of  $\pi$ - $\pi$  stacking.<sup>64</sup> In 2D COFs, there are not only covalent bonds in conjugated 2D sheets but also weak interactions (for example,  $\pi$ - $\pi$  stacking, hydrogen bonds and van der Waals' forces) in interlayers, which offer 2D COFs superior crystallinity and stability.<sup>49</sup> Secondly,  $\pi$  conjugation is always interrupted in 3D COFs caused by the core selection.<sup>65</sup> Since most 3D core molecules introduce at least one  $sp^3$ -hybridized carbon which lead to the loss of a major requirement for conjugation ( $sp/sp^2$  hybridization). Most 3D COFs cores include tetrahedral molecules, in which the center atoms or molecules are bonded with terminal groups via  $sp^3$  carbon or related atoms. For example, tetraphenylmethane, tetraphenylsilane, spirobifluorene and adamantane decorated with boronic acid, amino, aldehyde, nitroso, acyl chloride terminals are some of the most common cores (as shown in Figure 2).<sup>66, 67, 68, 69, 70</sup> These limited  $\pi$  conjugation often leads to undesirable effects in the optoelectronic performance of such 3D COFs. The optical and electrical properties, for example highest occupied molecular orbital (HOMO), lowest unoccupied molecular orbital (LUMO), band gaps, carrier density, carrier mobilities and conductivities, are very important to evaluate their suitability in optoelectronic and energy storage devices, such as solar cells and rechargeable batteries.<sup>71, 72, 73</sup> The band-like transport of charge carriers in ordered 2D COFs are superior over 3D COFs with additional advantages of flexibility, which enables flexible devices to be manufactured.<sup>74, 75</sup> The extended  $\pi$ -conjugation associated with molecular interactions between the layers in their secondary structures could enhance the electrical conductivity. A well-known 1D-example is polythiophene, where the conductivity is improved by engineering the long range order and molecule orientation.<sup>76, 77</sup> 2D COFs could combine electrical properties, porosity and serve as platforms for reactive anchoring sites for active centers of catalytic transformations.<sup>73, 78, 79</sup> 2D COF could show conductivities in a range of 10 to  $10^{-10}$  S  $cm^{-1}$  as conductors or

semiconductors.<sup>73</sup> As this thesis will be focused on optoelectronic applications, the discussion is mainly focused on conductive and semiconductive 2D COFs.

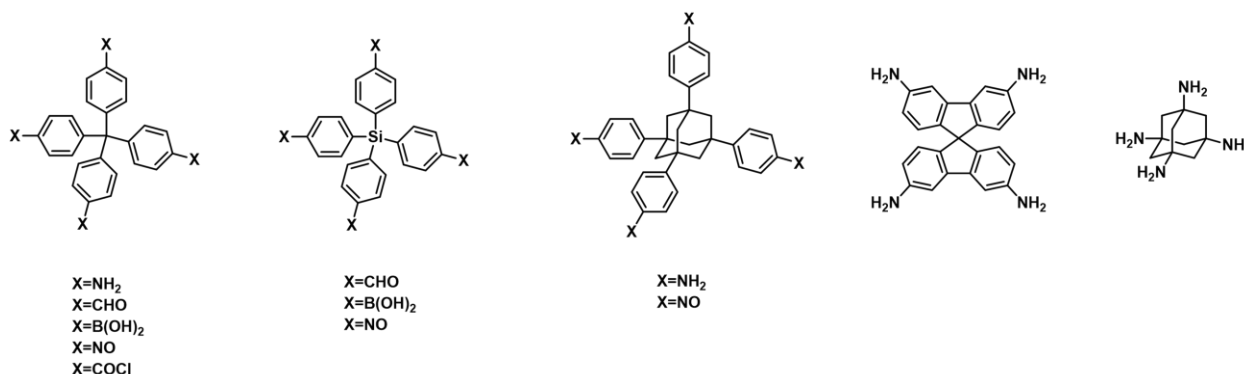


Figure 2. Tetrahedral cores.

### 1.2.1 Design principle

Similar with the synthesis of copolymers, the principle of COF synthesis is the polymerization of more than one species of monomers via different types of couplings. The essence of the topology design of COFs is combination of various cores and linkers into macrocycles with controlled formation of covalent bonds in a reversible bond formation process, together with a guided polymer backbone growth.<sup>24, 80</sup> Selecting molecules with relatively rigid backbones as cores or linkers would guarantee clear directions of covalent bonds forming. The formed covalent bonds would subsequently guide the assembly of the following molecular units and the spatial orientation. The following repeating steps guide directions of building blocks growth along with topology rules strictly. This topology diagram and the geometry of linkage molecules constitute the theoretical basis of COFs growth, which finally contribute to the extended highly ordered crystalline structure.<sup>24, 81</sup> Moreover, due to the equilibrium between framework and molecules, the formation of defects is relatively decreased compared to the irreversible growth of CMPs, thus leading to increased crystallinity. The formation of 2D COFs is also restricted in the rules of topology and molecule selections. 2D atomic COF layers would be generated by choosing planar molecules in the growth procedure, meanwhile periodically ordered open polygon spaces on the 2D x-y planes would also be formed. As most often selected molecules are aromatics with extended  $\pi$ -electron

system. layered structures are preferred to form because of  $\pi$ - $\pi$  stacking, which is a weak but attractive interlayer interaction. 2D atomic COF layers would stack with the neighboring layers in a manner of which each monomer unit is overlapped. This overlap would generate alignments of 2D COFs along the z direction, leading to 1D open pores, fully ordered  $\pi$ -arrays and structures with spatial lattice orientation and crystallinity at the same time.<sup>72, 82, 83</sup> Straight and continued channels generated via  $\pi$  stacking are opened on top and bottom layers and interconnected inside the layers.

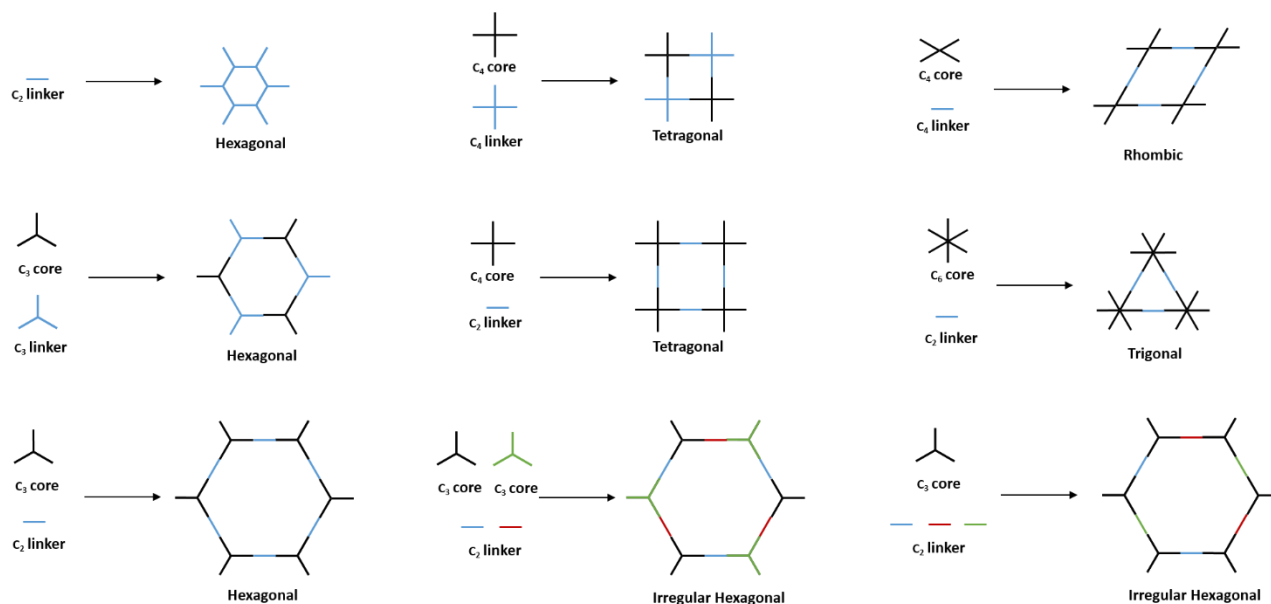


Figure 3. Basic topological diagrams for the design of COFs.

The design concept of COFs can be simplified to combinations of cores and linkers molecules with different geometry (shown in figure 3). The geometry is defined by  $C_n$ , which represent the n-fold principal axis of rotation.<sup>80</sup> The core molecule is the branched molecule which determines directions of covalent bonds formation and extends the building blocks into 2D or 3D frameworks, while linker refers to the monomer which connects the respective cores. The empty space inside the macrocycles surrounded by the connected cores and linkers represents different pore constructions. According to the number of cores and linkers for COFs building, design strategies can be divided into [1 core + 1 linker], [1 core + 2 linkers], [1 core + 3 linkers], [2 cores + 1 linker] and etc. The [1 linker] strategy is a special case, where molecules form cyclic oligomers, such as

dicyanobenzene<sup>47, 84</sup>, making them the linker and core unit at the same time. Depending on various geometry of molecules, design strategies can be separated into  $[C_3 + C_3]$ ,  $[C_3 + C_2]$ ,  $[C_4 + C_4]$ ,  $[C_4 + C_2]$ ,  $[C_6 + C_2]$  etc. (as shown in Figure 3). Various types of pore shapes and sizes can be generated with different design strategies.  $[C_3 + C_3]$ ,  $[C_3 + C_2]$ ,  $[C_3 + C_2 + C_2]$  and  $[C_3 + C_2 + C_2 + C_2]$  strategies would generate hexagonal pores, while the lattice generated by  $[C_3 + C_2 + C_2]$  and  $[C_3 + C_2 + C_2 + C_2]$  strategies consist of two and three types of trigonal pores with different sizes. Tetragonal pore structure would be formed via  $[C_4 + C_4]$ ,  $[C_4 + C_2]$  diagrams, while trigonal pores would be created by the  $[C_6 + C_2]$  strategy.<sup>83, 85, 86, 87</sup> Some  $[C_4 + C_4]$  diagrams would yield rhombic channels.<sup>80</sup> The regular polygons and isotropic tile structures are generated within the [1 core + 1 linker] strategy (also be called symmetric topologies) lead to a limited diversity of COFs. The introduction of multiple species to COFs design strategy would overcome this [1 core + 1 linker] strategy diversity limitation, which includes [1 core + 2 linkers], [1 core + 3 linkers] and [2 cores + 1 linker] design strategies (also be called asymmetric topologies).<sup>88, 89</sup> Within the multiple component strategy, lattice complexity is enhanced, pore types can be adjusted, at the same time, functional units can be integrated into COFs endowing specific properties. For example, multiple-component donor and acceptor units can be combined into COFs, in which specific arrays of donor and acceptor columns form intercolumnar pathways for charge carriers, finally endowing both hole and electron conductivity to COFs.<sup>24, 88, 90, 91</sup> Pore walls are constructed by the repeating building blocks and their stacking into 2D COF layers, allowing for an ordering in z direction (Figure 4 a). The formed angles between two neighboring faces can also be used to describe the geometry of pores or the polygonal frameworks, which are normally  $60^\circ$  (trigonal),  $90^\circ$  (tetragonal) and  $120^\circ$  (hexagonal), respectively (Figure 4 b).<sup>80</sup>



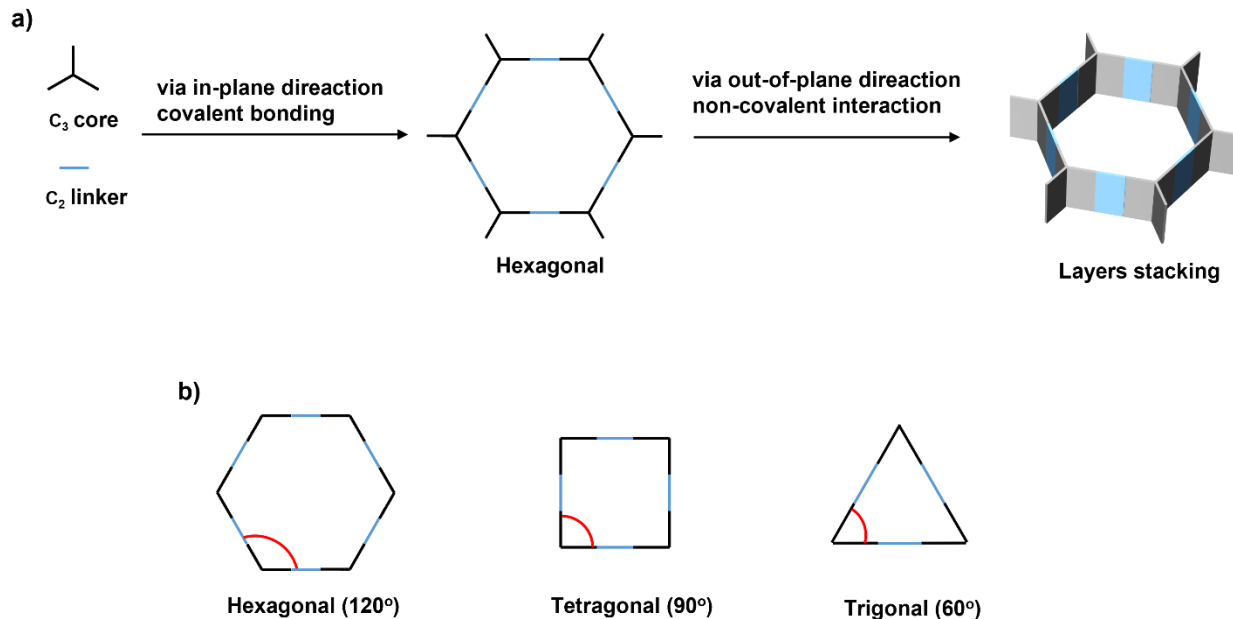


Figure 4. a) Combination of cores and linkers to form COFs (via in-plane, directional covalent bonding), COF layers stacking (via out-of-plane directional, non-covalent interaction) under formation of walls and channels. b) Different angles of polygonal COFs.

## 1.2.2 Properties and characterization of COFs

Crystallinity is the basic property to evaluate the structure of COFs, which can be measured by powder X-ray diffraction (PXRD).<sup>92</sup> COFs generate PXRD patterns with intense diffraction peaks, which reflect distinct orientation, highly ordered stacking and excellent homogeneity of structural periodicity.<sup>93</sup> Matching measured PXRD patterns with simulated structures can identify the pre-designed COFs structure. As different stacking types, eclipsed AA stacking represents lattices of neighboring successive layers that are exactly overlapped. In contrast, in the staggered AB stacking each second of repeat units overlaps.<sup>94</sup> Slipped AA-stacking is intermediate state between eclipsed AA stacking and staggered AB stacking, which gain superior stability. The PXRD patterns of slipped AA-stacking type COFs with different slip distances are similar due to broad signals which are hardly to distinguish.<sup>94</sup> *In situ* small-angle and wide-angle X-ray scattering (SAXS/WAXS) are advanced methods to monitor polymerization and crystallization of COFs

directly.<sup>95, 96</sup> Grazing-incidence X-ray diffraction (GID) measurements are used to gain information on preferred orientation of the COF thin films.<sup>74, 97, 98, 99</sup> Porosity, surface area and pore size are another basic property of COFs, which can be evaluated by gas sorption isotherm measurements. Gas sorption isotherm measurements are very important to describe quality of COFs, because it not only reveals surface areas but also allows pore size distributions to be calculated. Especially for heterogeneous pores in COFs, the different species of pores with various diameters derived from pore size distributions give a clear evidence for the present structure. Morphology of pores can be measured by transmission electron microscopy (TEM) or high resolution (HR) TEM. Notably, high energy of electron beam of HR-TEM can easily damage COF structure, which could be overcome by low-dose TEM techniques.<sup>100, 101</sup> Besides, the detailed information of COFs structure, such as chemical components and linkage types can be analyzed by Fourier transform infrared spectroscopy (FT-IR), or solid-state nuclear magnetic resonance (ssNMR) spectroscopy. Stability can be evaluated by thermogravimetric analysis (TGA).

### 1.2.3 Synthesis

Different from other organic porous materials like CMPs or most PIMs, COFs are always constructed through reversible reactions, in which mismatched covalent linkages are rebuilt in equilibrium with the corresponding monomers under formation of the favored ordered structure.<sup>102, 103</sup> This reversible process includes “proofreading” leading to mostly ordered, crystalline structures of COFs, which are more important for multiple component COFs synthesis without formation of defects. Reversible polycondensations are the most commonly used reaction for COF synthesis.<sup>104, 105</sup> However, some irreversible reactions under phenazine, dioxin or C=C formation have been used for COFs synthesis as well.<sup>48, 106, 107, 108, 109</sup>

Most COFs are synthesized through solvothermal methods, for which building blocks are required to be considerably soluble and reactive. Here, reaction conditions including temperature, time, solvent combinations, catalyst type and concentration are the most important parameters to be considered. In a standard solvothermal procedure, a mixture of core and linker molecules, suitable solvents and catalyst are filled into a reaction vessel, which is sonicated, sealed, degassed and heated to a specific temperature for a determinate period of time. The insoluble product is usually washed with a suitable solvent to remove residual solvents and oligomers. The as-prepared solid

is dried under high vacuum (HV) or supercritical fluid conditions.<sup>24, 110</sup> Microwave synthesis is a rapid method to prepare boronate-ester-links and imine links porous crystalline COFs.<sup>111, 112, 113</sup> The advantages of microwave synthesis are not only reduced reaction times, but also improved the “removal” of residual oligomers to form COFs of increased porosity.<sup>111</sup> The COFs prepared with the methods mentioned above are usually insoluble solids. Therefore, COF thin film fabrication is desirable and can be accomplished by interfacial synthesis (Figure 5). COF thin films are formed at the interface of organic and aqueous phase, which dissolve building blocks and catalyst, respectively. The thickness of COF thin films can be tuned from 5 to 200 nm with this approach.<sup>114, 115, 116, 117</sup>

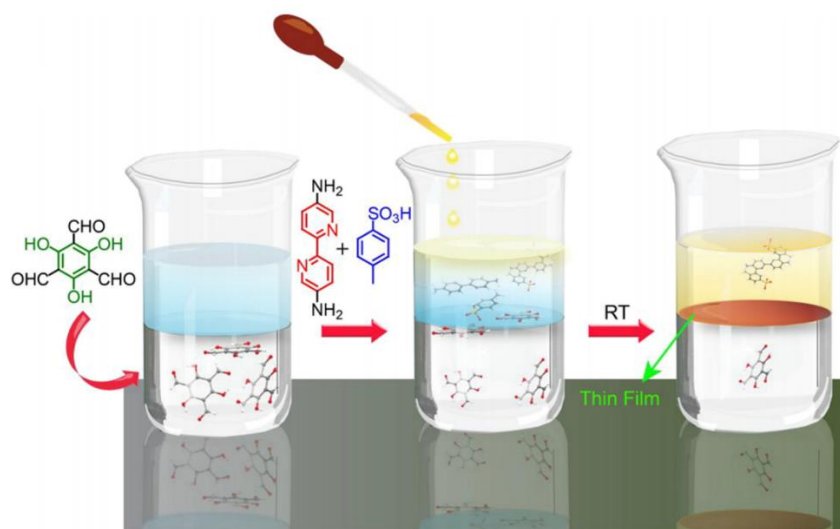


Figure 5. Formation of COF thin films by interfacial synthesis.<sup>114</sup>

## 1.2.4 Linkages and reaction conditions

The knots between cores and linkers are defined as linkages, which can also be considered as bonding types for the different reactions. Most core and linker molecules for COFs possess rigid  $\pi$ -backbones. The solubility of cores and linkers is strongly depended on the size of  $\pi$ -system and molecular rigidity. Normally, both polar and nonpolar solvent are employed as reaction medium for reversible covalent bond generation. One common type of used linkages are boronate-esters<sup>44, 118</sup>, imine<sup>67, 119, 120</sup>, boroxine<sup>121</sup>, triazine<sup>47</sup>, borazine<sup>122</sup>, azine<sup>123</sup>, phenazine<sup>124</sup>, imide<sup>125</sup>,  $C=C$ <sup>48, 126</sup>,

amide<sup>127</sup> and 1,4-dioxin<sup>108</sup>.(as shown in Figure 5.) According to different elemental compositions, the above linkages can be classified as B-O bonding, C-N bonding and C-C bonding linkages. For example, boronic ester and boroxine linkages belong to B-O bonding linkages, imine, triazine, azine, phenazine and imide linkages are classified into C-N bonding. C-C single bond and C=C double bond linkages are ranged into C-C bonding linkages. Among these linkages, some of them require specific reaction conditions. For example, ortho-difluoro-benzene or -pyridine and catechol derivatives are required as cores and linkers, respectively, to generate 1,4-dioxin linkages through condensation with base as catalyst. The as-prepared COFs show better chemical stability because they contain irreversible dioxin linkages.<sup>108, 109</sup> Triazine linkages are specific linkages for CTFs, which are formed by cyclotrimerization of e.g. 1,4-benzonitrile in molten ZnCl<sub>2</sub> on 450°C.<sup>47</sup> The crystallinity of CTFs is relative low due to the limited reversibility of the cyclotrimerization reaction. The number of CTFs is also low because of the lack of diversity from the requirement of reacting monomers with cyano groups. Trifluoromethanesulfonic acid can be used to replace molten ZnCl<sub>2</sub> as catalyst reagent to overcome disadvantages of high temperature and ZnCl<sub>2</sub> residuals.<sup>128</sup> C-C linkages are generated e.g. via Suzuki coupling, which is an irreversible reaction often leading to less crystalline COFs.<sup>117</sup> Borosilicate linkages result in an interruption of the conjugated system resulting it lower conductivity. As this thesis focusses on photoelectric application, we pay more attention to linkages that allow for better conductivity values.

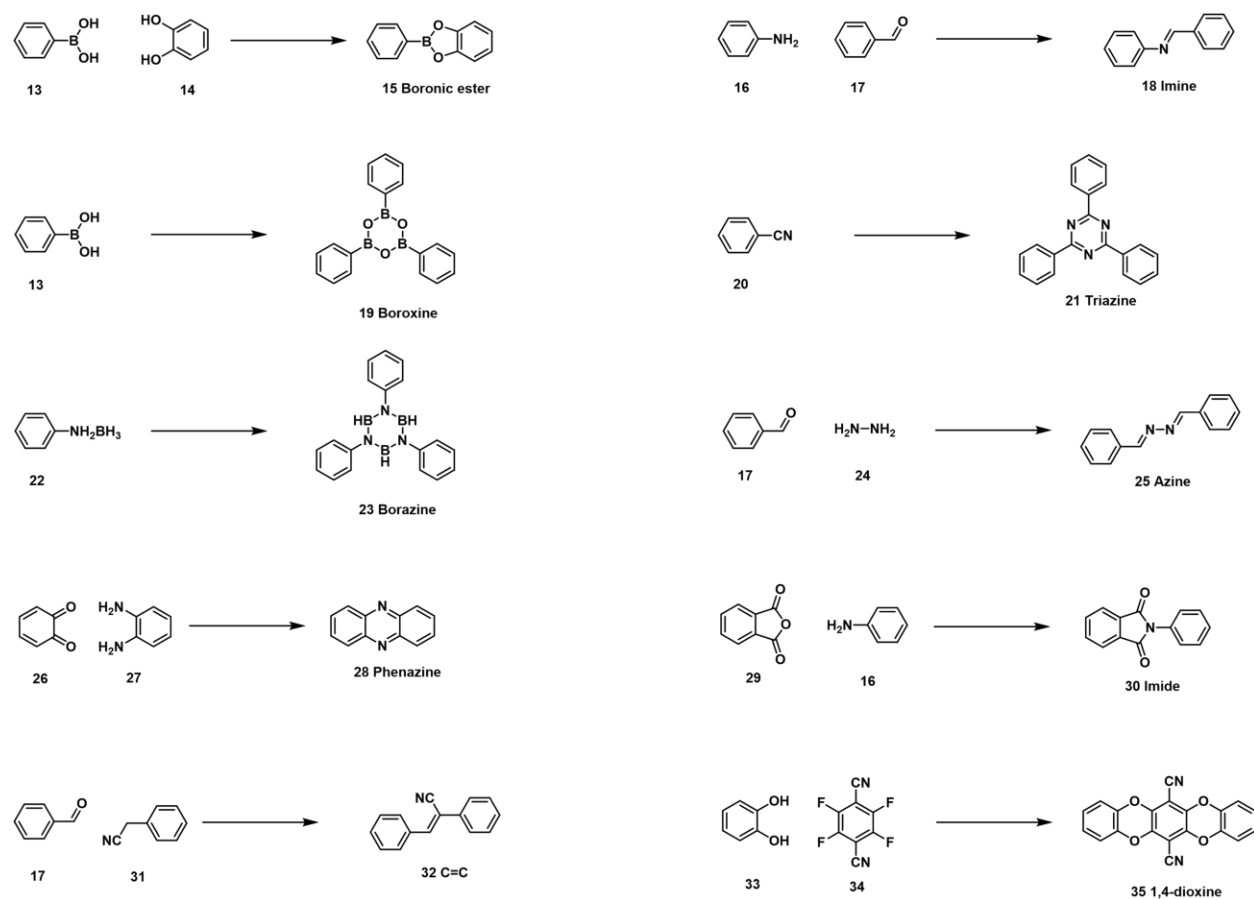


Figure 6. Various linkages for COFs synthesis.

Imine linkages are another type of commonly used linkages, which are usually generated through Schiff-base condensation reactions of aromatic amine and aldehyde formations by using Brønsted acids, for example acetic acid, as catalyst. Similar to imine linkages, imide linkages are formed by condensation of amine derivatives and acetic anhydride, but this requires higher temperatures, which can be higher than 250 °C. This reaction is less reversible, leading to less crystalline COFs. These two linkages are typical C-N linkages. The standard conditions for C-N linkages formation are comparable to the formation conditions for B-O linking, including solvothermal conditions and the necessity of catalysts. (Shown in Table 1) The first C-N type electrically conductive 2D-COFs were reported in 2011 by Yaghi, with charge carrier mobilities comparable to polycrystalline silicon.<sup>129</sup> Compared to B-O linked COFs, C-N linked COFs possess superior chemical stability and higher electrical conductivity due to the existence of electron-rich N atoms. Conductivity can

be further improved by introducing additional functional units into building blocks. For example, electron-donating tetrathiafulvalene was used to synthesize electrically conductive 2D COF, which showed remarkable electrical performance as p-type semiconductors with charge carrier mobilities of up to  $0.2 \text{ cm}^2 \text{ V}^{-1} \text{ s}^{-1}$ . The high conductivity was attributed to conduction channels formed in the highly crystalline  $\pi$ -arrays. Further, smaller interlayer distances also contribute to higher charge carrier mobilities.<sup>98, 130</sup>

Table 1. Various reaction conditions of C-O-and C-N-type COFs.

COFs	Linkage type	Solvents (v/v)	Catalyst	Temperature (°C)	Reaction time (d)
COF-8 <sup>131</sup>	C-O	Dioxane/Mesitylene (1/1)		85	3
DBA-3D-COF <sup>132</sup>	C-O	Dioxane/Mesitylene (10/1)		95	3
H <sub>2</sub> P-COF <sup>133</sup>	C-O	Dioxane/Mesitylene (1/9)		120	4
TT-COF <sup>134</sup>	C-O	Dioxane/Mesitylene (1/1)		150	3
D <sub>TP</sub> -A <sub>Pyridi</sub> -COF <sup>58</sup>	C-O	DMAc/DCB (1/1)		120	7
Py-1P COF <sup>135</sup>	C-N	Dioxane/Mesitylene (1/2)	6 M AcOH	120	3
BF-COF-1 <sup>136</sup>	C-N	Mesitylene	3 M AcOH	120	5
CCOF-7 <sup>137</sup>	C-N	EtOH/Mesitylene (3/1)	9 M AcOH	120	3
SP-3D-COF-1 <sup>138</sup>	C-N	o-DCB/BuOH (7/3)	AcOH	130	3
TAPB-PDA COF <sup>139</sup>	C-N	Dioxane/Mesitylene (4/1)	7.5 $\mu\text{M}$ Sc(OTf) <sub>3</sub>	20	3

## 1.2.5 Reaction mechanisms

The mechanism of porous crystalline COFs generation can be separated into two steps, which are polycondensation and crystallization that occur in a concerted fashion. The polycondensation starts with the coupling reaction of cores and linkers leading to oligomers with varying numbers of repeat

units. The formed oligomers will further react with each other to generate polymers of different molecular weight extension. After crystallization of these polymers under specific conditions, porous crystalline COFs are formed. As C-N-type COFs offer superior stability over B-O-type COFs, the reaction mechanism discussion will be focused on C-N-type COFs. The generation of C-N COFs is based on the dynamic nature of imine bond formation.<sup>140</sup> In a standard procedure, core and linker molecules are dissolved in suitable solvent systems to form a homogeneous solution. After addition of aqueous acetic acid as catalyst, a solid as amorphous polymer with very low specific surface area precipitates immediately. Finally, the amorphous polymer transforms into crystalline COFs under specific conditions. The absence of “free” monomer will not inhibit this transformation, but the absence of acetic acid will. The increased BET surface area indicates the successful transformation from amorphous polymers to crystalline COFs during elongated reaction times. Another important condition is the pH value, which is controlled between 6 to 7 to assist the transformation from low crystallinity polymers to high crystallinity COFs.<sup>141</sup> Besides, both the average size of COF particles and crystalline domains will be decreased with the reduced concentration of core and linker monomers, and the growth of COF particles occurs faster than crystallization, which are proved by in situ SAXS/WAXS.<sup>96</sup>

## 1.2.6 Functional Exploration and Applications

Similar with other porous materials, COFs were initially designed for applications of gas storage and separation due to the advantages of lightweight element composition, low specific weight and high surface area.<sup>142, 143</sup> Considering the increasing pressure of environmental challenges, research fields of hydrogen storage, carbon capture technologies and the production and storage of renewable energies are of great importance. COFs are highly interesting for many of such applications, like hydrogen and energy storage, which will be shortly introduced. But the most interesting part of COF is the diversity of structural design, that various functional groups or building blocks can be incorporated into COF skeletons with atomic precision to endowing new properties. Especially semiconductor property given by the incorporation of electron donating or withdrew units offers functionalized COFs potential applications in the fields of electrocatalysis and photovoltaic devices what is not possible with the “original” COFs. Continuously connected  $\pi$ -orbitals in their backbones form extended conjugated system of organic semiconductors. After

absorbing light or other suitable energy, electrons in the HOMO (highest occupied molecular orbital) are excited to the LUMO (lowest unoccupied molecular orbital) through bandgap (gap between HOMO and LUMO). The excited electrons can move freely or flow to specific direction forming photocurrent based on different devices. The COFs act as semiconductor since the skeletons of them possess extended  $\pi$ -conjugated system. Besides, similar with other well-known organic semiconductors, COFs can be designed as p-type, n-type and ambipolar semiconductor COFs based on their structure. p-type COFs are generated through incorporation of electron-donating groups or building blocks into the skeletons, in which triphenylene, pyrene, porphyrin, and phthalocyanine are the most common ones. By contrast, n-type COFs are produced by incorporating electron-deficient units, such as nickel phthalocyanine and benzothiadiazole into skeletons. When electron-rich donor (D) and electron-deficient acceptor (A) units are together incorporated into one skeletons ambipolar COFs result.<sup>144</sup> In this thesis, the use of COFs in perovskite solar cells (PSCs) will be investigated. Therefore, the basic principle of PSCs will be discussed later.

COF-based materials are widely used in supercapacitors and rechargeable batteries. For example, COFs resulting from 2,6-diaminoanthraquinone (DAQ) and 1,3,5-triformylphloroglucinol (TFP) are (DAQ-TFP COF) show charge-discharge ability due to the pseudo-capacities introduced by TFP cores and DAQ linkers. Two-electron and two-proton processes occurring in the reversible redox reaction between anthraquinone and 9,10-dihydroxyanthracenes offer pseudo-capacity to DAQ-TFP COF (as shown in Figure 7 A).

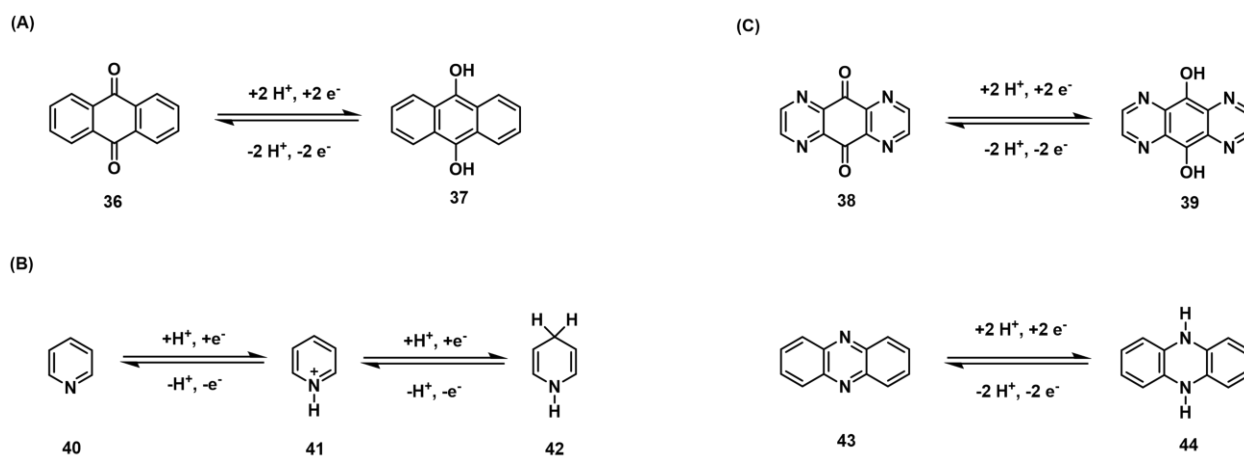


Figure 7. (A) Reversible redox reaction of anthraquinone (A), pyridine (B) and phenazine (C).



TaPa-Py COF are synthesized by condensation of TFP cores and diaminopyridine (DAP) linkers containing a pyridine unit, which also show reversible electrochemical activity in 1 M H<sub>2</sub>SO<sub>4</sub> electrolyte. The reversible electrochemical reaction starts with the formation of pyridinyl radical, in which pyridine absorbs one proton together with an electron. The resulting dihydropyridine is generated by absorption of another proton electron pair (processes are shown in Figure 7 B). Imides, quinones and their derivatives are the most widely used building blocks in organic electrode materials due to their high specific capacity and electrochemical charging reversibility of carbonyl groups (as shown in Figure 8).

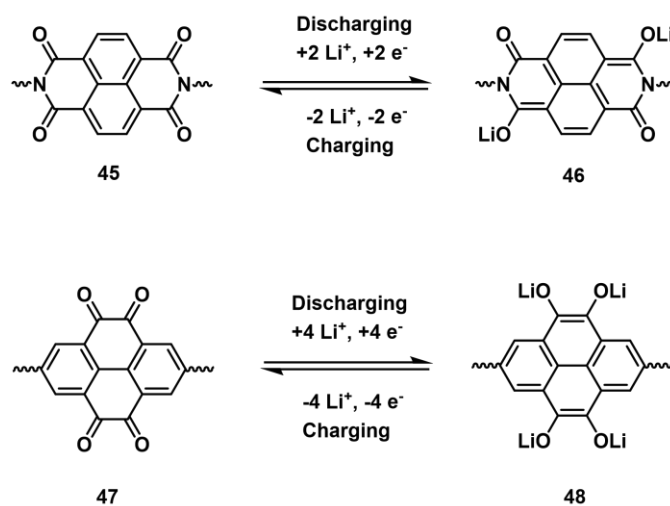
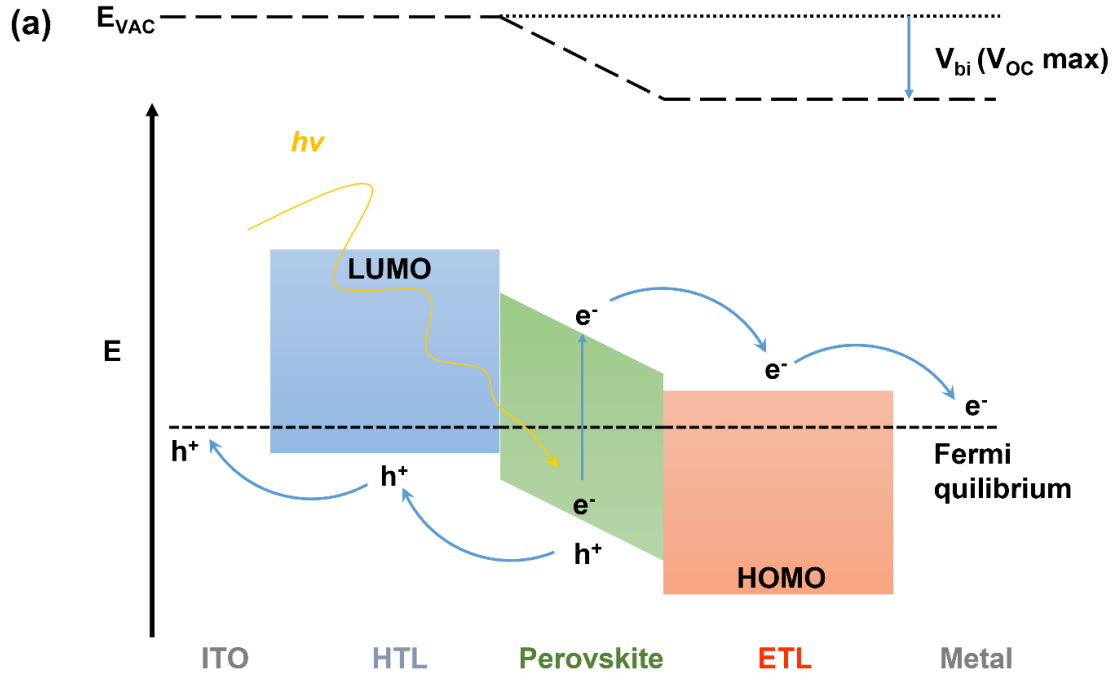


Figure 8. Charging/discharging mechanism of typical carbonyl-based materials for Li-ion batteries.

OSCs can be simplified to a model which is composed of a donor-acceptor junction sandwiched by two electrodes with different work function. Build-in electric field (work function difference) is created when two electrodes get touched because driven by the Fermi equilibrium (chemical potential equilibrium). When solar energy radiates to the donor-acceptor junction, excitons (a pair of electron and hole) are generated, electrons are excited from the HOMO to the LUMO across the gap, holes are left. Electrons and holes are diffused in donor and separated at the interface of donor-acceptor junction driven by an offset in the LOMO ( $\Delta\text{LUMO}=\text{LUMO}_{\text{donor}}-\text{LUMO}_{\text{acceptor}}$ ) or the HOMO ( $\Delta\text{HOMO}=\text{HOMO}_{\text{donor}}-\text{HOMO}_{\text{acceptor}}$ ) during their lifetime. Once the separation occurring, the electrons and holes are transported to the cathode and anode respectively, due to the driving

force of build-in field, forming a closed conductive pathway. The principle of PSCs is a little different from OSCs. A perovskite active layer is sandwiched between hole transport layers (HTLs) and electron transport layer (ETLs), where excitons are generated by solar energy absorption, and separated into electrons and holes. Later the separated electrons and holes are transported to cathode and anode from ETLs and HTLs respectively. PSCs, a promising new type of photovoltaic device, received much attention because of their rapid development in efficiency from 3.8% in 2009 to 25.7% in 2022.<sup>145, 146, 147, 148</sup> The working principle of PSCs are similar to those described before (Figure 9 a). Until now, most PSCs with high photoelectric conversion efficiency (PCE) are constructed by organic–inorganic hybrid perovskite with  $ABX_3$  formular, in which A represents an organic cation such as methylammonium ( $MA^+$ ), formamidinium ( $FA^+$ ) or their mixture, B equals inorganic cation  $Pb^{2+}$  and X is  $Br^-$ ,  $I^-$  or mixture of these (Perovskite crystal structure and formation scheme samples of perovskite are shown in Figure 9 b). Much effort have been given to achieve improved performances of PSCs, such as compositional tuning of the perovskite active layer<sup>149</sup>, developing new charge transport materials<sup>150</sup>, optimizing interfaces<sup>151</sup> and engineering defects<sup>152</sup>.



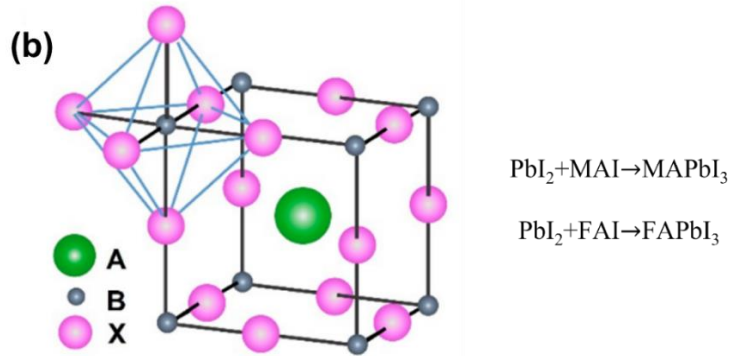


Figure 9. a) Energy-level diagram and the working process of PSCs. b) Perovskite crystal structure, where large cation A represents  $\text{MA}^+$  or  $\text{FA}^+$ , small cation B represents  $\text{Pb}^{2+}$  and X anion represents a halogen ion, such as  $\text{Br}^-$ ,  $\text{I}^-$ , respectively.<sup>153</sup>

The publications on COF application in PSCs are rare. Zhao and co-workers synthesized two COFs, namely SP-3D-COF 1 and SP-3D-COF 2, which are highly conjugated 3D COFs with 3,3',6,6'-tetraamine-9,9'-spirobifluorene as core unit linked by 1,4-phthalaldehyde or 4,4'-biphenyldicarbaldehyde. Both materials are assembled with  $\text{CH}_3\text{NH}_3\text{PbI}_3$  as photoactive material to constitute p-i-n devices by directly mixing COFs bulk into the perovskite precursor solution. Compared with the undoped devices, the COF-doped PSCs show diode characteristics with a lower leakage current, along with improved  $J_{\text{SC}}$  (short circuit current density) and FF (fill factor) leading to devices with increased PCEs of up to 19.07 %. The doped COFs serve as template or heterogenous nucleation sites for  $\text{CH}_3\text{NH}_3\text{PbI}_3$  crystallization leading to an improved crystal structure formation of the perovskite. The formation of a closer and larger contact with the perovskite is attributed to an increased electron mobility.<sup>138</sup> Kuo and co-workers synthesized two 2D imine linked Car-ETTA and TFPPy-ETTA COFs with 4,4',4'',4'''-(ethene-1,1,2,2-tetrayl)tetraaniline (ETTA) as core, 3,3',6,6'-tetraformyl-9,9'-bicarbazole (Car-4CHO) and 1,3,6,8-tetra(4-formylphenyl)pyrene (TFPPy) as linkers, respectively. These two COFs were spin-coated on top of poly[bis(4-phenyl)(2,4,6-trimethylphenyl)amine (PTAA) as interlayer to fabricate p-i-n PSCs device with  $(\text{FAPbI}_3)_{0.83}(\text{MAPbBr}_3)_{0.17}(\text{CsPbI}_3)_{0.05}$  as photo active layer. The PCEs are increased up to 19.79 for TFPPy-ETTA COFs and Car-ETTA, respectively. These two COFs are able to modify the PTAA layer by improving the charge transfer efficiency across the

perovskite/PTAA interface. This is due to the well-conjugated structure of the COFs and due to a better quality of the perovskite films caused by the template effect of COFs. The improved  $V_{oc}$  (open circuit voltage) can be attributed to the decreased charge recombination at the perovskite/PTAA interface and the better HOMO (highest occupied molecular orbital) level alignment between perovskite layer and COF-modified PTAA layer.<sup>154</sup>

### 1.3 Motivation and Objectives

Recombination at interfaces is the core factor to performance losses for PSCs. Attempts have been made to minimize the interfacial recombination between ETL and perovskite or HTL and perovskite by optimizing existing materials or exploiting new materials. On this point of view, various novel molecules and polymers were synthesized as HTLs or ETLs to fit with the energy levels of perovskite layers and to build optimized interfaces towards high performance PSCs. For “ideal” HTLs or ETLs materials, various fundamental requirements should be considered, such as suitable energy levels and high hole/electron mobility. Processability is another key factor among these requirements. We set HTLs materials as example to explain in the most commonly used solution process. In p-i-n OSCs, HTLs materials should be soluble/processable in common solvents (e.g. chlorobenzene) but insoluble in the perovskite precursor solvents (e.g. NMP, DMF and DMSO), allowing for the formation of a controllable and defined HTL/perovskite interface. In n-i-p devices, the HTL materials should be soluble in solvents which cannot dissolve the as-deposited perovskite layer, avoiding blending of both materials. COFs are stable frameworks that will not dissolve in any solvent after formation, which constitutes the theoretical basis for the objective to apply COFs as charge transport layers in PSCs. Additionally, designability of HOMO, LUMO, band gap and charge mobility of COFs offer additional possibilities. The major objectives of this thesis as included in the following chapters are:

- Synthesis of small molecules to be used as HTL materials of COF precursor.
- Assembly of PSCs with COF films as HTL.

### 1.4 References

1. Little, M. A.; Cooper, A. I., *Adv. Funct. Mater.* **2020**, *30* (41), 1909842.

2. Tian, Y.; Zhu, G., *Chem. Rev.* **2020**, *120* (16), 8934.
3. Lee, J. M.; Cooper, A. I., *Chem. Rev.* **2020**, *120* (4), 2171.
4. Das, S.; Heasman, P.; Ben, T.; Qiu, S., *Chem. Rev.* **2017**, *117* (3), 1515.
5. Zhang, Y.; Riduan, S. N., *Chem. Soc. Rev.* **2012**, *41* (6), 2083.
6. Kaur, P.; Hupp, J. T.; Nguyen, S. T., *ACS Catal.* **2011**, *1* (7), 819.
7. Gui, B.; Lin, G.; Ding, H.; Gao, C.; Mal, A.; Wang, C., *Acc. Chem. Res.* **2020**, *53* (10), 2225.
8. Li, Y.; Chen, W.; Xing, G.; Jiang, D.; Chen, L., *Chem. Soc. Rev.* **2020**, *49* (10), 2852.
9. Sun, Q.; Aguila, B.; Song, Y.; Ma, S., *Acc. Chem. Res.* **2020**, *53* (4), 812.
10. Meng, X.; Xiao, F. S., *Chem. Rev.* **2014**, *114* (2), 1521.
11. Heidarinejad, Z.; Dehghani, M. H.; Heidari, M.; Javedan, G.; Ali, I.; Sillanpää, M., *Environ. Chem. Lett.* **2020**, *18* (2), 393.
12. Yu, L.; Hu, L.; Anasori, B.; Liu, Y.-T.; Zhu, Q.; Zhang, P.; Gogotsi, Y.; Xu, B., *ACS Energy Lett.* **2018**, *3* (7), 1597.
13. Moller, K.; Bein, T., *Chem. Soc. Rev.* **2013**, *42* (9), 3689.
14. Roth, W. J.; Nachtigall, P.; Morris, R. E.; Cejka, J., *Chem. Rev.* **2014**, *114* (9), 4807.
15. Serrano, D. P.; Escola, J. M.; Pizarro, P., *Chem. Soc. Rev.* **2013**, *42* (9), 4004.
16. Perez-Ramirez, J.; Christensen, C. H.; Egeblad, K.; Christensen, C. H.; Groen, J. C., *Chem. Soc. Rev.* **2008**, *37* (11), 2530.
17. Chen, L. H.; Sun, M. H.; Wang, Z.; Yang, W.; Xie, Z.; Su, B. L., *Chem. Rev.* **2020**, *120* (20), 11194.
18. Bacakova, L.; Vandrovцова, M.; Kopova, I.; Jirka, I., *Biomater. Sci.* **2018**, *6* (5), 974.
19. Kerstens, D.; Smeyers, B.; Van Waeyenberg, J.; Zhang, Q.; Yu, J.; Sels, B. F., *Adv. Mater.* **2020**, *32* (44), 2004690.
20. Dusselier, M.; Davis, M. E., *Chem. Rev.* **2018**, *118* (11), 5265.
21. Slater, A. G.; Cooper, A. I., *Science* **2015**, *348* (6238), 988.
22. Ji, Z.; Wang, H.; Canossa, S.; Wuttke, S.; Yaghi, O. M., *Adv. Funct. Mater.* **2020**, *30* (41), 2000238.
23. Furukawa, H.; Cordova, K. E.; O'Keeffe, M.; Yaghi, O. M., *Science* **2013**, *341* (6149), 1230444.
24. Geng, K.; He, T.; Liu, R.; Dalapati, S.; Tan, K. T.; Li, Z.; Tao, S.; Gong, Y.; Jiang, Q.; Jiang, D., *Chem. Rev.* **2020**, *120* (16), 8814.
25. Xu, Y.; Jin, S.; Xu, H.; Nagai, A.; Jiang, D., *Chem. Soc. Rev.* **2013**, *42* (20), 8012.
26. Kratochvil, P.; Septo, R.; Suter, U., *Pure Appl. Chem.* **1996**, *68*, 2287.
27. Giri, N.; Del Pópolo, M. G.; Melaugh, G.; Greenaway, R. L.; Rätzke, K.; Koschine, T.; Pison, L.; Gomes, M. F. C.; Cooper, A. I.; James, S. L., *Nature* **2015**, *527* (7577), 216.
28. O'Reilly, N.; Giri, N.; James, S. L., *Chem. Eur. J.* **2007**, *13* (11), 3020.
29. Holst, J. R.; Trewin, A.; Cooper, A. I., *Nat. Chem.* **2010**, *2* (11), 915.
30. Chen, H.; Tu, H.; Hu, C.; Liu, Y.; Dong, D.; Sun, Y.; Dai, Y.; Wang, S.; Qian, H.; Lin, Z.; Chen, L., *J. Am. Chem. Soc.* **2018**, *140* (3), 896.
31. Bunck, D. N.; Dichtel, W. R., *J. Am. Chem. Soc.* **2013**, *135* (40), 14952.
32. Hu, Y.; Dunlap, N.; Wan, S.; Lu, S.; Huang, S.; Sellinger, I.; Ortiz, M.; Jin, Y.; Lee, S.-h.; Zhang, W., *J. Am. Chem. Soc.* **2019**, *141* (18), 7518.
33. Slater, A. G.; Cooper, A. I., *Science* **2015**, *348* (6238), 988.
34. McKeown, N. B.; Budd, P. M., *Macromolecules* **2010**, *43* (12), 5163.

35. Wood, C. D.; Tan, B.; Trewin, A.; Niu, H.; Bradshaw, D.; Rosseinsky, M. J.; Khimyak, Y. Z.; Campbell, N. L.; Kirk, R.; Stöckel, E.; Cooper, A. I., *Chem. Mater.* **2007**, *19* (8), 2034.
36. Lee, J. Y.; Wood, C. D.; Bradshaw, D.; Rosseinsky, M. J.; Cooper, A. I., *Chem. Commun.* **2006**, (25), 2670.
37. Lu, W.; Yuan, D.; Zhao, D.; Schilling, C. I.; Plietzsch, O.; Muller, T.; Bräse, S.; Guenther, J.; Blümel, J.; Krishna, R.; Li, Z.; Zhou, H.-C., *Chem. Mater.* **2010**, *22* (21), 5964.
38. Plietzsch, O.; Schade, A.; Hafner, A.; Huuskonen, J.; Rissanen, K.; Nieger, M.; Muller, T.; Bräse, S., *Eur. J. Org. Chem.* **2013**, *2013* (2), 283.
39. Jia, J.; Chen, Z.; Jiang, H.; Belmabkhout, Y.; Mouchaham, G.; Aggarwal, H.; Adil, K.; Abou-Hamad, E.; Czaban-Jóźwiak, J.; Tchalala, M. R.; Eddaoudi, M., *Chem* **2019**, *5* (1), 180.
40. Ashraf, S.; Liu, C.; Li, S.; Haq, I.-u.; Mehmood, M.; Li, P.; Wang, B., *ACS Appl. Mater. Interfaces* **2020**, *12* (36), 40372.
41. Liu, M.; Guo, L.; Jin, S.; Tan, B., *J. Mater. Chem. A* **2019**, *7* (10), 5153.
42. Yuan, S.; Feng, L.; Wang, K.; Pang, J.; Bosch, M.; Lollar, C.; Sun, Y.; Qin, J.; Yang, X.; Zhang, P.; Wang, Q.; Zou, L.; Zhang, Y.; Zhang, L.; Fang, Y.; Li, J.; Zhou, H. C., *Adv. Mater.* **2018**, *30* (37), 1704303.
43. Mancuso, J. L.; Mroz, A. M.; Le, K. N.; Hendon, C. H., *Chem. Rev.* **2020**, *120* (16), 8641.
44. Côté, A. P.; Benin, A. I.; Ockwig, N. W.; O'Keeffe, M.; Matzger, A. J.; Yaghi, O. M., *Science* **2005**, *310* (5751), 1166.
45. Fischbach, D. M.; Rhoades, G.; Espy, C.; Goldberg, F.; Smith, B. J., *Chem. Commun.* **2019**, *55* (25), 3594.
46. Ma, T.; Kapustin, E. A.; Yin, S. X.; Liang, L.; Zhou, Z.; Niu, J.; Li, L.-H.; Wang, Y.; Su, J.; Li, J.; Wang, X.; Wang, W. D.; Wang, W.; Sun, J.; Yaghi, O. M., *Science* **2018**, *361* (6397), 48.
47. Kuhn, P.; Antonietti, M.; Thomas, A., *Angew. Chem. Int. Ed.* **2008**, *47* (18), 3450.
48. Zhuang, X.; Zhao, W.; Zhang, F.; Cao, Y.; Liu, F.; Bi, S.; Feng, X., *Polym. Chem.* **2016**, *7* (25), 4176.
49. Guan, X.; Chen, F.; Fang, Q.; Qiu, S., *Chem. Soc. Rev.* **2020**, *49* (5), 1357.
50. Wang, Z.; Zhang, S.; Chen, Y.; Zhang, Z.; Ma, S., *Chem. Soc. Rev.* **2020**, *49* (3), 708.
51. Keller, N.; Bein, T., *Chem. Soc. Rev.* **2021**, *50* (3), 1813.
52. Yang, S.; Streater, D.; Fiankor, C.; Zhang, J.; Huang, J., *J. Am. Chem. Soc.* **2021**, *143* (2), 1061.
53. Guo, J.; Jiang, D., *ACS Cent. Sci.* **2020**, *6* (6), 869.
54. Zhao, X.; Pachfule, P.; Thomas, A., *Chem. Soc. Rev.* **2021**, *50* (12), 6871.
55. Liu, R.; Tan, K. T.; Gong, Y.; Chen, Y.; Li, Z.; Xie, S.; He, T.; Lu, Z.; Yang, H.; Jiang, D., *Chem. Soc. Rev.* **2021**, *50* (1), 120.
56. Calik, M.; Auras, F.; Salonen, L. M.; Bader, K.; Grill, I.; Handloser, M.; Medina, D. D.; Dogru, M.; Löbermann, F.; Trauner, D.; Hartschuh, A.; Bein, T., *J. Am. Chem. Soc.* **2014**, *136* (51), 17802.
57. Kim, T. W.; Jun, S.; Ha, Y.; Yadav, R. K.; Kumar, A.; Yoo, C.-Y.; Oh, I.; Lim, H.-K.; Shin, J. W.; Ryoo, R.; Kim, H.; Kim, J.; Baeg, J.-O.; Ihee, H., *Nat. Commun.* **2019**, *10* (1), 1873.
58. Jin, S.; Furukawa, K.; Addicoat, M.; Chen, L.; Takahashi, S.; Irle, S.; Nakamura, T.; Jiang, D., *Chem. Sci.* **2013**, *4* (12), 4505.
59. Liu, X.; Huang, D.; Lai, C.; Zeng, G.; Qin, L.; Wang, H.; Yi, H.; Li, B.; Liu, S.; Zhang, M.; Deng, R.; Fu, Y.; Li, L.; Xue, W.; Chen, S., *Chem. Soc. Rev.* **2019**, *48* (20), 5266.
60. Li, M.; Liu, J.; Zhang, T.; Song, X.; Chen, W.; Chen, L., *Small* **2021**, *17* (22), 2005073.
61. Sun, T.; Xie, J.; Guo, W.; Li, D. S.; Zhang, Q., *Adv. Energy Mater.* **2020**, *10* (19), 1904199.

62. Yang, J.; Kang, F.; Wang, X.; Zhang, Q., *Mater. Horiz.* **2021**, DOI: 10.1039/d1mh00809a.
63. Waller, P. J.; Gandara, F.; Yaghi, O. M., *Acc. Chem. Res.* **2015**, *48* (12), 3053.
64. Kandambeth, S.; Dey, K.; Banerjee, R., *J. Am. Chem. Soc.* **2019**, *141* (5), 1807.
65. Tan, C.; Cao, X.; Wu, X. J.; He, Q.; Yang, J.; Zhang, X.; Chen, J.; Zhao, W.; Han, S.; Nam, G. H.; Sindoro, M.; Zhang, H., *Chem. Rev.* **2017**, *117* (9), 6225.
66. El-Kaderi, H. M.; Hunt, J. R.; Mendoza-Cortés, J. L.; Côté, A. P.; Taylor, R. E.; O'Keeffe, M.; Yaghi, O. M., *Science* **2007**, *316* (5822), 268.
67. Uribe-Romo, F. J.; Hunt, J. R.; Furukawa, H.; Klöck, C.; O'Keeffe, M.; Yaghi, O. M., *J. Am. Chem. Soc.* **2009**, *131* (13), 4570.
68. Beaudoin, D.; Maris, T.; Wuest, J. D., *Nat. Chem.* **2013**, *5* (10), 830.
69. Stewart, D.; Antypov, D.; Dyer, M. S.; Pitcher, M. J.; Katsoulidis, A. P.; Chater, P. A.; Blanc, F.; Rosseinsky, M. J., *Nat. Commun.* **2017**, *8* (1), 1102.
70. Li, Z.; Li, H.; Guan, X.; Tang, J.; Yusran, Y.; Li, Z.; Xue, M.; Fang, Q.; Yan, Y.; Valtchev, V.; Qiu, S., *J. Am. Chem. Soc.* **2017**, *139* (49), 17771.
71. Bessinger, D.; Ascherl, L.; Auras, F.; Bein, T., *J. Am. Chem. Soc.* **2017**, *139* (34), 12035.
72. Ding, X.; Guo, J.; Feng, X.; Honsho, Y.; Guo, J.; Seki, S.; Maitrad, P.; Saeki, A.; Nagase, S.; Jiang, D., *Angew. Chem. Int. Ed.* **2011**, *50* (6), 1289.
73. Bian, G.; Yin, J.; Zhu, J., *Small* **2021**, *17* (22), 2006043.
74. Colson, J. W.; Woll, A. R.; Mukherjee, A.; Levendorf, M. P.; Spitler, E. L.; Shields, V. B.; Spencer, M. G.; Park, J.; Dichtel, W. R., *Science* **2011**, *332* (6026), 228.
75. Sahabudeen, H.; Qi, H.; Glatz, B. A.; Tranca, D.; Dong, R.; Hou, Y.; Zhang, T.; Kuttner, C.; Lehnert, T.; Seifert, G.; Kaiser, U.; Fery, A.; Zheng, Z.; Feng, X., *Nat. Commun.* **2016**, *7* (1), 13461.
76. Brinkmann, M., *J. Polym. Sci. B: Polym. Phys.* **2011**, *49* (17), 1218.
77. Koch, F. P. V.; Rivnay, J.; Foster, S.; Müller, C.; Downing, J. M.; Buchaca-Domingo, E.; Westacott, P.; Yu, L.; Yuan, M.; Baklar, M.; Fei, Z.; Luscombe, C.; McLachlan, M. A.; Heaney, M.; Rumbles, G.; Silva, C.; Salleo, A.; Nelson, J.; Smith, P.; Stingelin, N., *Prog. Polym. Sci.* **2013**, *38* (12), 1978.
78. Banerjee, T.; Haase, F.; Savasci, G.; Gottschling, K.; Ochsenfeld, C.; Lotsch, B. V., *J. Am. Chem. Soc.* **2017**, *139* (45), 16228.
79. Wang, X.; Chen, L.; Chong, S. Y.; Little, M. A.; Wu, Y.; Zhu, W.-H.; Clowes, R.; Yan, Y.; Zwijnenburg, M. A.; Sprick, R. S.; Cooper, A. I., *Nat. Chem.* **2018**, *10* (12), 1180.
80. Li, Z.; He, T.; Gong, Y.; Jiang, D., *Acc. Chem. Res.* **2020**, *53* (8), 1672.
81. Smith, B. J.; Dichtel, W. R., *J. Am. Chem. Soc.* **2014**, *136* (24), 8783.
82. Feng, X.; Ding, X.; Jiang, D., *Chem. Soc. Rev.* **2012**, *41* (18), 6010.
83. Ding, X.; Chen, L.; Honsho, Y.; Feng, X.; Saengsawang, O.; Guo, J.; Saeki, A.; Seki, S.; Irle, S.; Nagase, S.; Parasuk, V.; Jiang, D., *J. Am. Chem. Soc.* **2011**, *133* (37), 14510.
84. Kuhn, P.; Thomas, A.; Antonietti, M., *Macromolecules* **2009**, *42* (1), 319.
85. Zhai, L.; Huang, N.; Xu, H.; Chen, Q.; Jiang, D., *ChemComm.* **2017**, *53* (30), 4242.
86. Dalapati, S.; Addicoat, M.; Jin, S.; Sakurai, T.; Gao, J.; Xu, H.; Irle, S.; Seki, S.; Jiang, D., *Nat. Commun.* **2015**, *6* (1), 7786.
87. Wan, S.; Guo, J.; Kim, J.; Ihee, H.; Jiang, D., *Angew. Chem. Int. Ed.* **2009**, *48* (30), 5439.
88. Huang, N.; Zhai, L.; Couprie, D. E.; Addicoat, M. A.; Okushita, K.; Nishimura, K.; Heine, T.; Jiang, D., *Nat. Commun.* **2016**, *7* (1), 12325.
89. Pang, Z.-F.; Xu, S.-Q.; Zhou, T.-Y.; Liang, R.-R.; Zhan, T.-G.; Zhao, X., *J. Am. Chem. Soc.* **2016**, *138* (14), 4710.

90. Crowe, J. W.; Baldwin, L. A.; McGrier, P. L., *J. Am. Chem. Soc.* **2016**, *138* (32), 10120.
91. Chen, X.; Addicoat, M.; Jin, E.; Xu, H.; Hayashi, T.; Xu, F.; Huang, N.; Irle, S.; Jiang, D., *Sci. Rep.* **2015**, *5* (1), 14650.
92. Yu, S.-B.; Lyu, H.; Tian, J.; Wang, H.; Zhang, D.-W.; Liu, Y.; Li, Z.-T., *Polym. Chem.* **2016**, *7* (20), 3392.
93. Tylianakis, E.; Klontzas, E.; Froudakis, G. E., *Nanoscale* **2011**, *3* (3), 856.
94. Koo, B. T.; Dichtel, W. R.; Clancy, P., *J. Mater. Chem.* **2012**, *22* (34), 17460.
95. Smith, B. J.; Parent, L. R.; Overholts, A. C.; Beaucage, P. A.; Bisbey, R. P.; Chavez, A. D.; Hwang, N.; Park, C.; Evans, A. M.; Gianneschi, N. C.; Dichtel, W. R., *ACS Cent. Sci.* **2017**, *3* (1), 58.
96. Li, Rebecca L.; Flanders, N. C.; Evans, A. M.; Ji, W.; Castano, I.; Chen, L. X.; Gianneschi, N. C.; Dichtel, W. R., *Chem. Sci.* **2019**, *10* (13), 3796.
97. DeBlase, C. R.; Hernández-Burgos, K.; Silberstein, K. E.; Rodríguez-Calero, G. G.; Bisbey, R. P.; Abruña, H. D.; Dichtel, W. R., *ACS Nano* **2015**, *9* (3), 3178.
98. Cai, S.-L.; Zhang, Y.-B.; Pun, A. B.; He, B.; Yang, J.; Toma, F. M.; Sharp, I. D.; Yaghi, O. M.; Fan, J.; Zheng, S.-R.; Zhang, W.-G.; Liu, Y., *Chem. Sci.* **2014**, *5* (12), 4693.
99. Medina, D. D.; Werner, V.; Auras, F.; Tautz, R.; Dogru, M.; Schuster, J.; Linke, S.; Döblinger, M.; Feldmann, J.; Knochel, P.; Bein, T., *ACS Nano* **2014**, *8* (4), 4042.
100. Peng, Y.; Huang, Y.; Zhu, Y.; Chen, B.; Wang, L.; Lai, Z.; Zhang, Z.; Zhao, M.; Tan, C.; Yang, N.; Shao, F.; Han, Y.; Zhang, H., *J. Am. Chem. Soc.* **2017**, *139* (25), 8698.
101. Li, X.; Zhang, C.; Cai, S.; Lei, X.; Altoe, V.; Hong, F.; Urban, J. J.; Ciston, J.; Chan, E. M.; Liu, Y., *Nat. Commun.* **2018**, *9* (1), 2998.
102. Zhang, K.-D.; Matile, S., *Angew. Chem. Int. Ed.* **2015**, *54* (31), 8980.
103. Wilson, A.; Gasparini, G.; Matile, S., *Chem. Soc. Rev.* **2014**, *43* (6), 1948.
104. Jin, Y.; Yu, C.; Denman, R. J.; Zhang, W., *Chem. Soc. Rev.* **2013**, *42* (16), 6634.
105. Jin, Y.; Wang, Q.; Taynton, P.; Zhang, W., *Acc. Chem. Res.* **2014**, *47* (5), 1575.
106. Lyle, S. J.; Osborn Popp, T. M.; Waller, P. J.; Pei, X.; Reimer, J. A.; Yaghi, O. M., *J. Am. Chem. Soc.* **2019**, *141* (28), 11253.
107. Bi, S.; Yang, C.; Zhang, W.; Xu, J.; Liu, L.; Wu, D.; Wang, X.; Han, Y.; Liang, Q.; Zhang, F., *Nat. Commun.* **2019**, *10* (1), 2467.
108. Zhang, B.; Wei, M.; Mao, H.; Pei, X.; Alshimri, S. A.; Reimer, J. A.; Yaghi, O. M., *J. Am. Chem. Soc.* **2018**, *140* (40), 12715.
109. Guan, X.; Li, H.; Ma, Y.; Xue, M.; Fang, Q.; Yan, Y.; Valtchev, V.; Qiu, S., *Nat. Chem.* **2019**, *11* (6), 587.
110. Xu, L.; Ding, S.-Y.; Liu, J.; Sun, J.; Wang, W.; Zheng, Q.-Y., *ChemComm.* **2016**, *52* (25), 4706.
111. Campbell, N. L.; Clowes, R.; Ritchie, L. K.; Cooper, A. I., *Chem. Mater.* **2009**, *21* (2), 204.
112. Ritchie, L. K.; Trewin, A.; Reguera-Galan, A.; Hasell, T.; Cooper, A. I., *Microporous Mesoporous Mater.* **2010**, *132* (1), 132.
113. Wei, H.; Chai, S.; Hu, N.; Yang, Z.; Wei, L.; Wang, L., *ChemComm.* **2015**, *51* (61), 12178.
114. Dey, K.; Pal, M.; Rout, K. C.; Kunjattu H, S.; Das, A.; Mukherjee, R.; Kharul, U. K.; Banerjee, R., *J. Am. Chem. Soc.* **2017**, *139* (37), 13083.
115. Matsumoto, M.; Valentino, L.; Stiehl, G. M.; Balch, H. B.; Corcos, A. R.; Wang, F.; Ralph, D. C.; Mariñas, B. J.; Dichtel, W. R., *Chem* **2018**, *4* (2), 308.
116. Hao, Q.; Zhao, C.; Sun, B.; Lu, C.; Liu, J.; Liu, M.; Wan, L.-J.; Wang, D., *J. Am. Chem. Soc.* **2018**, *140* (38), 12152.



117. Zhou, D.; Tan, X.; Wu, H.; Tian, L.; Li, M., *Angew. Chem. Int. Ed.* **2019**, *58* (5), 1376.
118. Wan, S.; Guo, J.; Kim, J.; Ihee, H.; Jiang, D., *Angew. Chem. Int. Ed.* **2008**, *47* (46), 8826.
119. Chen, X.; Addicoat, M.; Irle, S.; Nagai, A.; Jiang, D., *J. Am. Chem. Soc.* **2013**, *135* (2), 546.
120. Song, J.-R.; Sun, J.; Liu, J.; Huang, Z.-T.; Zheng, Q.-Y., *ChemComm.* **2014**, *50* (7), 788.
121. Fukui, T.; Kawai, S.; Fujinuma, S.; Matsushita, Y.; Yasuda, T.; Sakurai, T.; Seki, S.; Takeuchi, M.; Sugiyasu, K., *Nat. Chem.* **2017**, *9* (5), 493.
122. Jackson, K. T.; Reich, T. E.; El-Kaderi, H. M., *ChemComm.* **2012**, *48* (70), 8823.
123. Dalapati, S.; Jin, S.; Gao, J.; Xu, Y.; Nagai, A.; Jiang, D., *J. Am. Chem. Soc.* **2013**, *135* (46), 17310.
124. Guo, J.; Xu, Y.; Jin, S.; Chen, L.; Kaji, T.; Honsho, Y.; Addicoat, M. A.; Kim, J.; Saeki, A.; Ihee, H.; Seki, S.; Irle, S.; Hiramoto, M.; Gao, J.; Jiang, D., *Nat. Commun.* **2013**, *4* (1), 2736.
125. Fang, Q.; Zhuang, Z.; Gu, S.; Kaspar, R. B.; Zheng, J.; Wang, J.; Qiu, S.; Yan, Y., *Nat. Commun.* **2014**, *5* (1), 4503.
126. Lyu, H.; Diercks, C. S.; Zhu, C.; Yaghi, O. M., *J. Am. Chem. Soc.* **2019**, *141* (17), 6848.
127. Waller, P. J.; Lyle, S. J.; Osborn Popp, T. M.; Diercks, C. S.; Reimer, J. A.; Yaghi, O. M., *J. Am. Chem. Soc.* **2016**, *138* (48), 15519.
128. Liu, C.; Zhang, W.; Zeng, Q.; Lei, S., *Chem. Eur. J.* **2016**, *22* (20), 6768.
129. Wan, S.; Gándara, F.; Asano, A.; Furukawa, H.; Saeki, A.; Dey, S. K.; Liao, L.; Ambrogio, M. W.; Botros, Y. Y.; Duan, X.; Seki, S.; Stoddart, J. F.; Yaghi, O. M., *Chem. Mater.* **2011**, *23* (18), 4094.
130. Ding, H.; Li, Y.; Hu, H.; Sun, Y.; Wang, J.; Wang, C.; Wang, C.; Zhang, G.; Wang, B.; Xu, W.; Zhang, D., *Chem. Eur. J.* **2014**, *20* (45), 14614.
131. Côté, A. P.; El-Kaderi, H. M.; Furukawa, H.; Hunt, J. R.; Yaghi, O. M., *J. Am. Chem. Soc.* **2007**, *129* (43), 12914.
132. Baldwin, L. A.; Crowe, J. W.; Pyles, D. A.; McGrier, P. L., *J. Am. Chem. Soc.* **2016**, *138* (46), 15134.
133. Feng, X.; Liu, L.; Honsho, Y.; Saeki, A.; Seki, S.; Irle, S.; Dong, Y.; Nagai, A.; Jiang, D., *Angew. Chem. Int. Ed.* **2012**, *51* (11), 2618.
134. Dogru, M.; Handloser, M.; Auras, F.; Kunz, T.; Medina, D.; Hartschuh, A.; Knochel, P.; Bein, T., *Angew. Chem. Int. Ed.* **2013**, *52* (10), 2920.
135. Auras, F.; Ascherl, L.; Hakimoun, A. H.; Margraf, J. T.; Hanusch, F. C.; Reuter, S.; Bessinger, D.; Döblinger, M.; Hettstedt, C.; Karaghiosoff, K.; Herbert, S.; Knochel, P.; Clark, T.; Bein, T., *J. Am. Chem. Soc.* **2016**, *138* (51), 16703.
136. Fang, Q.; Gu, S.; Zheng, J.; Zhuang, Z.; Qiu, S.; Yan, Y., *Angew. Chem. Int. Ed.* **2014**, *53* (11), 2878.
137. Wu, X.; Han, X.; Xu, Q.; Liu, Y.; Yuan, C.; Yang, S.; Liu, Y.; Jiang, J.; Cui, Y., *J. Am. Chem. Soc.* **2019**, *141* (17), 7081.
138. Wu, C.; Liu, Y.; Liu, H.; Duan, C.; Pan, Q.; Zhu, J.; Hu, F.; Ma, X.; Jiu, T.; Li, Z.; Zhao, Y., *J. Am. Chem. Soc.* **2018**, *140* (31), 10016.
139. Matsumoto, M.; Dasari, R. R.; Ji, W.; Feriante, C. H.; Parker, T. C.; Marder, S. R.; Dichtel, W. R., *J. Am. Chem. Soc.* **2017**, *139* (14), 4999.
140. Xie, Y.-F.; Ding, S.-Y.; Liu, J.-M.; Wang, W.; Zheng, Q.-Y., *J. Mater. Chem. C* **2015**, *3* (39), 10066.
141. Gao, Q.; Bai, L.; Zeng, Y.; Wang, P.; Zhang, X.; Zou, R.; Zhao, Y., *Chem. Eur. J.* **2015**, *21* (47), 16818.

142. Li, J.-R.; Kuppler, R. J.; Zhou, H.-C., *Chem. Soc. Rev.* **2009**, 38 (5), 1477.
143. Han, S. S.; Furukawa, H.; Yaghi, O. M.; Goddard, W. A., *J. Am. Chem. Soc.* **2008**, 130 (35), 11580.
144. Wang, S.; Xu, X.; Yue, Y.; Yu, K.; Shui, Q.; Huang, N.; Chen, H., *Small Struct.* **2020**, 1 (2), 2000021.
145. Kojima, A.; Teshima, K.; Shirai, Y.; Miyasaka, T., *J. Am. Chem. Soc.* **2009**, 131 (17), 6050.
146. You, P.; Liu, Z.; Tai, Q.; Liu, S.; Yan, F., *Adv. Mater.* **2015**, 27 (24), 3632.
147. Tang, G.; You, P.; Tai, Q.; Yang, A.; Cao, J.; Zheng, F.; Zhou, Z.; Zhao, J.; Chan, P. K. L.; Yan, F., *Adv. Mater.* **2019**, 31 (24), 1807689.
148. Jeong, M.; Choi, I. W.; Go, E. M.; Cho, Y.; Kim, M.; Lee, B.; Jeong, S.; Jo, Y.; Choi, H. W.; Lee, J.; Bae, J.-H.; Kwak, S. K.; Kim, D. S.; Yang, C., *Science* **2020**, 369 (6511), 1615.
149. Tai, Q.; You, P.; Sang, H.; Liu, Z.; Hu, C.; Chan, H. L. W.; Yan, F., *Nat. Commun.* **2016**, 7 (1), 11105.
150. Kim, G. W.; Choi, H.; Kim, M.; Lee, J.; Son, S. Y.; Park, T., *Adv. Energy Mater.* **2020**, 10 (8), 1903403.
151. Shao, S.; Loi, M. A., *Adv. Mater. Interfaces* **2020**, 7 (1), 1901469.
152. Ball, J. M.; Petrozza, A., *Nat. Energy* **2016**, 1 (11), 16149.
153. Park, N.-G., *Mater. Today* **2015**, 18 (2), 65.
154. Mohamed, M. G.; Lee, C.-C.; El-Mahdy, A. F. M.; Lüder, J.; Yu, M.-H.; Li, Z.; Zhu, Z.; Chueh, C.-C.; Kuo, S.-W., *J. Mater. Chem. A* **2020**, 8 (22), 11448.

# 2 Triphenylamine-based hole transport materials for p-i-n perovskite solar cells

## 2.1 Introduction

Triarylamine (TAA, Figure 10 a) is ammonia substituted by three aryl groups, in which the basic and simplest structure is triphenylamine (TPA). Various TPA-based materials have been synthesized with functionalized TAAs as building blocks through aryl–aryl bond formation reactions such as Suzuki, Ullmann and Hartwig–Buchwald coupling. Aggregation state and carrier mobility of molecules are strongly based on molecular configuration and electronic properties. For TPA, the central nitrogen atom is connected with three  $sp^2$ -hybridized carbon atoms via C–N bond within a length of 1.42 Å and an angle of  $120^\circ$  between each other.<sup>155, 156</sup> The three phenyl groups are bonded with the central nitrogen atom with a propeller-like structure, which processes a torsion angle of  $41.7^\circ$ .<sup>155, 157</sup> This propeller-like structure contributes to a suppression of aggregation and lead to the amorphous structure of TPA, which is beneficial to form homogeneous and smooth thin films in devices. At the same time, TPA has a low ionization potential of 6.80 eV, indicating strong electron-donating capability, beneficial to hole injection and hole transportation. These features combined with the facile synthesis with tunable optoelectronic properties made TPA-based materials widely used as hole-injecting or hole-transporting materials.<sup>158, 159</sup>

Large amounts of HTMs containing TPA have been developed, Nazeeruddin and co-workers synthesized TPA-MeOPh (Figure 10 b) showing a PCE of 10.79% in n-i-p configured perovskite PV in 2014.<sup>160</sup> Kloo and co-workers synthesized X1 and X14 improved PCE to 14.4% and 16.4%, respectively in 2017 (Figure 10 c).<sup>161</sup> Guo and co-workers synthesized MPA-BTTI showing a PCE of 21.17 % within p-i-n-type dopant-free devices in 2019.<sup>162</sup> (Figure 10 d) Yip and co-workers reported DTB-FL (Figure 10 e) showing a PCE of 21.5 % within n-i-p devices in 2020,<sup>163</sup> which are one of the highest PCE PSCs in p-i-n and n-i-p devices, respectively. But PTAA and spiro-OMeTAD are still the most widely used HTMs (as shown in Figure 10 f).<sup>164</sup>

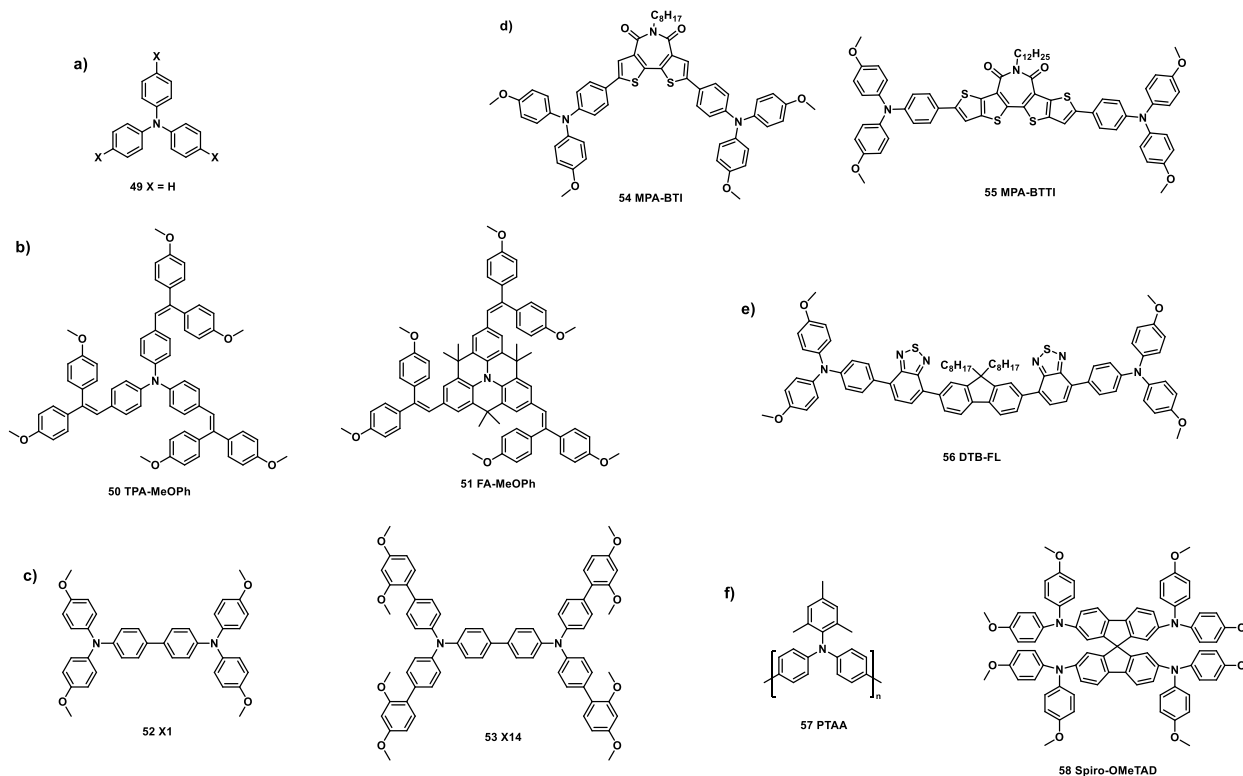


Figure 10. Structure of a) triarylamine (49), b) TPA-MeOPh (50) and FA-MeOPh (51),<sup>160</sup> c) Structure of X1 (52) and X14 (53),<sup>160</sup> d) MPA-BTI (54) and MPPA-BTTI (55),<sup>162</sup> e) DTB-FL (56),<sup>166</sup> f) PTAA (57) and spiro-OMeTAD (58), respectively.<sup>164</sup>

There are two common PSCs device concepts, which are mesoporous structure and planar architecture (as shown in Figure 11). The mesoporous structure of PSC devices follows the design of dye-sensitized solar cells (DSSCs), in which perovskite active layers are filled into mesoporous TiO<sub>2</sub> nanoparticles and to form a compact layer on top of the high surface area of TiO<sub>2</sub>. In this case, TiO<sub>2</sub> is used not only as scaffold to hold the perovskite but also as ETL to increase the interface as n-type semiconductor media to extract and transport electrons. On the other side, related HTLs are applied to transport holes to the counter electrode. Different from relatively short exciton diffusion length of normal organic semiconductors, perovskites gain much longer exciton diffusion lengths which can be >1 $\mu$ m.<sup>165</sup> Consequently, it is possible for perovskites to build a planar junction configuration, where perovskite intrinsic layers are sandwiched between n-type selective layer and p-type selective layers, leading to a conventional planar n-i-p configuration

(FTO/ETLs/perovskite/HTLs/counter electrode) or to an inverted planar p-i-n configuration (ITO/HTLs/perovskite/ETLs/counter electrode) (as shown in Figure 11). The commonly used HTL materials in conventional devices are normally n-type oxides, such as  $\text{TiO}_2$  and  $\text{SnO}_2$ , while p-type organic semiconductor are widely used in inverted devices as HTLs, for example PTAA and spiro-OMeTAD.<sup>150, 166</sup> Even though the high PCE PSCs are usually n-i-p configured, inverted p-i-n devices still draw attention due to several advantages, such as easier devices building procedure without high temperature annealing, better stability to air and humidity.

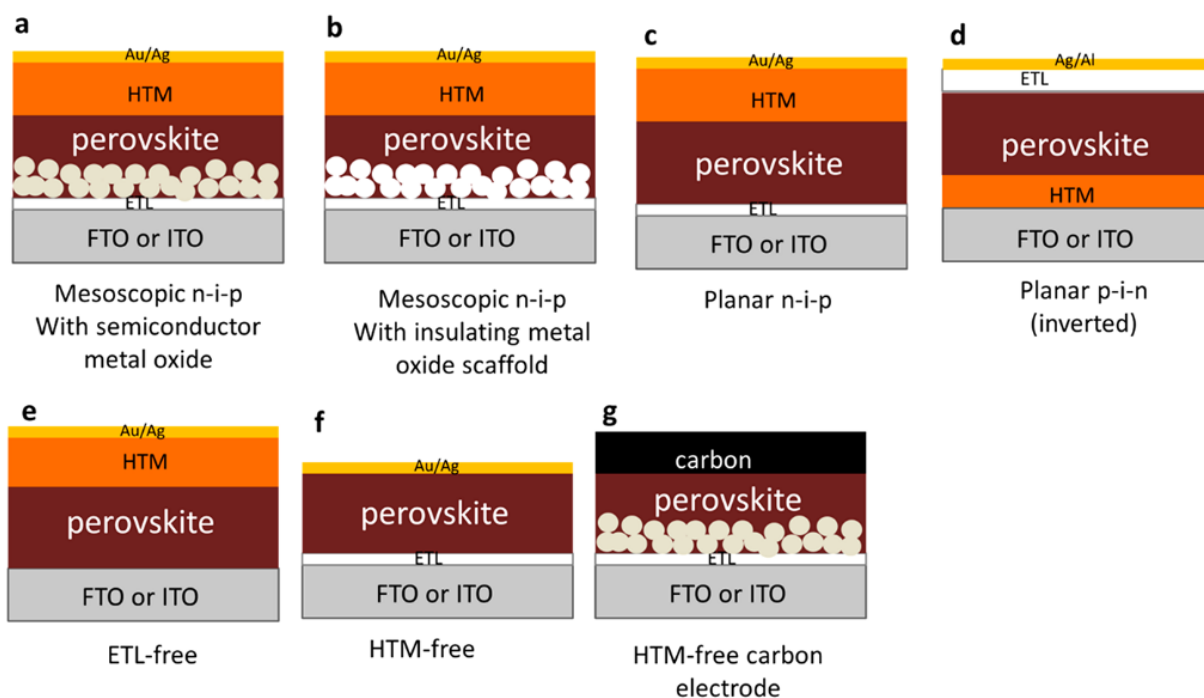


Figure 11. Variety of device architectures for perovskite solar cells.<sup>167</sup>

Building homogeneous and pin-hole free perovskite layer is decisive in preparing efficient PSCs.<sup>168</sup> Non-homogeneity morphology and pin-holes on perovskite layers cause the reduction of shunt resistance and open-circuit voltage, which will finally lead to the efficiency loss of PSCs.<sup>169</sup> Nucleation and crystal growth are key processes of perovskite layers formation no matter which deposition method is chosen. Commonly used perovskite layers deposition methods include antisolvent deposition,<sup>169</sup> two-step sequential deposition,<sup>170</sup> vapor deposition<sup>171</sup> and gas quenching<sup>172</sup>. Antisolvent deposition is the most well-known deposition method for perovskite

layers, in which a certain amount of antisolvent is added dropwise on top of the perovskite precursor layer during the spin-coating. The conditions of antisolvent deposition are hard to control including antisolvent dripping position and timing, which a slight difference in condition will result in different morphology and quality of perovskite layers.<sup>172</sup> Gas quenching is a mild, efficient and reproducible strategy to fabricate high quality perovskite layers.<sup>173</sup> In this method, perovskite precursor solution was spin-coated on ITO substrates, to which a dry compressed gas ( $N_2$  or Ar) flow with a certain pressure and distance between gas source and substrates was sprayed toward. Perovskite compact layers were obtained after annealing at 100°C for 10 min (processes are shown in Figure 12). The mechanism of gas quenching method is similar to antisolvent deposition, which includes nucleation and crystal growth in general process. As the solvent is removed from the perovskite precursor solution continually, the concentration of perovskite precursor solution exceeds the concentration specified by the value of solubility at equilibrium (in supersaturation state). Nucleation occurs when the concentration of perovskite precursor solution attains to the minimum supersaturation limit. Crystal growth processes with the further nucleation and stops after the concentration of perovskite precursor solution drops below the solubility limit. For antisolvent method, the concentration of perovskite precursor solution is reduced immediately when an antisolvent is dropped onto perovskite precursor layer when spin-coating and supersaturation state is created as the concentration is reduced continuously. For gas quenching method, the concentration of perovskite precursor solution is reduced slowly when solvent is evaporated via gas flow, with the supersaturation state creating and nucleation occurring. If DMF is the only solvent in perovskite precursor solution, DMF can be removed easily by gas quenching to give homogeneous and pin-hole free perovskite layers. When high boiling point solvent, such as DMSO and NMP are involved in perovskite precursor solution, a solvent-perovskite precursor intermediate phase (for example DMSO-MAI-PbI<sub>2</sub>) will be obtained after gas quenching. In this case, further annealing treatment is necessary to remove the residual DMSO or NMP to obtain compact perovskite layers.

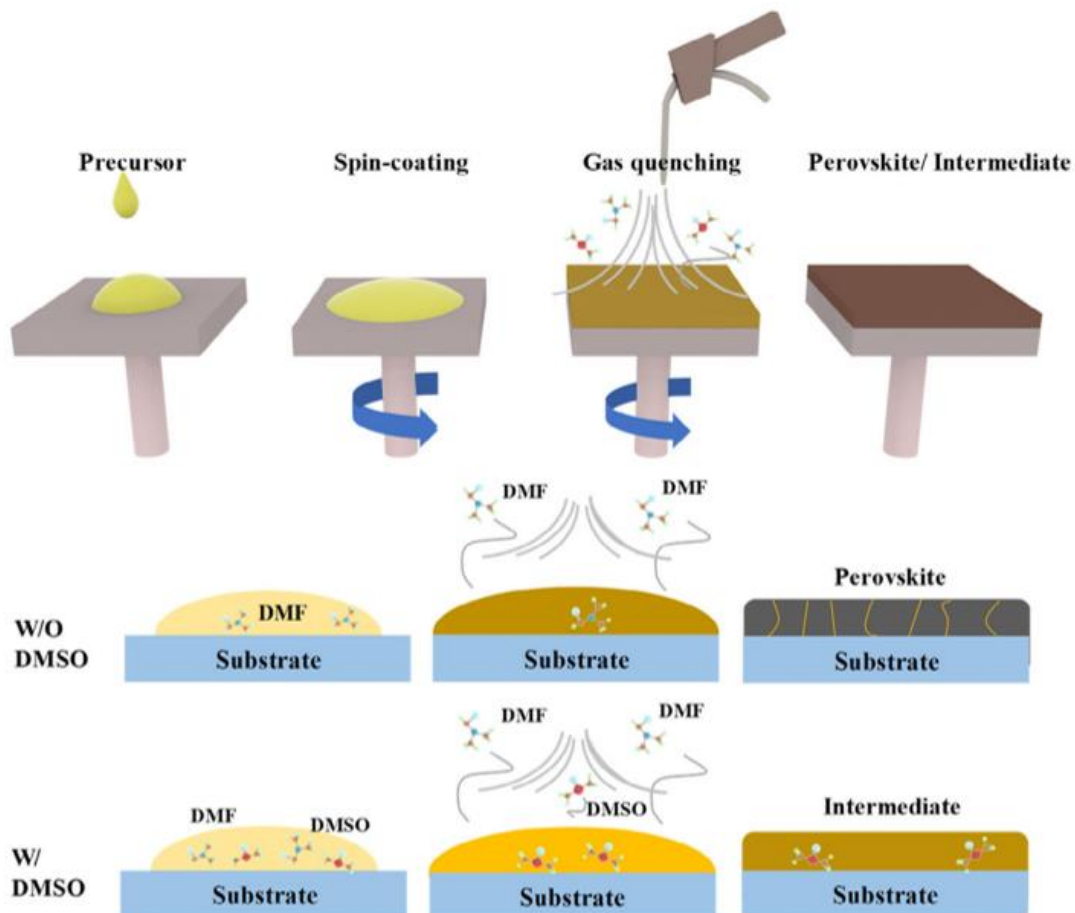


Figure 12. The processes of gas quenching method.<sup>172</sup>

In this thesis, it was preferred to start our investigations from inverted p-i-n devices because the final target are COF films on substrates, directly formed as HTLs via condensation reaction. As mentioned in the last section, condensation reaction conditions include water and acid, which are in general harmful to perovskite layers since they decompose the layers resulting in the loss of efficiency. To avoid damage, the better strategy is the synthesis of COF layers on ITO via condensation, followed by purification of this layer with different solvents. Considering the as-prepared COFs are insoluble in commonly used organic solvents and stable at high temperature, this cleaning procedure is quite safe. Subsequently, perovskite layers are deposited on top of the as-prepared COF-covered ITO substrates, followed by building ETLs and careful sputtering of the top electrode. In contrast, HTL small molecule will be also investigated as HTM of PSCs.

Structure-property relationships will be investigated considering the overall performance of the resulting PSCs.

## 2.2 Results and Discussions

### 2.2.1 Synthesis

In this chapter, triphenylbenzene (TPB), thiphenylamine (TPA) and trithienylbenzene (TTB) were investigated as core units for different triangular HTL molecules, combined with methoxy (-OMe)-substituted diphenylamine (DPA) and carbazole (Cz) as different terminals. Methoxy groups were chosen as electron-donor groups to achieve better photovoltaic performance, following a general design principle for HTL molecules, which were described as terminals in Figure 13.<sup>174</sup> The TPB-, TPA- and TTB-cores are linked with TPA- and Cz-based terminals to obtain HTL molecules via C-N or C=N linkers (bonds). The HTL molecules were synthesized by Suzuki-, Ullman- and Buchwald-Hartwig-type couplings for C-N-bonding HTL molecules or condensation reactions for C=N-bonded HTL molecules. The structures and the corresponding names are shown in Figure 13. These molecules can be divided into two classes, where cores and terminals are connected either by carbon-nitrogen single bonds (metal-catalyzed C-N bond formation) or carbon-nitrogen double bonds (acid-catalyzed C=N condensation). The general nomenclature used in this thesis gives the structure of the HTL molecule as “*Cores-bonds-terminals*”. The core abbreviations were explained above. The C-N is left out (for example, C-N single bond is skipped for TPB-DPAOMe), while the C=N is abbreviated as CN or NC (such as, TPB-CN-TPAOMe or TPB-NC-TPAOMe). CN and NC indicates different positions (or orientations) of N in C=N bands (which is marked in red in Figure 13). CN indicates that the cores were the aldehyde moieties, while the terminals were amines. In contrast, NC indicates the terminal precursors were introduced as aldehydes. All details of synthesis are shown in the experimental section below.



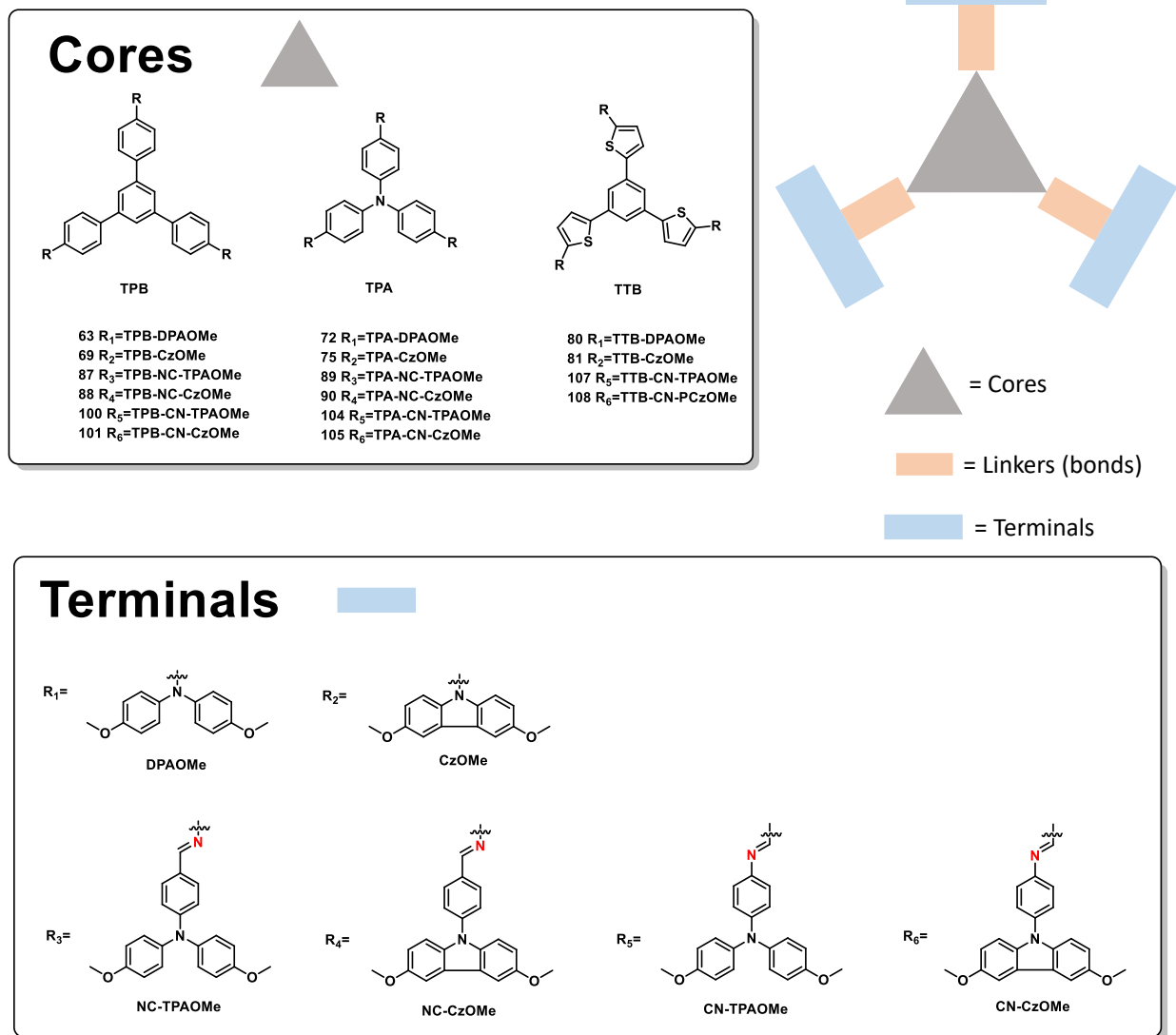
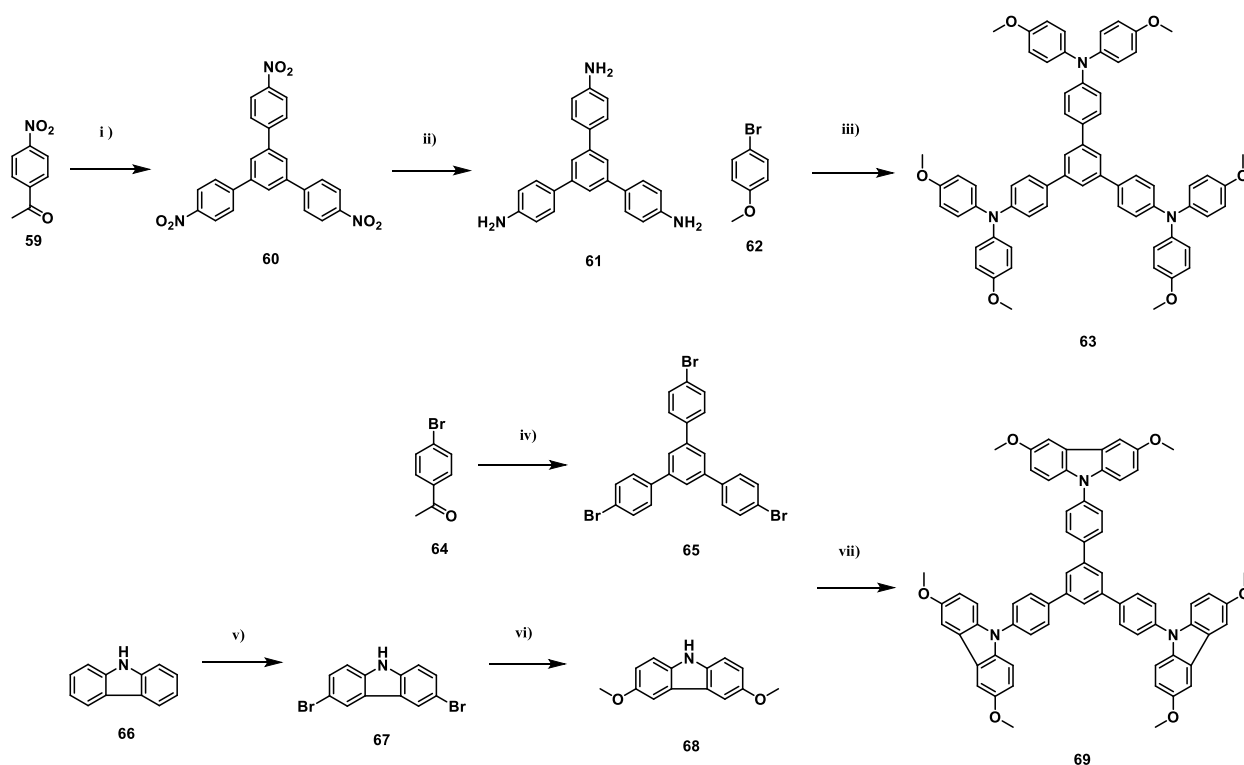


Figure 13. Designed HTL molecules for PSCs HTLs.

The syntheses of two types of HTL small molecules involve three to six steps. C-N type HTL molecules were synthesized via coupling between cores and terminals (as shown in Scheme 1).

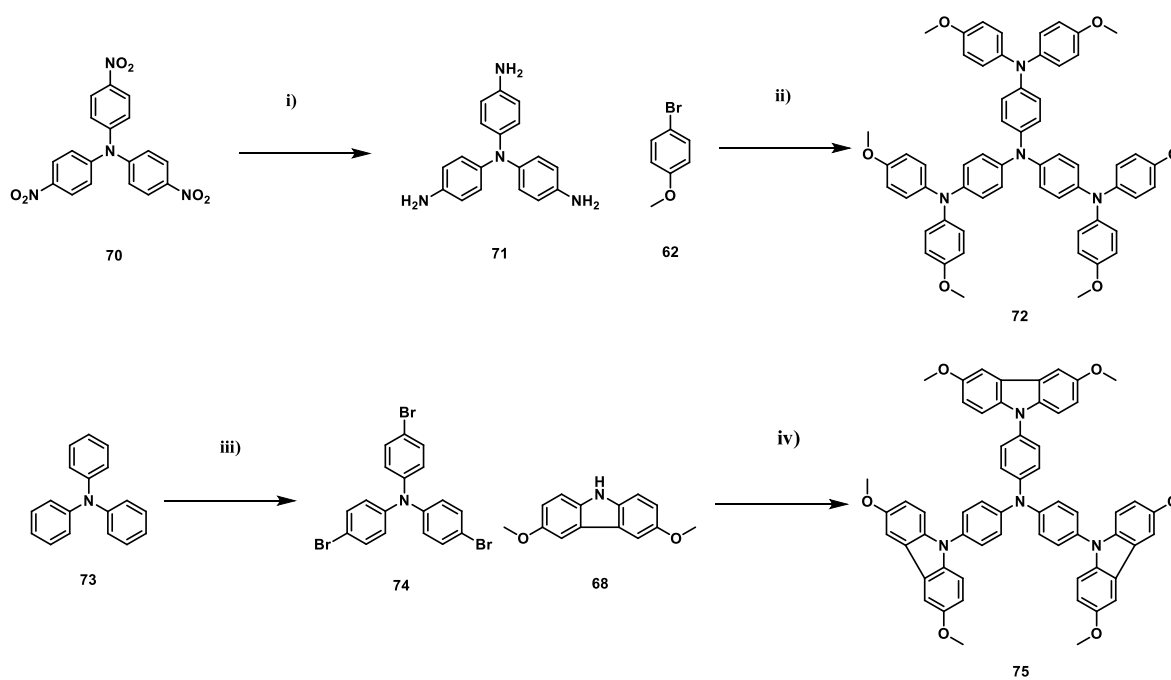


Scheme 1: Synthesis of HTL molecules 63 and 69. Reaction conditions: i)  $\text{SiCl}_4$ , EtOH, 80 °C, 24 h, (40 %); ii) Pd/C,  $\text{N}_2\text{H}_4$ , EtOH, 90 °C, 2 d, (85 %); iii)  $\text{Pd}_2(\text{dba})_3$ ,  ${}^t\text{Bu}_3\text{P}$ ,  $\text{NaO}^t\text{Bu}$ , Tol, 130 °C, 24 h, (71 %); iv)  $\text{SiCl}_4$ , EtOH, 80°C, 24 h, (61 %); v) NBS, EtOAc, r.t., 18 h, (66 %); vi) Na, MeOH, CuI, DMF, 80°C, 24 h, (92 %); vii)  $\text{Pd}(\text{OAc})_2$ ,  ${}^t\text{Bu}_3\text{P}$ ,  $\text{K}_2\text{CO}_3$ , Tol, 130°C, 48 h, (55 %).

For HTL molecule 63, the synthesis started with 1,3,5-tris(4-aminophenyl)benzene core 61. 60 was prepared by cyclotrimerization of 59 with  $\text{SiCl}_4$  in dry EtOH at 80 °C for 24 h in yield of 40 %. 61 was prepared by reduction (hydration) of 60 with Pd/C and  $\text{N}_2\text{H}_4$  in EtOH on 90 °C in the dark in 85 % yield. This reaction can also be preceded in autoclave under  $\text{H}_2$  within Pd/C with a similar yield (yield is not shown here). HTL molecule 63 was synthesized by Buchwald–Hartwig coupling of 61 and 4-bromoanisole 62 with  $\text{Pd}_2(\text{dba})_3$ ,  ${}^t\text{Bu}^3\text{P}$ ,  $\text{NaO}^t\text{Bu}$  in dry toluene at 130°C for 24 h under Ar and in the dark in yield of 71 %. The results of NMR confirmed the successful synthesis of HTL molecule 63. For synthesis of HTL molecule 69, 65 was prepared by cyclotrimerization of 64 with  $\text{SiCl}_4$  in dry EtOH at 80 °C with yield of 61 % for this core unit. Terminal synthesis started with bromination of carbazole (carbazole is commercially available and was used without further

purification) 66 to give 67 with NBS in EtOAc at r.t. for 18 h under in the dark in yield of 66 %. Terminal 68 was prepared from 67 with Na, MeOH, CuI in DMF at 80 °C for 24 h in yield of 92 %. HTL molecule 69 was synthesized via Buchwald–Hartwig coupling between core 65 and terminal 68 with Pd(OAc)<sub>2</sub>, <sup>t</sup>Bu<sup>3</sup>P, K<sub>2</sub>CO<sub>3</sub> in toluene at 130°C for 48 h under Ar and in the dark with 55 % yield. The structure of molecule 69 was identified by NMR.

Compared with HTL molecules 63 and 69, the core of HTL molecules 72 and 75 is constructed by a substitution of TPB by TPA. The synthesis strategy is similar to that of HTL molecules 63 and 69 (shown in Scheme 2).

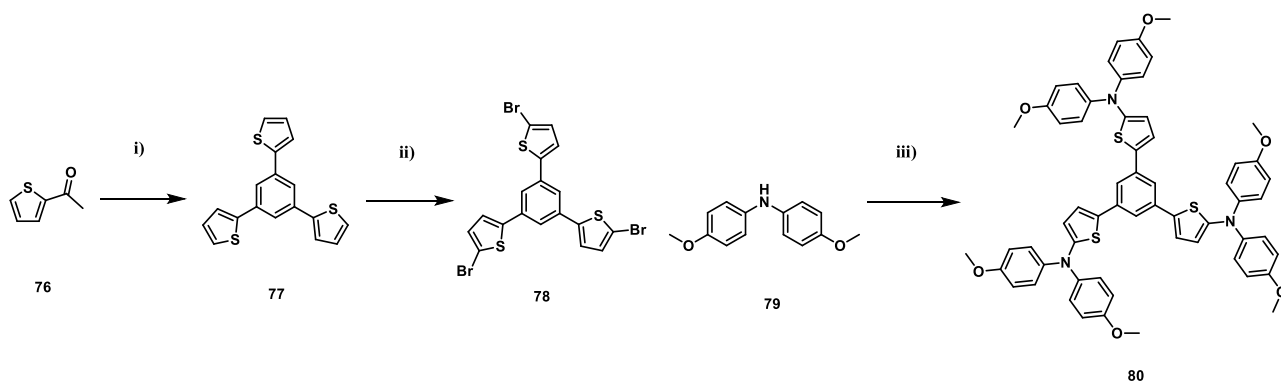


Scheme 2: Synthesis of HTL molecule 72 and 75. Reaction conditions: i) Pd/C, N<sub>2</sub>H<sub>4</sub>, EtOH, 90 °C, 2 d, (92 %); ii) Pd<sub>2</sub>(dba)<sub>3</sub>, <sup>t</sup>Bu<sup>3</sup>P, NaO<sup>t</sup>Bu, Tol, 130 °C, 24 h, (62 %); iii) NBS, DMF, r.t., 3 h, (62 %); iv) Pd(OAc)<sub>2</sub>, <sup>t</sup>Bu<sup>3</sup>P, K<sub>2</sub>CO<sub>3</sub>, Tol, 130 °C, 48 h, (84 %).

HTL molecule 72 was synthesized via Buchwald–Hartwig coupling between 71 and six equivalents of 62 with Pd<sub>2</sub>(dba)<sub>3</sub>, <sup>t</sup>Bu<sup>3</sup>P and NaO<sup>t</sup>Bu in toluene on 130°C under Ar and in the dark for 24 h with 62 % yield. HTL molecule 75 was synthesized by Buchwald–Hartwig coupling

between core 74 and three equivalents of terminal 68 with Pd(OAc)<sub>2</sub>, <sup>t</sup>Bu<sup>3</sup>P, K<sub>2</sub>CO<sub>3</sub> in toluene at 130 °C for 48 h under Ar and in the dark in yield of 84 %. The structure of HTL molecules 72 and 75 were confirmed by NMR.

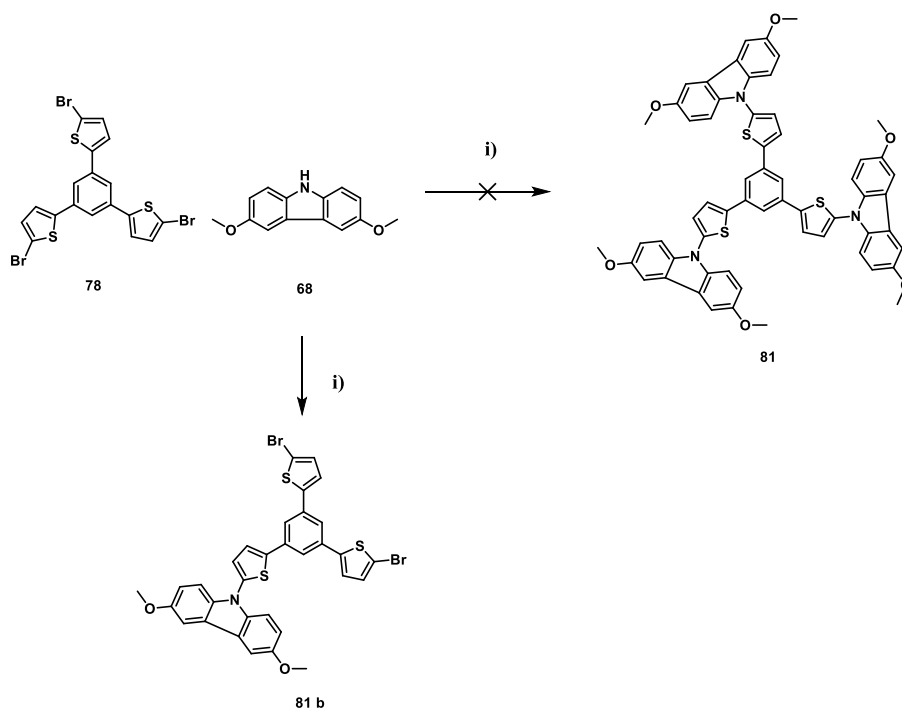
As the core of HTL molecules 80 and 81, TTB is used. The synthesis of HTL molecules 80 is different from previous syntheses (as shown in Scheme 3), because 1,3,5-tris(5-aminothiophen-2-yl)benzene could not be synthesized. The new route was a coupling of 1,3,5-tris(5-bromothiophen-2-yl)benzene (78) with commercially available bis(4-methoxyphenyl)amine (79) via Buchwald–Hartwig coupling to give HTL molecule 80. 77 was synthesized via cyclotrimerization of 76 with SiCl<sub>4</sub> in dry EtOH at 80 °C for 24 h in yield of 54 %, followed by bromination with NBS to give core 78 with 78% yield. HTL molecule 80 was synthesized by Buchwald–Hartwig coupling between 78 and 79 with Pd<sub>2</sub>(dba)<sub>3</sub>, <sup>t</sup>Bu<sup>3</sup>P, NaO<sup>t</sup>Bu in toluene at 130 °C under Ar and in the dark for 24 h with 42 % yield. The results of a NMR analysis confirmed that HTL molecule 80 was synthesized successfully.



Scheme 3: Synthesis of HTL molecule 80. Reaction conditions: i) SiCl<sub>4</sub>, EtOH, r.t., 24 h, (54 %); ii) NBS, MeCN, r.t., 2 h, (78 %); iii) Pd<sub>2</sub>(dba)<sub>3</sub>, <sup>t</sup>Bu<sub>3</sub>P, NaOtBu, Tol, 130°C, 48 h, (42 %).

HTL molecule 81 cannot be synthesized via Buchwald–Hartwig coupling of core 78 and terminal 68. Four different catalyst systems were applied to improve Buchwald–Hartwig coupling (reaction conditions were shown in Scheme 4). The isolated products were not the HTL molecule 81. Mass spectrometry results showed that the isolated product matched with the structure of TTB core with only one terminal coupled to product 81 b in a yield of 17 % (as shown in Figure 14). HTL

molecule 81 could be synthesized in two subsequent further Buchwald–Hartwig coupling steps starting from the intermediate product 81 b in a poor yield.



Scheme 4: Unsuccessful synthesis of HTL molecule 81 via Buchwald–Hartwig coupling. Reaction conditions: i) ①  $\text{Pd}(\text{OAc})_2$ ,  ${}^t\text{Bu}_3\text{P}$ ,  $\text{K}_2\text{CO}_3$ , Tol, 130 °C, 48 h; ②  $\text{Pd}_2(\text{dba})_3$ ,  ${}^t\text{Bu}^3\text{P}$ ,  $\text{NaO}^t\text{Bu}$ , Tol, 130 °C, 48 h; ③  $\text{Pd}_2(\text{dba})_3$ ,  $\text{P}^t\text{Bu}_3\text{BF}_4$ ,  $\text{NaO}^t\text{Bu}$ , Tol, 130 °C, 48 h; ④  $\text{Pd}(\text{dba})_2$ , XPhos,  $\text{NaO}^t\text{Bu}$ , Tol, 130 °C, 48 h.

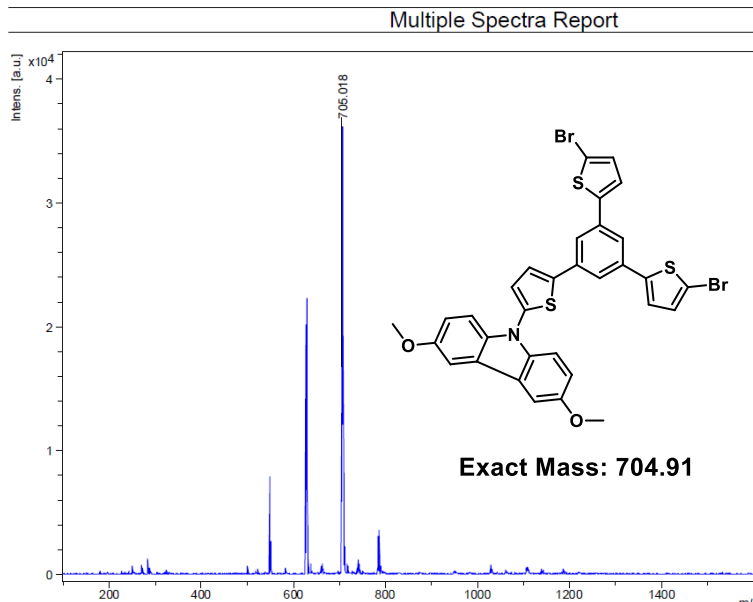
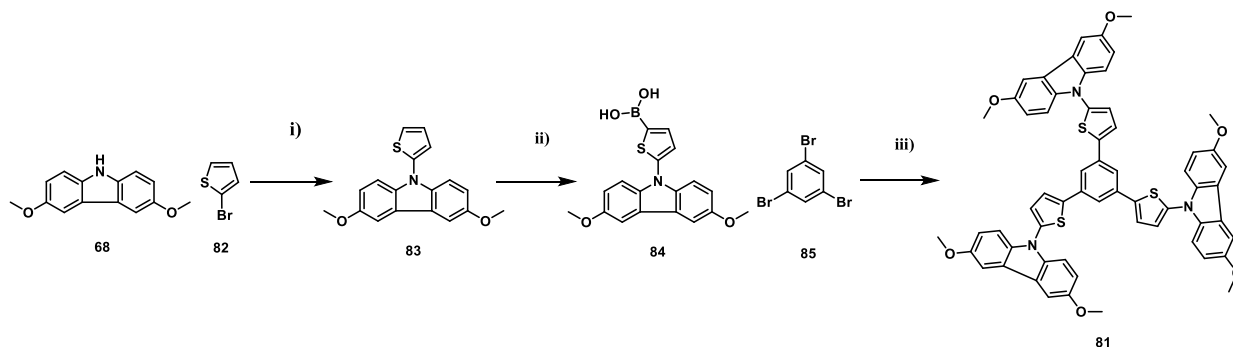


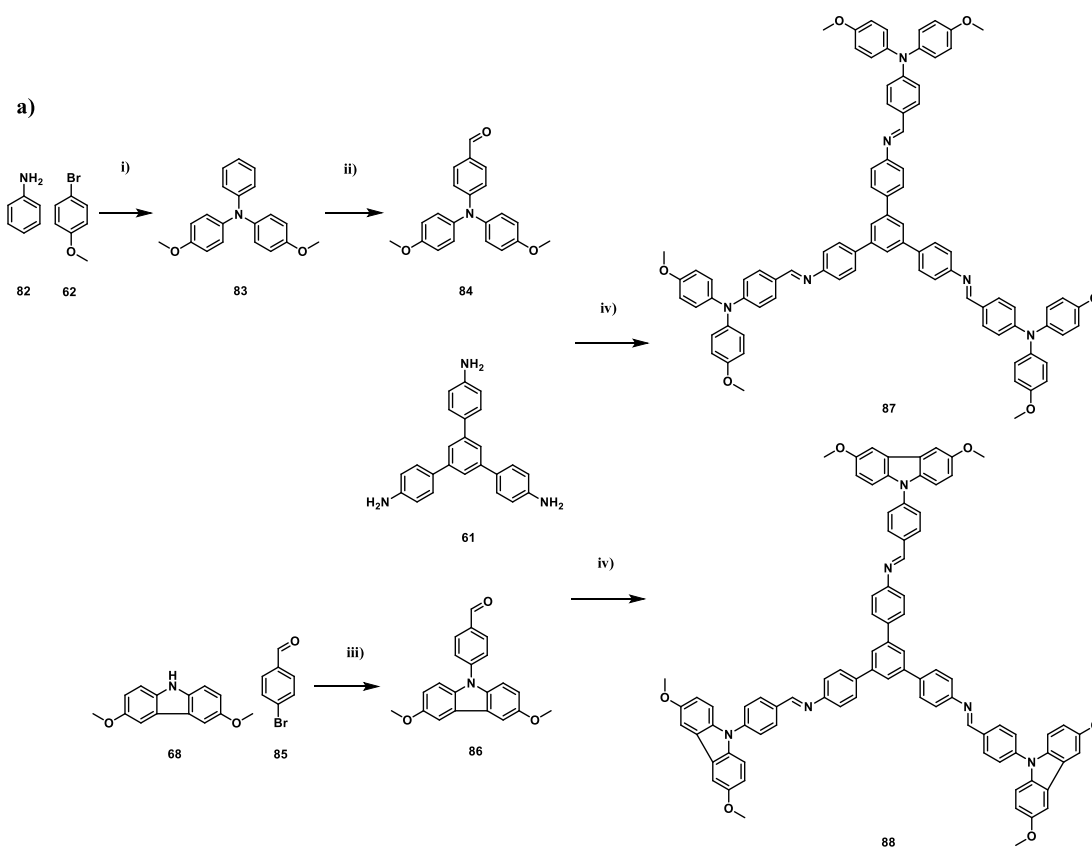
Figure 14. Mass spectrum of 81 b.

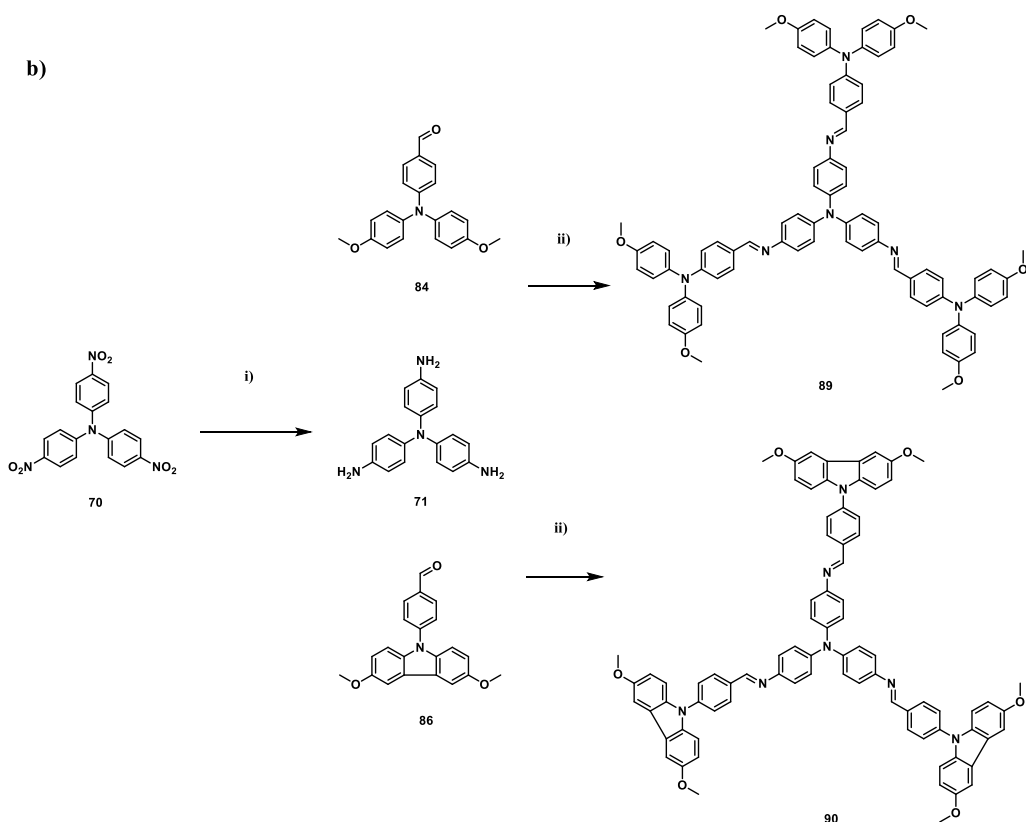
Suzuki coupling can be applied to prepare HTL molecule 81 (as shown in Scheme 5). 2-bromothiophene 82 was first coupled with 68 via Buchwald–Hartwig coupling with Pd(dba)<sub>2</sub> and XPhos as catalyst system to give 83 with 76 % yield. The boronic acid 84 were synthesized with n-BuLi and trimethyl borate in THF. HTL molecule 81 was synthesized via Suzuki coupling of 1,3,5-tribromobenzene 85 and flash-made boronic acid 84 with Pd(Ph<sub>3</sub>P)<sub>4</sub> and Na<sub>2</sub>CO<sub>3</sub> in a degassed THF/H<sub>2</sub>O mixture at 80 °C for 24 h in yield of 99 %. The structure of HTL molecule 81 was confirmed by NMR.



Scheme 5: Synthesis of HTL molecule 81. Reaction conditions: i) Pd(dba)<sub>2</sub>, XPhos, NaO<sup>t</sup>Bu, Tol, 130 °C, 24 h, (76 %); ii) n-BuLi, Trimethyl borate, THF, r.t., 16 h, (65 %); iii) Pd(Ph<sub>3</sub>P)<sub>4</sub>, Na<sub>2</sub>CO<sub>3</sub>, THF, H<sub>2</sub>O, 80 °C, 24 h, (99 %).

HTL molecules 87, 88, 89 and 90 (NC type HTL molecules) were synthesized via condensation reactions of amine cores and aldehyde terminals, in which 87 and 88 were built by TPB amine cores while 89 and 90 were constructed by TPA amine cores. Synthesis routes of TPB and TPA amine cores were shown in Scheme 1 and 2. Buchwald–Hartwig coupling were applied to give 83 with Pd(OAc)<sub>2</sub>, P<sup>t</sup>Bu<sub>3</sub> and NaO<sup>t</sup>Bu in toluene, at 130 °C with 99 % yield. After formation with POCl<sub>3</sub> in DMF, aldehyde-type terminal 84 was achieved. Aldehyde terminal 86 was synthesized via Buchwald–Hartwig coupling with Pd(OAc)<sub>2</sub>, P<sup>t</sup>Bu<sub>3</sub> and NaO<sup>t</sup>Bu in toluene. HTL molecules 87 and 88 were prepared with the TPB amine core and aldehyde terminals 84 and 86, with trifluoroacetic acid as catalyst in CHCl<sub>3</sub> at 80 °C for 5 h in yield of 76% and 72 % respectively (reaction conditions were shown in Scheme 6 a). HTL molecules 89 and 90 were synthesized within same methods (reaction conditions were shown in Scheme 6 b)). The results of NMR spectroscopy confirmed that the NC type HTL molecules 87, 88, 89 and 90 was synthesized successfully.



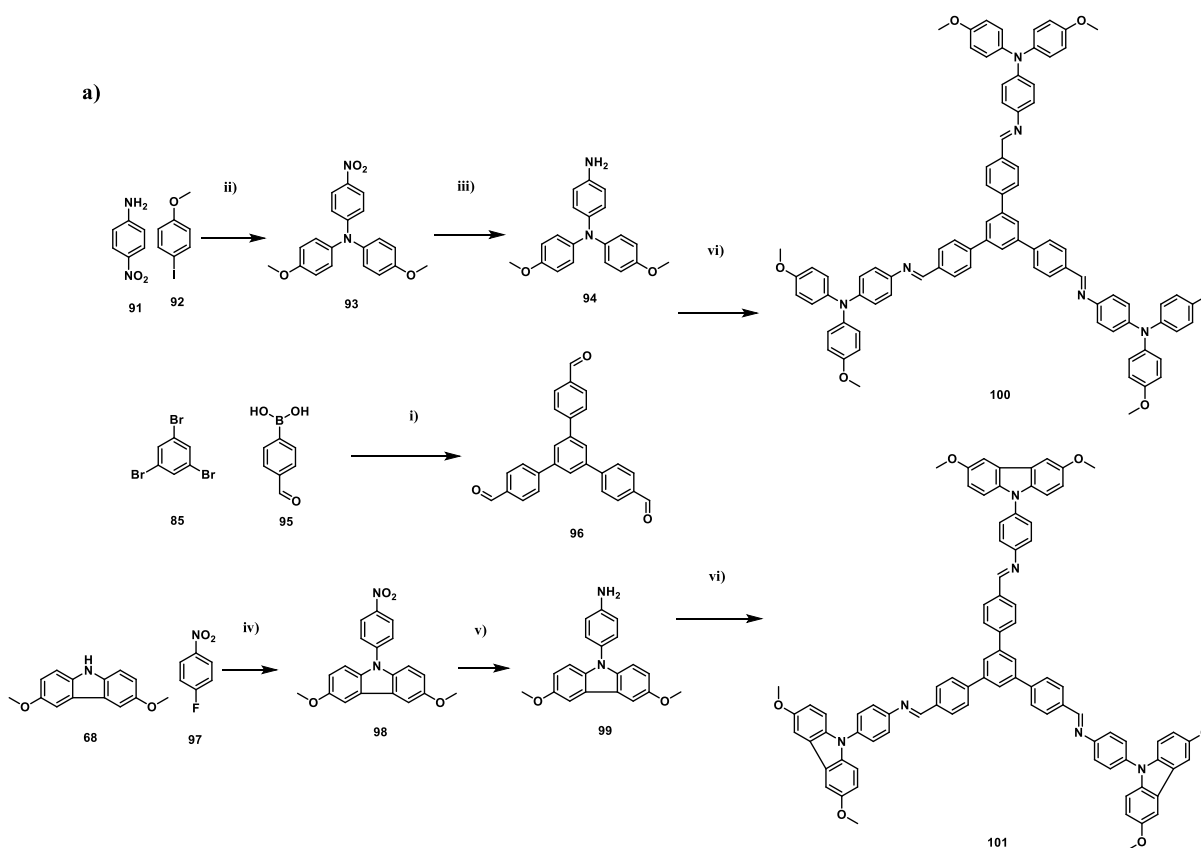


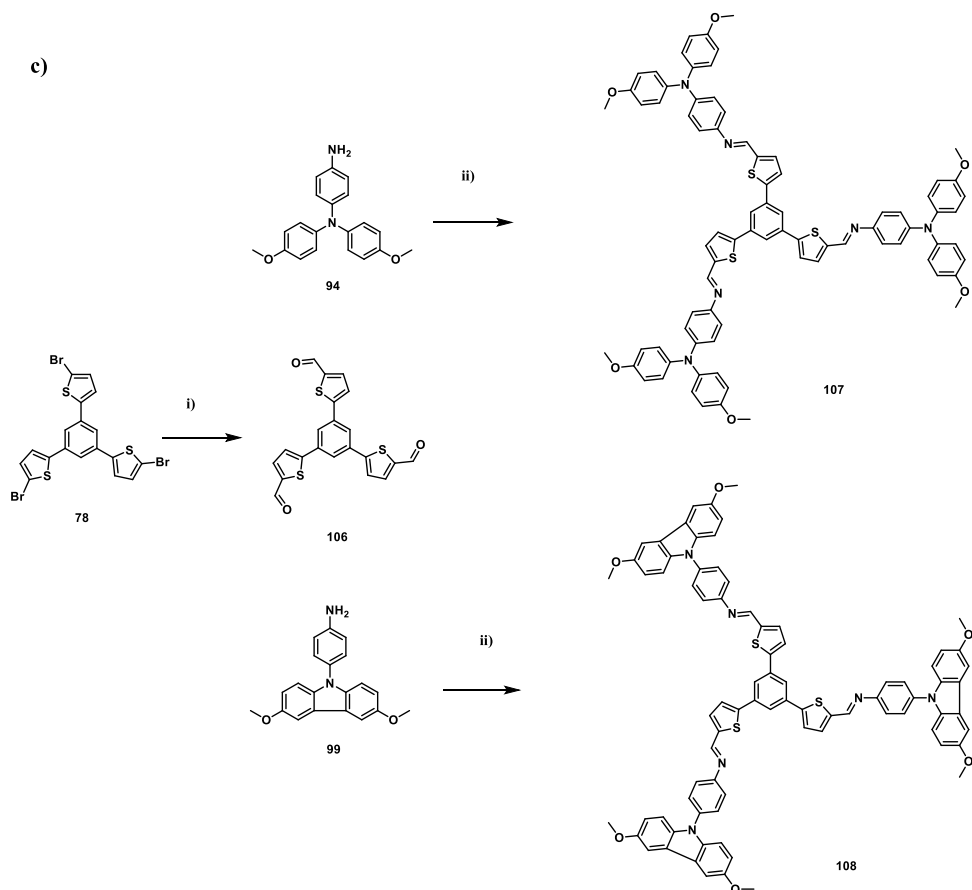
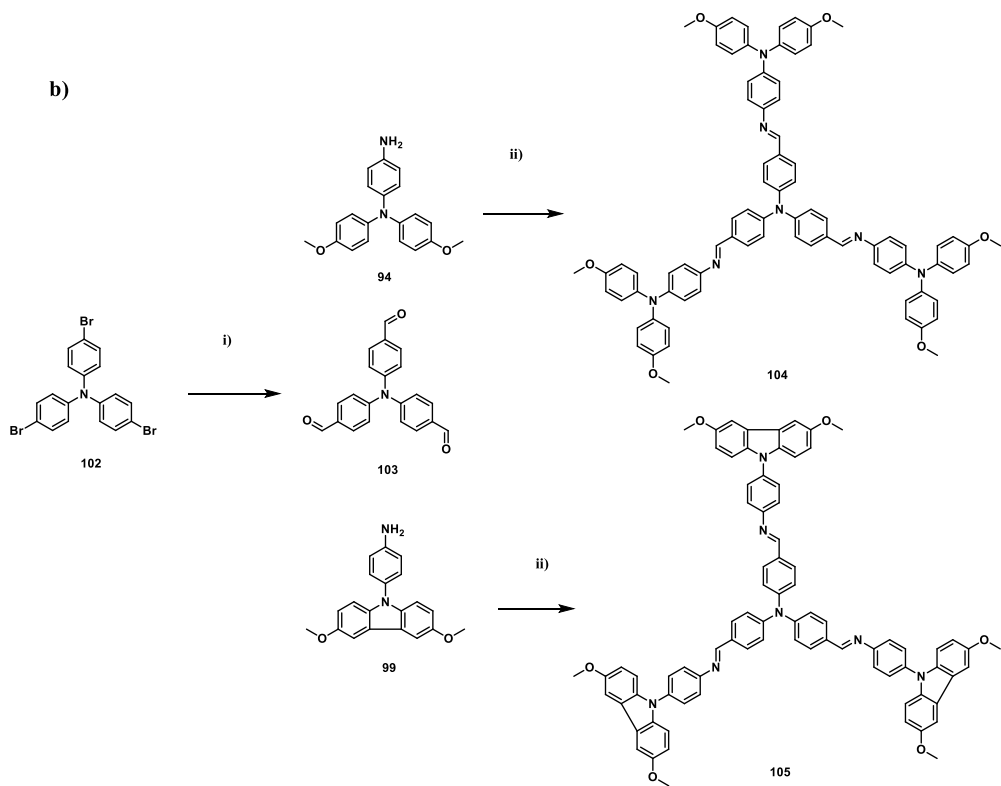
Scheme 6 a) Synthesis of NC-type HTL molecule 87, 88, 89 and 90. Reaction conditions: i)  $\text{Pd}(\text{OAc})_2$ ,  $\text{P}^t\text{Bu}_3$ ,  $\text{NaO}^t\text{Bu}$ , Tol,  $130\text{ }^\circ\text{C}$ , 24 h, (99 %); ii)  $\text{POCl}_3$ , DMF,  $90\text{ }^\circ\text{C}$ , 3 h, (92 %); iii)  $\text{Pd}(\text{OAc})_2$ ,  $^t\text{Bu}_3\text{P}$ ,  $\text{K}_2\text{CO}_3$ , Tol,  $130^\circ\text{C}$ , 24 h, (80 %); iv) trifluoroacetic acid,  $\text{CHCl}_3$ ,  $80\text{ }^\circ\text{C}$ , 5 h 87 (76%), 88 (72 %). b) Synthesis of HTL molecule 89 and 90. Reaction conditions: i)  $\text{Pd}/\text{C}$ ,  $\text{N}_2\text{H}_4$ , EtOH,  $90\text{ }^\circ\text{C}$ , 2 d, (92 %); ii) trifluoroacetic acid,  $\text{CHCl}_3$ ,  $80\text{ }^\circ\text{C}$ , 5 h, 89 (78 %), 90 (75 %).

CN-type HTL molecules 100, 101, 104, 105, 107 and 108 were synthesized via condensation reaction with TPB, TPA and TTB aldehyde cores and amine terminals, respectively. Reaction routes were shown in Scheme 7. Similar to NC-type HTL molecules syntheses, For CN-type HTL molecules, cores were synthesized first by condensed with different terminals. For CN-type HTL molecules 100 and 101, core molecule 96 was synthesized from 1,3,5-trisbromobenzene (85, commercial product without further purification) and 4-formylphenylboronic acid (95, commercial product without further purification) vis Suzuki-type coupling in THF with  $\text{PdCl}_2$  at  $100^\circ\text{C}$  for 24 h with a yield of 24%. 4-Nitroaniline (91, commercial product without further purification) and 4-



iodoanisole were coupled into 93 with Cu, 18-crown-6 and K<sub>2</sub>CO<sub>3</sub> in *o*-DCB at 188°C for 2 d and followed by reduction reaction with Pd/C, N<sub>2</sub>H<sub>4</sub> in EtOH at 90°C for 2 d to give 94 in a yield of 99%. Core 96 was condensed with terminal 94 to give HTL molecule 100 with trifluoroacetic acid as catalyst in CHCl<sub>3</sub> at 80°C for 5 h with a yield of 60%. Terminal 99 was synthesized by coupling 68 and 4-fluoronitrobenzene (97, commercial product without further purification) with CsF as catalyst in DMSO at 140 °C for 18 h, followed by reduction with Pd/C, N<sub>2</sub>H<sub>4</sub> in EtOH at 90°C for 2 d. HTL molecule 101 was synthesized via condensation between core 96 and terminal 99 with trifluoroacetic acid as catalyst in CHCl<sub>3</sub> at 80°C for 5 h with a yield of 60%. HTL molecules 104 and 105 were synthesized in similar condensation reactions, in which the core molecule 96 was substituted by molecule 103. HTL molecules 107 and 108 were also synthesized under the similar conditions, where the core unit was substituted by 106. The structure of the CN-type HTL molecules 100, 101, 104, 105, 107 and 108 were confirmed by NMR spectroscopy.





Scheme 7 a) Synthesis of CN-type HTL molecule 100 and 101. Reaction conditions: i) PdCl<sub>2</sub>, K<sub>2</sub>CO<sub>3</sub>, H<sub>2</sub>O, THF, 100 °C, 24 h, (24%); ii) Cu, 18-crown-6, K<sub>2</sub>CO<sub>3</sub>, o-DCB, 188°C, 2 d, (87 %); iii) Pd/C, N<sub>2</sub>H<sub>4</sub>, EtOH, 90 °C, 2 d, (99%); iv) CsF, DMSO, 140 °C, 18 h, (78 %); v) Pd/C, N<sub>2</sub>H<sub>4</sub>, EtOH, 90 °C, 2 d, (100 %); vi) trifluoroacetic acid, CHCl<sub>3</sub>, 80 °C, 5 h, 100 (60 %), 101 (60 %). b) Synthesis of HTL molecule 104 and 105. Reaction conditions: i) n-BuLi, DMF, THF, r.t. 3h; (47 %); ii) trifluoroacetic acid, CHCl<sub>3</sub>, 80°C, 5 h, 100 (53 %), 101 (56 %). c) Synthesis of HTL molecule 107 and 108. Reaction conditions: i) SiCl<sub>4</sub>, EtOH, r.t., 24 h, (54 %); ii) trifluoroacetic acid, CHCl<sub>3</sub>, 80 °C, 5 h, 107 (67 %), 108 (62 %).

Some NMR spectra results of CN- or NC- type HTL molecules showed the occurrence of impurities. Here, the <sup>1</sup>H NMR spectrum of HTL molecule 90 is given as example (Figure 15). The impurity signals marked by blue spots may belong to the starting material 86. And the impurity signals marked by orange spots may be attributed to only mono- or di-functionalized tris(4-aminophenyl)benzene cores. This assumption was confirmed by MALDI mass spectra of HTL molecule 90 (as shown in Figure 16). The two signals on 603.346 and 916.517 were attributed to the masses of mono- or di-functionalized tris(4-aminophenyl)benzene cores, respectively. These results indicate that CN- and NC-type HTL molecules may be decomposed under atmospheric conditions (moisture) or the reactions were not complete even after 3 d, because condensation reactions are reversible. The products may be not completely formed since water as by-product cannot be removed completely. All the CN- or NC- type HTL molecules were purified by solvent washing and recrystallization. The impurity may be more likely attributed to the decomposition instead of incomplete synthesis.

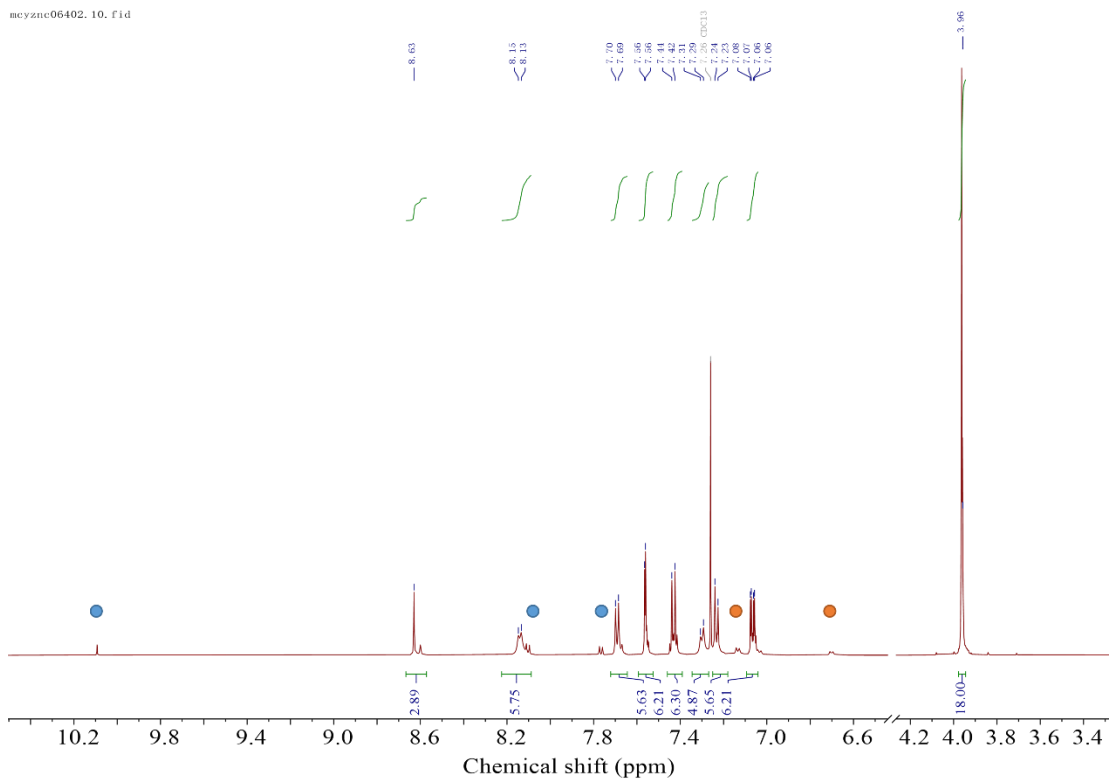


Figure 15. NMR result of HTL molecule 90.

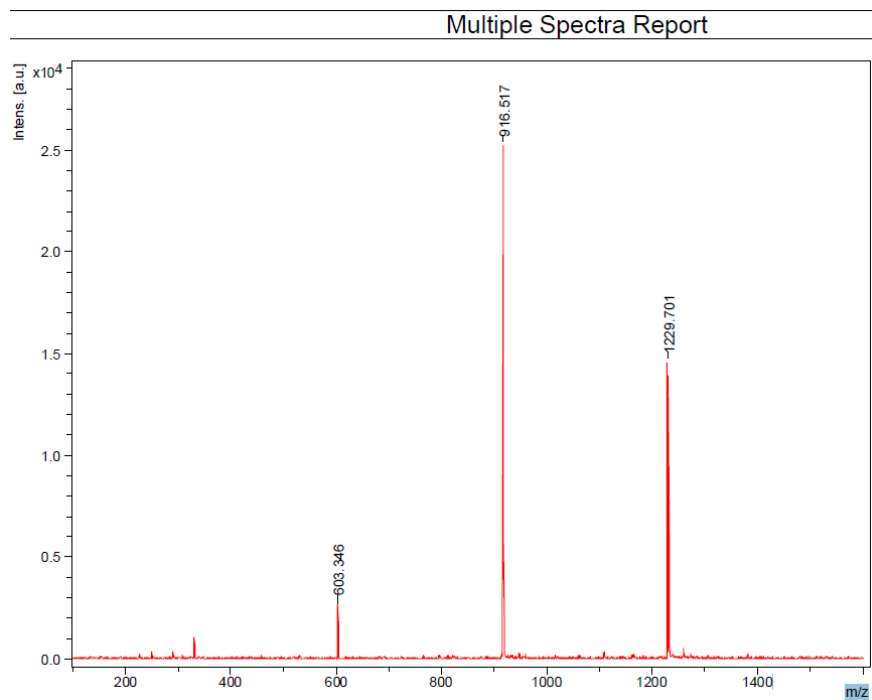


Figure 16. MALDI mass spectrum of HTL molecule 90.

## 2.2.2 Optoelectronic properties

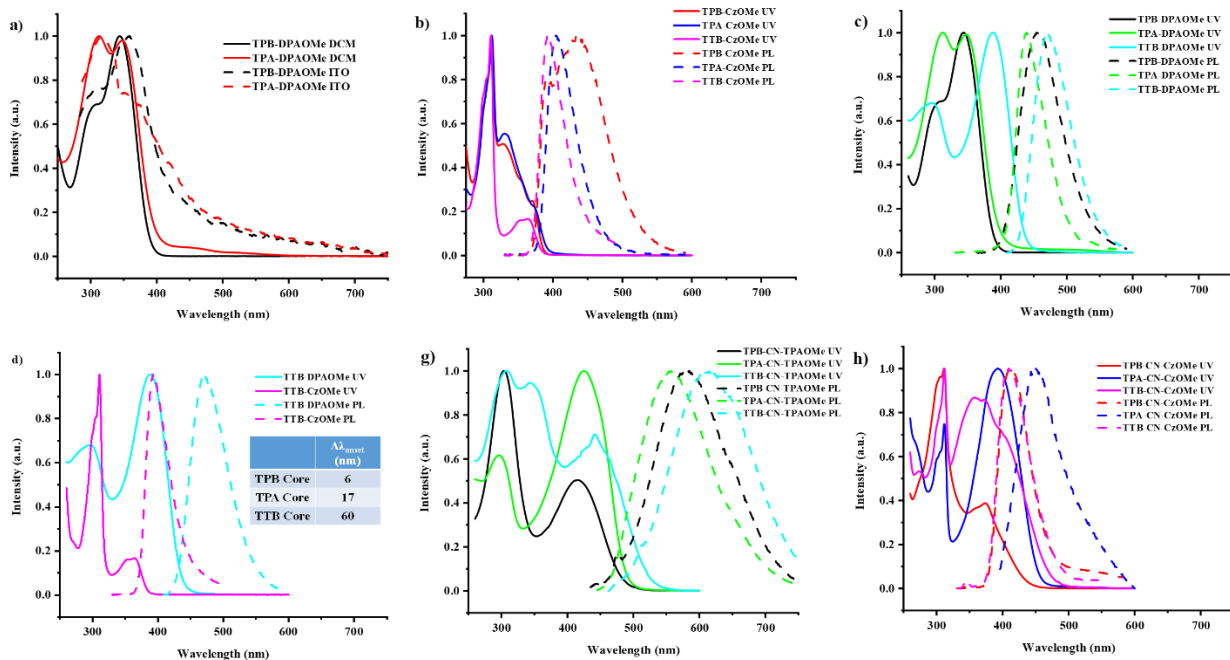
The optical properties of all designed HTM molecules were measured by UV-vis and photoluminescence (PL) spectroscopy within solid state as films and in solution with DCM as solvent, respectively (Results are summarized in Table 2). Most molecules show an absorption in the UV-region. Compared with absorption in solvent, the absorption peak of all molecules in films (in solid state) are always shifted bathochromically. The small difference of the spectra for all molecules solutions and in films indicates very weak intermolecular interactions and no significant crystallization in solid state.<sup>175, 176</sup> The absorption peak in the range of 290–310 nm belongs to characteristic absorption of TPA units.<sup>177</sup> The absorption peak located in the visible range from 400 to 600 nm is attributed to a HOMO-to-LUMO transition with partial charge transfer (CT) between the donor and acceptor units in the D-A structure.<sup>178</sup> Optical band gaps of all the model molecules are in the range from 2.21 to 3.30 eV, which are shown in Table 2 and calculated from the absorption onset as described in the experimental part. The maxima of emission for most molecules are located in the range of 400–600 nm with broad bands. Broad absorption and emission bands with planar molecular structure indicate twisted intramolecular charge transfer states (TICT).<sup>179</sup> Stokes shift of these HTM molecules were calculated from the difference between the maxima of absorption and emission, which are located in the range from 8 nm to 176 nm. Larger Stokes shifts indicate higher geometric structure differences based on structural relaxations of the excited state compared with the ground state, while small Stokes shift indicate a relatively rigid nature of the molecular structure.<sup>180, 181</sup> Due to the diversity of different molecular structures in this chapter, the optical spectra will be discussed in more detail.

Table 2. Optical properties of HTL molecules.

a) Absorption max of HTL molecules in DCM; b) value was taken from the intersection of the normalized absorption and emission spectra;<sup>182</sup> c) excitation at  $\lambda_{\text{abs}}$ ; d) optical gap was calculated from the formula of  $1240/\lambda_{\text{onset}}$ ; e) measured by AC-2 measurement; f) LUMO was calculated from the formula of  $E_{\text{LUMO}} = E_{\text{HOMO}} + E_{\text{g}}$  (eV); g) The difference between  $\lambda_{\text{abs}}$  and  $\lambda_{\text{emi}}$ .

	Name	$\lambda_{\text{abs}}$ <sup>a)</sup> (nm)	$\lambda_{\text{onset}}$ <sup>b)</sup> (nm)	$\lambda_{\text{emi}}$ <sup>c)</sup> (nm)	$E_{\text{g}}$ <sup>d)</sup> (eV)	HOMO <sup>e)</sup> (eV)	LUMO <sup>f)</sup> (eV)	Stokes shift <sup>g)</sup> (nm)
1	TPB-DPAOMe	344	389	454	3.18	-5.23	-2.05	110
2	TPB-CzOMe	371	387	391	3.20	-5.44	-2.24	20

3	TPA-DPAOMe	348	390	439	3.18	-4.99	-1.81	101
4	TPA-CzOMe	372	392	402	3.16	-5.31	-2.15	30
5	TTB-DPAOMe	389	435	471	2.85	-5.23	-2.38	82
6	TTB-CzOMe	365	382	394	3.25	-5.40	-2.15	29
7	TPB-NC-TPAOMe	391	450	558	2.76	-5.27	-2.51	167
8	TPB-NC-CzOMe	376	425	534	2.92	-5.39	-2.47	158
9	TPA-NC-TPAOMe	419	482	524	2.57	-5.02	-2.45	105
10	TPA-NC-CzOMe	418	479	531	2.59	-5.20	-2.61	113
11	TPB-CN-TPAOMe	417	486	582	2.55	-5.23	-2.68	165
12	TPB-CN-CzOMe	375	438	413	2.83	-5.42	-2.59	38
13	TPA-CN-TPAOMe	425	484	558	2.56	-5.17	-2.61	133
14	TPA-CN-CzOMe	392	450	450	2.76	-5.40	-2.64	48
15	TTB-CN-TPAOMe	442	518	618	2.81	-5.19	-2.38	176
16	TTB-CN-CzOMe	358	468	407	2.65	-5.36	-2.71	34



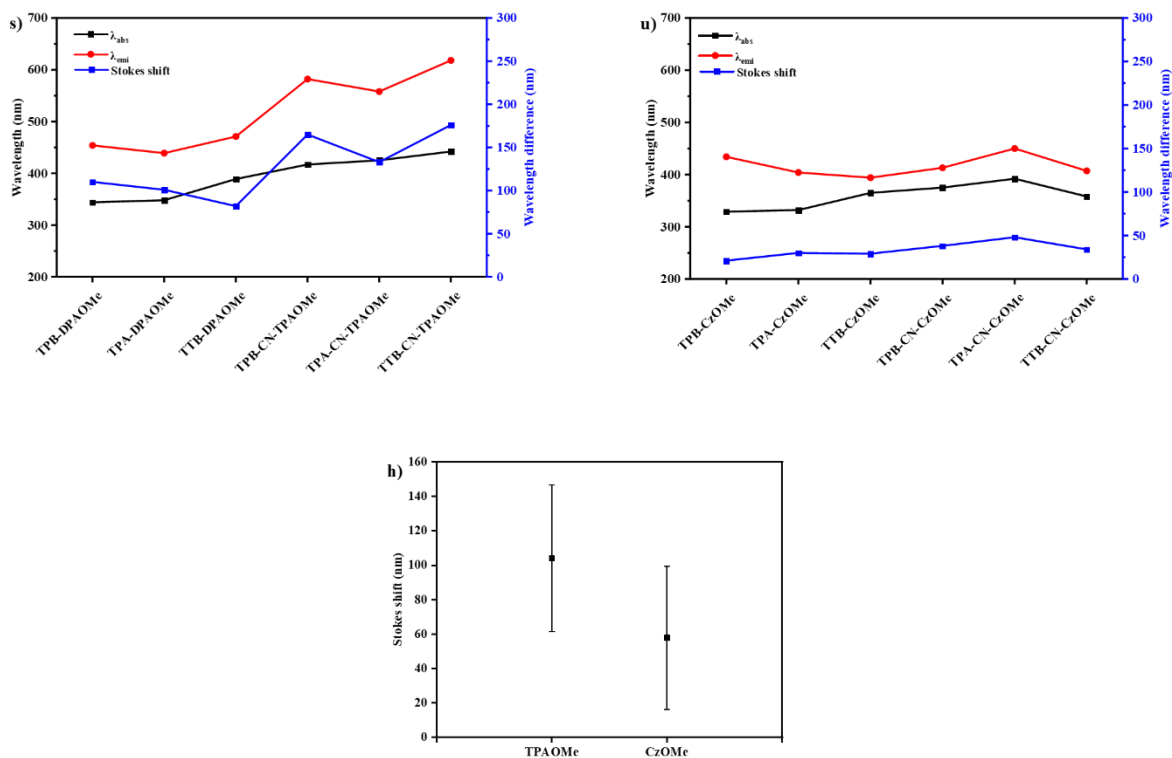


Figure 17. UV-vis absorption and PL spectra of HTL molecules with TPAOMe and CzOMe terminals.

The small shifts of the UV-absorption for TPB-DPAOMe and TPA-DPAOMe between DCM solution and in films are 14 and 3 nm, respectively, which represent weak intermolecular interactions for these molecules transformed from solution to solid state (as shown in Figure 17 a). The remaining molecules show a similar trend, revealing an absorption peak difference of 15 nm or less.

To systematically discuss the results, firstly, the influence of the varying core was investigated. The C-C linked molecules, namely TPB-CzOMe, TPA-CzOMe and TTB-CzOMe, exhibited characteristic and intense absorption peaks at 311 nm (as shown in Figure 17 b). The characteristic peak at 311 nm can be assigned to the CzOMe terminal, which dominates the absorption spectrum, while these characteristic peaks are not observable for TPB-DPAOMe, TPA-DPAOMe and TTB-DPAOMe. As shown in Figure 17 c, the maximum of the absorption is red-shifted in the following order: TPB-DPAOMe (344 nm), TPA-DPAOMe (348 nm) and TTB-DPAOMe (389 nm). The  $\lambda_{onset}$  is also bathochromically shifted in the same order. For DPAOMe-terminated molecules,

change of the cores influence the conjugation of these molecules, which can be explained by the enhanced electron-donation ability of the core molecules,<sup>183</sup> while for CzOMe-terminated molecules change of cores does not exhibit clear trends in UV absorption. In the following, the different terminals will be compared (As shown in Figure 17 d). The obvious red-shift was found from TTB-CzOMe to TTB-DPAOMe which was around 60 nm. Slight red-shifts were observed for TPB and TBA core molecules, which were 6 and 17 nm respectively.

For C=N linked molecules, no obvious trends were observed. Both  $\lambda_{\text{abs}}$  and  $\lambda_{\text{onset}}$  were red-shifted in the order of TPB-CN-TPAOMe, TPA-CN-TPAOMe and TTB-CN-TPAOMe (as shown in Figure 17 e). For TPB-CN-CzOMe, TPA-CN-CzOMe and TTB-CN-CzOMe, (as shown in Figure 17 f) there were also characteristic intense absorption peak located at 311 nm. But only  $\lambda_{\text{onset}}$  of these three molecules were found red-shifted in this order. Similar with C-C linked molecules, change of cores for C=N linked molecules influenced the UV-absorption due to different electron-donation ability of these cores. When cores were fixed to compare different terminals, similar trends were found associated with C-C linked molecules. Red-shifts of 63, 32 and 52 nm were found for TPB, TPA and TTB core molecules (figures were not shown here). The introduction of C=N linkages led to significant red-shifts comparison of molecules with same cores and terminals between C-C and C=N linkage. No obvious trends were found in comparison of molecules with same cores and terminals between N=C and C=N linkage (figures were not shown here).

The maxima of absorption and emission of all molecules are shown in the figures and Table 2. Stokes shifts are calculated from the difference between  $\lambda_{\text{abs}}$  and  $\lambda_{\text{emi}}$ . Stoke shifts of these HTM molecules based on different terminals are shown in Figure 17 g-h. Compared with TPAOMe-terminated molecules, CzOMe-terminated induced smaller Stoke shifts. The smaller Stokes shift can be attributed to a more rigid structure of carbazole which lead to less geometric difference upon relaxation of the excited state compared with the ground state. A big Stokes shift usually indicates larger molecular flexibility which can improve the pore filling and the hole transport ability of such materials.<sup>174</sup>

Optical gaps are calculated based on the absorption onset which is shown in Table 2. HOMO energy level of all the designed molecules is estimated by using photoelectron spectroscopy in air (PESA/AC-2). LUMO energy levels of each molecule are calculated from the formula of  $E_{\text{LUMO}} =$



$E_{\text{HOMO}} + E_g$  (eV). The HOMO, LUMO energy level alignment of designed molecules, and the valence, conduction band energies of MAPbI<sub>3</sub> and FA<sub>0.94</sub>CS<sub>0.06</sub>PbI<sub>3</sub> are shown in Figure 18. Except for TPA-DPAOMe and TPA-NC-TPAOMe, the remaining molecules possess deeper HOMO level than PTAA (-5.10 eV), which could lead to better energy band alignment with the HOMO of the actively light-absorbing perovskite materials. A smaller difference of HOMO value between the perovskite active layer and the HTM would enhance the hole extraction and transport by reduced charge recombination and loss of energy transfer, which lead to increased  $V_{\text{OC}}$ . It is important to note that all HOMO levels of same core molecules with CzOMe terminals are deeper than those of molecules with TPAOMe terminals (as shown in figure 18). All the HOMO level of molecules with TPB and TTB cores are deeper than that of TPA core, when connected to the same terminals. These trends would be guidance of molecular structure design for HTMs with controllable energy levels for better energy band alignment. The LUMO level off set of all designed molecules are high enough to inhibit diffusion of electrons to perovskite layers as well as recombination with holes, which would be beneficial for improved efficiency.

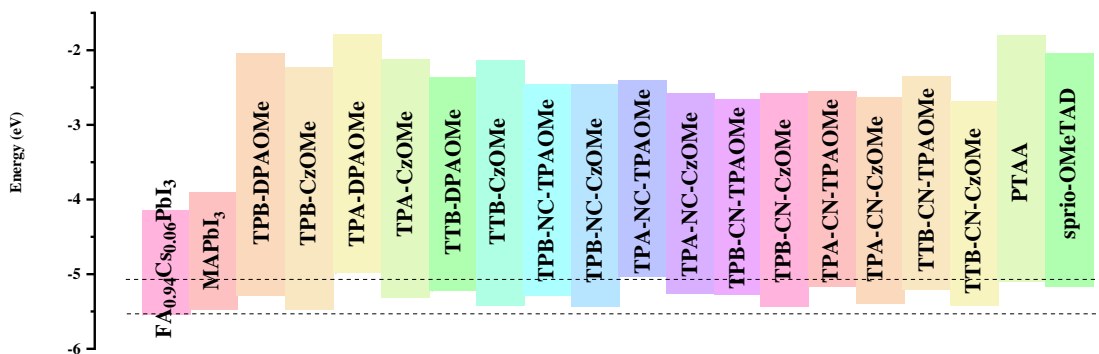


Figure 18. The HOMO, LUMO energy level alignment diagram of PTAA, spiro-OMeTED, the HTL molecules investigated, and the valence, conduction band energies of MAPbI<sub>3</sub> and FA<sub>0.94</sub>CS<sub>0.06</sub>PbI<sub>3</sub>.

During the preparation of the various semiconductor devices especially the organic photovoltaic devices, several different functional layers are stacked together, where interfaces, for examples, the donor/acceptor interface, the active layer/HTL (or ETL) interfaces and HTL (or ETL)/electrodes interfaces are formed between the functional layers. After absorbing solar energy,

excitons are generated and separated into electrons and holes. These two carriers are derived to corresponding electrodes crossing the above-described interfaces with different potential barriers. Choosing functional layers with appropriate energy levels aligning with the neighboring layers is very important to reduce the offset between layers and improve the  $V_{oc}$  of devices. However, discussing about energy level alignment based on HOMO and LUMO level is a simplified description especially for organic semiconductors. Inorganic semiconductors possess wide bandwidths, in which electrons and holes are considered as delocalized. Different from the case of inorganic semiconductors, continuous bands are not present in organic semiconductors (or very narrow bandwidths exist in organic semiconductor crystals), where electrons and holes are considered as localized. The carrier transport mechanism for organic semiconductors change to hopping and tunneling instead of band transport for inorganic semiconductors. Remarkable electronic polarization effect is introduced in organic semiconductors when adding or removing charged particles. These carriers localization and molecular polarization complicate the energy level alignment for organic semiconductors. When a charge is introduced into a molecule (adding an electron to LUMO or removing an electron from HOMO of this molecule to produce a charged molecule), this and surrounding molecules are polarized followed by the formation of polarization cloud (also known as polaron, which is defined as product of the charge and the surrounding polarization area) simultaneously, which relates to the stabilization energy  $P^+$  for cations (holes) and  $P^-$  for anions (electrons).<sup>184</sup> The HOMO and LUMO will shift to the new position (polaron levels)  $E_{P+}$  and  $E_{P-}$ , respectively, separated by a new reduced transport gap ( $E_T$ ).<sup>184, 185</sup> These new energy levels are different from the original HOMO and LUMO of the isolated non-ionized gas molecule separated by the energy gap  $E_0$ . The polarization energy is defined as  $E_P = E_{P+} + E_{P-}$ . The transport gap is defined as  $E_T = E_0 - E_P$ . The exciton binding energy can be described as  $E_{exc} = E_T - E_{opt}$  ( $E_{opt}$ , energy of formation of electron-hole pair) approximately.<sup>186, 187</sup> Since the HOMO and LUMO will be shifted in different cases resulting in errors on judgement of energy levels alignment, stokes shift is applied to estimate the deviation from practical energy levels to the HOMO and LUMO data were shown on table 2 and in figure 18. The less stokes shift represents the smaller energy levels deviation (schematic diagram is shown if Figure 19).

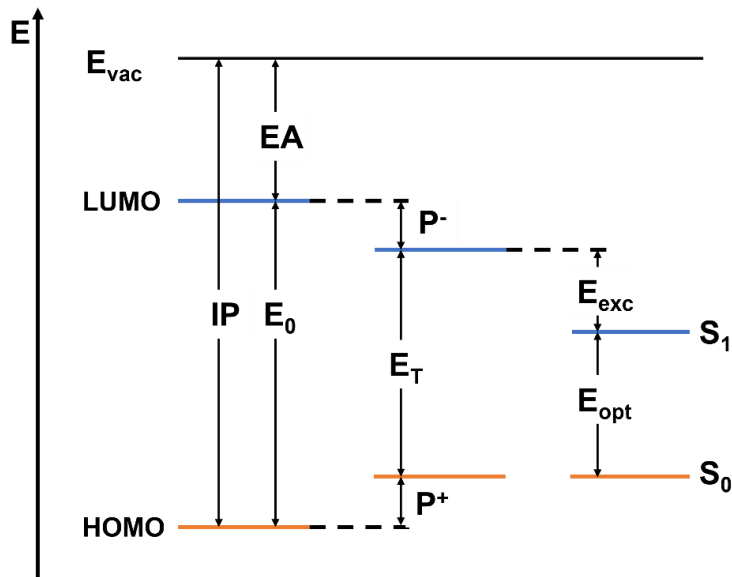


Figure 19. Schematic diagram of ionization potential (IP), electron affinity (EA) energy gap ( $E_0$ ), transport gap ( $E_T$ ), exciton binding energy ( $E_{exc}$ ) and energy of formation of electron-hole pair ( $E_{opt}$ ).

### 2.2.3 Photovoltaic performance of perovskite solar cells (PSC)

Before the characterization of photovoltaic performance, the quality of perovskite layers deposited on all designed HTL molecules should be assessed. The influence of the different HTL molecule layers to the perovskite morphology was estimated by using top-view scanning electron microscopy (SEM). Perovskite films with uniform, smooth, pin-hole free surface and significant crystallinity are beneficial for improved performance of the resulting devices. SEM images of perovskite layers deposited on PTAA, TPB-DPAOMe, TPB-CzOMe, TPA-DPAOMe, TPA-CzOMe, TTB-DPAOMe layers are shown in figure 20. Only 5 HTL molecules with PTAA as reference are shown here and are representative for all materials (The SEM results of all HTL molecules are quite similar, which are not shown here). The perovskite films coated on the molecules are dense and uniform without observed pin-holes. The grain size of perovskite is around 1  $\mu\text{m}$ , which is comparable with the reference on PTAA. The homogeneous perovskite layer with large grain size can be attributed to excellent wetting of perovskite precursor solvent (DMF and NMP) on HTL molecules layers. The following procedure after spin-coating of HTL molecules was the deposition of the perovskite layer, in which the perovskite precursor solution

including  $\text{PbI}_2$ , MAI and thiourea is spin-coated on top of HTL to form the corresponding perovskite after gas quenching and annealing, in which DMF and NMP are used as solvent. DMF and NMP demonstrate good solubility for model molecules. It is worth to verify if the HTL will be damaged after deposition of perovskite layer or not. There are no direct measurements to describe the quality of the HTL after perovskite layer deposition. We can only estimate the results based on SEM and photovoltaic performance of the final devices. Homogeneous and compact perovskite layer would not obtain via same standard perovskite deposition procedure on top of ITO instead of HTL covered ITO due to different surface energy (SEM results are not shown here). Since the perovskite layers obtained here on top of HTL molecules are dense and uniform without observes pin-holes, we could estimate the HTLs are not damaged by the subsequent spin-coating of the photo-active perovskite layer. Besides, according to the results of photovoltaic performance of the final devices, where the J-V curves and power conversion efficiency are close to ideal perovskite solar cells, which is unlikely with damaged HTLs, we also could estimate HTLs are not destroyed by DMF and NMP (the results of photovoltaic performance will be discussed below).

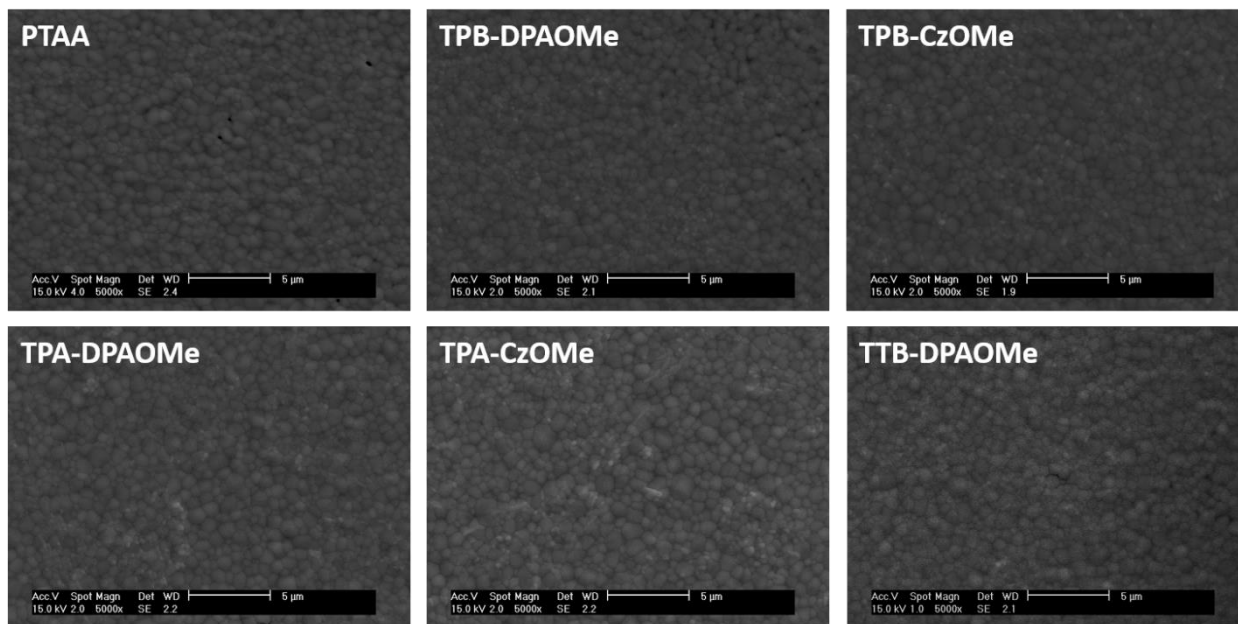


Figure 20. SEM images of perovskite layers deposited on PTAA, TPB-DPAOMe, TPB-CzOMe, TPA-DPAOMe, TPA-CzOMe, TTB-DPAOMe layers.

Upon completion of new HTM characterization, all designed molecules were employed in inverted (p-i-n) devices to study the impact on PCE as different dopant-free hole-transport layers. The procedure of PSC devices with the same architecture (ITO/designed molecules/perovskite layers/PCBM/AZO (Al doped Zinc Oxide)/Ag) were described in the experimental section. SEM cross-section images of the TPB-DPAOMe based device are shown in figure 21. HTL was spin-coated on top of ITO, which is too thin to observe in the SEM image (The thickness is under 20 nm which cannot be measured by DEKTAK). On top of HTL, dense, uniform and pin-hole free perovskite layer with around 500 nm thickness were covered. Later, PCBM and AZO were spin-coated with thickness of around 120 and 20 nm respectively. Finally, Ag electrode with thickness of 100 nm is thermal evaporated on top of AZO.

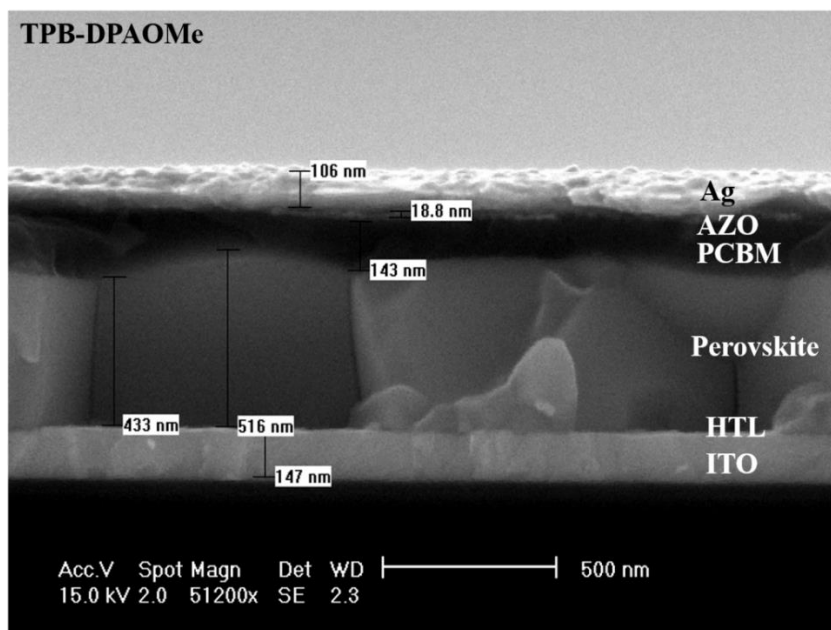


Figure 21. SEM cross-section images of the TPB-DPAOMe based device.

To evaluate the device performance of these designed model molecules as dopant-free HTMs in inverted perovskite solar cells, all the PSC devices with the same architecture of ITO/designed molecules/perovskite layers/PCBM/AZO/Ag were tested in both reverse and forward scan directions under AM 1.5G solar illumination. To optimize conditions for building better performance PSCs, TPB-DPAOMe were chosen as standard molecules and built into devices as HTL with different conditions such as plasma treatment on ITO substrates, concentration, spin-coat speed, anneal temperature, different concentration of PCBM.

Plasma treatment on ITO was applied to change surface energy of ITO, enhance the interfacial contacts, modifying the surface properties of ITO and overcome wetting issues from different solvents, which are beneficial for upper layer building. The photovoltaic parameters of PTAA and TPB-DPAOMe on ITO substrates with and without plasma treatment (only on ITO) are shown in Table 3 and Figure 22, respectively. The concentrations of both, PTAA and TPB-DPAOMe was 2.5 mg/ml. For PTAA samples, FF of PTAA samples without plasma treatment decreases from 75.31 % to 67.18 % compared with that with plasma treatment.  $J_{SC}$  also shows reduction from 21.12 mA/cm<sup>2</sup> to 19.47 mA/cm<sup>2</sup>.  $V_{OC}$  nearly maintains at the same level of around 1.02 V. The PCE decreases 3 % from 16.38% to 13.34 %. The small decrease of PCE indicate that PTAA films formed by spin-coating procedure may not be sensitive to plasma treatment, while the situation is opposite for TPB-DPAOMe. FF of TPB-DPAOMe samples without plasma treatment demonstrates obvious decrease from 79.37 % to 42.56 % compared with the same samples with plasma treatment. Besides,  $J_{SC}$  also shows reducing from 22.84 mA/cm<sup>2</sup> to 19.64 mA/cm<sup>2</sup>. Even  $V_{OC}$  shows small increasing, but PCE decreases significantly from 13.78 % to 7.33 %. This obvious decrease indicates TPB-DPAOMe is more sensitive to plasma treatment than PTAA, which plasma treatment on ITO is beneficial to form superior film quality of TPB-DPAOMe on spin-coating procedure. The better HTL films offer enhanced interfacial contacts to perovskite layer leading better photovoltaic performance. From the energy level diagram, TPB-DPAOMe shows deeper HOMO level than PTAA, but  $V_{OC}$  of TPB-DPAOMe is still lower than that with PTAA, which may also relate to inferior film quality and worse interfacial contacts of TPB-DPAOMe.

Table 3. Photovoltaic Parameters of PTAA and TPB-DPAOMe on ITO substrates with and without plasma treatment, respectively.

	Name	Conc. (mg/ml)	PCE (%)	FF (%)	$V_{OC}$ (V)	$J_{sc}$ (mA cm <sup>-2</sup> )
1	PTAA (w/ plasma)	2.5	16.38	75.31	1.03	21.12
2	PTAA (w/o plasma)	2.5	13.34	67.18	1.02	19.47
3	TPB-DPAOMe (w/ plasma)	2.5	13.78	79.37	0.76	22.84
4	TPB-DPAOMe (w/o plasma)	2.5	7.33	42.56	0.81	19.64

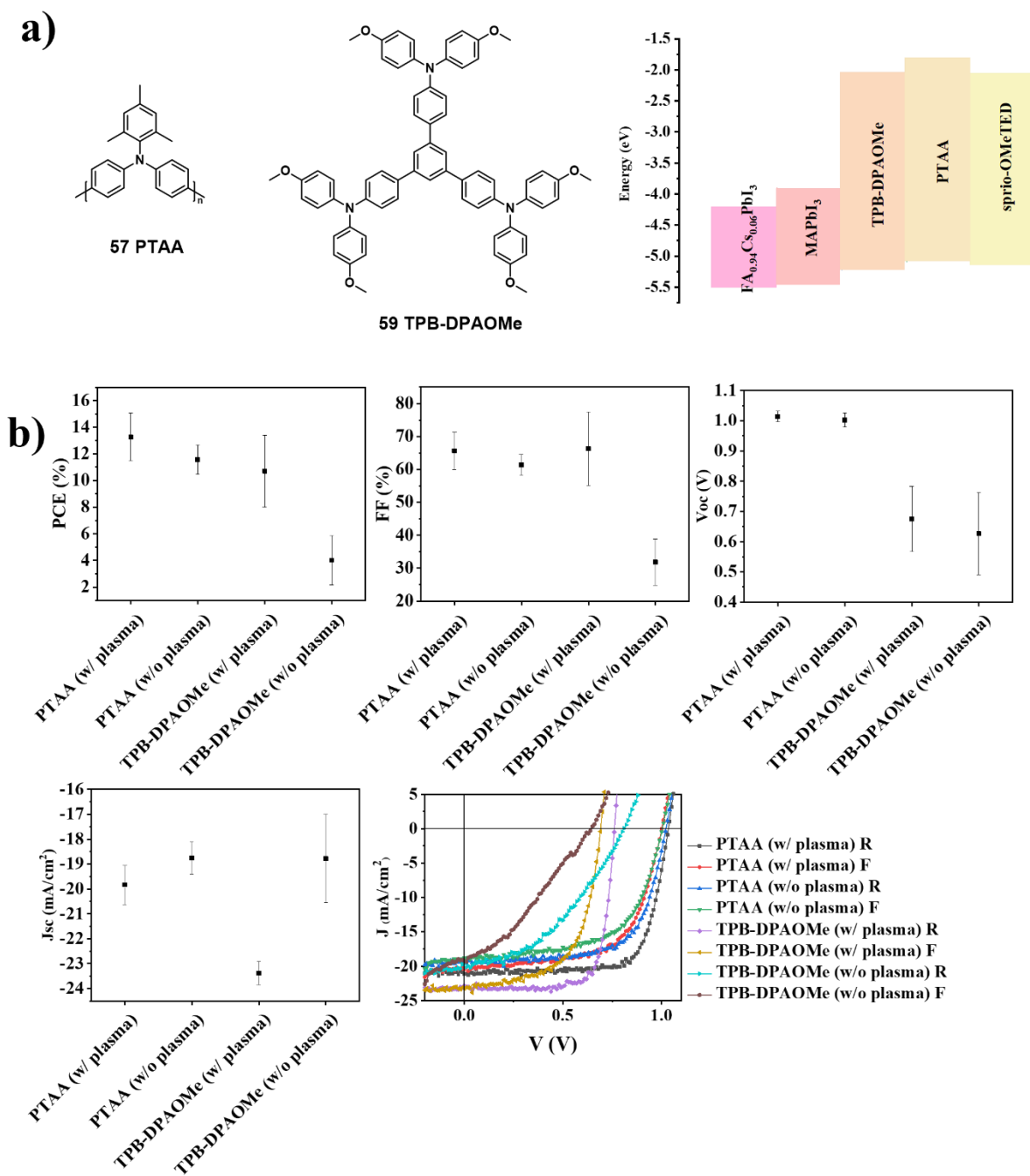


Figure 22. a) Structure of PTAA and TPB-DPAOMe. Energy level diagram of  $\text{FA}_{0.94}\text{CS}_{0.06}\text{PbI}_3$ ,  $\text{MAPbI}_3$ , TPB-DPAOMe, PTAA and spiro-OMeTED. b) Statistics of photovoltaic Parameters for PTAA and TPB-DPAOMe on ITO substrates with and without plasma treatment, J-V curves of PTAA and TPB-DPAOMe on ITO substrates with and without plasma treatment, respectively.

Amorphous molecules would transform into paracrystalline (which is defined as crystal having short- and medium-range ordering in the lattice) molecules on suitable temperature, which would increase hole mobility in HTLs. Photovoltaic parameters of PTAA and TPB-DPAOMe with different annealing temperature are shown in Table 4 and Figure 23. FF of TPB-DPAOMe with annealing temperature of 150 °C increased from 74.58 to 79.37 % compared with annealing at 135 °C.  $V_{OC}$  of TPB-DPAOMe maintains same level for both temperatures. Even  $J_{SC}$  decreases slightly, but the PCE still increases from 13.33 to 13.78 %. Crystallinity of HTM molecule films can be detected by XRD. XRD results are unsatisfactory, since the thicknesses of HTM films is about 15 nm, and therefore too thin to be detected, results are not shown here. As a result, 150 °C is chosen as optimized temperature for further devices building.

Table 4. Photovoltaic Parameters of PTAA and TPB-DPAOMe with different annealing temperature.

	Name	Temp. (°C)	Conc. (mg/ml)	PCE (%)	FF (%)	$V_{OC}$ (V)	$J_{SC}$ (mA cm <sup>-2</sup> )
1	PTAA (w/ plasma)	120	2.5	16.38	75.31	1.03	21.12
2	TPB-DPAOMe (w/ plasma)	135	2.5	13.33	74.58	0.75	23.82
3	TPB-DPAOMe (w/ plasma)	150	2.5	13.78	79.37	0.76	22.84



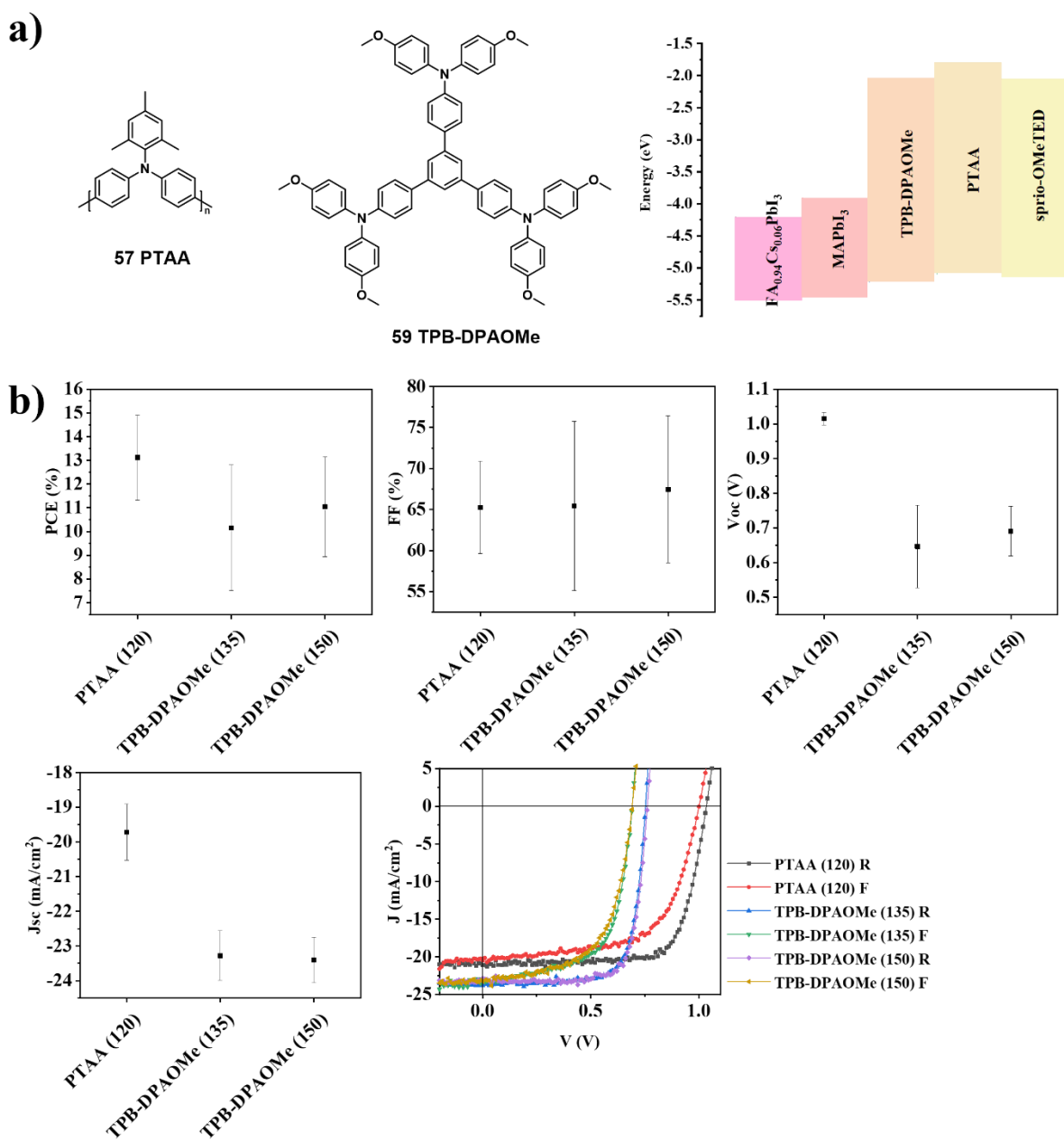


Figure 23. a) Structure of PTAA and TPB-DPAOMe. Energy level diagram of  $\text{FA}_{0.94}\text{Cs}_{0.06}\text{PbI}_3$ ,  $\text{MAPbI}_3$ , TPB-DPAOMe, PTAA and sprio-OMeTED. b) Statistics of photovoltaic parameters for TPB-DPAOMe-HTLs at different annealing temperature, J-V curves of PTAA and TPB-DPAOMe-based perovskite solar cell at different annealing temperature, respectively.

The photovoltaic parameters of PTAA and TPB-DPAOMe with different concentrations are shown in Table 5 and Figure 24, respectively. FF firstly rises from 69.36 % to 72.20 % as concentration is increased from 1 to 1.5 mg/ml and decreases to 59.00 % when continually increasing the concentration from 1.5 to 20 mg/ml. But the trend of  $V_{OC}$  is opposite with that of FF, which  $V_{OC}$  is firstly decreased as concentration rising from 1 to 1.5 mg/ml. FF,  $J_{SC}$  and PCE are reduced obviously when concentration is increased to 20 mg/ml. The optimized concentration of TPB-DPAOMe would be between 1 to 5 mg/ml.

Table 5. Photovoltaic parameters of PTAA-and TPB-DPAOMe-based perovskite solar cells at different concentrations.

	Name	Conc. (mg/ml)	PCE (%)	FF (%)	$V_{OC}$ (V)	$J_{sc}$ (mA cm <sup>-2</sup> )
1	PTAA (w/ plasma)	2.5	16.38	75.31	1.03	21.12
2	TPB-DPAOMe (w/ plasma)	1	10.80	69.36	0.82	18.99
3	TPB-DPAOMe (w/ plasma)	1.5	10.60	72.20	0.77	19.07
4	TPB-DPAOMe (w/ plasma)	2.5	10.32	70.39	0.80	18.33
5	TPB-DPAOMe (w/ plasma)	5	10.32	68.73	0.83	18.08
6	TPB-DPAOMe (w/ plasma)	10	9.34	62.33	0.88	17.02
7	TPB-DPAOMe (w/ plasma)	20	8.45	59.00	0.85	16.28

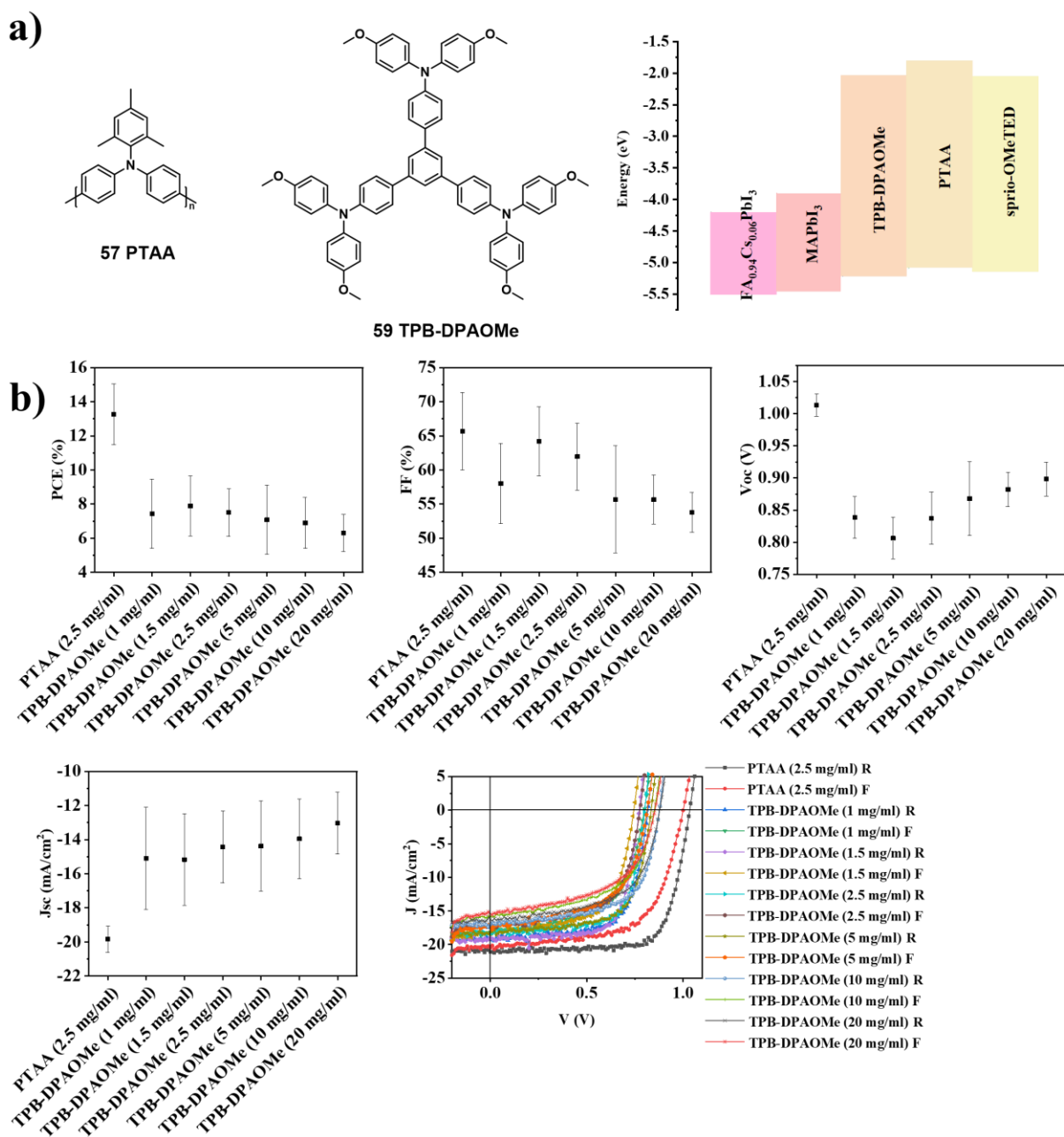


Figure 24. a) Structure of PTAA and TPB-DPAOMe. Energy level diagram of  $\text{FA}_{0.94}\text{CS}_{0.06}\text{PbI}_3$ ,  $\text{MAPbI}_3$ , TPB-DPAOMe, PTAA and sprio-OMeTED b) Statistics of photovoltaic parameters for TPB-DPAOMe with different concentration, J-V curves of PTAA and TPB-DPAOMe with different concentration respectively.

The equipment for plasma treatment was inoperable for several months, however, the data for optimization show a great benefit of this procedure on the overall device performances and were therefore included into this thesis. The optimization of concentration was repeated with another batch without plasma treatment under static (spin-coating after dropping solution) or dynamic spin-coating conditions (drop solution during spin-coating, as shown in Table 6 and Figure 25). As discussed above, the optimized concentration should be between 1 to 5 mg/ml, TPB-DPAOMe were spin-coated under static or dynamic conditions with concentrations of 1, 2.5 and 5 mg/ml. The photovoltaic performance of statically generated devices always behaved a little better than that of the dynamically generated ones for the same concentrations, respectively. Additionally, TPB-DPAOMe as HTL was spin-coated under static conditions with a concentration of 2.5 mg/ml showed best PCE and  $V_{OC}$ , which is 7.33 % and 0.81 V, respectively. Thus, concentration of 2.5 mg/ml and static spin-coating conditions are chosen as the most optimized conditions. It should be mentioned, because the working condition of plasma equipment was unstable, all the devices which will be discussed later were built without plasma treatment to eliminate negative effects of different plasma treatment, guaranteeing that all photovoltaic performance results can be discussed under the same conditions.

Table 6. Photovoltaic parameters of PTAA and TPB-DPAOMe-based perovskite solar cells at different concentration and spin-coating conditions.

	Name	Spincoating modle	Conc. (mg/ml)	PCE (%)	FF (%)	Voc (V)	Jsc (mA cm <sup>-2</sup> )
1	PTAA (w/o plasma)	Static	1.3	16.18	76.94	1.03	20.42
2	TPB-DPAOMe (w/o plasma)	Static	1	6.04	38.78	0.79	19.72
3	TPB-DPAOMe (w/o plasma)	Dynamic	1	5.16	33.21	0.64	21.10
4	TPB-DPAOMe (w/o plasma)	Static	2.5	7.33	42.56	0.81	19.64
5	TPB-DPAOMe (w/o plasma)	Dynamic	2.5	5.41	38.88	0.72	19.31

6	TPB-DPAOMe (w/o plasma)	Static	5	6.56	45.79	0.71	20.91
7	TPB-DPAOMe (w/o plasma)	Dynamic	5	6.40	44.75	0.70	20.43

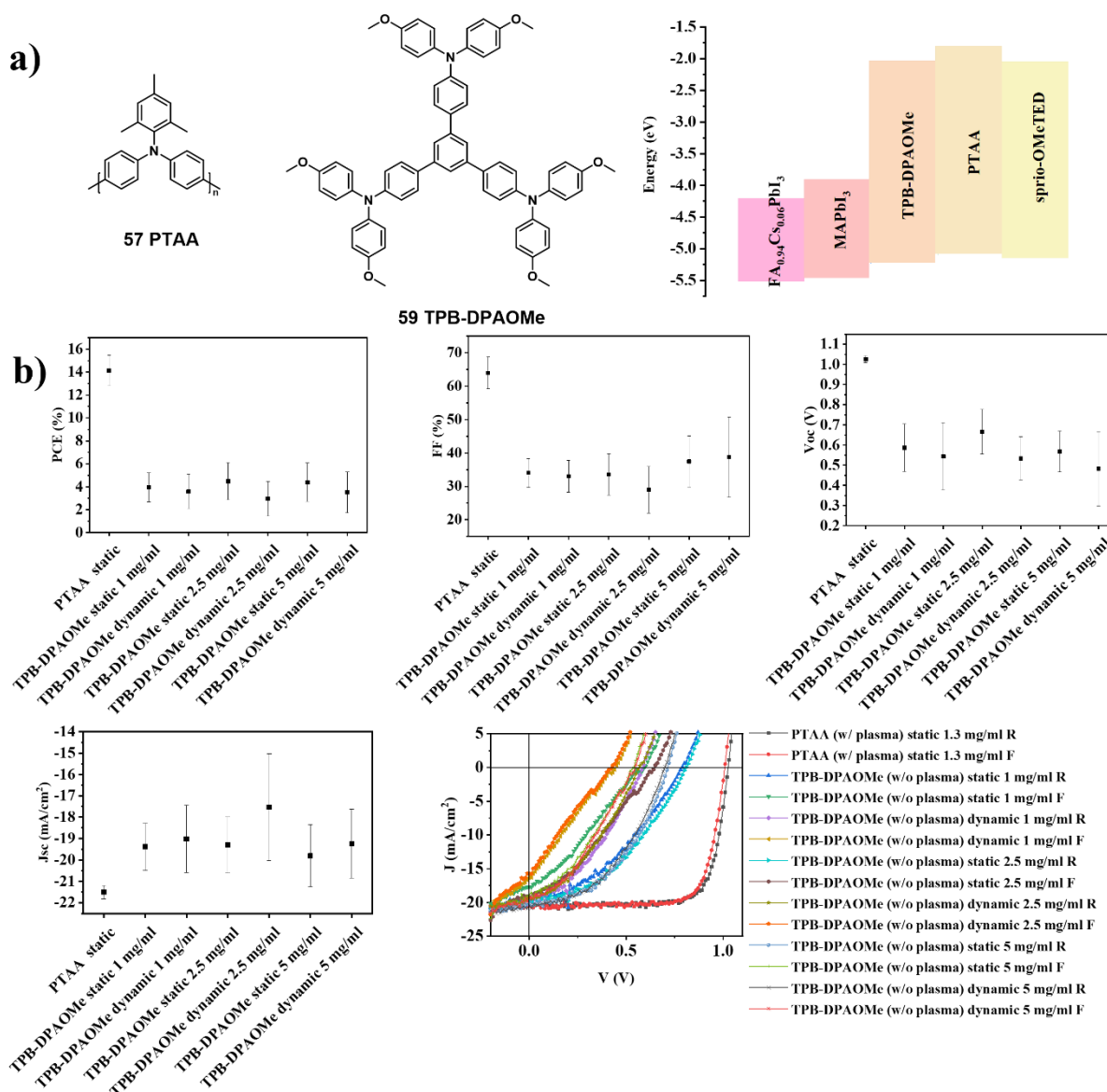


Figure 25. Structure of PTAA and TPB-DPAOMe. Energy level diagram of  $\text{FA}_{0.94}\text{Cs}_{0.06}\text{PbI}_3$ ,  $\text{MAPbI}_3$ , TPB-DPAOMe, PTAA and spiro-OMeTED. b) Statistics of photovoltaic parameters for TPB-DPAOMe-based perovskite solar cells at different spin-coating conditions and concentrations, J-V curves of PTAA and TPB-DPAOMe-based perovskite solar cells at different spin-coating conditions and concentrations, respectively.

The thickness of HTLs is controlled by tuning the speed of spin-coating. Photovoltaic parameters of PTAA and TPB-DPAOMe-based devices with different spin-coating speeds and time are shown in Table 7 and Figure 26. Obviously, TPB-DPAOMe-based devices with spin-coating speeds of 4000 rpm cause the best photovoltaic performance, which PCE, FF,  $V_{OC}$  and  $J_{SC}$  are 8.49 %, 50.83 %, 1.00 V and 16.70 mA/cm<sup>2</sup>, respectively. For TPB-DPAOMe-based devices with spin-coating speeds of 2000, 3000 and 5000 rpm s-shape in J-V curves are observed, which are strongly related to the thickness of HTLs. As a result, 4000 rpm was chosen as the optimized condition for devices building.

Table 7. Photovoltaic parameters of PTAA and TPB-DPAOMe-based perovskite solar cells with different spin-coating speeds and time.

	Name	Speed, time (rpm, s)	Conc. (mg/ml)	PCE (%)	FF (%)	$V_{OC}$ (V)	$J_{SC}$ (mA cm <sup>-2</sup> )
1	PTAA (w/o plasma)	6000, 20	1.3	16.74	67.60	1.08	22.92
2	TPB-DPAOMe (w/o plasma)	2000, 20	2.5	2.79	26.09	0.9	11.87
3	TPB-DPAOMe (w/o plasma)	3000, 20	2.5	2.94	27.44	0.96	11.17
4	TPB-DPAOMe (w/o plasma)	4000, 20	2.5	8.49	50.83	1.00	16.70
5	TPB-DPAOMe (w/o plasma)	5000, 20	2.5	2.27	25.23	0.86	10.45

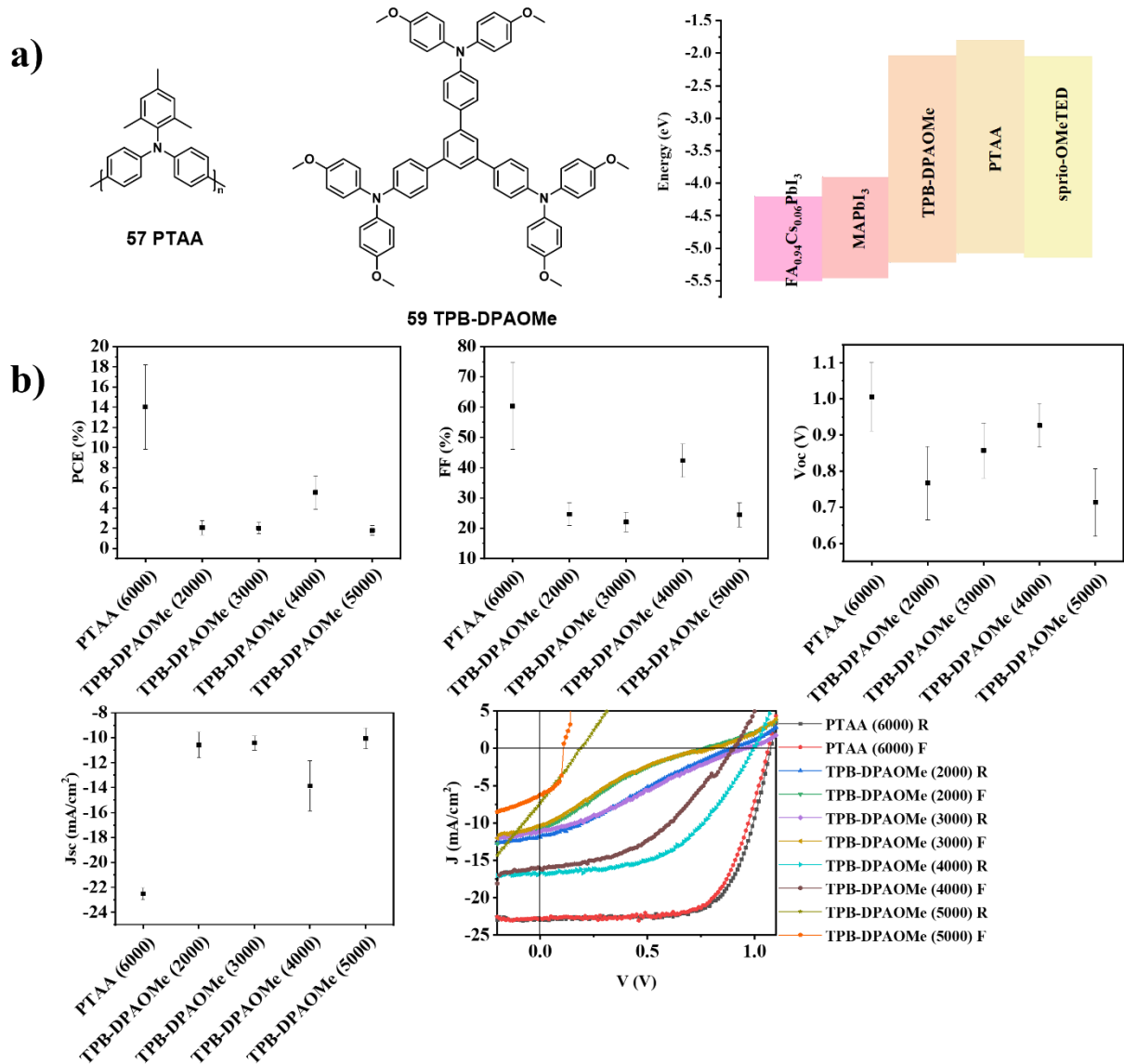


Figure 26. a) Structure of PTAA and TPB-DPAOMe. Energy level diagram of  $\text{FA}_{0.94}\text{CS}_{0.06}\text{PbI}_3$ ,  $\text{MAPbI}_3$ , TPB-DPAOMe, PTAA and sprio-OMeTED. b) Statistics of photovoltaic parameters for TPB-DPAOMe-based perovskite solar cells with different spin-coating speeds and time, J-V curves of PTAA and TPB-DPAOMe-based perovskite solar cells with different spin-coating speeds and time, respectively.

It is widely observed that the involvement of PCBM ETLs is beneficial to alleviate or eliminate hysteresis and enhanced electron transfer at perovskite/AZO surface. Photovoltaic parameters of PTAA and TPB-DPAOMe-based perovskite solar cells with different concentration of PCBM are shown in Table 8 and Figure 27. The trends for TPB-DPAOMe-based perovskite solar cells with different concentrations of PCBM solutions are not obvious. Only photovoltaic performance for PCBM concentration of 25 mg/ml are decreased much compared with that of both lower and higher concentration. As a result, 30 mg/ml concentration of PCBM is chosen as the optimized condition for devices building.

Table 8. Photovoltaic parameters of PTAA and TPB-DPAOMe-based perovskite solar cells with different concentrations for PCBM as ETL generation.

	Name	PCBM conc. (mg/ml)	Speed, time (rpm, s)	Conc. (mg/ml)	PCE (%)	FF (%)	V <sub>oc</sub> (V)	J <sub>sc</sub> (mA cm <sup>-2</sup> )
1	PTAA (w/o plasma)	25	6000, 20	1.3	18.46	76.38	1.05	23.01
2	TPB-DPAOMe (w/o plasma)	20	4000, 20	2.5	8.35	53.72	0.99	15.69
3	TPB-DPAOMe (w/o plasma)	25	4000, 20	2.5	2.91	26.01	0.86	13.01
4	TPB-DPAOMe (w/o plasma)	30	4000, 20	2.5	8.56	55.60	1.00	15.96
5	TPB-DPAOMe (w/o plasma)	35	4000, 20	2.5	6.01	42.42	0.96	14.75



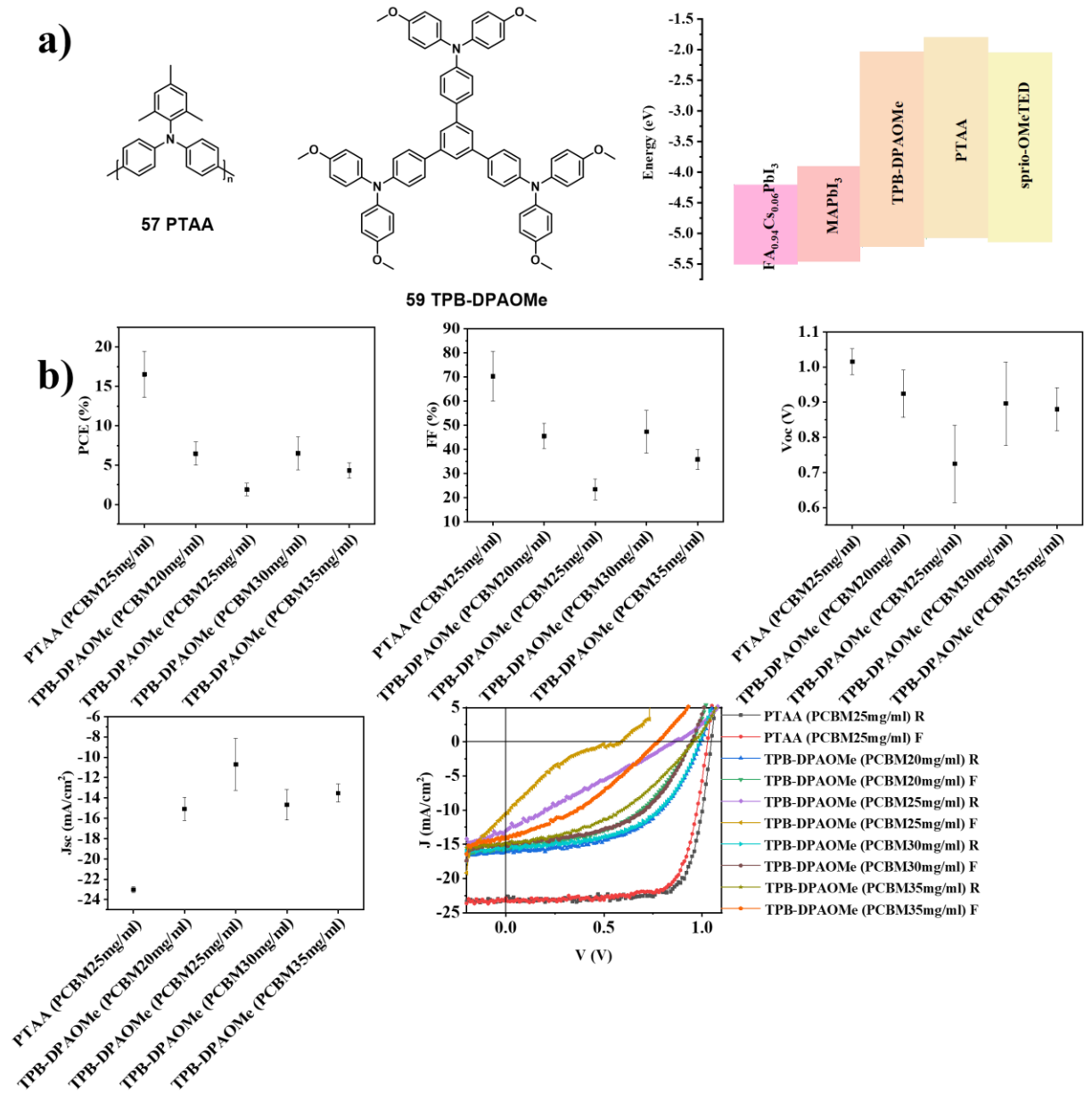


Figure 27. a) Structure of PTAA and TPB-DPAOMe. Energy level diagram of  $\text{FA}_{0.94}\text{Cs}_{0.06}\text{PbI}_3$ ,  $\text{MAPbI}_3$ , TPB-DPAOMe, PTAA and sprio-OMeTED. b) Statistics of photovoltaic parameters for TPB-DPAOMe-based perovskite solar cells with different concentration of PCBM for ETL generation, J-V curves of PTAA and TPB-DPAOMe-based perovskite solar cells with different concentration of PCBM solutions respectively.

The electronic dipole is defined as a couple of equal and opposite point charges (-q and +q) which are separated by a distance (d). The product of these two-point charges and the distance in between is described as dipole moment, which also can be understood as the strength of a dipole moment (as shown in Figure 28). Dipole moment is a vector. The direction of a dipole moment is pointing from the negative charge to the positive charge. The magnitude of a dipole moment is defined mathematically as  $\vec{p} = q\vec{d}$  ( $\vec{p}$  represents dipole moment vector, q is the magnitude of the charge and  $\vec{d}$  equals to the displacement vector). In chemistry, electronic dipoles are present in organic molecules or compounds commonly. Asymmetry of chemical bonds or molecules caused by unbalanced electronegativity gives rise to the dipoles.<sup>188</sup> In this case, these molecules can be considered as dipoles (for example, a water molecule, H<sub>2</sub>O). In devices engineering, electronic dipoles are present in interfaces widely, since different functionalized layers are packeted to compose designed interfaces, for example, donor-acceptor interfaces and metal-organic interfaces. Asymmetry of these interfaces would cause an alignment with chemical bonds, rearrangement of molecules and result in forming of dipole moments. When a large number of dipole moments are introduced in an interlayer, they tend to occur abreast rearrangement and form a dipole moment layer. This dipole moment layer would shift the vacuum level of the electron energy band at the interface, change the work function of the bottom electrodes and affect the charge carrier transport across the interface. Scanning Kelvin probe microscopy (SKPM) is used to characterize the interfacial dipole by measuring the  $\Delta$  work function of ITO electrodes before and after spin-coating of different HTL molecules.<sup>189</sup>  $\Delta$  work function is defined as  $\Delta = \Phi - \Phi'$ , where  $\Phi$  is work function of electrodes and  $\Phi'$  represent work function after spin-coating of HTL molecules (as shown in Figure 28).

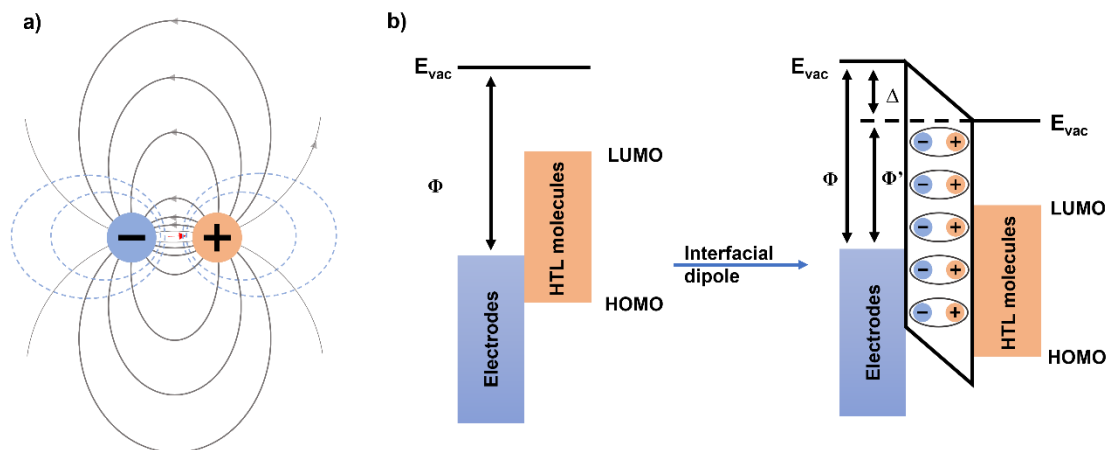


Figure 28. (a) Schematic of an electric dipole with electronic field lines (gray solid line), equipotential lines (blue dashed line), direction of electronic field (gray arrow) and direction of dipole moment (red arrow). (b) Energy level and work function of electrodes/HTL molecules interface with and without interfacial dipole.

The optimized condition based on the above results are plasma treatment on ITO substrates, molecule concentration of 2.5 mg/ml for HTL generation, spin-coating speed of 4000 rpm for 20 s, annealing temperature of 150 °C and PCBM concentration of 30 mg/ml for ETL generation. These conditions are used to test different molecules as HTLs in p-i-n dopant-free PSCs. We first focus on the HTL molecules without C=N linkage. The photovoltaic performances are shown in Table 9 and Figure 29, in which doping free PTAA-HTL serve as reference. The reference PTAA-based devices exhibit a  $PCE_{max}$  of 16.48% with FF of 76.94%,  $V_{OC}$  of 1.03 V and  $J_{SC}$  of 20.41  $mA/cm^2$  in the reverse scan. TPB-DPAOMe-, TPA-DPAOMe-, TPA-CzOMe- and TTB-DPAOMe-HTLs show obvious higher  $PCE_{max}$ , which are 11.20, 12.35, 11.59, 10.96%, respectively, if compared to TPB-CzOMe-HTLs with 5.31 % in the reverse scan. Similar with trend of PCE, TPB-CzOMe-HTLs also show remarkable decreases in FF and  $J_{SC}$ , which are 43.15% and 13.68  $mA/cm^2$ .  $V_{OC}$  TPB-CzOMe-HTLs also indicate slight decreasing from around 0.97 V of the other molecules to 0.90 V. The reduction of photovoltaic performance for TPB-CzOMe actually is hard to understand because it possesses small stokes shift,  $\Delta$  work function and small HOMO gap with  $FA_{0.94}Cs_{0.06}PbI_3$ .  $\Delta$  work function of 0 represents eliminating of the hinder effect leaded by dipole. And the deep HOMO of TPB-CzOMe with tiny HOMO gap with

FA<sub>0.94</sub>CS<sub>0.06</sub>PbI<sub>3</sub> means well-matched band alignment with active layer, which is beneficial to increase V<sub>OC</sub>. From statistics of photovoltaic performance, all the molecules behave much close to PTAA reference in average except TPB-CzOMe. The possible reason may relate to the plane molecules structure with less electron donating groups.

Table 9. Photovoltaic parameters of PTAA, TPB-DPAOMe-, TPB-CzOMe-, TPA-DPAOMe-, TPA-CzOMe-, TTB-DPAOMe- and TTB-CzOMe-HTL in perovskite solar cell devices.

Name	Stokes shift (nm)	Work function (eV)	$\Delta$ Work function (eV)	Scan direction	PCE (%)	FF (%)	V <sub>OC</sub> (V)	J <sub>SC</sub> (mA cm <sup>-2</sup> )
1 PTAA		4.61	0	Reverse	16.48	76.94	1.03	-20.41
				Forward	15.82	76.64	1.01	-20.44
2 TPB-DPAOMe	110	4.59	0.02	Reverse	11.20	62.53	0.96	-18.65
				Forward	8.92	55.25	0.88	-18.34
3 TPB-CzOMe	20	4.61	0	Reverse	5.31	43.15	0.90	-13.68
				Forward	2.99	33.51	0.69	-12.90
4 TPA-DPAOMe	91	4.25	0.36	Reverse	12.35	67.86	0.95	-19.57
				Forward	10.9	61.17	0.87	-19.53
5 TPA-CzOMe	30	4.62	-0.01	Reverse	11.59	62.50	1.01	-18.37
				Forward	8.89	55.44	0.88	-18.21
6 TTB-DPAOMe	82	4.46	0.15	Reverse	10.96	59.36	0.99	-18.66
				Forward	7.20	47.16	0.85	-17.97
7 TTB-CzOMe	29	4.47	0.14	Reverse				
				Forward				

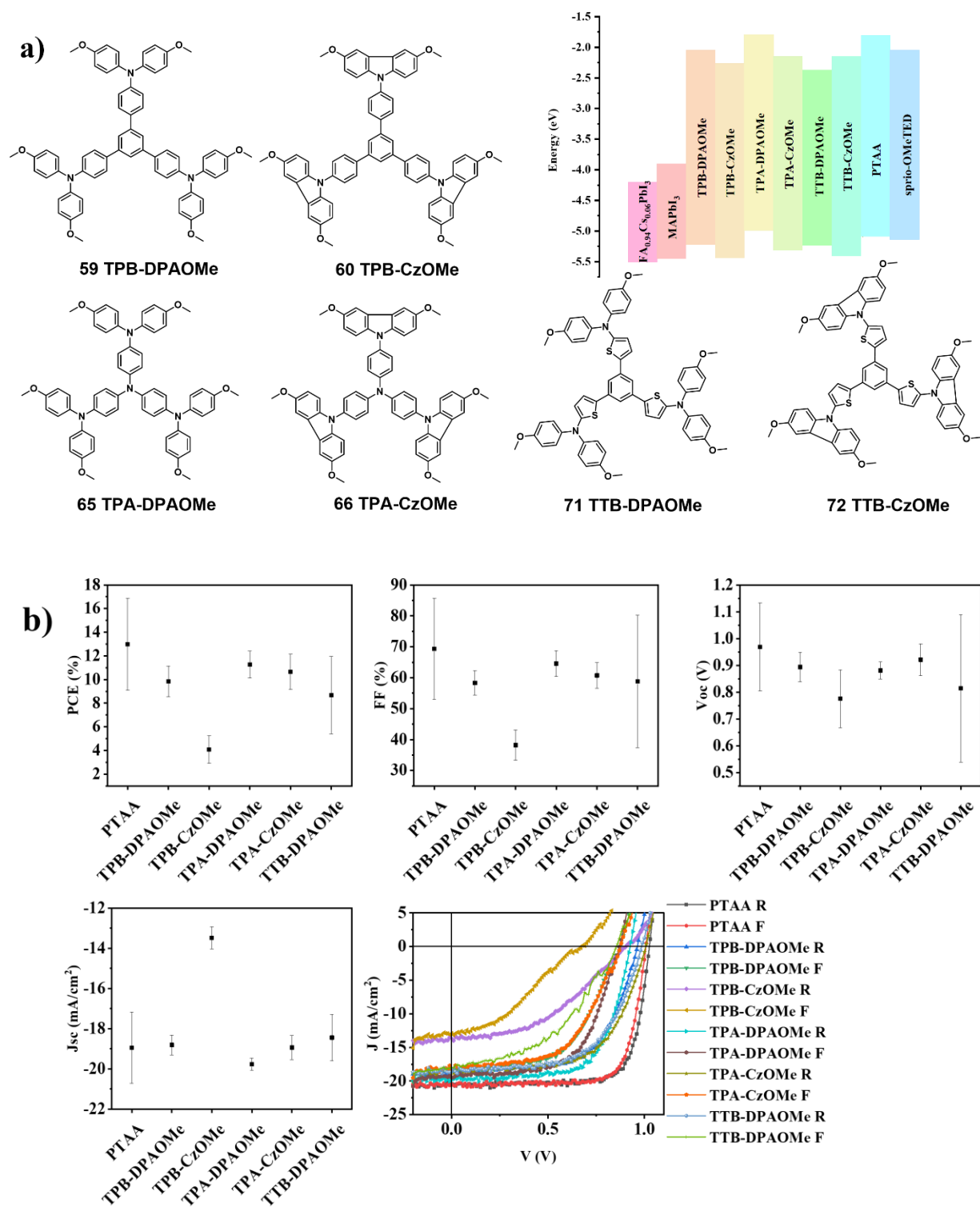


Figure 29. a) Structure of TPB-DPAOMe, TPB-CzOMe, TPA-DPAOMe, TPA-CzOMe, TTB-DPAOMe and TTB-CzOMe. Energy level diagram of FA<sub>0.94</sub>Cs<sub>0.06</sub>PbI<sub>3</sub>, MAPbI<sub>3</sub>, TPB-

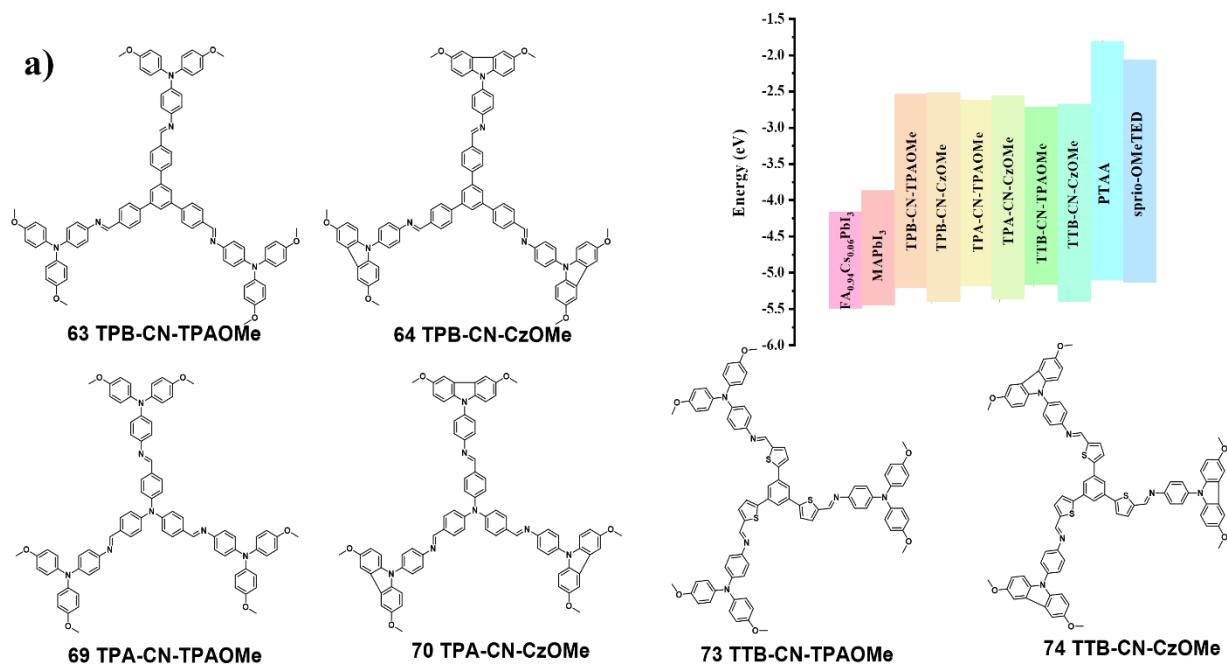
DPAOMe, TPB-CzOMe, TPA-DPAOMe, TPA-CzOMe, TTB-DPAOMe and TTB-CzOMe, PTAA and sprio-OMeTED. b) Statistics of photovoltaic parameters for TPB-DPAOMe-, TPB-CzOMe-, TPA-DPAOMe-, TPA-CzOMe-, TTB-DPAOMe- and TTB-CzOMe-based perovskite solar cells, J-V curves of PTAA- and TPB-DPAOMe-, TPB-CzOMe-, TPA-DPAOMe-, TPA-CzOMe-, TTB-DPAOMe- and TTB-CzOMe-based perovskite solar cells, respectively.

In the following the photovoltaic performances of HTL molecules with C=N linkages will be discussed. The results of photovoltaic performance are shown in Table 10 and Figure 30. TPA-CN-TPAOMe shows best photovoltaic performance among this group of molecules, which exhibit a  $PCE_{max}$  of 12.76 % with FF of 66.31 %,  $V_{OC}$  of 0.94 V and  $J_{SC}$  of  $-20.47 \text{ mA/cm}^2$  in the reverse scan. TPB-CN-PCzOMe- and TPA-CN-PCzOMe-HTLs possess comparable  $V_{OC}$  with TPA-CN-TPAOMe, which are 0.89 and 0.94 V, respectively, but relative lower FF,  $J_{SC}$  and PCE. TTB-CN-PCzOMe HTLs gave similar FF as TPA-CN-TPAOMe HTLs, which is 62.91 %, but reduced  $V_{OC}$ ,  $J_{SC}$  and PCE. TPA-CN-TPAOMe HTLs possess a HOMO level at  $-5.17 \text{ eV}$ , which gains largest HOMO level offset with a  $FA_{0.94}Cs_{0.06}PbI_3$  active layer among all molecules in this group, but TPA-CN-TPAOMe HTLs gave the highest  $V_{OC}$ .

Table 10. Photovoltaic parameters of PTAA-, TPB-CN-TPAOMe-, TPB-CN-PCzOMe-, TPA-CN-TPAOMe-, TPA-CN-PCzOMe-, TTB-CN-TPAOMe- and TTB-CN-PCzOMe- based perovskite solar cells.

Name	Stokes shift (nm)	Work function (eV)	$\Delta$ Work function (eV)	Scan direction	PCE (%)	FF (%)	$V_{OC}$ (V)	$J_{SC}$ ( $\text{mA cm}^{-2}$ )
1 PTAA		4.61	0	Reverse	16.48	76.94	1.03	-20.41
				Forward	15.82	76.64	1.01	-20.44
2 TPB-CN-TPAOMe	165	4.43	0.18	Reverse				
				Forward				
3 TPB-CN-CzOMe	38	4.64	-0.03	Reverse	5.28	42.57	0.89	-13.93
				Forward	2.71	31.36	0.65	-13.29

4	TPA-CN-TPAOMe	133	4.39	0.22	Reverse	12.76	66.31	0.94	-20.47
					Forward	10.33	60.04	0.85	-20.25
5	TPA-CN-CzOMe	58	4.67	-0.06	Reverse	5.54	42.38	0.94	-13.92
					Forward	3.03	32.11	0.74	-12.77
6	TTB-CN-TPAOMe	176	4.46	0.15	Reverse				
					Forward				
7	TTB-CN-CzOMe	49	4.68	-0.07	Reverse	7.37	62.91	0.76	15.42
					Forward	5.61	61.44	0.67	15.06



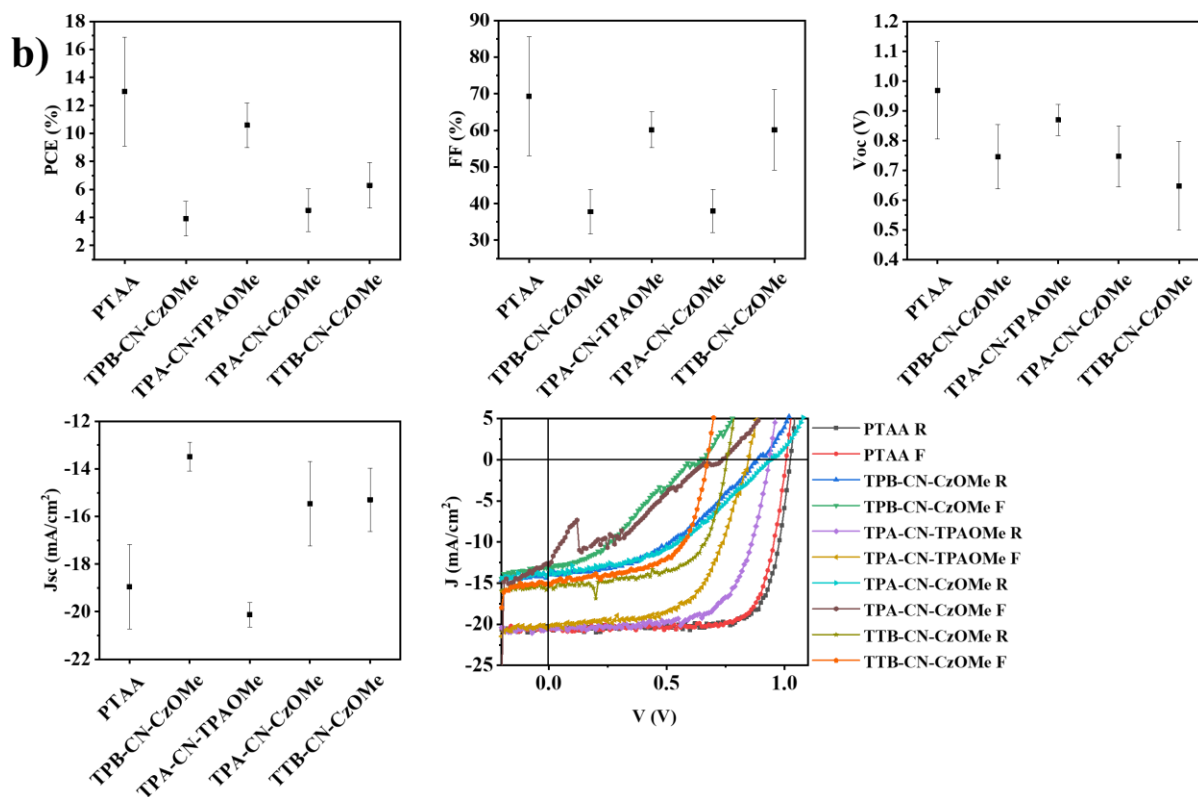


Figure 30. a) Structure of TPB-CN-TPAOMe, TPB-CN-PCzOMe, TPA-CN-TPAOMe, TPA-CN-PCzOMe, TTB-CN-TPAOMe and TTB-CN-PCzOMe. Energy level diagram of FA<sub>0.94</sub>Cs<sub>0.06</sub>PbI<sub>3</sub>, MAPbI<sub>3</sub>, TPB-CN-TPAOMe, TPB-CN-PCzOMe, TPA-CN-TPAOMe, TPA-CN-PCzOMe, TTB-CN-TPAOMe and TTB-CN-PCzOMe PTAA and spiro-OMeTED. b) Statistics of photovoltaic parameters for TPB-CN-TPAOMe-, TPB-CN-PCzOMe-, TPA-CN-TPAOMe-, TPA-CN-PCzOMe-, TTB-CN-TPAOMe- and TTB-CN-PCzOMe- based perovskite solar cells, J-V curves of PTAA- and TPB-CN-TPAOMe-, TPB-CN-PCzOMe-, TPA-CN-TPAOMe-, TPA-CN-PCzOMe-, TTB-CN-TPAOMe- and TTB-CN-PCzOMe-based perovskite solar cells, respectively.

The following discussion focusses on molecules with N=C linkage (different direction if compared to C=N linkages). The results of photovoltaic performance are shown in Table 11 and Figure 31. TPA-NC-TPAOMe-HTLs shows best photovoltaic performance with PCE<sub>max</sub> of 9.76% with FF of 55.80%, V<sub>oc</sub> of 0.85 V and J<sub>sc</sub> of -20.58 mA/cm<sup>2</sup> in the reverse scan. J<sub>sc</sub> of TPA-NC-TPAOMe-



HTLs is nearly in the same level with the PTAA reference, but  $V_{OC}$  and FF are reduced if compared to PTAA. TPB-NC-TPAOMe- and TPB-NC-PCzOMe-HTLs show the worst photovoltaic performance with PCE of 1.18% and 2.25% respectively. Remarkable s-shape are observed in J-V curves for TPB-NC-TPAOMe- and TPB-NC-PCzOMe-HTLs, which may relate to thickness issues. The trends of  $V_{OC}$  for molecules in this group do not match the band alignment situation. The lower HOMO level of HTL would offer higher  $V_{OC}$ . In this group, CzOMe terminal HTL molecules process lower HOMO level, but the  $V_{OC}$  of the CzOMe terminal HTL molecules-based devices decreases.

Table 11. Photovoltaic parameters of PTAA-, TPB-NC-TPAOMe-, TPB-NC-CzOMe-, TPA-NC-TPAOMe-, TPA-NC-CzOMe-, TTB-NC-TPAOMe- and TTB-NC-CzOMe-based perovskite solar cells.

Name	Stokes shift (nm)	Work function (eV)	$\Delta$ Work function (eV)	Scan direction	PCE (%)	FF (%)	$V_{OC}$ (V)	$J_{sc}$ ( $\text{mA cm}^{-2}$ )
1 PTAA		4.61	0	Reverse	16.48	76.94	1.03	-20.41
				Forward	15.82	76.64	1.01	-20.44
2 TPB-NC-TPAOMe	167	4.43	0.18	Reverse	1.18	18.33	0.78	-8.26
				Forward	0.47	14.58	0.61	-5.33
3 TPB-NC-CzOMe	158	4.55	0.06	Reverse	2.25	31.98	0.71	-9.89
				Forward	1.57	24.39	0.51	-8.45
4 TPA-NC-TPAOMe	105	4.29	0.32	Reverse	9.76	55.80	0.85	-20.58
				Forward	6.62	46.19	0.73	-19.64
5 TPA-NC-CzOMe	113	4.47	0.14	Reverse	5.21	43.69	0.77	-15.53
				Forward	2.46	29.40	0.59	-14.19

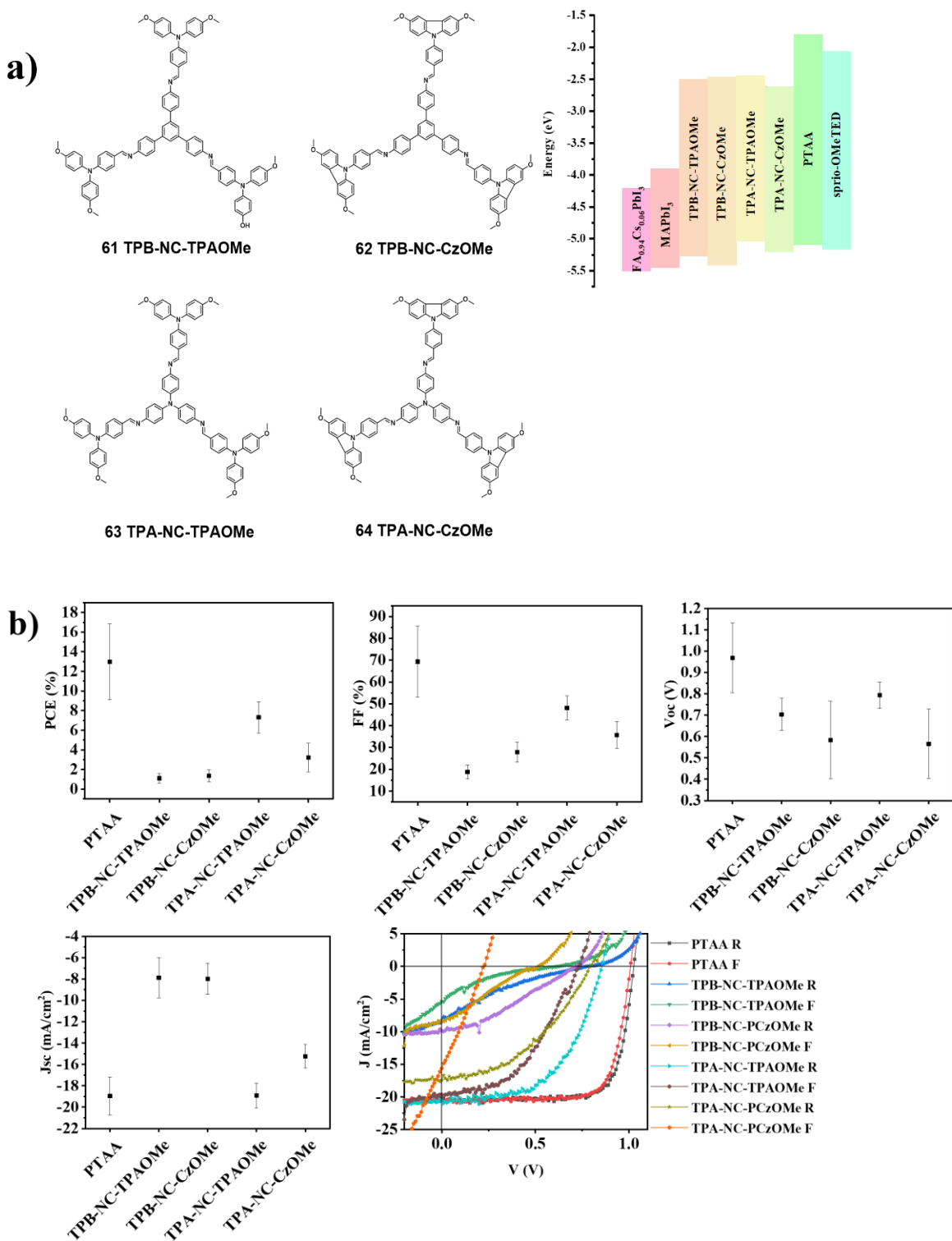


Figure 31. a) Structure of TPB-NC-TPAOMe, TPB-NC-PCzOMe, TPA-NC-TPAOMe, TPA-NC-PCzOMe. Energy level diagram of FA<sub>0.94</sub>Cs<sub>0.06</sub>PbI<sub>3</sub>, MAPbI<sub>3</sub>, TPB-NC-TPAOMe, TPB-NC-

PCzOMe, TPA-NC-TPAOMe, TPA-NC-PCzOMe PTAA and sprio-OMeTED. b) Statistics of photovoltaic parameters for TPB-NC-TPAOMe-, TPB-NC-PCzOMe-, TPA-NC-TPAOMe-, TPA-NC-PCzOMe-based perovskite solar cells, J-V curves of PTAA- and TPB-NC-TPAOMe-, TPB-NC-PCzOMe-, TPA-NC-TPAOMe-, TPA-NC-PCzOMe-based perovskite solar cells, respectively.

It is obvious that the photovoltaic performance of these molecules does not perfectly match that of an ideal PSC and even some gap exists compared with PTAA-based reference PSCs. These PSCs possess additional electrical losses, which can be attributed to shunt and series resistance. Several effects would give rise to resistance in a PSC, which include the Ohm resistance that electrons would suffer when passing through semiconductor materials or interfaces between several semiconductor materials, the contact resistance between semiconductor and electrode and intrinsic resistance of metal electrodes. (Shown in Figure 32 a) In the equivalent circuit of an ideal solar cell, a light generated current source and a P-N diode are parallelly connected, where a series resistance is connected. After current is generated by perovskite layer, some voltage would be lost over this series resistance. For shunt resistance, the rising effect may be defects in solar cell device, which provide alternative pathway for light generated electrons, such as cracks, current path at edge and pin-holes. In equivalent circuit of an actual PSC, a shunt resistance is connected in parallel with the electric elements of light generated current source and a P-N diode. A small shunt resistance represents large amount of photocurrent would go through the shunt resistance, which lead to large photocurrent loss. While a large shunt resistance represents no photocurrent would go through shunt meanwhile no photocurrent would be wasted through this resistance. A large series resistance indicates light generated electron would be reduced partially in the series resistance, which lead to loss of voltage. An actual PSC is required to possess large shunt resistance and small series resistance to approach an ideal PSC (Shown in Figure 32 b).

In J-V curves, if the series resistance is increased, the slope around  $V_{OC}$  point will become flatter. Consequently, the FF decreases as the series resistance increases. If the shunt resistance is reduced, the slope around  $J_{SC}$  point will become steeper So, the FF will be decreased as the increasing of shunt resistance and  $J_{SC}$  would not be changed as voltage equals 0 at the point of short-circuit current. To obtain optimized PSCs, the shunt resistance should be controlled as large as possible

and series resistance should be controlled as small as possible. An estimated value of the shunt resistance for PSCs can be determined from the slope of the points near the short-circuit current in J-V curves, which is 1/slope in  $J_{SC}$  point. Correspondently, an estimated value of the series resistance for PSCs can be determined from the slope of the points near the open-circuit voltage in J-V curves, which is 1/slope of  $V_{OC}$  point. The results of slope of  $J_{SC}$  and  $V_{OC}$  point and corresponding shunt and series resistance of PTAA-based reference PSCs and the designed molecules PSCs are shown in Table 12. The  $R_{sh}$  and  $R_s$  of PTAA are 1201.92 and 0.65  $\Omega \text{ cm}^2$ . TPA-DPAOMe- and TPA-CN-TPAOMe-based PSCs shows increased  $R_{sh}$  and decreased  $R_s$ , which are 3584.23, 1.37  $\Omega \text{ cm}^2$  and 1367.99, 1.03  $\Omega \text{ cm}^2$ , indicating lower leakage current and higher charge extraction and transport efficiency. The other HTL molecules-based devices show either smaller  $R_{sh}$  or larger  $R_s$ . The results of  $R_{sh}$  and  $R_s$  match the result of photovoltaic performance, which TPA-DPAOMe- and TPA-CN-TPAOMe-based PSCs showing higher FF and PCE than the other molecules. A TPA-NC-TPAOMe-based PSCs shows lower shunt resistance compared with PTAA but also lower series resistance, which are 666.67 and 0.94  $\Omega \text{ cm}^2$ , respectively. TPA-NC-TPAOMe-based PSCs possess relatively good photovoltaic performance.

Table 12. Shunt resistance and series resistance of HTL molecules-based devices.

Name	Slope near $J_{SC}$ ( $\text{mA cm}^{-2}/\text{V}$ )	$R_{sh}$ ( $\Omega \text{ cm}^2$ )	Slope near $V_{OC}$ ( $\text{mA cm}^{-2}/\text{V}$ )	$R_s$ ( $\Omega \text{ cm}^2$ )
<b>0</b> PTAA	8.32E-04	1201.92	0.65	1.54
<b>1</b> TPB-DPAOMe	1.69E-03	591.72	0.61	1.64
<b>2</b> TPB-CzOMe	2.45E-03	408.16	0.48	2.08
<b>3</b> TPA-DPAOMe	2.79E-04	3584.23	0.73	1.37
<b>4</b> TPA-CzOMe	1.62E-03	617.28	0.55	1.82
<b>5</b> TTB-DPAOMe	1.53E-03	653.59	0.58	1.72
<b>6</b> TTB-CzOMe				
<b>7</b> TPB-NC-TPAOMe	1.40E-02	71.43	0.41	2.44
<b>8</b> TPB-NC-PCzOMe	4.60E-03	217.39	1.35	0.74
<b>9</b> TPA-NC-TPAOMe	1.50E-03	666.67	1.06	0.94
<b>10</b> TPA-NC-PCzOMe	2.70E-03	370.37	0.87	1.15
<b>11</b> TPB-CN-TPAOMe				

12	TPB-CN-PCzOMe	2.60E-03	384.62	0.64	1.56
13	TPA-CN-TPAOMe	7.31E-04	1367.99	0.97	1.03
14	TPA-CN-PCzOMe	3.10E-03	322.58	0.42	2.38
15	TTB-CN-TPAOMe				
16	TTB-CN-PCzOMe	1.20E-03	833.33	1.53	0.65

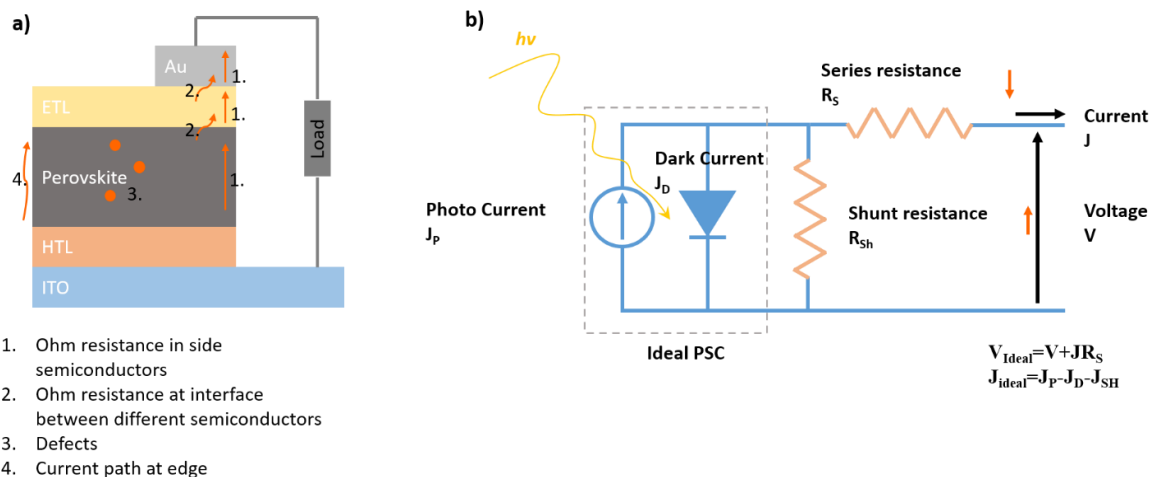


Figure 32. a) Effects causing series resistance and shunt resistance. b) Equivalent circuit of PSCs.

## 2.3 Conclusion

TPA-DPAOMe, TPA-CN-TPAOMe and TPA-NC-TPAOMe are the best performing molecules as HTLs for PSCs, which possess 12.35% of PCE, 67.86% of FF, 0.95 V of  $V_{OC}$ ,  $-19.57 \text{ mA/cm}^2$  of  $J_{SC}$ , 12.76 of PCE, 66.31% of FF, 0.94 V of  $V_{OC}$ ,  $-20.47 \text{ mA/cm}^2$  of  $J_{SC}$  and 9.76 of PCE, 55.80% of FF, 0.85 V of  $V_{OC}$ ,  $-20.58 \text{ mA/cm}^2$  of  $J_{SC}$  respectively. The possible reason for the low photovoltaic performance is that all of them show low shunt resistance and high series resistance. The results also indicate energy gap, HOMO level alignment, stokes shift and work function difference are not significantly affect the photovoltaic performance. From the molecular design, the TPA based structure is beneficial for better photovoltaic performance PSC, no matter for cores or terminals with and without C=N linkages.

As the conjugated  $\pi$ -systems are extended from small molecules to polymers, HOMO level would be increased, LUMO level would be decreased, and the energy gap would become narrower. As

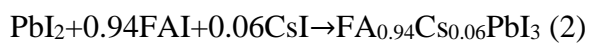
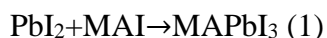
we discussed above, the HOMO level should not be deeper than that of perovskite to avoid transport barriers for holes. LUMO level should be high enough to block electrons preventing recombination. The results of chapter 2 would give us guidance for the coming chapter, which use COF films as HTLs for perovskite solar cells. These HTL molecules are synthesized by coupling different terminals with the same three cores that are also used for COF films building in the next chapter, which are triphenylbenzene, trisphenylamine and trithiophenebenzene. All the HTL molecules show suitable HOMO and LUMO level and acceptable photovoltaic performance which may indicate these three cores would be candidates for COF-type HTL films applied in perovskite solar cells.

## 2.4 Experimental Section

### 2.4.1 Device Preparation

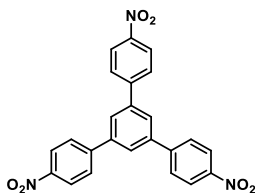
The layer construction of p-i-n device was glass/indium tin oxide (ITO)/PTAA/perovskite/PCBM/AZO/Ag. The full device preparation procedures were finished in a nitrogen-filled glovebox. 17 × 17 mm ITO-coated glass covered by a patterned photoresist (within 3.14 mm<sup>2</sup> active area) were used as devices substrates. ITO-coated glass substrates were cleaned with ultrasonic in deionized water with detergent and isopropanol for 15 min respectively. After brushing with detergent, all the ITO substrates were rinsed with deionized water and acetone followed by drying with clean dry air. PTAA (Sigma-Aldrich) was dissolved in dry toluene as 1.3 mg ml<sup>-1</sup> solution. PTAA solution (50 μl) was spin-coated statically at 6000 rpm for 30 s and followed by annealing at 120 °C for 30 min. For MAPbI<sub>3</sub> perovskite precursor solution, a 1 M solution of PbI<sub>2</sub> (lead iodide, ultradry, Alpha Aesar) and MAI (methylammonium iodide, Greatcell Solar) with 5% excessive PbI<sub>2</sub> (for passivation<sup>190</sup>) was prepared with a solvent mixture of DMF/NMP with volume ratios of 7/3. For FA<sub>0.94</sub>Cs<sub>0.06</sub>PbI<sub>3</sub>, 0.94 M FAI (formamidinium iodide, Greatcell Solar) and 0.06 M CsI (caesium iodine, ultradry, Alpha Aesar) were used instead of MAI. The precursor solution was stirred by covering light on 80°C overnight. 0.1 M thiourea was added into precursor solution freshly before deposition of perovskite layer for the purpose of seed management and concomitant enhancement of the size of the crystallites.<sup>191</sup> The perovskite precursor solutions were spin-coated on PTAA covered ITO substrates at 3000 rpm for 120 s with

an acceleration speed of 300 rpm s<sup>-1</sup>. After various delay times (15 s for MAPbI<sub>3</sub> and 5 s for FA<sub>0.94</sub>CS<sub>0.06</sub>PbI<sub>3</sub> respectively), a continuous nitrogen gas flow with a pressure of 7 bars (filtered with 5 μm PTFE filter) was aimed (incident angle = 90°) at the substrate with specific distance 10 cm to form the intermediate (10 cm for MAPbI<sub>3</sub> and 2 cm for FA<sub>0.94</sub>CS<sub>0.06</sub>PbI<sub>3</sub> respectively). The color will change from light yellow to drake brown within the maintained gas flow, which indicated the formation of the intermediate. Afterward, substrates were immediately transferred to a hotplate and annealed at 100 °C with 10 min for MAPbI<sub>3</sub> and 20 min for FA<sub>0.94</sub>CS<sub>0.06</sub>PbI<sub>3</sub>, respectively (formular equations are shown below). PCBM was dissolved in chlorobenzene with stirring on 80°C overnight as 50 mg mL<sup>-1</sup> solution, which was spin-coated on top of perovskite layer at 1000 rpm for 30 s. After spin-coating of PCBM, AZO nanoparticles (Avantama AG N21X, 2.5 wt % in IPA) were spin-coated dynamically at 8000 rpm for 30 s directly, which followed by annealing at 80 °C for 30 min. After annealing, 100 nm thick silver electrode were evaporated at 10<sup>-6</sup> torr.

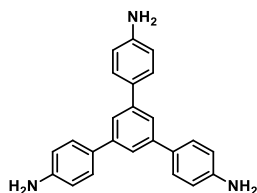


## 2.4.2 Synthesis of molecules

**1,3,5-Tris(4-nitrophenyl)benzene (60).** SiCl<sub>4</sub> (176 mmol, 20 ml) was added dropwise to a dry ethanol solution (1028 mmol, 60 ml) containing (60.6 mmol, 10 g) p-nitroacetophenone at 0 °C. A yellow precipitate was formed immediately and then the mixture was refluxed for 24 h. After the mixture was cooled to room temperature, saturated NH<sub>4</sub>Cl aqueous solution (100 ml) was added and stirred for 10 min. The obtained yellow precipitate was filtered, washed several times with hot DMF and dried under HV. The as-prepared product was insoluble light yellow solid and can be used directly in the next step, yield: 3.53g (39.6%).

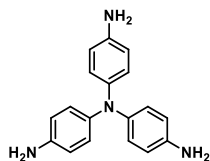


**1,3,5-Tris(4-aminophenyl)benzene (61).** 1,3,5-Tris(4-nitrophenyl)benzene (8 mmol, 3.53 g) and palladium on active carbon (10 % Wt, 0.592 mmol, 0.3 g) were suspended in ethanol (680 mmol, 40 mL) and refluxed. At reflux, hydrazine monohydrate (64 % Wt, 205 mmol, 9.93 mL) was added dropwise and refluxed 3d. After cooling, the suspension is filtered with celite to remove the catalyst. The filtrate was concentrated by rotary evaporation yielding white crystals (2.4 g, 85 %). 1, 3, 5-Tris(4-aminophenyl)benzene can also be synthesized by hydrogenation in autoclave with hydrogen.  $^1\text{H}$  NMR (400 MHz,  $\text{DMSO-}d_6$ )  $\delta$  7.51 – 7.44 (m, 3H), 6.67 (d,  $J$  = 8.2 Hz, 2H), 5.19 (s, 2H).  $^{13}\text{C}$  NMR (151 MHz,  $\text{DMSO-}d_6$ )  $\delta$  148.29, 127.99, 127.36, 120.31, 114.12.

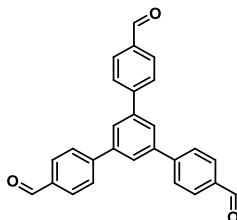


**1,3,5-Tris(4-aminophenyl)amine (71).** 1,3,5-Tris(4-nitrophenyl)amine (5.26mmol, 2 g) was dissolved in a mixture of ethanol (40 ml) and dioxane (20 mL) in a 250 mL round-bottom two-neck flask. Palladium on active carbon (10 % Wt, 1.052 mmol, 1.12 g) was added carefully under an atmosphere of argon. The reaction mixture was heated up to 80 °C. Hydrazine monohydrate (64 % Wt, 142 mmol, 7 ml) was added dropwise under vigorous stirring, After the addition of hydrazine the reaction mixture was further stirred under reflux overnight. Then, the reaction was cooled down to room temperature. The catalyst was removed by filtration through a pad of celite, which was washed few times with methanol (40 mL). The filtrate was concentrated by rotary evaporation yielding white crystals (1.5 g, 98 %). But the white crystals changed to light grey solid in a short time. 1, 3, 5-Tris(4-aminophenyl)amine can also be synthesized by hydrogenation in autoclave with hydrogen. A 250 ml autoclave was filled with dry THF (50 ml), tris(4-nitrophenyl)amine (2.63 mmol, 1 g), palladium on carbon (0.868 mmol, 0.92 g) and purged with argon 3 times. The mixture was stirred under 2 bar hydrogen pressure at room temperature till the pressure would not decrease. After the reaction, the mixture was filtered through celite carefully and washed with ethyl acetate or THF several times to remove the catalyst. The filtrate was concentrated with rotary evaporation to give a grey solid with a yield of 92% (0.7 g).  $^1\text{H}$  NMR (600 MHz,  $\text{DMSO-}d_6$ )  $\delta$  6.59 (d,  $J$  = 8.0 Hz, 1H), 6.44 (d,  $J$  = 8.7 Hz, 1H), 4.68 (s, 1H).

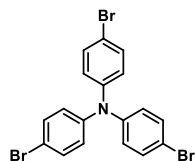




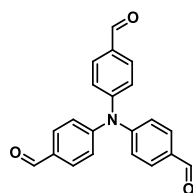
**1,3,5-Tris(4-formylphenyl)benzene (96).** 1,3,5-Tris(4-bromophenyl)amine (3.18 mmol, 1 g) and 4-formylphenylboronic acid (9.34 mmol, 1.4 g) were dissolved in THF (80 ml). Aqueous solution of potassium carbonate (197 mmol, 27.2 g in 50 ml H<sub>2</sub>O) was added into the solution under nitrogen atmosphere. After the addition of bis(triphenylphosphine)palladium(II) dichloride (0.43 mmol, 30 mg), the mixture was refluxed for overnight. After cooling, the solution was extracted twice with dichloromethane (3 × 100 ml). The obtained organic layer was washed with plenty of water. The obtained residue was purified by column chromatography, giving a yellow solid (1.24 g, 24.2 %). <sup>1</sup>H NMR (400 MHz, chloroform-*d*) δ 10.11 (s, 1H), 8.03 (d, *J* = 8.4 Hz, 2H), 7.91 (s, 1H), 7.88 (d, *J* = 8.4 Hz, 2H). <sup>13</sup>C NMR (101 MHz, CDCl<sub>3</sub>) δ 191.68, 146.29, 141.62, 135.81, 130.43, 127.98, 126.48.



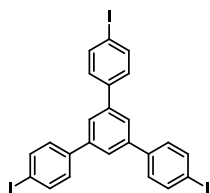
**1,3,5-Tris(4-bromophenyl)amine (74).** To a solution of triphenylamine (20 mmol, 4.91 g) in DMF (75 ml) at 0 °C, NBS (60.0 mmol, 10.68 g) in DMF (25 ml) was dropwise added. The mixture was stirred for 3 h at 0 °C then warmed to r.t. stirred overnight. Then ice water was added to the mixture to produce a white precipitate. After filtration and drying, the obtained white solid was recrystallized from CHCl<sub>3</sub>/MeOH to afford tris(4-bromophenyl) amine in 62% yield (6 g). <sup>1</sup>H NMR (400 MHz, chloroform-*d*) δ 7.36 (d, *J* = 8.8 Hz, 1H), 6.92 (d, *J* = 8.8 Hz, 1H). <sup>13</sup>C NMR (101 MHz, CDCl<sub>3</sub>) δ 146.09, 132.54, 125.63, 116.10.



**1,3,5-Tris(4-formylphenyl)amine (103).** To a THF solution (100 ml) of 1,3,5-tris(4-bromophenyl)amine (10.37 mmol, 5 g) at -70 °C under nitrogen was added n-BuLi (1.6 M, 36.3 mmol, 22.7 ml) dropwise. The solution was then stirred at this temperature for 1h before anhydrous DMF (36.3 mmol, 2.8 ml) was added dropwise. Then the reaction mixture was allowed to warm to r.t. and stirred overnight. The reaction was quenched with an aqueous solution of hydrochloric acid. The mixture was poured into water and extracted with dichloromethane (DCM) (2×20 mL). The combined organic layers were dried over MgSO<sub>4</sub> and concentrated. The resulting residue was purified by column chromatography using DCM as eluent to give a yellow solid (1.6 g, 46.8%). <sup>1</sup>H NMR (600 MHz, DMSO-*d*<sub>6</sub>) δ 9.94 (s, 1H), 7.91 (d, *J* = 8.6 Hz, 2H), 7.28 (d, *J* = 8.6 Hz, 2H).

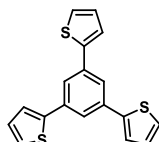


**1,3,5-Tris(4-iodophenyl)benzene (yznc051-2).** SiCl<sub>4</sub> (117 mmol, 13.4 ml) was added dropwise to a dry ethanol solution (677 mmol, 40 ml) containing (40.6 mmol, 10 g) p-nitroacetophenone at 0 °C. A yellow precipitate was formed immediately and then the mixture was refluxed for 24 h. After the mixture was cooled to room temperature, saturated aqueous NH<sub>4</sub>Cl solution (100 mL) was added and stirred for 10 min. The obtained yellow precipitate was filtered and recrystallized from toluene (yeild:9.7g, 64.7%). <sup>1</sup>H NMR (600 MHz, chloroform-*d*) δ 7.81 (d, *J* = 8.4 Hz, 2H), 7.68 (s, 1H), 7.40 (d, *J* = 8.4 Hz, 2H). <sup>13</sup>C NMR (151 MHz, CDCl<sub>3</sub>) δ 141.62, 140.22, 138.03, 129.12, 124.93, 93.61.

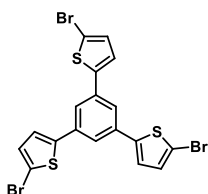


**1,3,5-Tri(thiophen-2-yl)benzene (77).** SiCl<sub>4</sub> (159 mmol, 18.2 ml) was added dropwise with stirring to a solution of 2-acetylthiophene (79 mmol, 8.56 ml) in absolute EtOH (80 mL) at 0 °C. The reaction mixture was stirred in the drak at 0 °C with ice bath overnight, then warmed to r. t. and stirred another day. At the conclusion of the reaction (TLC monitoring), the dark reaction

mixture was poured into ice-cold H<sub>2</sub>O and extracted with CH<sub>2</sub>Cl<sub>2</sub>. The combined organic fraction was washed with H<sub>2</sub>O. Evaporation of the solvent and purification of the crude product by column chromatography (silica gel) with hexane as an eluent yielded the product (8.57 g, 54.8%). <sup>1</sup>H NMR (400 MHz, chloroform-*d*) δ 7.75 (s, 1H), 7.42 (dd, *J* = 3.6, 1.2 Hz, 1H), 7.34 (dd, *J* = 5.1, 1.2 Hz, 1H), 7.13 (dd, *J* = 5.1, 3.6 Hz, 1H). <sup>13</sup>C NMR (151 MHz, CDCl<sub>3</sub>) δ 143.53, 135.70, 128.08, 125.37, 123.86, 122.77.

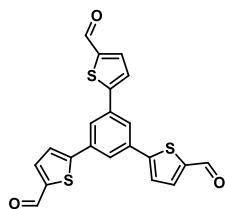


**1,3,5-Tris(5-bromothiophen-2-yl)benzene (78).** NBS (39.4 mmol, 7.02 g) solution (in 20 ml DMF) was dropped into solution of 1,3,5-tris(thiophen-2-yl)benzene (12.33 mmol, 4 g) in DMF (40 ml) dropwise. After stirring in the dark overnight, the reaction was quenched with saturated, aqueous NaHCO<sub>3</sub> (30 mL) and extracted with ethyl acetate (50 mL × 3). The combined organic layers were washed with brine, dried over anhydrous MgSO<sub>4</sub> and concentrated to afford a residue, which was purified by recrystallization with DCM/MeOH to give white solid (5.4 g, 78 %). <sup>1</sup>H NMR (600 MHz, chloroform-*d*) δ 7.53 (s, 1H), 7.13 (d, *J* = 3.8 Hz, 1H), 7.08 (d, *J* = 3.8 Hz, 2H). <sup>13</sup>C NMR (151 MHz, CDCl<sub>3</sub>) δ 144.40, 135.26, 131.00, 124.23, 122.19, 112.45.

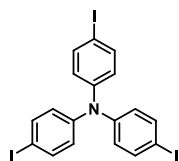


**1,3,5-Tris(5-formylthiophene-2-yl)benzene (106).** n-BuLi (12.03 mmol, 1.1 M, 10.93 ml) was dropped into a THF solution (25 mL) contained 1,3,5-tris(5-bromothiophen-2-yl)benzene (1.5 g) at -70 °C under Ar. The solution was then stirred at this temperature for 1h before anhydrous N-formylpiperidine (10.69 mmol, 1.2 ml) was added dropwise. Then the reaction mixture was allowed to warm to r.t. and stirred overnight. The reaction was quenched with an aqueous solution of hydrochloric acid. The mixture was poured into water and extracted with DCM. The combined organic layers were dried over MgSO<sub>4</sub> and concentrated. The resulting residue was purified by

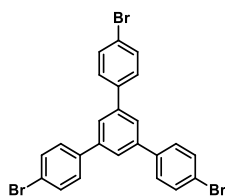
column chromatography using DCM as eluent to give a yellow solid (0.33 g, 30.2%).  $^1\text{H}$  NMR (600 MHz,  $\text{DMSO-}d_6$ )  $\delta$  7.72 (s, 1H), 7.62 (d,  $J = 3.9$  Hz, 1H), 7.33 (d,  $J = 3.9$  Hz, 1H).



**1,3,5-Tris(4-iodophenyl)amine (yznc059-1).** To a stirred solution of triphenylamine (20.38 mmol, 5g) and KI (40.8 mmol, 6.8g) in 175 mL acetic acid and 15 mL water at 80 °C,  $\text{KIO}_3$  (28.5 mmol, 6.1g) was added slowly. After stirring at 50 °C overnight, 200 ml water was added to get crude product. The precipitate was filtered under vacuum and washed with ethanol to give the product as a white powder (10.3 g, 81 %).  $^1\text{H}$  NMR (400 MHz, Chloroform- $d$ )  $\delta$  7.54 (d,  $J = 8.8$  Hz, 1H), 6.81 (d,  $J = 8.8$  Hz, 1H).  $^{13}\text{C}$  NMR (151 MHz,  $\text{CDCl}_3$ )  $\delta$  146.60, 138.47, 126.06, 86.56.

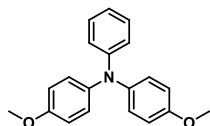


**1,3,5-Tris(4-bromophenyl)benzene (65).**  $\text{SiCl}_4$  (113 mmol, 13 mL) was added dropwise to a dry ethanol solution (40 mL) containing (25.1 mmol, 5 g) *p*-nitroacetophenone at 0 °C. A yellow precipitate was formed immediately and then the mixture was refluxed for 24 h. After the mixture was cooled to r.t., saturated  $\text{NH}_4\text{Cl}$  aqueous solution (100 mL) was added and stirred for 30 min. The obtained yellow precipitate was filtered and recrystallized (2.75 g, 60.5 %).  $^1\text{H}$  NMR (400 MHz, Chloroform- $d$ )  $\delta$  7.69 (s, 1H), 7.61 (d,  $J = 8.7$  Hz, 1H), 7.53 (d,  $J = 8.7$  Hz, 1H).

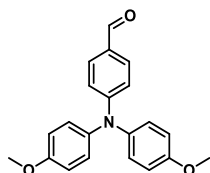


**N,N-Bis(4-methoxyphenyl)aniline (83).** The reaction was started with preparation of catalyst system, which was obtained by stirring  $\text{Pd}(\text{OAc})_2$  (0.329 mmol, 74 mg) and  $\text{PtBu}_3$  (0.53 ml, 0.11 g) in dry toluene (1 ml) under Ar at r.t. for 30 minutes. The yellow solution was transferred to a

flask containing aniline (10.95 mmol, 1.0 ml), 4-bromoanisole (23.96 mmol, 3.0 ml) and NaO<sup>t</sup>Bu (32.67 mmol, 3.14 g) in dry toluene (12 ml) and refluxed overnight under vigorous stirring. After cooling to r.t., saturated NH<sub>4</sub>Cl aqueous solution (20 ml) was added. The aqueous phase was extracted with EtOAc and dried over MgSO<sub>4</sub> before removing the solvent under vacuum. The crude was purified by column chromatography to give the product as off-white solid (3.3 g, 99%). <sup>1</sup>H NMR (400 MHz, chloroform-*d*) δ 7.17 (dd, *J* = 8.7, 7.3 Hz, 2H), 7.04 (d, *J* = 9.0 Hz, 4H), 6.94 (dt, *J* = 7.9, 1.1 Hz, 2H), 6.90 – 6.85 (m, 1H), 6.82 (d, *J* = 8.9 Hz, 4H), 3.79 (s, 6H). <sup>13</sup>C NMR (101 MHz, CDCl<sub>3</sub>) δ 155.73, 148.81, 141.21, 128.91, 126.38, 120.98, 120.59, 114.67, 55.49.

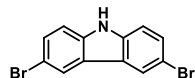


**4-N,N-[Bis(4-methoxyphenyl)amino]benzaldehyde (84).** N,N-Bis(4-methoxyphenyl)aniline (3.27 mmol, 1 g) was dissolved in DMF (5 ml) at 0 °C. POCl<sub>3</sub> (13.10 mmol, 1.2 ml) was added dropwise at 0 °C. The mixture was stirred for 30 mins at 0 °C and then, until changing the color of the mixture to reddish, the mixture was stirred at r.t.. After color changed, the mixture was stirred at 90 °C for overnight. After cooling, the reaction mixture was poured into ice slowly. NaHCO<sub>3</sub> (0.5 M) was added to neutralize the mixture. Then, the mixture was extracted with EA. The organic solvent was removed under reduced pressure. The residue was washed with H<sub>2</sub>O, A yellow sticky liquid was obtained (1 g, 92 %). <sup>1</sup>H NMR (400 MHz, chloroform-*d*) δ 9.76 (s, 1H), 7.63 (d, *J* = 9.0 Hz, 2H), 7.13 (d, *J* = 8.8 Hz, 4H), 6.89 (d, *J* = 8.8 Hz, 4H), 6.85 (d, *J* = 9 Hz, 2H), 3.82 (s, 6H).

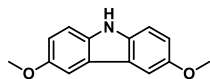


**3,6-Dibromo-9H-carbazole (67).** To a solution of ethyl acetate (150 ml) carbazole (20.2 mmol, 3.37 g), NBS (7.16 g, 40.2 mmol) was added under Ar at 0 °C with in the drake in an ice bath. After 30 min stirring, the ice bath was removed, and the reaction mixture was stirred at r.t. overnight. The reaction mixture was extracted three times with ethyl acetate and brine. After removal of the solvents in vacuo the residue was recrystallized from DCM/MeOH to give product

(6.2 g, 93 %).  $^1\text{H}$  NMR (600 MHz, Chloroform-*d*)  $\delta$  8.13 (dt,  $J = 1.9, 0.7$  Hz, 2H), 7.52 (dd,  $J = 8.6, 1.9$  Hz, 2H), 7.31 (dd,  $J = 8.6, 0.6$  Hz, 2H), 2.77 (s, 1H).  $^{13}\text{C}$  NMR (151 MHz,  $\text{CDCl}_3$ )  $\delta$  138.38, 129.34, 124.14, 123.29, 112.68, 112.22.

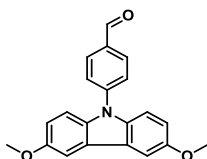


**3,6-Dimethoxy-carbazole (68).** The reaction was slowly started by dissolving Na (308 mmol, 7g) in dry MeOH (84mL) under Ar at 0 °C (be careful because of the release of  $\text{H}_2$ ). 3,6-dibromo-9H-carbazole (15.4 mmol, 5g), CuI (30.8 mmol, 5.9g) and DMF (168 ml) were added into the mixture at r.t. and the mixture stirred at 80 °C overnight. After cooling to r.t., the mixture was filtered through celite, and the solvent removed. Water (60 mL) and EtOAc (100 mL) were added to the reaction mixture. The organic layer was extracted with ethyl acetate/brine, dried over  $\text{MgSO}_4$ , filtered, and concentrated in vacuo. Purification by flash silica chromatography gave the title product as white solid (3.2 g, 92%).  $^1\text{H}$  NMR (600 MHz, Chloroform-*d*)  $\delta$  7.75 (s, 2H), 7.52 (d,  $J = 2.5$  Hz, 2H), 7.26 (d,  $J = 8.8$  Hz, 2H), 7.07 (dd,  $J = 8.8, 2.5$  Hz, 2H), 3.94 (s, 6H).  $^{13}\text{C}$  NMR (151 MHz,  $\text{CDCl}_3$ )  $\delta$  153.58, 135.27, 123.67, 115.20, 111.50, 102.90, 56.05.

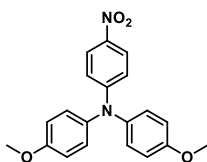


**4-(3,6-Dimethoxy-carbazol-9-yl)benzaldehyde (86).** This reaction was started with the preparation of the catalyst, for which PdOAc (1.056 mmol, 0.24 g) and  $(t\text{-Bu})_3\text{P}$  (1.584 mmol, 0.32 g) were dissolved in dry toluene (3 ml) under Ar. A two-necked flask equipped with a magnetic stirrer was charged with 3,6-dimethoxy-9H-carbazole (24.6 mmol, 6 g), 4-bromobenzaldehyde (31.7 mmol, 5.9 g),  $\text{K}_2\text{CO}_3$  (79 mmol, 11g), as prepared catalyst, and toluene (10 mL). The reaction mixture was refluxed at 130 °C for 24.0 h and cooled to room temperature. The reaction was quenched with  $\text{H}_2\text{O}$  and extracted with ethyl acetate three times. The extract was then dried over magnesium sulfate and filtered. After evaporation at reduced pressure, the residue was purified by column chromatography to give the compound as yellow solid (6.3 g, 72%).  $^1\text{H}$  NMR (400 MHz, Chloroform-*d*)  $\delta$  10.09 (s, 1H), 8.10 (d,  $J = 8.5$  Hz, 2H), 7.76 (d,  $J = 8.5$  Hz, 2H), 7.61 – 7.49 (m, 2H), 7.44 (dd,  $J = 8.9, 0.6$  Hz, 2H), 7.06 (dd,  $J = 8.9, 2.5$  Hz, 2H), 3.96 (s, 6H).  $^{13}\text{C}$  NMR (101

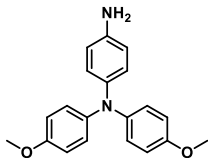
MHz, CDCl<sub>3</sub>)  $\delta$  190.86, 154.71, 143.96, 135.36, 134.13, 131.38, 126.12, 124.53, 115.35, 110.80, 103.21, 56.09.



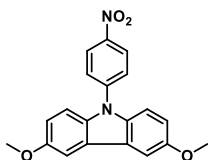
**4-N,N-[Bis(4-methoxy)phenyl]amino-nitrobenzene (93).** Two necks round flask was charged with copper (56.6 mmol, 3.6 g), 18-crown-6 (3.04 mmol, 0.8 g), K<sub>2</sub>CO<sub>3</sub> (115 mmol, 15.8 g), 4-nitroaniline (14.48 mmol, 2 g) and 1-iodo-4-methoxybenzene (5.6 mmol, 13.3 g) under Ar. Degassed o-DCB (100 ml) was injected into the flask. The mixture was stirred and heated to reflux for 2 days. After cooling to r.t., the mixture was filtered with celite and extracted with DCM. The organic layer was dried over MgSO<sub>4</sub>, the solvent was removed under reduced pressure, and purified by column chromatography to give a yellow solid (4.9 g, 97 %). <sup>1</sup>H NMR (600 MHz, Chloroform-*d*)  $\delta$  8.00 (d, *J* = 9.4 Hz, 2H), 7.13 (d, *J* = 8.9 Hz, 4H), 6.91 (d, *J* = 8.9 Hz, 4H), 6.75 (d, *J* = 9.4 Hz, 2H), 3.82 (s, 6H). <sup>13</sup>C NMR (151 MHz, CDCl<sub>3</sub>)  $\delta$  157.71, 154.16, 139.07, 138.33, 128.13, 125.57, 115.79, 115.23, 55.52.



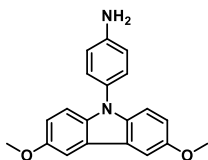
**N,N-Bis(4-methoxyphenyl)benzene-1,4-diamine (94).** 4-N,N-[Bis(4-methoxy)phenyl]amino-nitrobenzene (3.14 mmol, 1.1 g), Pd/C (10 Wt%, 0.22 mmol, 0.23 g) were under Ar charged in a 250-mL three-neck round-bottom flask containing EtOH (20 ml). The mixture was heated to reflux, and hydrazine monohydrate (64 Wt%, 0.78 mmol, 3.9 ml) was added slowly to the mixture, then the solution was stirred at reflux temperature overnight. After reaction, the solution was filtered to remove Pd/C, and the filtrate was cooled to precipitate. The product was collected by filtration and dried under HV to give off-white crystals (1 g, 99 %). <sup>1</sup>H NMR (400 MHz, DMSO-*d*<sub>6</sub>)  $\delta$  6.80 (s, 8H), 6.71 (d, *J* = 8.6 Hz, 2H), 6.51 (d, *J* = 8.6 Hz, 2H), 4.89 (s, 2H), 3.69 (s, 6H).



**3,6-Dimethoxy-9-(4-nitrophenyl)-carbazole (98).** 3,6-Dimethoxycarbazole (8.8 mmol, 2 g), 4-fluoronitrobenzene (9.68 mmol, 1.37 g) and CsF (8.8 mmol, 1.34 g) were dissolved in 40 mL of DMSO (8 ml) and heated to 140 °C under Ar overnight. After cooling, the mixture was poured into 200 mL of methanol, and the precipitated compound was collected by filtration and washed thoroughly with methanol and hot water. The crude product was filtered and recrystallized from DMF/methanol to give orange crystals (2.8 g, 91 %). <sup>1</sup>H NMR (600 MHz, chloroform-*d*) δ 8.45 (d, *J* = 9.0 Hz, 2H), 7.76 (d, *J* = 9.0 Hz, 2H), 7.54 (d, *J* = 2.5 Hz, 2H), 7.43 (d, *J* = 8.9 Hz, 2H), 7.07 (dd, *J* = 8.9, 2.6 Hz, 2H), 3.96 (s, 6H).

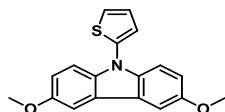


**4-(3,6-Dimethoxy-carbazol-9-yl)aniline (99).** 3,6-Dimethoxy-9-(4-nitrophenyl)-carbazole (1.44 mmol, 0.5 g) and Pd/C (10 Wt %, 0.1 mmol, 0.11 g) were charged in a 100-mL three-neck round-bottom flask containing EtOH (20 ml) under Ar. The suspension was heated to reflux, and hydrazine monohydrate (64 Wt %, 36 mmol, 1.8 ml) was added slowly to the mixture. Then the solution was stirred at reflux temperature overnight. After reaction, the solution was filtered to remove Pd/C, and the filtrate was cooled to precipitate. The product was collected by filtration and dried under HV to give off-white crystals (0.47 g, 99 %). <sup>1</sup>H NMR (400 MHz, chloroform-*d*) δ 7.54 (d, *J* = 2.5 Hz, 2H), 7.35 (d, *J* = 8.6 Hz, 2H), 7.24 (d, *J* = 8.7 Hz, 2H), 7.07 – 6.99 (m, 4H), 5.72 (s, 2H), 3.94 (s, 6H). <sup>13</sup>C NMR (101 MHz, CDCl<sub>3</sub>) δ 153.89, 136.84, 128.20, 123.31, 117.73, 115.13, 110.59, 102.97, 56.18.

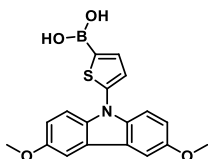




**3,6-Dimethoxy-9-(thiophen-2-yl)-carbazole (83).** This reaction was started with preparation of the catalyst, in which Pd(dba)<sub>2</sub> (0.053 mmol, 0.033 g) and XPhos (0.106 mmol, 0.05 g) were dissolved in dry toluene (1 ml) under Ar. A two-necked flask equipped with a magnetic stirrer was charged with 3,6-dimethoxy-carbazole (1.32 mmol, 0.3 g), 2-bromothiophene (1.45 mmol, 0.24 g), NaO<sup>t</sup>Bu (11.88 mmol, 1.142 g), as prepared catalyst, and toluene (10 mL). The reaction mixture was refluxed at 130 °C for 24 h and cooled to r.t.. The reaction was quenched with H<sub>2</sub>O and extracted with ethyl acetate three times. The extract was then dried over MgSO<sub>4</sub> and filtered. After evaporation of the solvent at a reduced pressure, the residue was purified by column chromatography to give the target compound as yellow solid (0.31 g, 76%). <sup>1</sup>H NMR (400 MHz, Chloroform-*d*) δ 7.52 (d, *J* = 2.5 Hz, 2H), 7.36 (d, *J* = 8.9 Hz, 2H), 7.33 (dd, *J* = 5.3, 1.7 Hz, 1H), 7.17 – 7.12 (m, 2H), 7.06 (dd, *J* = 8.9, 2.5 Hz, 2H), 3.94 (s, 6H).

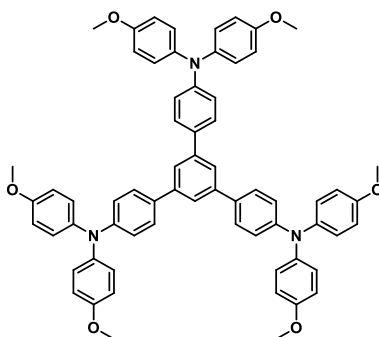


**[5-(3,6-Dimethoxy-carbazol-9-yl)thiophen-2-yl]boronic acid (84).** n-BuLi (1.2 M, 6.30 mmol, 5.25 ml) was added into a solution of 3,6-dimethoxy-9-(thiophen-2-yl)-carbazole (4.20 mmol, 1.3 g) in dry THF (50 ml) at -78 °C. The mixture was kept -78 °C for 1 h, followed by the addition of trimethyl borate (6.72 mmol, 0.75 ml), the reaction mixture was stirred at -78 °C for 1 h before warming up to r.t., and stirred overnight at r.t.. The mixture was treated with aqueous HCl (2M, 10 ml), extracted with DCM, dried by MgSO<sub>4</sub>, recrystallized from DCM/hexane to give the product (0.96 g, 64.7 %). <sup>1</sup>H NMR (600 MHz, DMSO-*d*<sub>6</sub>) δ 8.35 (s, 2H), 7.81 (d, *J* = 2.6 Hz, 2H), 7.76 (d, *J* = 3.6 Hz, 1H), 7.44 (d, *J* = 8.9 Hz, 2H), 7.34 (d, *J* = 3.6 Hz, 1H), 7.07 (dd, *J* = 8.9, 2.6 Hz, 2H), 6.50 (s, 1H), 3.88 (s, 6H).

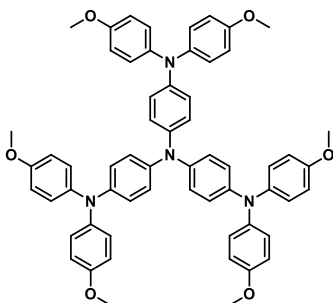


**1,3,5-Tris[4-N,N-bis(4-methoxyphenyl)aminophenyl]benzene (63).** The reaction started with the preparation of catalyst system, in which tris(dibenzylideneacetone)dipalladium (0) (Pd<sub>2</sub>(dba)<sub>3</sub>, 0.094 mmol, 0.056 g) and tri-*tert*-butylphosphine (P(<sup>t</sup>Bu)<sub>3</sub>, 0.188 mmol, 0.038 g) were dissolved

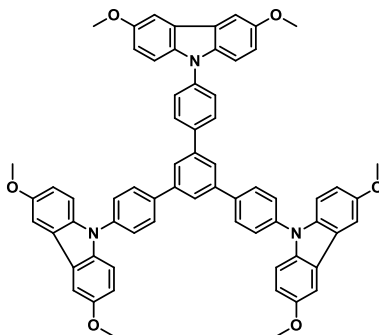
in toluene (2 ml) and stirred for 30 min at r.t. under dark and Ar to undergo ligand exchange. The catalyst system were added into a three-necked round-bottom flask containing 4-bromoanisole (18.50 mmol, 3.46 g), 1,3,5,-tris(4-aminophenyl)benzene (2.85 mmol, 1 g), sodium tert-butoxide (NaO<sup>t</sup>Bu, 23.50 mmol, 2.26 g) and anhydrous toluene (25 ml) in the dark. The reaction mixture was refluxed overnight. After cooling to r.t., the mixture was diluted with DCM and filtered through celite. The filtrate was purified by flash column chromatography. After that column, the obtained yellow sticky liquid was dissolved in DCM and dropped in to MeOH to give a white precipitate, which was filtrated off and dried to give white solid (2 g, 71 %). <sup>1</sup>H NMR (400 MHz, chloroform-*d*) δ 7.63 (s, 3H), 7.49 (d, *J* = 7.7 Hz, 6H), 7.09 (s, 12H), 7.04 – 6.97 (m, 6H), 6.85 (d, *J* = 8.9 Hz, 12H), 3.81 (s, 18H).



**1,3,5-Tris[4-N,N-bis(4-methoxyphenyl)aminophenyl]amine (72).** The reaction started with the preparation of catalyst system, in which tris(dibenzylideneacetone)dipalladium (0) (Pd<sub>2</sub>(dba)<sub>3</sub>, 0.057 mmol, 0.052 g) and tri-tert-butylphosphine (P(<sup>t</sup>Bu)<sub>3</sub>, 0.114 mmol, 0.023 g) were dissolved in toluene (2 ml) and stirred for 30 min at r.t. to undergo ligand exchange under dark and Ar. The catalyst system was added into a three-necked round-bottom flask containing 4-bromoanisole (11.19 mmol, 2.1 g), 1,3,5-tris(4-aminophenyl)amine (1.72 mmol, 0.5 g), sodium tert-butoxide (NaO<sup>t</sup>Bu, 14.22 mmol, 1.37 g) and anhydrous toluene (12 ml) in the dark. The reaction mixture was refluxed overnight. After cooling to r.t., the mixture was diluted with DCM and filtered through celite. The filtrate was purified by flash column chromatography to give a yellow solid (1 g, 62.6 %). <sup>1</sup>H NMR (400 MHz, DMSO-*d*<sub>6</sub>) δ 6.96 (d, *J* = 9.1 Hz, 12H), 6.91 – 6.83 (m, 18H), 6.76 (d, *J* = 8.9 Hz, 6H), 3.72 (s, 18H).

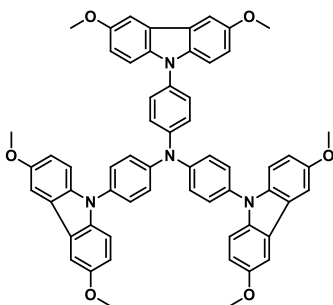


**1,3,5-[4-Tris(3,6-dimethoxycarbazol-9-yl)phenyl]benzene (69).** The reaction started with the preparation of catalyst system, in which Pd(OAc)<sub>2</sub> (0.037 mmol, 8.3 mg) and P(<sup>t</sup>Bu)<sub>3</sub> (0.055 mmol, 0.011 g) were dissolved in toluene (2 ml) and stirred for 30 min at r.t. to undergo ligand exchange under dark and Ar. The catalyst system was added into a three-necked round-bottom flask containing 1,3,5-tris(4-bromophenyl)benzene (0.92 mmol, 0.5 g), 3,6-dimethoxy-9H-carbazole (3.31 mmol, 0.75 g), NaO<sup>t</sup>Bu (8.29 mmol, 0.8 g) and anhydrous toluene (12 ml) in the dark. The reaction mixture was refluxed overnight. After cooling to r.t., the mixture was diluted with DCM and filtered by celite. The filtrate was purified by flash column chromatography to give a yellow solid (0.5 g, 55.3 %). <sup>1</sup>H NMR (400 MHz, chloroform-*d*) δ 8.01 (s, 3H), 7.99 (d, *J* = 8.4 Hz, 6H), 7.72 (d, *J* = 8.5 Hz, 6H), 7.59 (d, *J* = 2.4 Hz, 6H), 7.45 (dd, *J* = 8.9, 0.5 Hz, 6H), 7.08 (dd, *J* = 8.9, 2.5 Hz, 6H), 3.97 (s, 18H).

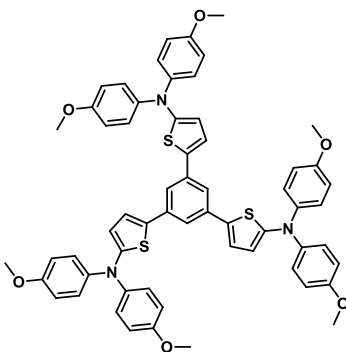


**Tris[4-(3,6-dimethoxy-carbazol-9-yl)phenyl]amine (75).** The reaction started with the preparation of the catalyst system, in which Pd(OAc)<sub>2</sub> (0.041 mmol, 9.3 mg) and P(<sup>t</sup>Bu)<sub>3</sub> (0.062 mmol, 0.013 g) were dissolved in toluene (2 ml) and stirred for 30 min at r.t. to undergo ligand exchange under dark and Ar. The catalyst system was added into a three-necked round-bottom flask containing 1,3,5-tris(4-bromophenyl)amine (1.04 mmol, 0.5 g), 3,6-dimethoxy-carbazole (3.73 mmol, 0.85 g), NaO<sup>t</sup>Bu (9.34 mmol, 0.9 g) and anhydrous toluene (12 ml) in the dark. The

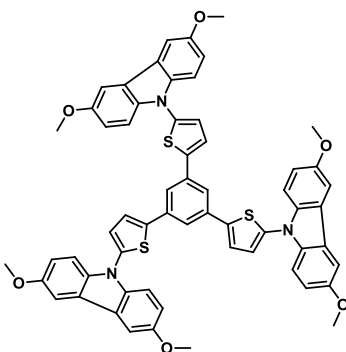
reaction mixture was refluxed overnight. After cooling to r.t., the mixture was diluted with DCM and filtered through celite. The filtrate was purified by flash column chromatography to give a yellow solid (0.8 g, 84 %).  $^1\text{H NMR}$  (400 MHz, chloroform-*d*)  $\delta$  7.57 (d,  $J = 2.5$  Hz, 6H), 7.54 (d,  $J = 8.8$  Hz, 6H), 7.47 (d,  $J = 8.5$  Hz, 6H), 7.42 (d,  $J = 8.9$  Hz, 6H), 7.08 (dd,  $J = 8.9, 2.5$  Hz, 6H), 3.96 (s, 18H).



**1,3,5-Tris[5-N,N-bis(4-methoxyphenyl)amino-thiophene-2-yl]benzene (80).** The reaction started with the preparation of the catalyst system, in which  $\text{Pd}_2\text{dba}_3$  (0.036 mmol, 0.033 g) and  $\text{P}(\text{tBu})_3$  (0.071 mmol, 0.014 g) were dissolved in toluene (2 ml) and stirred for 30 min at r.t. to undergo ligand exchange under dark and Ar. The catalyst system was added into a three-necked round-bottom flask containing 1,3,5-tris(5-bromothiophen-2-yl)benzene (0.89 mmol, 0.5 g), bis(4-methoxyphenyl)amine (2.94 mmol, 0.67 g),  $\text{NaO}^t\text{Bu}$  (8.02 mmol, 0.77 g) and anhydrous toluene (12 ml) in the dark. The reaction mixture was refluxed overnight. After cooling to r.t., the mixture was diluted with DCM and filtered through celite. The filtrate was purified by flash column chromatography to give a yellow solid (0.4 g, 46 %).  $^1\text{H NMR}$  (400 MHz, chloroform-*d*)  $\delta$  7.41 (s, 3H), 7.14 (d,  $J = 9.0$  Hz, 12H), 7.09 (d,  $J = 2.7$  Hz, 3H), 6.85 (d,  $J = 9.0$  Hz, 12H), 6.45 (s, 3H), 3.82 (s, 18H).



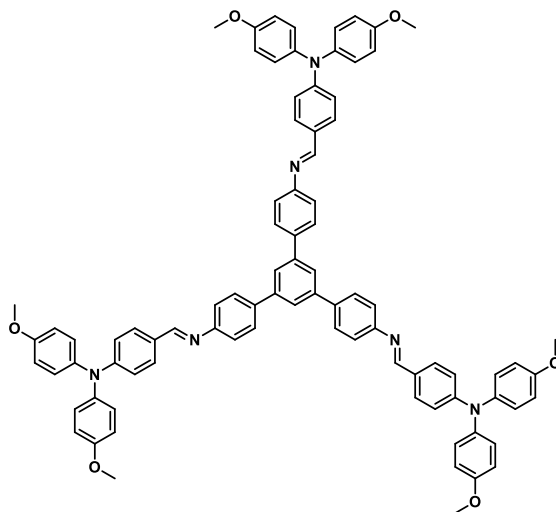
**1,3,5-Tris[5-(3,6-dimethoxycarbazol-9-yl)thiophene-2-yl]benzene (81).** 1,3,5-tribromobenzene (0.45 mmol, 0.14 g), (5-(3,6-Dimethoxy-carbazol-9-yl)thiophen-2-yl)boronic acid (2.72 mmol, 0.96 g), Pd(Ph<sub>3</sub>P)<sub>4</sub> (0.136 mmol, 0.16 g), K<sub>2</sub>CO<sub>3</sub> (4.08 mmol, 0.56 g) were dissolved in degassed THF (8 ml) and H<sub>2</sub>O (2 ml) under Ar and in the dark. The reaction mixture was heated to reflux and stirred overnight. After cooling, the reaction mixture was filtrated through celite, washed several times with ethyl acetate and extracted 3 times with ethyl acetate/brine and concentrated to yield a solid. The resulting residue was purified by flash column chromatography to give a yellow solid (0.45 g, 99 %). <sup>1</sup>H NMR (400 MHz, chloroform-*d*) δ 7.52 (d, *J* = 2.5 Hz, 6H), 7.36 (dd, *J* = 8.8, 0.5 Hz, 6H), 7.33 (dd, *J* = 5.3, 1.7 Hz, 3H), 7.19 – 7.12 (m, 6H), 7.06 (dd, *J* = 8.9, 2.5 Hz, 6H), 3.94 (s, 18H). <sup>13</sup>C NMR (101 MHz, CDCl<sub>3</sub>) δ 154.53, 139.59, 137.46, 126.08, 123.98, 123.84, 123.56, 115.28, 111.09, 103.06, 56.15.



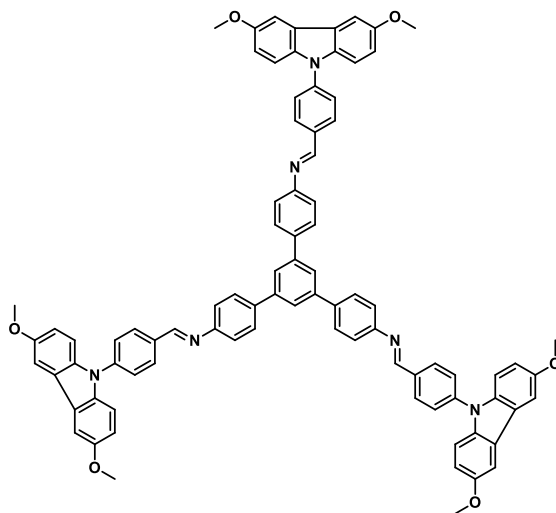
The following THL molecules are synthesized by reacting 1 eq core molecules and 3.3 eq terminal monomers in a condensation reaction, see the following general procedure. The names of HTL molecules are represented by numbers. Core (1 eq) and terminal monomer (3.3 eq) were dissolved in dry chloroform (20 ml). After addition of catalytic amount of trifluoroacetic acid (one drop), the reaction mixture was refluxed for 5 h under Ar and protected from light. After cooling to r.t. the reaction mixture was slowly poured into an isopropanol/hexane mixture (120 mL), which also contained 0.2 mL of trimethylamine to neutralize the acid. The precipitate was obtained via filtration and additionally washed twice with isopropanol/hexane and purified by recrystallization. The products were dried under HV conditions.

(87) . 1,3,5-Tris(4-aminophenyl)benzene (0.142 mmol, 0.05 g), 4-(bis(4-methoxyphenyl)amino)benzaldehyde (0.512 mmol, 0.171 g) and a catalytic amount of trifluoroacetic acid were dissolved in DCM (3 ml) and refluxed 5 h under Ar and in the dark to

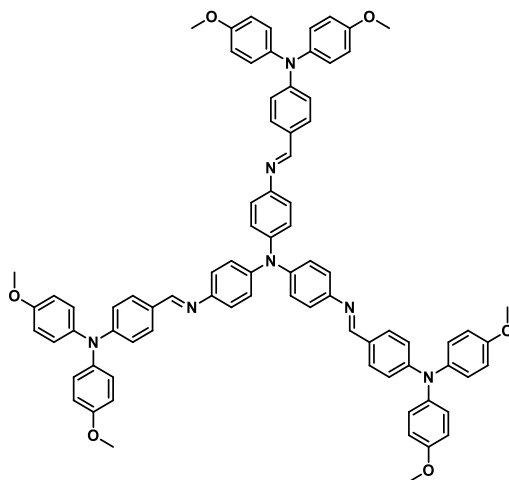
give a yellow solid after filtration and drying (0.15 g, 89.5 %).  $^1\text{H NMR}$  (600 MHz, chloroform-*d*)  $\delta$  8.40 (t,  $J = 2.4$  Hz, 3H), 7.72 (ddt,  $J = 16.0, 7.7, 2.0$  Hz, 12H), 7.56 – 7.48 (m, 3H), 7.30 (dt,  $J = 8.4, 6.8$  Hz, 6H), 7.12 (d,  $J = 8.9$  Hz, 12H), 6.93 (d,  $J = 8.5$  Hz, 6H), 6.88 (d,  $J = 8.9$  Hz, 12H), 3.82 (s, 18H).



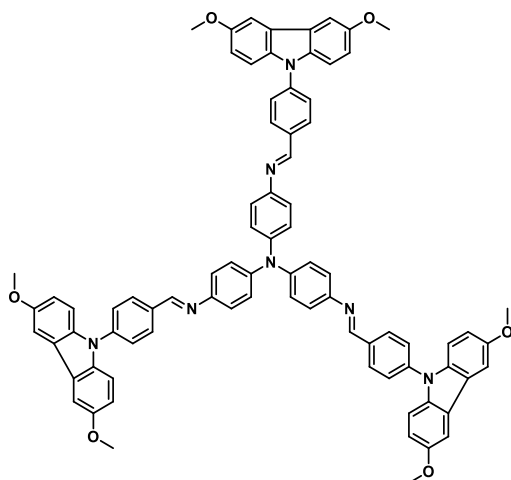
**(88).** 1,3,5-Tris(4-aminophenyl)benzene (0.142 mmol, 0.05 g), 4-(3,6-dimethoxy-carbazol-9-yl)benzaldehyde (0.512 mmol, 0.170 g) and a catalytic amount of trifluoroacetic acid were dissolved in DCM (3 ml) and refluxed 5 h under Ar and in the dark to give a yellow solid after filtration and drying (0.14 g, 76 %).  $^1\text{H NMR}$  (600 MHz, chloroform-*d*)  $\delta$  8.66 (s, 3H), 8.19 – 8.14 (m, 6H), 7.89 (s, 3H), 7.85 – 7.76 (m, 12H), 7.73 – 7.68 (m, 6H), 7.57 (t,  $J = 2.1$  Hz, 6H), 7.48 – 7.38 (m, 12H), 7.07 (dt,  $J = 8.9, 2.1$  Hz, 6H), 3.97 (s, 18H).



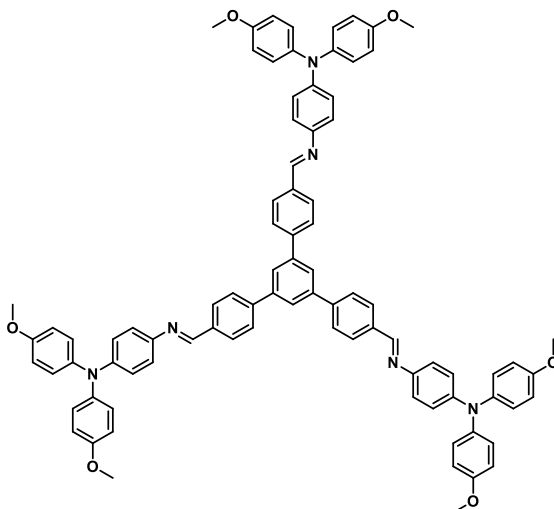
**(89).** 1,3,5-Tris(4-aminophenyl)amine (0.172 mmol, 0.05 g), 4-(bis(4-methoxyphenyl)amino)benzaldehyde (0.620 mmol, 0.207 g) and a catalytic amount of trifluoroacetic acid were dissolved in DCM (3 ml) and refluxed 5 h under Ar and in the dark to give a yellow solid after filtration and drying (0.09 g, 42.3 %).  $^1\text{H NMR}$  (600 MHz, chloroform-*d*)  $\delta$  8.37 (s, 3H), 7.66 (dd,  $J = 8.6, 6.2$  Hz, 6H), 7.17 – 7.07 (m, 24H), 6.94 – 6.89 (m, 6H), 6.86 (dd,  $J = 9.0, 2.2$  Hz, 12H), 3.81 (d,  $J = 0.9$  Hz, 18H).



**(90).** 1,3,5-Tris(4-aminophenyl)amine (0.172 mmol, 0.05 g), 4-(3,6-dimethoxy-carbazol-9-yl)benzaldehyde (0.620 mmol, 0.25 g) and a catalytic amount of trifluoroacetic acid were dissolved in DCM (3 ml) and refluxed 5 h under Ar and in the dark to give a yellow solid after filtration and drying (0.09 g, 42.3 %).  $^1\text{H NMR}$  (600 MHz, Chloroform-*d*)  $\delta$  8.37 (s, 3H), 7.66 (dd,  $J = 8.6, 6.2$  Hz, 6H), 7.17 – 7.07 (m, 24H), 6.94 – 6.89 (m, 6H), 6.86 (dd,  $J = 9.0, 2.2$  Hz, 12H), 3.81 (d,  $J = 0.9$  Hz, 18H).  $^1\text{H NMR}$  (600 MHz, chloroform-*d*)  $\delta$  8.63 (s, 3H), 8.13 (d,  $J = 8.1$  Hz, 6H), 7.74 – 7.64 (m, 6H), 7.56 (d,  $J = 2.6$  Hz, 6H), 7.43 (d,  $J = 8.9$  Hz, 6H), 7.32 – 7.27 (m, 6H), 7.23 (d,  $J = 8.7$  Hz, 6H), 7.07 (dd,  $J = 8.9, 2.5$  Hz, 6H), 3.96 (d,  $J = 2.2$  Hz, 18H).

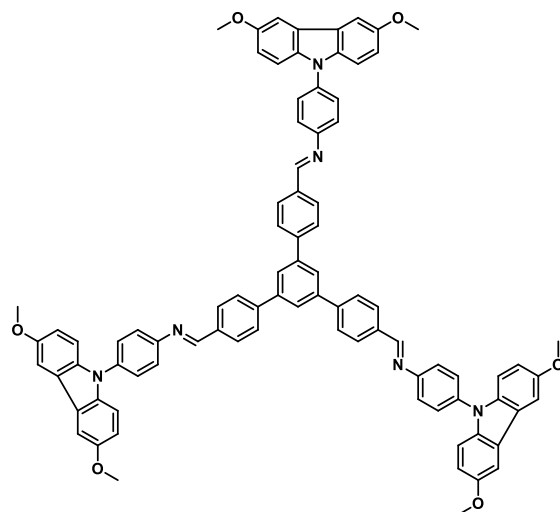


**(100).** 1,3,5-Tris(4-formylphenyl)benzene (0.128 mmol, 0.05 g), N1,N1-bis(4-methoxyphenyl)benzene-1,4-diamine (0.423 mmol, 0.135 g) and a catalytic amount of trifluoroacetic acid were dissolved in DCM (3 ml) and refluxed 5 h under Ar and in the dark to give a yellow solid after filtration and drying (0.1 g, 60 %).  $^1\text{H}$  NMR (600 MHz, chloroform-*d*)  $\delta$  8.57 (d,  $J = 3.1$  Hz, 3H), 8.11 – 7.96 (m, 6H), 7.93 – 7.85 (m, 3H), 7.84 – 7.69 (m, 6H), 7.24 – 7.13 (m, 6H), 7.12 – 7.04 (m, 12H), 6.98 (d,  $J = 8.8$  Hz, 6H), 6.89 – 6.79 (m, 12H), 3.81 (s, 18H).

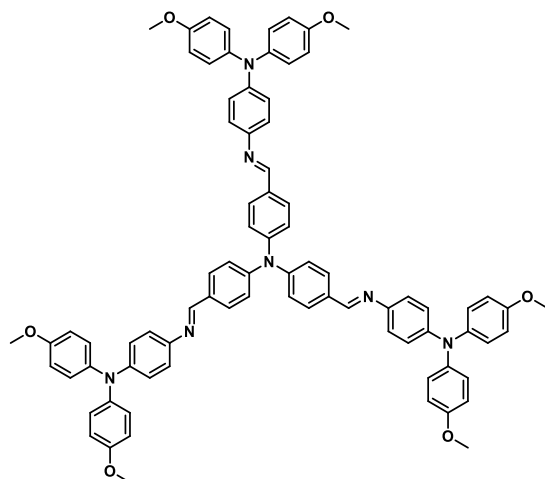


**(101).** 1,3,5-Tris(4-formylphenyl)benzene (0.128 mmol, 0.05 g), 4-(3,6-Dimethoxy-carbazol-9-yl)aniline (0.423 mmol, 0.135 g) and a catalytic amount of trifluoroacetic acid were dissolved in DCM (3 ml) and refluxed 5 h under Ar and in the dark to give a yellow solid after filtration and drying (0.1 g, 60 %).

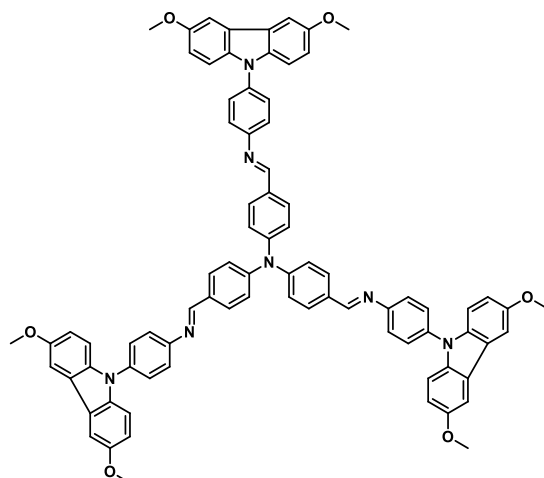




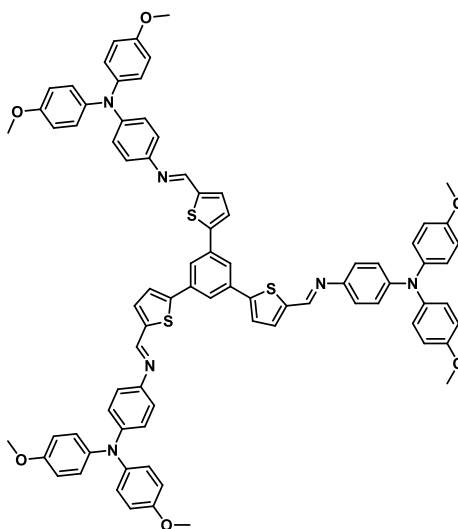
**(104).** 1,3,5-Tris(4-formylphenyl)amine (0.152 mmol, 0.05 g), N1,N1-bis(4-methoxyphenyl)benzene-1,4-diamine (0.501 mmol, 0.161 g) and a catalytic amount of trifluoroacetic acid were dissolved in DCM (3 ml) and refluxed 5 h under Ar and in the dark to give a yellow solid after filtration and drying (0.1 g, 60 %).  $^1\text{H}$  NMR (600 MHz, chloroform-*d*)  $\delta$  8.45 (s, 3H), 7.81 (s, 6H), 7.21 (d,  $J = 8.3$  Hz, 6H), 7.13 (s, 6H), 7.09 – 7.03 (m, 12H), 6.96 (d,  $J = 8.6$  Hz, 6H), 6.86 – 6.80 (m, 12H), 3.80 (s, 18H).



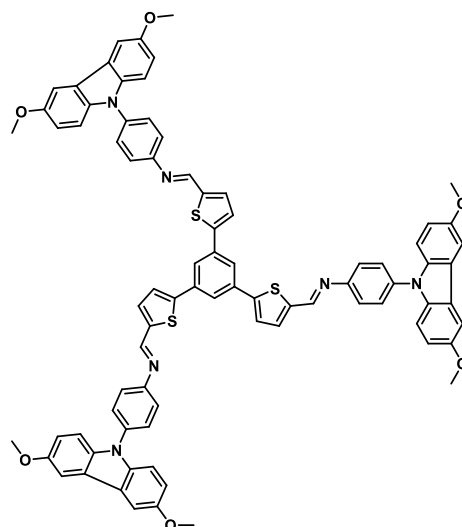
**(105).** 1,3,5-Tris(4-formylphenyl)amine (0.152 mmol, 0.05 g), 4-(3,6-dimethoxy-carbazol-9-yl)aniline (0.501 mmol, 0.159 g) and a catalytic amount of trifluoroacetic acid were dissolved in DCM (3 ml) and refluxed 5 h under Ar and in the dark to give a yellow solid after filtration and drying (0.1 g, 53.5 %).



**(107).** 5,5',5''-(Benzene-1,3,5-triyl)tris(thiophene-2-carbaldehyde) (0.122 mmol, 0.05 g), N,N-bis(4-methoxyphenyl)benzene-1,4-diamine (0.404 mmol, 0.129 g) and a catalytic amount of trifluoroacetic acid were dissolved in DCM (3 ml) and refluxed 5 h under Ar and in the dark to give a yellow solid after filtration and drying (0.1 g, 62 %).  $^1\text{H NMR}$  (600 MHz, chloroform-*d*)  $\delta$  8.59 (d,  $J = 1.5$  Hz, 3H), 7.89 (s, 3H), 7.44 (s, 3H), 7.22 – 7.15 (m, 6H), 7.07 (d,  $J = 9.0$  Hz, 12H), 6.99 – 6.93 (m, 6H), 6.84 (d,  $J = 9.0$  Hz, 12H), 3.81 (s, 18H).



**(108).** 5,5',5''-(Benzene-1,3,5-triyl)tris(thiophene-2-carbaldehyde) (0.122 mmol, 0.05 g), 4-(3,6-dimethoxy-carbazol-9-yl)aniline (0.404 mmol, 0.129 g) and a catalytic amount of trifluoroacetic acid were dissolved in DCM (3 ml) and refluxed 5 h under Ar and in the dark to give a yellow solid after filtration and drying (0.1 g, 62 %).



## 2.5 References

150. Kim, G. W.; Choi, H.; Kim, M.; Lee, J.; Son, S. Y.; Park, T., *Adv. Energy Mater.* **2020**, *10* (8), 1903403.
155. Sobolev, A. N.; Belsky, V. K.; Romm, I. P.; Chernikova, N. Y.; Guryanova, E. N., *Acta Crystallogr. C* **1985**, *41* (6), 967.
156. Wang, J.; Liu, K.; Ma, L.; Zhan, X., *Chem. Rev.* **2016**, *116* (23), 14675.
157. Malagoli, M.; Brédas, J. L., *Chem. Phys. Lett.* **2000**, *327* (1), 13.
158. Zhan, C.-G.; Nichols, J. A.; Dixon, D. A., *J. Phys. Chem. A* **2003**, *107* (20), 4184.
159. Shirota, Y.; Kageyama, H., *Chem. Rev.* **2007**, *107* (4), 953.
160. Choi, H.; Park, S.; Paek, S.; Ekanayake, P.; Nazeeruddin, M. K.; Ko, J., *J. Mater. Chem. A* **2014**, *2* (45), 19136.
161. Liu, P.; Xu, B.; Hua, Y.; Cheng, M.; Aitola, K.; Sveinbjörnsson, K.; Zhang, J.; Boschloo, G.; Sun, L.; Kloo, L., *J. Power Sources* **2017**, *344*, 11.
162. Wang, Y.; Chen, W.; Wang, L.; Tu, B.; Chen, T.; Liu, B.; Yang, K.; Koh, C. W.; Zhang, X.; Sun, H.; Chen, G.; Feng, X.; Woo, H. Y.; Djurisic, A. B.; He, Z.; Guo, X., *Adv. Mater.* **2019**, *31* (35), 1902781.
163. Niu, T.; Zhu, W.; Zhang, Y.; Xue, Q.; Jiao, X.; Wang, Z.; Xie, Y.-M.; Li, P.; Chen, R.; Huang, F.; Li, Y.; Yip, H.-L.; Cao, Y., *Joule* **2021**, *5* (1), 249.
164. Rombach, F. M.; Haque, S. A.; Macdonald, T. J., *Energy Environ. Sci.* **2021**, *14* (10), 5161.
165. Xing, G.; Mathews, N.; Sun, S.; Lim, S. S.; Lam, Y. M.; Grätzel, M.; Mhaisalkar, S.; Sum, T. C., *Science* **2013**, *342* (6156), 344.
166. Lin, X.; Cui, D.; Luo, X.; Zhang, C.; Han, Q.; Wang, Y.; Han, L., *Energy Environ. Sci.* **2020**, *13* (11), 3823.
167. Jena, A. K.; Kulkarni, A.; Miyasaka, T., *Chem. Rev.* **2019**, *119* (5), 3036.

168. Heo, J. H.; Im, S. H.; Noh, J. H.; Mandal, T. N.; Lim, C.-S.; Chang, J. A.; Lee, Y. H.; Kim, H.-j.; Sarkar, A.; Nazeeruddin, M. K.; Grätzel, M.; Seok, S. I., *Nat. Photon.* **2013**, *7* (6), 486.
169. Ghosh, S.; Mishra, S.; Singh, T., *Adv. Mater. Interfaces* **2020**, *7* (18), 2000950.
170. Burschka, J.; Pellet, N.; Moon, S.-J.; Humphry-Baker, R.; Gao, P.; Nazeeruddin, M. K.; Grätzel, M., *Nature* **2013**, *499* (7458), 316.
171. Liu, M.; Johnston, M. B.; Snaith, H. J., *Nature* **2013**, *501* (7467), 395.
172. Yu, Y.; Zhang, F.; Hou, T.; Sun, X.; Yu, H.; Zhang, M., *Sol. RRL* **2021**, *5* (10), 2100386.
173. Brinkmann, K. O.; He, J.; Schubert, F.; Malerczyk, J.; Kreusel, C.; van gen Hassend, F.; Weber, S.; Song, J.; Qu, J.; Riedl, T., *ACS Appl. Mater. Interfaces* **2019**, *11* (43), 40172.
174. Li, H.; Fu, K.; Hagfeldt, A.; Grätzel, M.; Mhaisalkar, S. G.; Grimsdale, A. C., *Angew. Chem. Int. Ed.* **2014**, *53* (16), 4085.
175. Pham, H. D.; Do, T. T.; Kim, J.; Charbonneau, C.; Manzhos, S.; Feron, K.; Tsoi, W. C.; Durrant, J. R.; Jain, S. M.; Sonar, P., *Adv. Energy Mater.* **2018**, *8* (16), 1703007.
176. Pham, H. D.; Hayasake, K.; Kim, J.; Do, T. T.; Matsui, H.; Manzhos, S.; Feron, K.; Tokito, S.; Watson, T.; Tsoi, W. C.; Motta, N.; Durrant, J. R.; Jain, S. M.; Sonar, P., *J. Mater. Chem. C* **2018**, *6* (14), 3699.
177. Liu, X.; Zhu, L.; Zhang, F.; You, J.; Xiao, Y.; Li, D.; Wang, S.; Meng, Q.; Li, X., *Energy Technol.* **2017**, *5* (2), 312.
178. Ma, Y.; Cao, X.; Li, G.; Wen, Y.; Yang, Y.; Wang, J.; Du, S.; Yang, L.; Gao, H.; Song, Y., *Adv. Funct. Mater.* **2010**, *20* (5), 803.
179. Rettig, W., *Appl. Phys. B* **1988**, *45* (3), 145.
180. Maciejczyk, M.; Ivaturi, A.; Robertson, N., *J. Mater. Chem. A* **2016**, *4* (13), 4855.
181. Pham, H. D.; Jain, S. M.; Li, M.; Wang, Z.-K.; Manzhos, S.; Feron, K.; Pitchaimuthu, S.; Liu, Z.; Motta, N.; Durrant, J. R.; Sonar, P., *Adv. Electron. Mater.* **2020**, *6* (4), 1900884.
182. Rodríguez-Seco, C.; Méndez, M.; Roldán-Carmona, C.; Pudi, R.; Nazeeruddin, M. K.; Palomares, E. J., *Angew. Chem. Int. Ed.* **2020**, *59* (13), 5303.
183. Chi, W.-J.; Zheng, D.-Y.; Chen, X.-F.; Li, Z.-S., *J. Mater. Chem. C* **2017**, *5* (38), 10055.
184. Zahn, D. R. T.; Gavrilă, G. N.; Salvan, G., *Chem. Rev.* **2007**, *107* (4), 1161.
185. Seo, J. H.; Jin, Y.; Brzezinski, J. Z.; Walker, B.; Nguyen, T.-Q., *ChemPhysChem* **2009**, *10* (7), 1023.
186. Tsiper, E. V.; Soos, Z. G.; Gao, W.; Kahn, A., *Chem. Phys. Lett.* **2002**, *360* (1), 47.
187. Hill, I. G.; Kahn, A.; Soos, Z. G.; Pascal, J. R. A., *Chem. Phys. Lett.* **2000**, *327* (3), 181.
188. Chen, Q.; Wang, C.; Li, Y.; Chen, L., *J. Am. Chem. Soc.* **2020**, *142* (43), 18281.
189. Ishii, H.; Sugiyama, K.; Ito, E.; Seki, K., *Adv. Mater.* **1999**, *11* (8), 605.
190. Jacobsson, T. J.; Correa-Baena, J.-P.; Halvani Anaraki, E.; Philippe, B.; Stranks, S. D.; Bouduban, M. E. F.; Tress, W.; Schenk, K.; Teuscher, J.; Moser, J.-E.; Rensmo, H.; Hagfeldt, A., *J. Am. Chem. Soc.* **2016**, *138* (32), 10331.
191. Petrović, M.; Maksudov, T.; Panagiotopoulos, A.; Serpetzoglou, E.; Konidakis, I.; Stylianakis, M. M.; Stratakis, E.; Kymakis, E., *Nanoscale Advances* **2019**, *1* (8), 3107.

# 3 COF films as hole transport layers in p-i-n Perovskite solar cells

## 3.1 Introduction

In the past 10 years, hybrid organic–inorganic perovskite solar cells underwent outstanding developments. The power conversion efficiency of hybrid organic–inorganic perovskite solar cells achieved ca. 25% which is comparable to those of commercialized polycrystalline silicon solar cells. The most reported high-performance PSCs focus on the regular planar and mesoporous device structures, which normally use n-type metal oxide, for example TiO<sub>2</sub> as hole transport layer. The formation process of TiO<sub>2</sub> requires high temperatures treatment up to 450°C, which would increase costs and hinder profitability of commercially produced PSCs. In contrast, inverted *p-i-n* architecture PSCs with *p*-type organic small molecules and polymers as hole transport layers can avoid the high temperature treatment. The simplified fabrication process provides easy processability and scalability for large area and flexible photovoltaic devices.<sup>192</sup>

Currently, the most common used commercial *p*-type hole transport materials (HTMs) for inverted *p-i-n* PSCs are 2,2',7,7'-tetrakis(N,N-bis(*p*-methoxyphenyl)amino)-9,9'-spirobifluorene (spiro-OMeTAD), poly-[bis(4-phenyl)(2,4,6-trimethylphenyl)amine] (PTAA) and poly(3,4-ethylenedioxythiophene)–poly(styrenesulfonate) (PEDOT:PSS). Spiro-OMeTAD is a kind of amorphous, semiconductive small molecule which was first synthesized as in the 1990's as HTMs, and first applied in PSCs in 2012 reaching efficiencies of up to 9.7%.<sup>193, 194</sup> Spiro-OMeTAD has a low hole mobility ( $\approx 10^{-5}$  cm<sup>2</sup> V<sup>-1</sup> S<sup>-1</sup>) and lower hole conductivity ( $\approx 10^{-8}$  S cm<sup>-1</sup>), what is attributed to enhanced intermolecular distances due to the sp<sup>3</sup>-hybridized N atom with pyramidal structure and reduced  $\pi$ - $\pi$  stacking due to intermolecular steric hindrance. Both low hole mobility and hole conductivity can be overcome through doping by additives such as lithium bis(trifluoromethanesulfonyl)imide (Li-TFSI), cobalt complexes, tris(2-(1H-pyrazol-1-yl)-4-tert-butylpyridine)-cobalt(III) tris(bis(trifluoromethylsulfonyl)imide) (FK209) or 2,3,5,6-tetrafluoro-7,7,8,8-tetracyanoquinodimethane (F4-TCNQ). However, the use of Li-TFSI dopants with salt-like nature in spiro-OMeTAD will increase the hydrophilicity of the HTL and lead to rapid degradation of the PSCs due to an increased instability against moisture. And the doping process

of spiro-OMeTAD with Li-TFSI requires oxygen, in which the degree of spiro-OMeTAD oxidation is hard to control.<sup>195</sup> For PTAA, addition of dopants can also be applied to increased hole mobility and reduce charge carrier recombination, but it is process also leads to instabilities of PSCs. Besides, PTAA suffered from high costs.<sup>196</sup> PEDOT:PSS mainly suffered from low chemical stability attributed to its acidity and insufficient electron blocking property.<sup>197</sup> These problems hinder their further development in PSCs. Therefore, it is necessary to develop cheap and available, dopant-free HTMs for PSCs.

For both molecule and polymer HTMs, the films are normally fabricated by spin-coating. This solution processible technology require suitable solubility of HTMs. For example, for *p-i-n* PSCs, the solubility of HTMs should be enough for spin-coating, but not too good in NMP, DMF and DMSO for avoiding redissolution in the coming step of perovskite layer deposition. In contrast, in *n-i-p* PSCs, HTMs are formed on top of the as-prepared perovskite layer. As known, hole mobility generally increases with crystallinity of organic semiconductors.<sup>198</sup> But most organic semiconductor polymers are too rigid to be dissolved in commonly used solvents. As discussed above, COFs are kind of highly ordered polymers with superior crystallinity, which are also insoluble in commonly used solvents. If COF films can be built on top of ITO directly, the problem of solution processing can be avoided. Besides, different HOMO levels of COFs can be designed by combining different cores and linkers to achieve an improved energy band alignment. In this chapter, different imine-linked COF layers were built on top of ITO directly for using as HTLs in PSCs. The imine-linked COFs were chosen because the necessary catalyst for COF formation is acetic acid, which can be easily removed. Both, as cores and linkers, the monomers used for COF formation were discussed in chapter 2.

## 3.2 Results and Discussions

### 3.2.1 Synthesis and naming of COFs

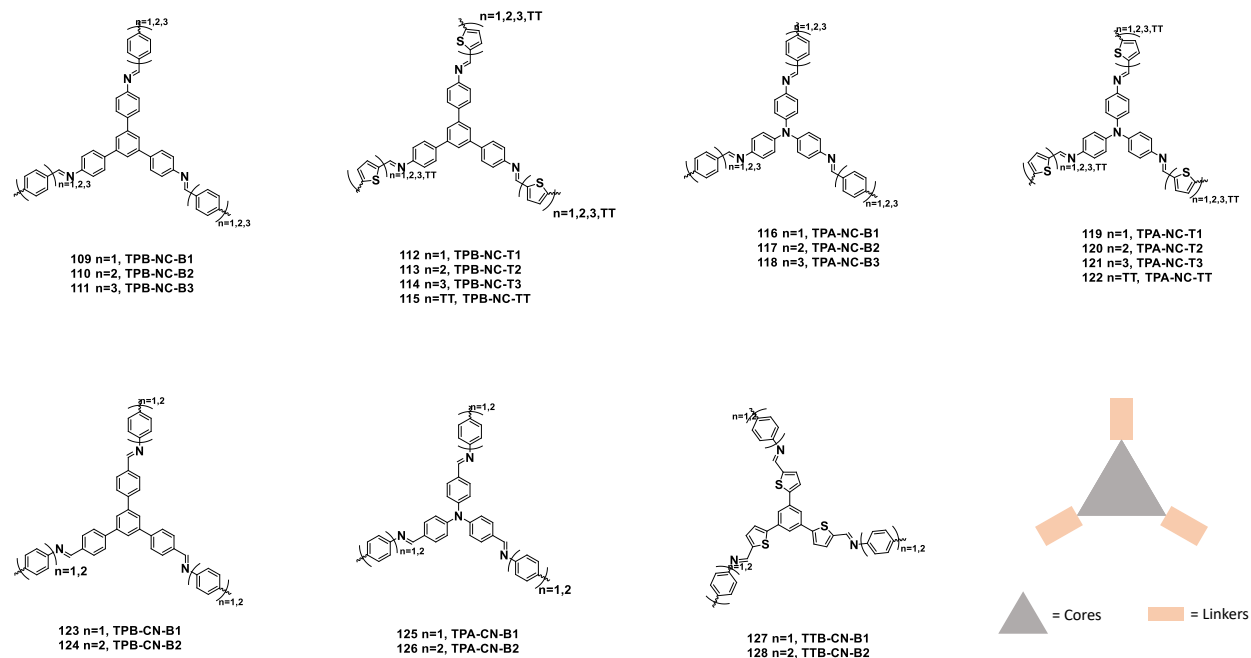
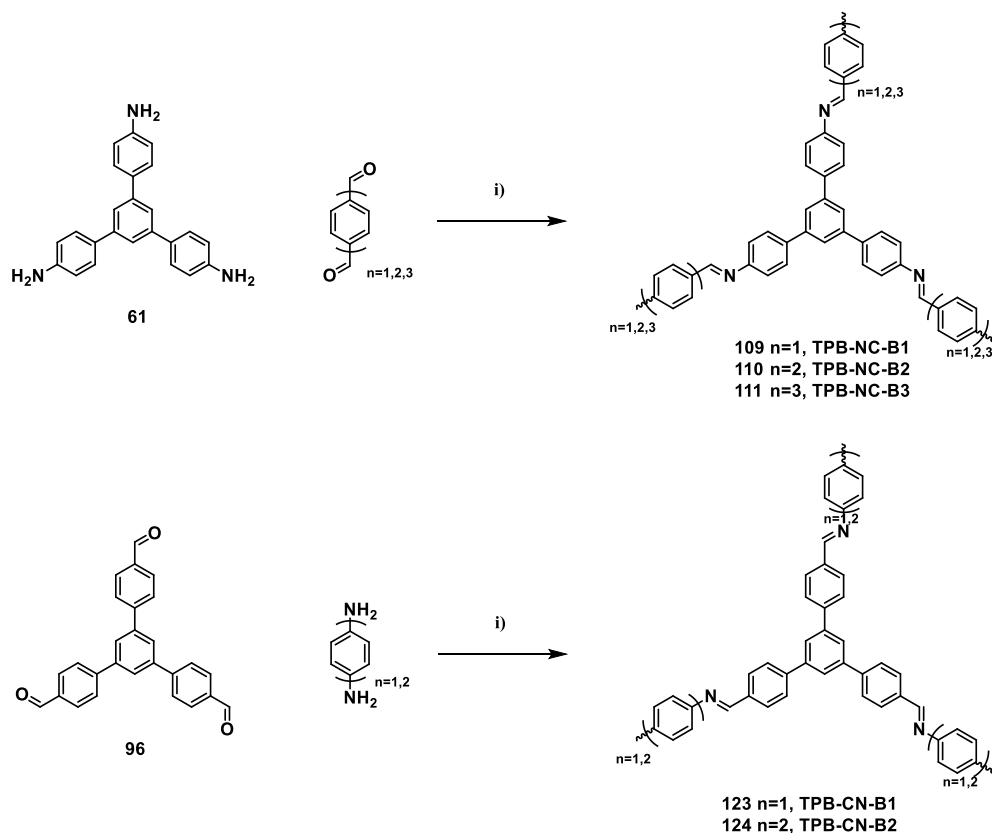


Figure 33 Structure of COF films for HTL.

All COFs of this study (as shown in Figure 33) are imine-linked COFs, which were synthesized by condensation reaction with acetic acid as the catalyst. 1,3,5-tris(4-aminophenyl)benzene, 1,3,5-tris(4-aminophenyl)amine, 1,3,5-tris(4-formylphenyl)benzene, 1,3,5-tris(4-formylphenyl)amine and 5,5',5''-(benzene-1,3,5-triyl)tris(thiophene-2-carbaldehyde) were chosen as cores, and 1,4-benzenedicarboxaldehyde, 4,4'-biphenyldicarboxaldehyde, [1,1':4',1''-terphenyl]-4,4''-dicarbaldehyde, 2,5-thiophenedicarboxaldehyde, 2,2'-bithiophene-5,5'-dicarboxaldehyde, 2,2':5',2''-terthiophene-5,5''-dicarboxaldehyde, thieno[3,2-b]thiophene-2,5-dicarboxaldehyde, 1,4-phenylenediamine, 4,4'-benzidine and 4,4'-dithiodianiline as linkers. In the short names, the number represents number of phenylene or thiophene repeat units. CN and NC represents different directions of C=N linkage. The general synthesis reactions were shown in Scheme 8, in which 1,4-dioxane/mesitylene (v/v = 4/1) were used as solvent systems and acetic acid (6 M) were used as catalyst.



Scheme 8: General synthesis of COF films. Reaction condition: i) 1,4-dioxane/mesitylene (v/v = 4/1), acetic acid (6 M), 120 °C, 3 d.

### 3.2.2 Optical and electrochemical properties

Figure 34 shows SEM image of COF films on ITO. The surface morphology of all the ITO/COF films are similar, thus TPB-NC-B1 was chosen as example. Both in small (Figure 34 a) and large scale (Figure 34 b) image TPB-NC-B1 COF films show homogeneous and smooth surface. The thickness of COF films can be controlled by adjusting speed of spin-coating (see Exp. part). Figure 34 c and d are SEM images of TPB-NC-B1 COF films spin-coated at 1000 or 10000 rpm, respectively. Both images are observed as uniform and smooth films. The thickness of TPB-NC-B1 COF films are 23 nm and 10 nm with a speed of 1000 or 10000 rpm, respectively. Figure 34 e and f represent AFM images of TPB-NC-B1 COF films spin-coated on ITO with a speed of 1000 or 10000 rpm, respectively, with mean average roughness value of 2 and 2.3 nm respectively.



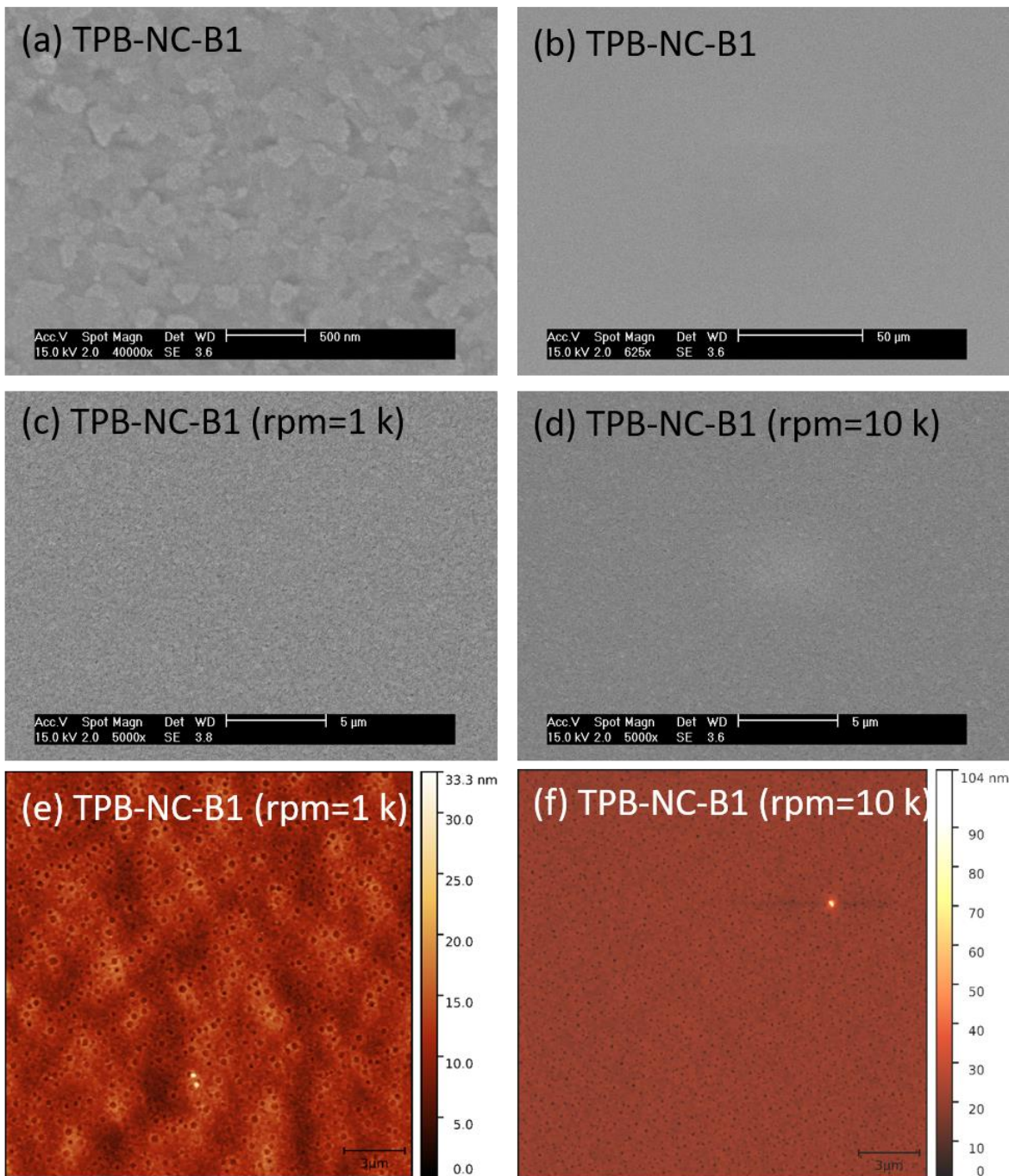


Figure 34 SEM images of TPB-NC-B1 COF films at small (a) or large (b) scale, spin-coated with speed of 1000 (c) or 10000 rpm (d), respectively. AFM images of TPB-NC-B1 COF with speed of spin-coated from 1000 (e) or 10000 rpm (f), respectively.

FTIR spectroscopy was applied to identify the formation of C=N linkages. As shown in Figure 35 a, the peaks at  $1685\text{ cm}^{-1}$  for terephthalaldehyde and at  $1602\text{ cm}^{-1}$  for 1,3,5-tris(4-

aminophenyl)benzene represent the stretching vibrations of the C=O bonds and C-N bonds respectively. The peak at  $1621\text{ cm}^{-1}$  is assigned to the stretching vibrations of C=N bonds for TPB-NC-B1, TPB-NC-B2, TPB-NC-B3, TPB-NC-T1, TPB-NC-T2, TPB-NC-T3 COFs, investigated as powders. The disappearing of C=O, C-N bonds and arising of C=N indicate the formation of C=N linkages and the disappearance of starting materials. Figure 35 b shows the FTIR comparison between TPB-NC-B1 COF powder and TPB-NC-B1 COF film on ITO. Both spectra the same signal at  $1621\text{ cm}^{-1}$  is found, which indicates the formation of C=N linkages in the COF films. The crystallinity of COFs was verified by powder X-ray diffraction (PXRD). Diffraction peaks of TPB-NC-B1 COF powders at  $2.63^\circ$ ,  $4.72^\circ$ ,  $5.50^\circ$ ,  $7.12^\circ$  correspond to the (100), (110), (200), (210) reflections, respectively (as shown in Figure 35 c).<sup>199</sup> Figure 35 d shows the XRD of TPB-NC-B1 COF film on ITO and of pure ITO substrates for comparison. No obvious diffraction peak are found indicating an amorphous structure of TPB-NC-B1 COF films.

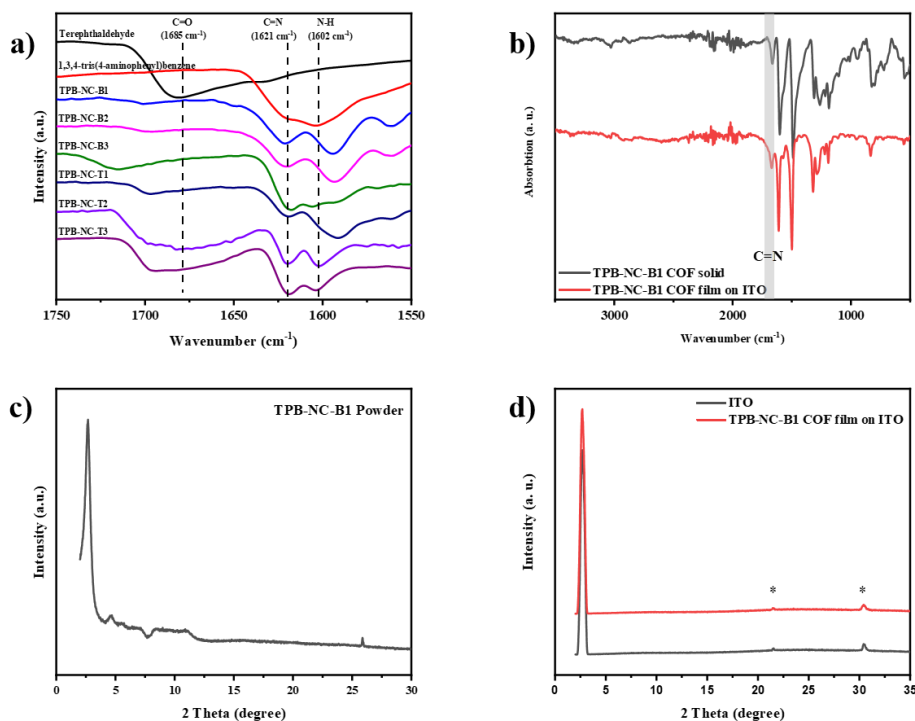


Figure 35 a) FTIR of terephthalaldehyde, 1,3,5-tris(4-aminophenyl)benzene, TPB-NC-B1, TPB-NC-B2, TPB-NC-B3, TPB-NC-T1, TPB-NC-T2 and TPB-NC-T3 COFs powder. b) FTIR of TPB-NC-B1 powder and TPB-NC-B1 COF film on ITO. c) XRD of TPB-NC-B1 powder. d) XRD of TPB-NC-B1 COF film on ITO and of the uncovered ITO substrate.

The optical properties of all designed COF films on quartz were measured by UV–vis and PL spectroscopy. The results are shown in Table 13 and Figure 36. In N=C-linked COF films, first COFs with fixed core are compared effect of different linkers. For TPB-cored COFs, TPB-NC-B1, TPB-NC-B2 and TPB-NC-B3 exhibit absorption peaks at 388 nm, 378 nm and 382 nm, which the absorption maximum is slightly blue-shifted with increasing number of benzene (as shown in Figure 36 a). This result does not match the general rules that absorption peak would be red-shifted as the  $\pi$ -conjugated system is extended. Different trends are found in another COF group with the TPB core and different thiophene linkers. As shown in Figure 36 b, TPB-NC-T1, TPB-NC-T2 and TPB-NC-T3 exhibit absorption peak at 413 nm, 437 nm and 462 nm, with the absorption maximum red-shifted with increasing number of thiophene rings of the repeating unit. TPB-NC-TT shows absorption peak at 427 nm, which is locked between those of TPB-NC-T1 and TPB-NC-T2. This results the match with the general trends. Similar trends are found for the UV results for the COFs with TPA cores. TPA-NC-B1, TPA-NC-B2 and TPA-NC-B3 exhibit absorption peak on 472 nm, 456 nm and 446 nm, with the absorption maximum slightly blue-shifted with increasing number of benzene rings of the repeating unit. However, TPA-NC-T1, TPA-NC-T2 and TPA-NC-T3 do not show red-shifted absorption maxima with increasing number of thiophene rings of the repeating unit with the absorption maxima nearly locked 507 nm. Only TPA-NC-TT exhibits an slightly red-shifted absorption maximum than the former three COFs (as shown in Figures 36 c, d). If the numbers of benzene or thiophene linkers are fixed, COFs with TPA cores exhibit red-shifted absorption maxima compared to that with TPB cores (as shown in Figure 36 e). No clear trends are found in the UV results of COFs with C=N linkages (as shown in Figure 36 f).

Table 13. Optical properties of COF films on quartz.

a) Absorption maxima of HTMs in DCM; b) value was taken from the intersection of the normalized absorption and emission spectra; c) excitation at  $\lambda_{\text{abs}}$ ; d) optical bandgap was calculated with the formula of  $1240/\lambda_{\text{onset}}$ ; e) measured by the AC-2 method; f) LUMO was calculated with the formula of  $E_{\text{LUMO}} = E_{\text{HOMO}} + E_{\text{g}}$  (eV); g) The difference between  $\lambda_{\text{abs}}$  and  $\lambda_{\text{emi}}$ .

	Name	$\lambda_{\text{abs}}$ <sup>a)</sup> (nm)	$\lambda_{\text{onset}}$ <sup>b)</sup> (nm)	$\lambda_{\text{emi}}$ <sup>c)</sup> (nm)	$E_{\text{g}}$ <sup>d)</sup> (eV)	HOMO <sup>e)</sup> (eV)	LUMO <sup>f)</sup> (eV)	Stokes shift <sup>g)</sup> (nm)
1	TPB-NC-B1	388	456	442	2.64	-5.6	-2.96	54
2	TPB-NC-B2	378	446	464	2.70	-5.69	-2.99	86

3	TPB-NC-B3	382	456	442	2.64	-5.63	-2.99	60
4	TPB-NC-T1	413	498	519	2.42	-5.62	-3.20	106
5	TPB-NC-T2	437	520	537	2.32	-5.63	-3.31	100
6	TPB-NC-T3	462	558	566	2.16	-5.51	-3.35	104
7	TPB-NC-TT	427	507	530	2.37	-5.63	-3.26	103
8	TPA-NC-B1	472	556	580	2.17	-5.23	-3.06	108
9	TPA-NC-B2	456	536	571	2.25	-5.31	-3.06	115
10	TPA-NC-B3	446	522	563	2.31	-5.29	-2.98	117
11	TPA-NC-T1	506	602	613	2.00	-5.33	-3.33	107
12	TPA-NC-T2	507	617	611	1.95	-5.3	-3.35	104
13	TPA-NC-T3	510	618	615	1.95	-5.28	-3.33	105
14	TPA-NC-TT	514	616	650	1.95	-5.33	-3.38	136
15	TPB-CN-B1	425	487	465	2.47	-5.62	-3.15	40
16	TPB-CN-B2	397	473	436	2.55	-5.58	-3.03	39
17	TPA-CN-B1	420	490	463	2.46	-5.66	-3.20	43
18	TPA-CN-B2	423	488	488	2.47	-5.58	-3.11	65
19	TTB-CN-B1	393	505	533	2.38	-5.59	-3.21	140
20	TTB-CN-B2	396	486	534	2.48	-5.58	-3.10	138

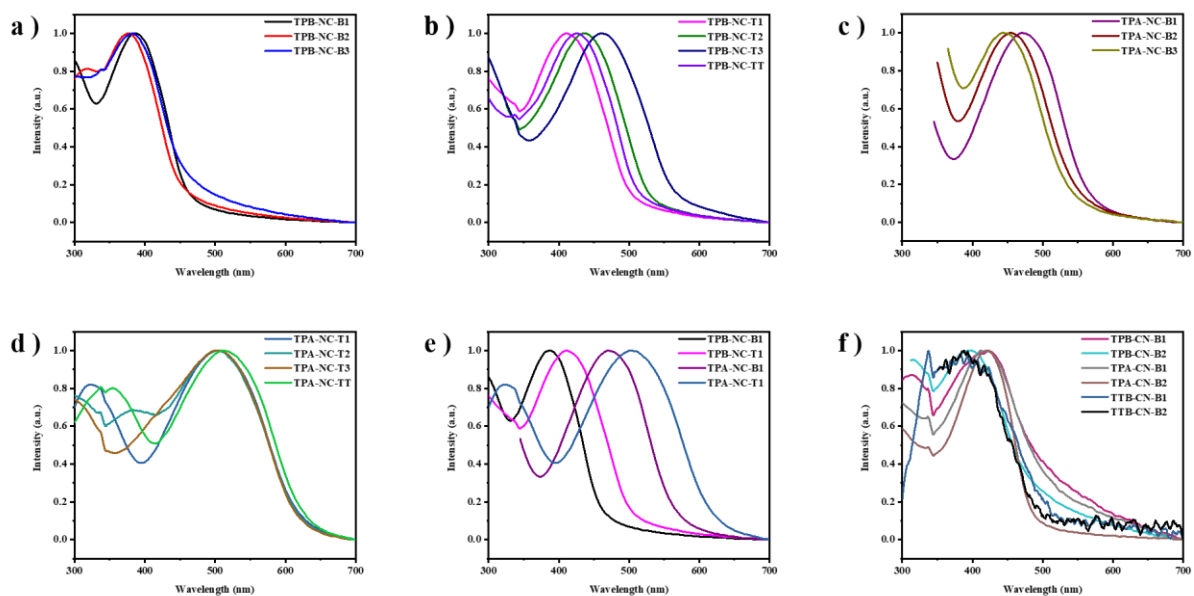


Figure 36 UV-vis results of different COF films on quartz.

The Stokes shifts for all COF films are shown in Table 13 and Figure 37, which are calculated based on the difference of absorption maximum and emission maximum of each COF films. Figures 37 a, b and c represent Stokes shift comparison for different linkages types, different cores and different linkers, respectively. Figure 37 d summarized the range of the Stokes shifts for N=C linkages, C=N linkages, TPB cores, TPA cores, benzene and thiophene linkers. N=C linked COF films possess increased Stokes shift from 70 nm to 100 nm in average compared to similar COFs with C=N linkages. This trend is hardly to explain because the only difference between these two types of COFs is the direction of C=N double bond. COF films with TPB cores show smaller Stokes shifts than those with TPA cores. And COF films with benzene linkers gain smaller Stokes shifts than those with thiophene linkers.

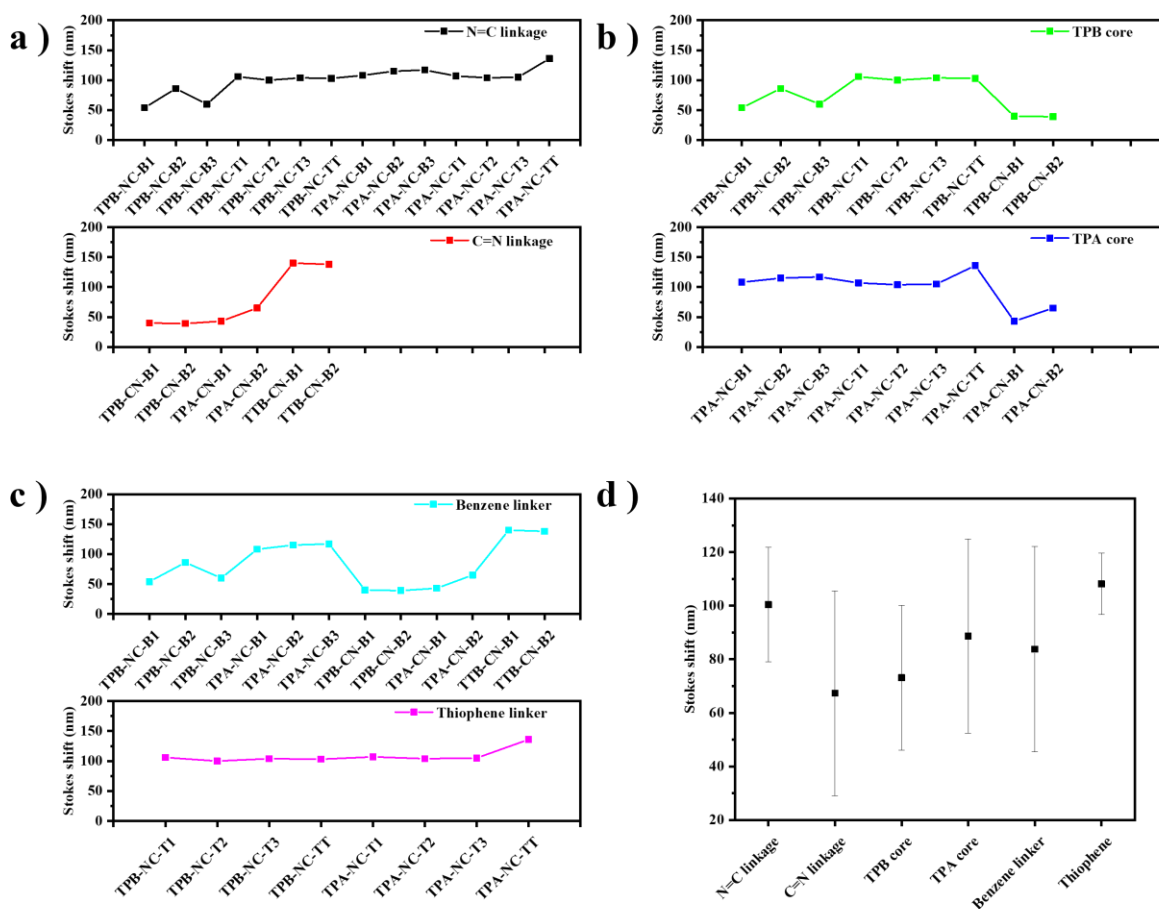


Figure 37. Stokes shift comparison between a) N=C linkage and C=N linkages, b) TPB and TPA cores and c) benzene and thiophene linkers. d) Summary of Stokes shift values for N=C linkages, C=N linkages, TPB cores, TPA cores, benzene linkers and thiophene linkers.

The HOMO, LUMO energy level alignment with perovskite for PTAA, sprio-OMeTED, and the here described COF films are shown in Figure 38. For N=C linked COF films, the HOMO level of COFs with TPB core is much deeper than HOMO level of COFs with TPA core, which is also slightly deeper than HOMO level of  $\text{FA}_{0.94}\text{Cs}_{0.06}\text{PbI}_3$ . This result indicates COF films with TPA core may be better HTM than COF films with TPB cores base on energy level alignment. For C=N linked COF films, both HOMO level of COFs with TPB and TPA core are deeper than the HOMO level of  $\text{FA}_{0.94}\text{Cs}_{0.06}\text{PbI}_3$ . These COFs only show 0.05 to 0.1 eV deeper HOMO level than  $\text{FA}_{0.94}\text{Cs}_{0.06}\text{PbI}_3$ , which indicate they still may have potential to be used as HTL in  $\text{FA}_{0.94}\text{Cs}_{0.06}\text{PbI}_3$  PSC. Considering there are large HOMO level gap between PTAA and  $\text{FA}_{0.94}\text{Cs}_{0.06}\text{PbI}_3$ , it was worth to test these COF films in devices as HTL, possibly to obtain higher  $V_{oc}$ .

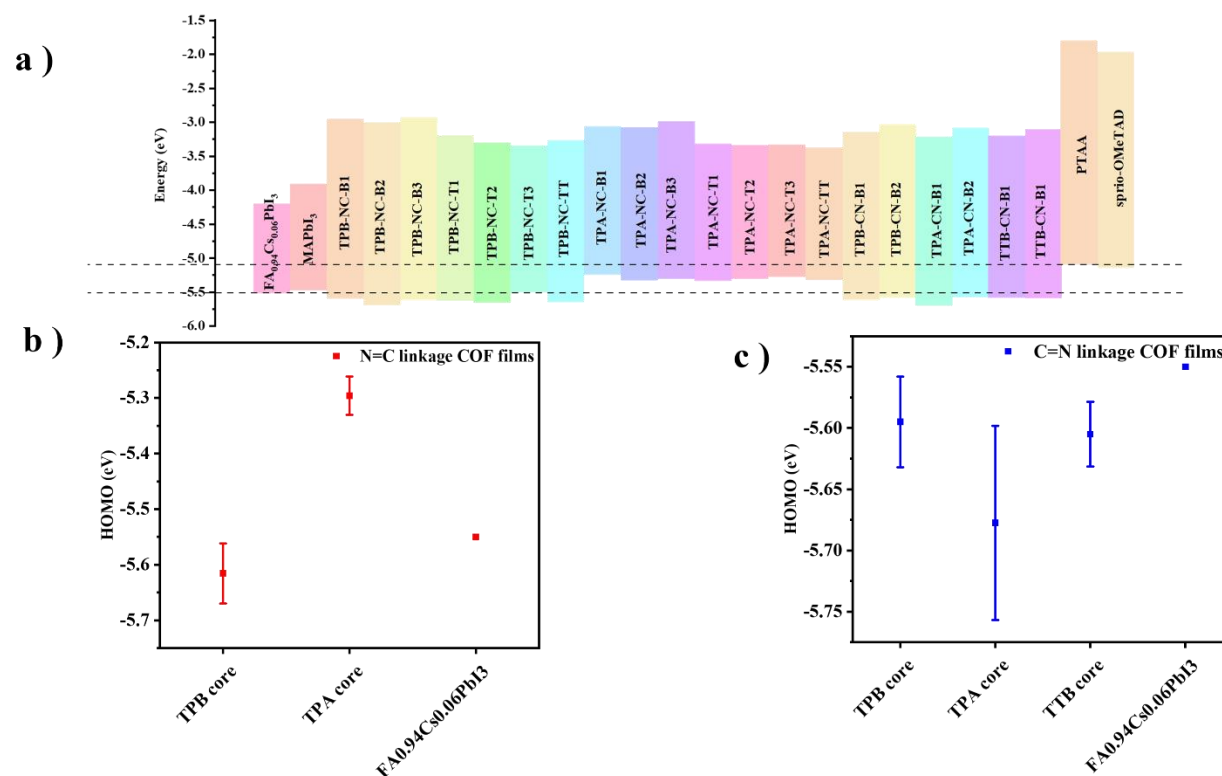


Figure 38. a) The HOMO, LUMO energy level diagrams for PTAA, sprio-OMeTED, and the here described COF films, and the valence, conduction band energies for  $\text{MAPbI}_3$  and  $\text{FA}_{0.94}\text{Cs}_{0.06}\text{PbI}_3$ . b) Summary for the HOMO level positions for N=C linked COFs and  $\text{FA}_{0.94}\text{Cs}_{0.06}\text{PbI}_3$ . c) Summary for the HOMO level position for C=N linked COFs and  $\text{FA}_{0.94}\text{Cs}_{0.06}\text{PbI}_3$ .

### 3.2.3 Perovskite layer forming on top of COF films

To characterize the quality of the perovskite layer on top of the COF films, contact angle measurements with the solvent needed for perovskite layer building on the COF films were applied (results are shown in Table 14). COF TPB-NC-B1 on ITO is chosen as standard system to measure the contact angles for three different conditions of COF formation, which are 10 mg/ml, 1 k; 5 mg/ml, 1 k and 5 mg/ml, 10 k. The 10 and 5 mg/ml are the concentration of the precursor solution for COF formation. The 10 k and 1 k are the speeds during spin-coating the COFs precursor solutions. Pure ITO substrates and ITO substrates covered with PTAA are measured as reference. The thickness of TPB-NC-B1 COF films built by 10 mg/ml, 1 k; 5 mg/ml, 1 k and 5 mg/ml, 10 k are around 23, 15 and 10 nm, respectively. The contact angle of TPB-NC-B1 COF films built by 5 mg/ml, 1 k and 5 mg/ml, 10 k show much smaller contact angles than PTAA films, which indicates thinner COF films would hinder the wetting issue during perovskite layer forming procedure.

The photograph and SEM image of  $\text{MAPbI}_3$  and  $\text{FA}_{0.94}\text{Cs}_{0.06}\text{PbI}_3$  layers deposited on top of TPB-NC-B1 COF films built by different spin-coating speed are shown in Figure 39. As shown in the photograph and SEM images for both  $\text{MAPbI}_3$  and  $\text{FA}_{0.94}\text{Cs}_{0.06}\text{PbI}_3$  layers, the formed perovskite layers become more homogeneous, and compact on top of TPB-NC-B1 COF films when the spin-coating speed of COF film building increased from 1 k to 8 k. TPB-NC-B1 COF films built by a spin-coating speed of 8 k are the best substrates for perovskite layer deposition, in which perovskite layers are deposited on COF films compactly without any pin-holes.

After confirming the best COF substrates for perovskite layer deposition, another important condition of gas-quenching should be optimized, which is the distance between  $\text{N}_2$  source and COF substrates (results are shown in Table 15). The other gas-quenching conditions for PTAA standard PSC are optimized in reference paper, which are spin-coating speed, time and gas-quenching time.<sup>173</sup> The SEM images of gas-quenching distance of 2 and 5 cm show more pin-holes than that of 3 cm, which indicates an impact and pin-hole free surface.

Table 14. Contact angle measurements with DMF, NMP, DMSO, 3 different solvent mixtures and the perovskite precursor mixture on COF films of different thickness, PTAA and ITO are studied as reference.

	TPB-NC-B1 10 mg/ml, 1k (°)	TPB-NC-B1 5 mg/ml, 1k (°)	TPB-NC-B1 5 mg/ml, 10 k (°)	PTAA (°)	ITO (°)
DMF	22.50	22.24	11.9	25.18	4.24
NMP	20.08	17.79	8.46	11.13	21.4
DMSO	50.30	39.64	25.45	48.20	14.60
NMP:DMF (1:9)	23.49	23.02	6.94	23.7	~0
NMP:DMF (3:7)	20.0	16.4	6.40	22.69	~0
DMSO:DMF (1:9)	19.5	19.76	5.86	29.02	~0
Precursor	37.56	28.01	19.88	36.33	16.22

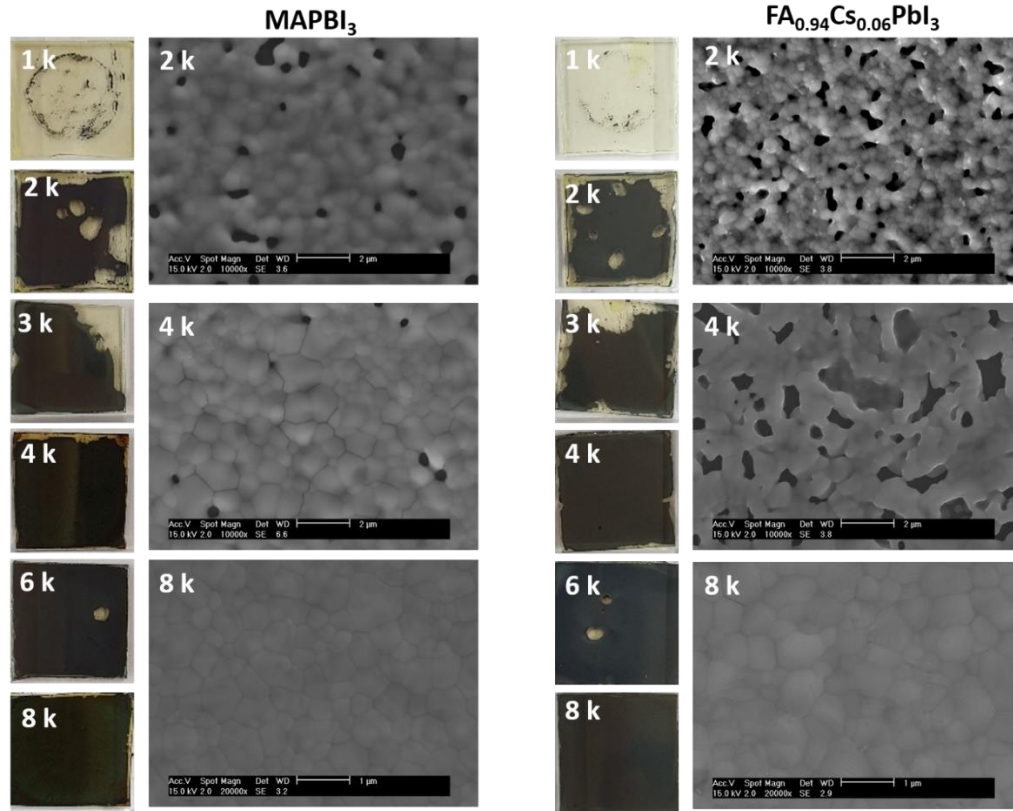
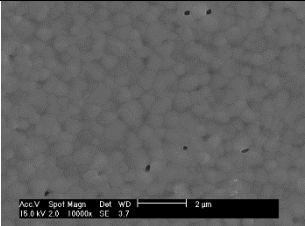
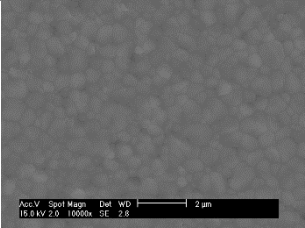
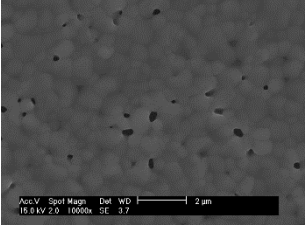


Figure 39. Photographs and SEM images of  $\text{MAPbI}_3$  and  $\text{FA}_{0.94}\text{Cs}_{0.06}\text{PbI}_3$  layers deposited on top of TPB-NC-B1 COF films built with spin-coating speeds of 2 k, 4 k and 8 k.



Table 15. Conditions and SEMs of perovskite layer formed for different distances between N<sub>2</sub> source and substrate (2, 3 and 5 cm).

	<b>name</b>	<b>spin-coating speed, time (k, s)</b>	<b>gas-quenching time (s)</b>	<b>gas-quenching distance (cm)</b>	<b>SEM results</b>
<b>1</b>	FA <sub>0.94</sub> CS <sub>0.06</sub> PbI <sub>3</sub> on TPB-NC-B1	3, 120	105	2	 SEM image showing a uniform, fine-grained perovskite layer. Technical details: Acc.V 15.0 kV, Spot 2.0, Magn 10000x, Def 3.7, WD 2.0 μm.
<b>2</b>	FA <sub>0.94</sub> CS <sub>0.06</sub> PbI <sub>3</sub> on TPB-NC-B1	3, 120	105	3	 SEM image showing a uniform, fine-grained perovskite layer. Technical details: Acc.V 15.0 kV, Spot 2.0, Magn 10000x, Def 2.6, WD 2.0 μm.
<b>3</b>	FA <sub>0.94</sub> CS <sub>0.06</sub> PbI <sub>3</sub> on TPB-NC-B1	3, 120	105	5	 SEM image showing a uniform, fine-grained perovskite layer. Technical details: Acc.V 15.0 kV, Spot 2.0, Magn 10000x, Def 3.7, WD 2.0 μm.

### 3.2.4 Photovoltaic performance of perovskite solar cells

All designed COF films are employed in inverted (*p-i-n*) PSC devices to study the impact of different dopant-free HTLs on photovoltaic performance. The procedures of PSC device formation with the same architecture (ITO/COF films/perovskite layers/PCBM/AZO/Ag) are described in the Experimental Section. SEM cross-section images of the TPB-NC-B1 device are shown in Figure 40. HTL is the TPB-NC-B1 COF film, which is too thin to observe in the SEM image. On top of HTL, uniform and pin-hole free perovskite layers with around 500 nm thickness were covered. Later, PCBM and AZO (Al doped zinc oxide) as ETL were spin-coated with thickness of around 150 and 20 nm, respectively. Finally, Ag electrodes with a thickness of 100 nm are evaporated on top of AZO.

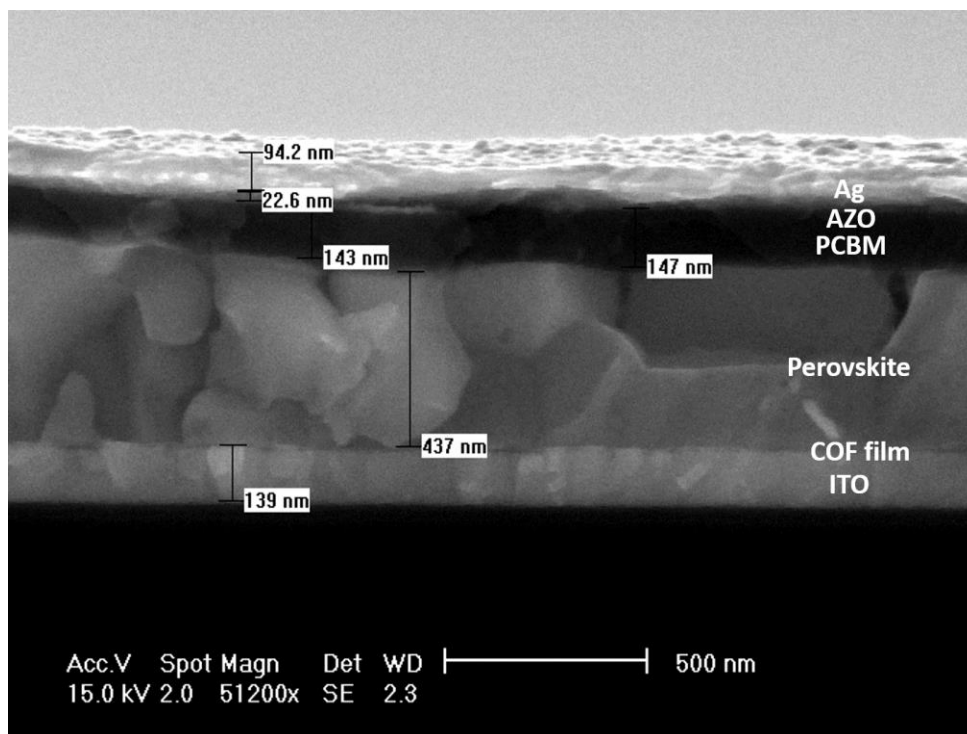
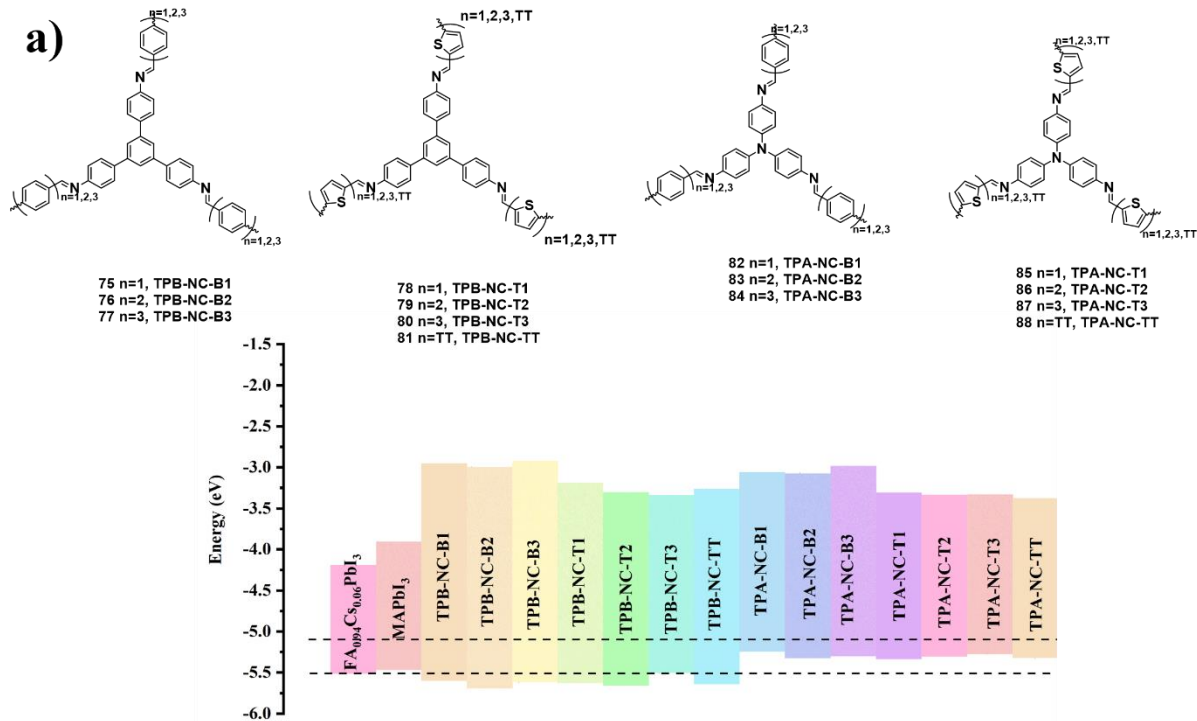


Figure 40. SEM cross-section image of a PSC device with a TPB-NC-B1 COF film as HTL.

The photovoltaic performance of all PSCs with both NC- and CN-type COF films as HTL are shown in Tables 16 and 17 and Figures 41 and 42. All devices with COF films show low  $J_{SC}$  except for TPA-NC-T1 and TPA-CN-T1, which are  $14.74 \text{ mA/cm}^2$  and  $15.81 \text{ mA/cm}^2$ . The  $V_{OC}$  of these devices increases from a range of 0.5 V to 0.95 V when the core of the HTL COF changes from TPB to TPA. The possible reason may be the better HOMO level alignment of COFs with TPA core than that with TPB core (as shown in Figure 41 c). FF of all COF films-based devices are in a range from 18 % to 30 %, which may be caused by the small shunt resistance and large series resistance. The obvious S-shaped J-V curves are found for all devices with COF films as HTL.

Table 16 Photovoltaic parameters, shunt resistance and series resistance of PSCs with N=C-type COF films as HTL.

	Name	PCE (%)	FF (%)	V <sub>oc</sub> (V)	J <sub>sc</sub> (mA/cm <sup>2</sup> )	R <sub>sh</sub> (Ω cm <sup>2</sup> )	R <sub>s</sub> (Ω cm <sup>2</sup> )
1	TPB-NC-B1	0.10	19.76	0.42	-1.38	151.52	4.76
2	TPB-NC-B2	0.08	24.70	0.43	-1.03	238.10	3.45
3	TPB-NC-B3	0.07	18.61	0.54	-0.69	357.14	166.67
4	TPB-NC-T1	0.73	23.78	0.52	-7.40	41.67	1.12
5	TPB-NC-T2	0.52	30.10	0.53	-4.46	62.50	0.88
6	TPB-NC-T3	0.40	18.67	0.67	-3.79	158.73	50.00
7	TPB-NC-TT	0.43	16.86	0.75	-3.58	71.43	16.67
8	TPA-NC-B1	1.08	14.43	0.96	-7.91	58.82	25.00
9	TPA-NC-B2	0.44	18.99	0.97	-3.92	100.00	1000.00
10	TPA-NC-B3	0.43	19.58	0.94	-3.73	13.16	1388.89
11	TPA-NC-T1	2.48	17.21	0.99	-14.74	62.50	333.33
12	TPA-NC-T2	0.28	17.40	0.64	-2.56	147.06	50.00
13	TPA-NC-T3	2.41	19.73	0.91	-15.81	52.63	100.00
14	TPA-NC-TT	1.12	18.36	0.99	-8.04	55.56	142.86



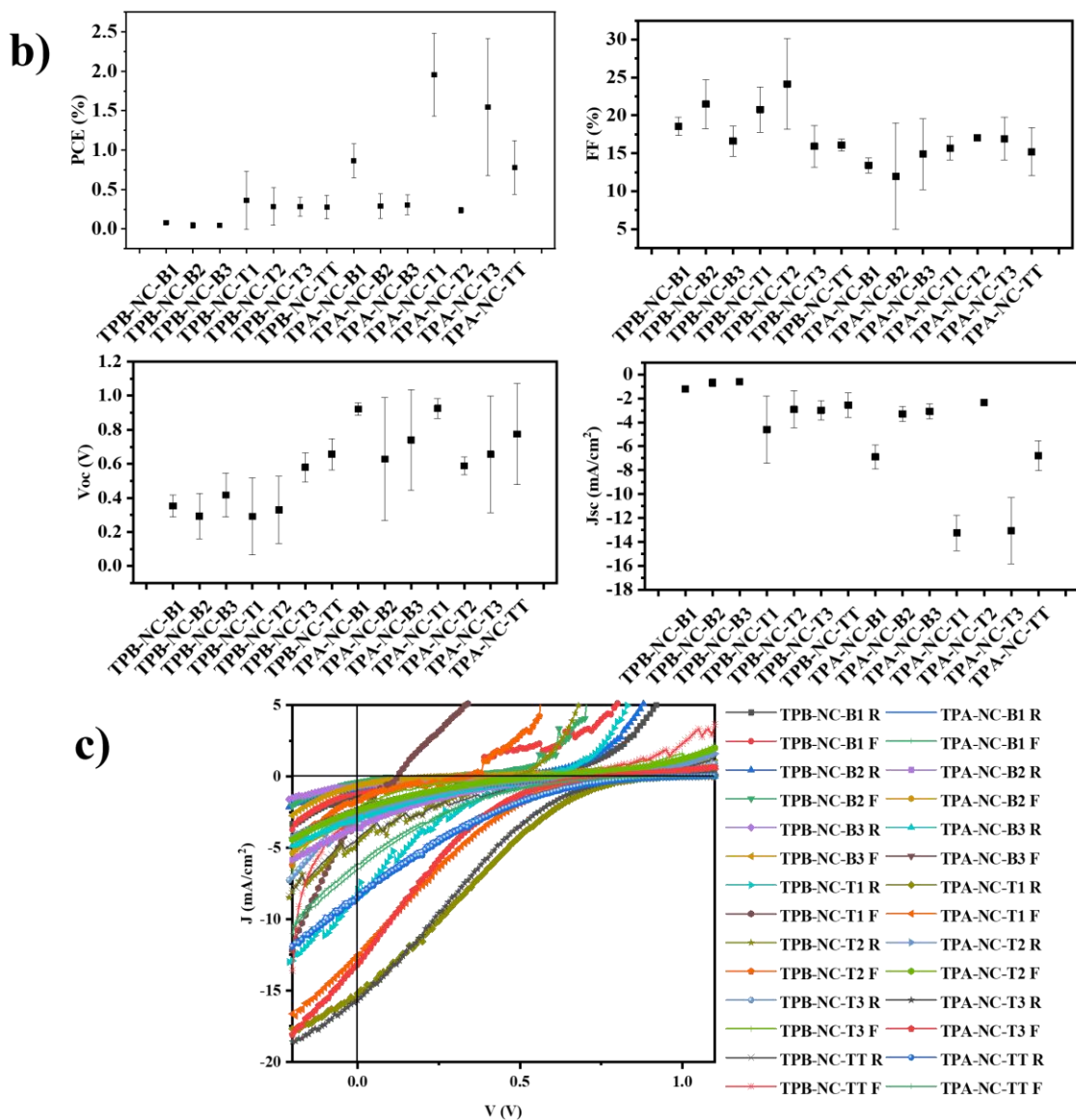
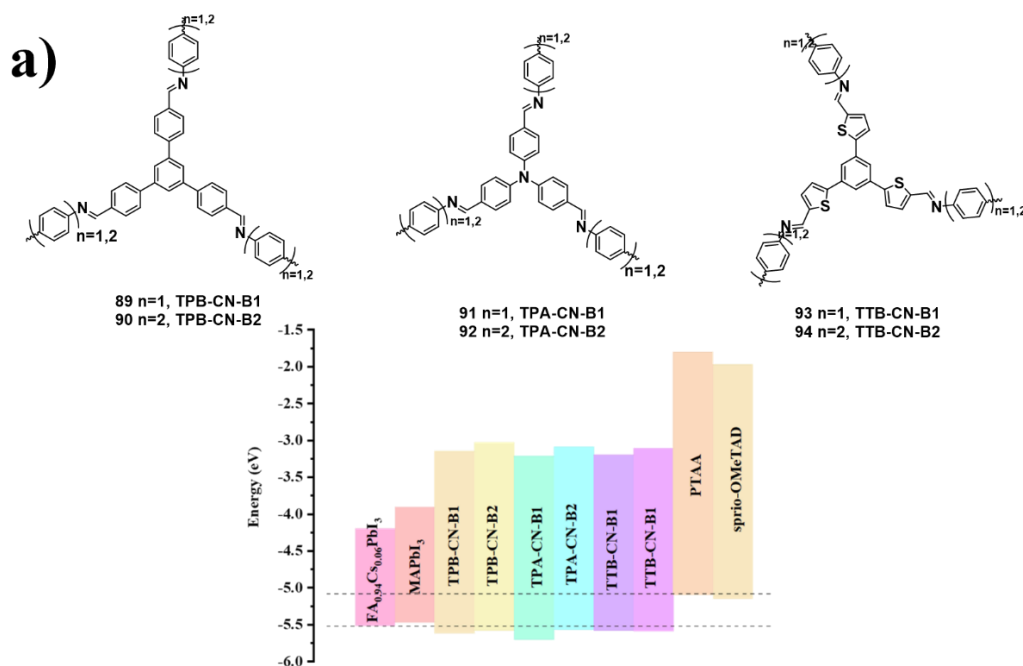


Table 17. Photovoltaic parameters, shunt resistance and series resistance of PSCs with investigated COFs with C=N-linkage as HTL.

	Name	PCE (%)	FF (%)	V <sub>oc</sub> (V)	J <sub>sc</sub> (mA/cm <sup>2</sup> )	R <sub>sh</sub> (Ω cm <sup>2</sup> )	R <sub>s</sub> (Ω cm <sup>2</sup> )
1	TPB-CN-B1	1.16	9.15	0.48	-11.04	35.71	0.65
2	TPB-CN-B2	1.57	19.40	0.73	-11.1	47.62	2.00
3	TPB-CN-B3	0.56	16.39	0.79	-4.33	76.92	4.76
4	TPB-CN-T1	0.85	18.25	0.59	-7.93	41.67	0.58
5	TPB-CN-T2	0.54	18.17	0.50	-6.02	38.46	0.70
6	TPB-CN-T3	0.91	16.21	0.80	-8.03	90.91	50.00



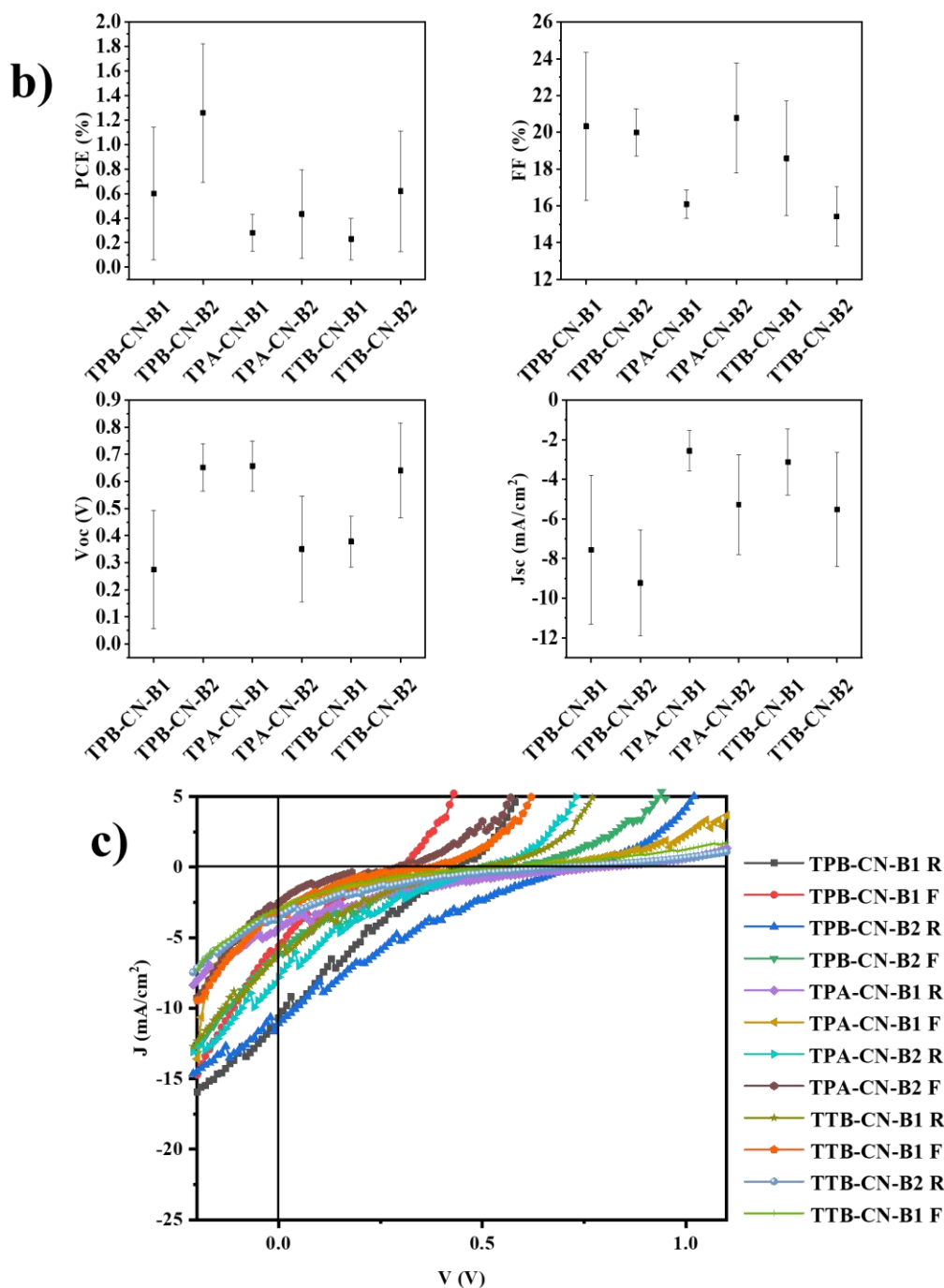


Figure 42. a) Structures of investigated COF films with C=N linkages. Energy level diagram of  $\text{FA}_{0.94}\text{Cs}_{0.06}\text{PbI}_3$ ,  $\text{MAPbI}_3$ , and investigated COF films. b) Summary of photovoltaic parameters of PSCs with investigated COFs as HTLs. c) J-V curves of PSCs with these COFs as HTL.

### 3.3 Conclusion

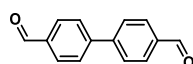
COF films with TPB, TPA and TTB cores and benzene or thiophene linkers can be built on ITO substrates directly through C=N linkage formation in the condensation reaction between amine- and aldehyde-based compounds. The thickness can be controlled by tuning the concentration of starting materials and the speed of spin-coating. After reaction, acetic acid used as catalyst can be easily removed by solvent washing, which may ruin when not removed the newly formed upper perovskite layer. The COF films built on ITO substrates show homogeneous and smooth surface, as confirmed by SEM and AFM measurements. The surface of COF films is accessible for perovskite precursor solutions due to contact angle measurements for the coming gas-quenching procedures. The COF films possess well-adjacent HOMO levels with respective perovskite layers, COF films with TPA cores possess slightly higher HOMO levels than the perovskites while COF films with TPB cores show slightly deeper lying HOMO levels than that of perovskites layer. The best thickness of COF films for building smooth perovskite layers on top is roughly 10 nm. The optimized gas-quenching conditions are 3 k of spin-coating speed, 120 s of spin-coating time, 105 s of gas-quenching time and 3 cm distance between COF films and N<sub>2</sub> source. The low PCE of all PSCs with COF films as HTL contribute to the low FF and J<sub>SC</sub> values.

The low photovoltaic performance of perovskite solar cell with COF films-based HTL may be attributed to several issues. The crystallinity of these COF films is uncertain as no characteristic signals were found in PXRD. The possible reasons may be the low thickness of the COF films otherwise the films may be amorphous leading to a decrease of hole mobility. Different amorphous polymers are used as HTL in perovskite solar cells but most of them need additional dopants to improve the originally inferior hole mobility.<sup>200</sup> Adding dopants would be an option to overcome the PCE issues. Because TPA cores has been verified as most suitable cores due to the good energy level alignment. TPA-based COFs should provide a driving force for the needed separation of electron/hole pairs.

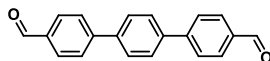
## 3.4 Experimental Section

### 3.4.1 Synthesis of molecules

**[1,1'-Biphenyl]-4,4'-dicarbaldehyde** (). A 500 ml round bottom flask was filled with 4-formylphenylboronic acid (33.3 mmol, 5 g), 4-bromobenzaldehyde (27.8 mmol, 5.14 g), Pd(PPh<sub>3</sub>)<sub>4</sub> (1.4 mmol, 1.62 g), 1 M aqueous solution of K<sub>2</sub>CO<sub>3</sub> (69.5 mmol, 9.6 g, 15 mL) and 1,2-dimethoxyethane (200 mL) under Ar in the dark. The mixture was refluxed overnight. After cooling down to room temperature, the solvent was filtrated and extracted with DCM. The resulting residue was purified by silicone gel column chromatography with toluene: EtOAc (10: 1, v:v) as eluent to afford white solid (3.8 g, 54.2 %). <sup>1</sup>H NMR (400 MHz, Chloroform-*d*) δ 10.09 (s, 1H), 8.00 (d, *J* = 8.6 Hz, 1H), 7.80 (d, *J* = 8.3 Hz, 2H). <sup>13</sup>C NMR (101 MHz, chloroform-*d*) δ 191.64, 145.57, 136.04, 130.35, 128.03.



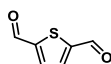
**[1,1':4',1''-Terphenyl]-4,4''-dicarbaldehyde** (). A 500 ml round bottom flask was filled with 4-formylphenylboronic acid (33.3 mmol, 5 g), 1,4-dibromobenzene (15.0 mmol, 3.54 g), Pd(PPh<sub>3</sub>)<sub>4</sub> (1.4 mmol, 1.62 g), 1 M aqueous solution of K<sub>2</sub>CO<sub>3</sub> (69.5 mmol, 9.6 g, 15 mL) and 1,2-dimethoxyethane (200 mL) under Ar in the dark. The mixture was refluxed overnight. After cooling down to room temperature, the solvent was filtrated and extracted with DCM. The resulting residue was purified by silicone gel column chromatography with toluene: EtOAc (10: 1, v:v) as eluent to afford white solid (3 g, 31.4 %). <sup>1</sup>H NMR (600 MHz, chloroform-*d*) δ 10.08 (s, 2H), 7.99 (d, *J* = 8.3 Hz, 3H), 7.82 (d, *J* = 8.2 Hz, 4H), 7.77 (s, 4H). <sup>13</sup>C NMR (151 MHz, Chloroform-*d*) δ 191.76, 146.04, 139.71, 135.35, 130.36, 127.99, 127.63.



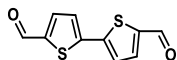
**Thiophene-2,5-dicarbaldehyde** (). A THF solution (100 mL) with 2,5-dibromothiophene (20 mmol, 4.8 g) was cooled with dry ice and ethyl acetate, to which n-BuLi (44 mmol, 27.5 mL, 1.6 M in hexane) was added dropwise under Ar in the dark. The solution was then stirred at this temperature for 1h before anhydrous DMF (60 mmol, 4.62 ml) was added dropwise. Then the



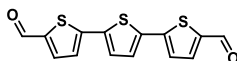
reaction mixture was allowed to warm to room temperature and stirred overnight. The reaction was quenched with a diluted aqueous solution of hydrochloric acid. The mixture was poured into water and extracted with dichloromethane (DCM) (2×20 mL). The combined organic layers were dried over Na<sub>2</sub>SO<sub>4</sub> and concentrated. The resulting residue was purified by column chromatography using DCM as eluent to give a yellow solid (1.6 g, yield 57.1 %). <sup>1</sup>H NMR (400 MHz, chloroform-*d*) δ 10.04 (s, 1H), 7.84 (s, 1H). <sup>13</sup>C NMR (101 MHz, Chloroform-*d*) δ 183.29, 149.21, 134.94.



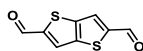
**[2,2'-Bithiophene]-5,5'-dicarbaldehyde (yznc09-1).** A THF solution (60 mL) with 2,2'-bithiophene (6.01 mmol, 1 g) was cooled with dry ice and ethyl acetate, to which *n*-BuLi (24 mmol, 15 mL, 1.6 M in hexane) was added dropwise under Ar in the dark. The solution was then stirred at this temperature for 1h before anhydrous DMF (48 mmol, 3.71 ml) was added dropwise. Then the reaction mixture was allowed to warm to room temperature and stirred overnight. The reaction was quenched with a diluted aqueous solution of hydrochloric acid. The mixture was poured into water and extracted with dichloromethane (DCM) (2×20 mL). The combined organic layers were dried over Na<sub>2</sub>SO<sub>4</sub> and concentrated. The resulting residue was purified by column chromatography using DCM as eluent to give a yellow solid (0.62 g, yield 46.4 %).



**[2,2':5',2''-Terthiophene]-5,5''-dicarbaldehyde (yznc010-1).** 2,5-Bis(tri-*n*-butylstannyl)thiophene (3.02 mmol, 2 g), 2-bromo-5-formylthiophene (6.64 mmol, 1.27 g) and (tetrakis triphenylphosphine)palladium (0.15 mmol, 0.17 g) was dissolved in DMF (40 mL) under Ar in the dark. The reaction mixture was refluxed overnight. The resulting solution was filtrated and extracted with ethyl acetate. The residue was recrystallized from DCM/MeOH to give product orange solid (0.56 g, 61 %). <sup>1</sup>H NMR (400 MHz, chloroform-*d*) δ 9.89 (s, 2H), 7.70 (d, *J* = 4.0 Hz, 2H), 7.32 (s, 2H), 7.30 (d, *J* = 3.9 Hz, 2H).



**Thieno[3,2-b]thiophene-2,5-dicarbaldehyde (yznc011-3).** A THF solution (60 mL) with thieno[3,2-b]thiophene (14.3 mmol, 2 g) was cooled with dry ice and ethyl acetate, to which n-BuLi (57.1 mmol, 35.7 mL, 1.6 M in hexane) was added dropwise under Ar in the dark. The solution was then stirred at this temperature for 1h before anhydrous DMF (114 mmol, 8.8 ml) was added dropwise. Then the reaction mixture was allowed to warm to room temperature and stirred overnight. The reaction was quenched with a diluted aqueous solution of hydrochloric acid. The mixture was poured into water and extracted with dichloromethane (DCM) (2×20 mL). The combined organic layers were dried over Na<sub>2</sub>SO<sub>4</sub> and concentrated. The resulting residue was purified by column chromatography using DCM as eluent to give a yellow solid (1 g, 35.7 %). <sup>1</sup>H NMR (400 MHz, Chloroform-*d*) δ 10.04 (s, 1H), 7.99 (s, 1H).



### 3.4.2 Synthesis of COF powders

**General procedure.** All COF powders were synthesized within the same procedure from different amine and aldehyde monomers via condensation reactions (as shown in Table 18). Under argon, a 20 ml micro-wave reaction tube was charged with amine, aldehyde and a mixture of 1,4-dioxane/mesitylene (v/v, 4/1, 10 ml). The tube was sealed with lid and transferred to oil bath to heat up to 120 °C until the solid was dissolved. After the reaction cooled down, acetic acid (6 M, 300 ul) was added into the reaction. The reaction was kept on 120 °C for 3 d. After reaction, the precipitate was filtrated, washed with THF three times and dried with supercritical CO<sub>2</sub> to give to a COF powder.

Table 18. Reaction conditions for the synthesis of all COF powders.

	COFs	Cores (M)	Linkers (M)	Solvents (V)	Cataylist (V)	Reactin temperature and time	Yield

5		4	3	2	1
<b>TPB-NC-T2</b>	<b>TPB-NC-T1</b>	<b>TPB-NC-B3</b>	<b>TPB-NC-B2</b>	<b>TPB-NC-B1</b>	
1,3,5-tris(4-aminophenyl)benzene (0.14 mmol, 50 mg)	1,3,5-tris(4-aminophenyl)benzene (0.14 mmol, 50 mg)	1,3,5-tris(4-aminophenyl)benzene (0.14 mmol, 50 mg)	1,3,5-tris(4-aminophenyl)benzene (0.14 mmol, 50 mg)	1,3,5-tris(4-aminophenyl)benzene (0.14 mmol, 50 mg)	1,3,5-tris(4-aminophenyl)benzene (0.14 mmol, 50 mg)
[2,2'-Bithiophene]-5,5'-dicarbaldehyde (0.23 mmol, 50.6 mg)	Thiophene-2,5-dicarbaldehyde (0.23 mmol, 30.5 mg)	[1,1':4,1''-Terphenyl]-4,4''-dicarbaldehyde (0.23 mmol, 56.2 mg)	[1,1'-Biphenyl]-4,4'-dicarbaldehyde (0.23 mmol, 47.9 mg)	terephthalaldehyde (0.23 mmol, 30.5 mg)	
1,4-dioxane/mesitylene (v/v, 4/1, 10 ml)	1,4-dioxane/mesitylene (v/v, 4/1, 10 ml)	1,4-dioxane/mesitylene (v/v, 4/1, 10 ml)	1,4-dioxane/mesitylene (v/v, 4/1, 10 ml)	1,4-dioxane/mesitylene (v/v=4/1, 10 ml)	
acetic acid (6 M, 300 ul)	acetic acid (6 M, 300 ul)	acetic acid (6 M, 300 ul)	acetic acid (6 M, 300 ul)	acetic acid (6 M, 300 ul)	acetic acid (6 M, 300 ul)
120 °C, 3 d	120 °C, 3 d	120 °C, 3 d	120 °C, 3 d	120 °C, 3 d	120 °C, 3 d
81 %	86 %	63 %	79 %	85 %	

10	9	8	7	6
<b>TPA-NC-B3</b>	<b>TPA-NC-B2</b>	<b>TPA-NC-B1</b>	<b>TPB-NC-TT</b>	<b>TPB-NC-T3</b>
1,3,5-tris(4-aminophenyl)amine (0.17 mmol, 50 mg)	1,3,5-tris(4-aminophenyl)amine (0.17 mmol, 50 mg)	1,3,5-tris(4-aminophenyl)amine (0.17 mmol, 50 mg)	1,3,5-tris(4-aminophenyl)benzene (0.14 mmol, 50 mg)	1,3,5-tris(4-aminophenyl)benzene (0.14 mmol, 50 mg)
[1,1':4,1''-Terphenyl]-4,4''-dicarbaldehyde (0.28 mmol, 79 mg)	[1,1'-Biphenyl]-4,4'-dicarbaldehyde (0.28 mmol, 57.9 mg)	terephthalaldehyde (0.28 mmol, 37 mg)	Thieno[3,2-b]thiophene-2,5-dicarbaldehyde (0.23 mmol, 44.7 mg)	[2,2':5,2''-Terthiophene]-5,5''-dicarbaldehyde (0.23 mmol, 69.3 mg)
1,4-dioxane/mesitylene (v/v, 4/1, 10 ml)	1,4-dioxane/mesitylene (v/v, 4/1, 10 ml)	1,4-dioxane/mesitylene (v/v, 4/1, 10 ml)	1,4-dioxane/mesitylene (v/v, 4/1, 10 ml)	1,4-dioxane/mesitylene (v/v, 4/1, 10 ml)
acetic acid (6 M, 300 ul)	acetic acid (6 M, 300 ul)	acetic acid (6 M, 300 ul)	acetic acid (6 M, 300 ul)	acetic acid (6 M, 300 ul)
120 °C, 3 d	120 °C, 3 d	120 °C, 3 d	120 °C, 3 d	120 °C, 3 d
63 %	85 %	85 %	71 %	72 %

15	14	13	12	11
<b>TPB-CN-B1</b>	<b>TPA-NC-TT</b>	<b>TPA-NC-T3</b>	<b>TPA-NC-T2</b>	<b>TPA-NC-T1</b>
1,3,5-1,3,5-Tris(4-formylphenyl)benzene (0.13 mmol, 50 mg)	1,3,5-tris(4-aminophenyl)amine (0.17 mmol, 50 mg)	1,3,5-tris(4-aminophenyl)amine (0.17 mmol, 50 mg)	1,3,5-tris(4-aminophenyl)amine (0.17 mmol, 50 mg)	1,3,5-tris(4-aminophenyl)amine (0.17 mmol, 50 mg)
benzene-1,4-diamine (0.21 mmol, 22.2 mg)	Thieno[3,2-b]thiophene-2,5-dicarbaldehyde (0.28 mmol, 54 mg)	[2,2':5',2''-Terthiophene]-5,5''-dicarbaldehyde (0.28 mmol, 84 mg)	[2,2'-Bithiophene]-5,5'-dicarbaldehyde (0.28 mmol, 61.2 mg)	Thiophene-2,5-dicarbaldehyde (0.28 mmol, 38.6 mg)
1,4-dioxane/mesitylene (v/v, 4/1, 10 ml)	1,4-dioxane/mesitylene (v/v, 4/1, 10 ml)	1,4-dioxane/mesitylene (v/v, 4/1, 10 ml)	1,4-dioxane/mesitylene (v/v, 4/1, 10 ml)	1,4-dioxane/mesitylene (v/v, 4/1, 10 ml)
acetic acid (6 M, 300 ul)	acetic acid (6 M, 300 ul)	acetic acid (6 M, 300 ul)	acetic acid (6 M, 300 ul)	acetic acid (6 M, 300 ul)
120 °C, 3 d	120 °C, 3 d	120 °C, 3 d	120 °C, 3 d	120 °C, 3 d
73 %	67 %	63 %	79 %	78 %

20	19	18	17	16
<b>TTB-CN-B2</b>	<b>TTB-CN-B1</b>	<b>TPA-CN-B2</b>	<b>TPA-CN-B1</b>	<b>TPB-CN-B2</b>
1,3,5-Tris(5-formylthiophene-2-yl)benzene (0.12 mmol, 50 mg)	1,3,5-Tris(5-formylthiophene-2-yl)benzene (0.12 mmol, 50 mg)	1,3,5-Tris(4-formylphenyl)amine (0.15 mmol, 50 mg)	1,3,5-Tris(4-formylphenyl)amine (0.15 mmol, 50 mg)	1,3,5-Tris(4-formylphenyl)benzene (0.13 mmol, 50 mg)
benzidine (0.20 mmol, 36.1 mg)	benzene-1,4-diamine (0.20 mmol, 21.2 mg)	benzidine (0.24 mmol, 44.8 mg)	benzene-1,4-diamine (0.24 mmol, 26.3 mg)	benzidine (0.21 mmol, 37.8 mg)
1,4-dioxane/mesitylene (v/v, 4/1, 10 ml)	1,4-dioxane/mesitylene (v/v, 4/1, 10 ml)	1,4-dioxane/mesitylene (v/v, 4/1, 10 ml)	1,4-dioxane/mesitylene (v/v, 4/1, 10 ml)	1,4-dioxane/mesitylene (v/v, 4/1, 10 ml)
acetic acid (6 M, 300 ul)	acetic acid (6 M, 300 ul)	acetic acid (6 M, 300 ul)	acetic acid (6 M, 300 ul)	acetic acid (6 M, 300 ul)
120 °C, 3 d	120 °C, 3 d	120 °C, 3 d	120 °C, 3 d	120 °C, 3 d
63 %	71 %	79 %	78 %	63 %

### 3.4.3 Synthesis of COF films on ITO

6 × 6 mm ITO-coated glass substrates were cleaned with ultrasonic sound in deionized water with detergent and isopropanol for 15 min, respectively. After brushing with detergent, all the ITO substrates were rinsed with deionized water and acetone followed by drying with clean dry air. All core and linkage molecules are dissolved in THF as 0.003 mmol/ml (1 eq) and 0.0048 mmol/ml (1.6 eq) solution, respectively. 50  $\mu$ l core molecules solution and 50  $\mu$ l linkage molecules solution was mixed as precursor solution, which were spin-coated on ITO at 2000 rpm for 30 s. All precursor covered ITO substrates are transferred into an autoclave together with an open glass bottle filled with 10  $\mu$ l acetic acid. The autoclave was kept on 120 °C for 2 days. After reaction, all the ITO substrates were washed with chloroform and acetone 3 times. These ITO substrates are used for UV, AC-2, XRD and SEM measurements.

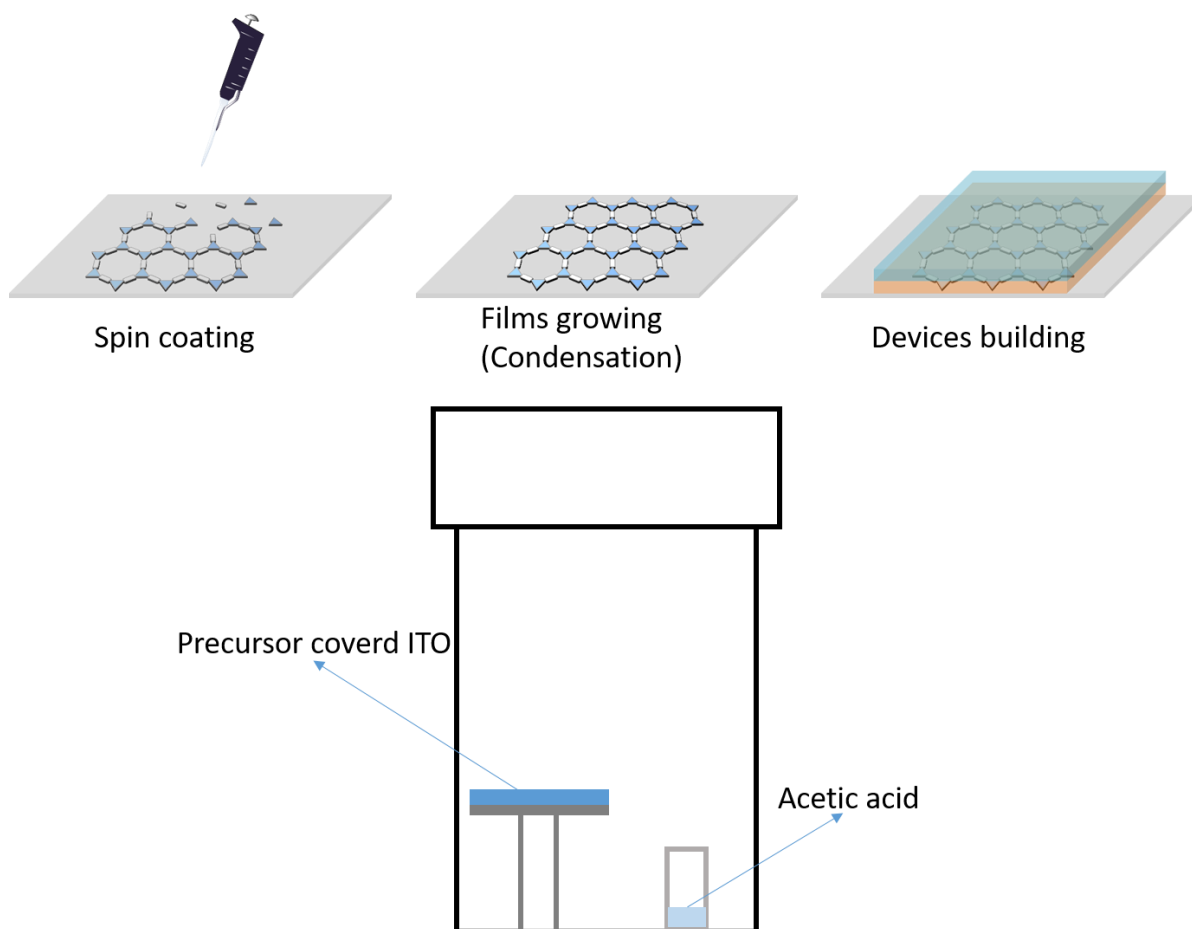


Figure 43. Illustration for synthesis of COF films on ITO.

### 3.4.4 Device Preparation

The layer construction of *p-i-n* device was glass/indium tin oxide (ITO)/COF films/perovskite/PCBM/AZO/Ag. The device preparation procedures were carried out in a nitrogen-filled glovebox.  $17 \times 17$  mm ITO-coated glass covered by a patterned photoresist (within  $3.14 \text{ mm}^2$  active area) were used as devices substrates. ITO-coated glass substrates were cleaned with ultrasonic sound in deionized water with detergent and isopropanol for 15 min respectively. After brushing with detergent, all the ITO substrates were rinsed with deionized water and acetone followed by drying with clean dry air. COF films were built as same method which described above. For MAPbI<sub>3</sub> perovskite precursor solution, a 1 M solution of PbI<sub>2</sub> (ultradry, Alpha Aesar) and MAI (Greatcell Solar) with 5% excessive PbI<sub>2</sub> was prepared with a solvent mixture of DMF/NMP with volume ratios of 7/3. For FA<sub>0.94</sub>Cs<sub>0.06</sub>PbI<sub>3</sub>, 0.94 M FAI (Greatcell Solar) and 0.06 M CsI (ultradry, Alpha Aesar) were used instead of MAI. The precursor solution was stirred by in the dark at 80 °C overnight. Freshly prepared aqueous 0.1 M thiourea was added into precursor solution before deposition. The perovskite layers were deposited with gas quenching procedure, which described as follows. The perovskite precursor solutions were spin-coated on COF films covered ITO substrates at 3000 rpm for 120 s with an acceleration of 300 rpm s<sup>-1</sup>. After various delay times (15 s for MAPbI<sub>3</sub> and 5 s for FA<sub>0.94</sub>Cs<sub>0.06</sub>PbI<sub>3</sub> respectively), a continuous nitrogen gas flow with a pressure of 7 bars (filtered with 5 μm PTFE filter) was blown (incident angle = 90°) over the substrate with specific distance 3 cm to form the intermediate (10 cm for MAPbI<sub>3</sub> and 3 cm for FA<sub>0.94</sub>Cs<sub>0.06</sub>PbI<sub>3</sub> respectively). The color will change from light yellow to drake brown within the maintained gas flow, which indicated the formation of the intermediate. Afterward, the substrates were immediately transferred to a hotplate and annealed at 100 °C (10 min for MAPbI<sub>3</sub> and 20 min for FA<sub>0.94</sub>Cs<sub>0.06</sub>PbI<sub>3</sub> respectively). PCBM was dissolved in chlorobenzene with stirring at 80°C overnight as 50 mg mL<sup>-1</sup> solution, which was spin-coated on top of perovskite layer at 1000 rpm for 30 s. After spin-coating of PCBM, AZO nanoparticles (Avantama AG N21X, 2.5 wt % in IPA) were immediately spin-coated dynamically at 8000 rpm for 30 s, which followed by annealing at 80 °C for 30 min. After annealing, 100 nm thick silver electrodes were evaporated at 10<sup>-6</sup> Torr.



### 3.5 References

173. Brinkmann, K. O.; He, J.; Schubert, F.; Malerczyk, J.; Kreusel, C.; van gen Hassend, F.; Weber, S.; Song, J.; Qu, J.; Riedl, T., *ACS Appl. Mater. Interfaces* **2019**, *11* (43), 40172.
192. Yin, X.; Song, Z.; Li, Z.; Tang, W., *Energy Environ. Sci.* **2020**, *13* (11), 4057.
193. Bach, U.; Lupo, D.; Comte, P.; Moser, J. E.; Weissörtel, F.; Salbeck, J.; Spreitzer, H.; Grätzel, M., *Nature* **1998**, *395* (6702), 583.
194. Kim, H.-S.; Lee, C.-R.; Im, J.-H.; Lee, K.-B.; Moehl, T.; Marchioro, A.; Moon, S.-J.; Humphry-Baker, R.; Yum, J.-H.; Moser, J. E.; Grätzel, M.; Park, N.-G., *Sci. Rep.* **2012**, *2* (1), 591.
195. Cappel, U. B.; Daeneke, T.; Bach, U., *Nano Lett.* **2012**, *12* (9), 4925.
196. Zhao, Q.; Wu, R.; Zhang, Z.; Xiong, J.; He, Z.; Fan, B.; Dai, Z.; Yang, B.; Xue, X.; Cai, P.; Zhan, S.; Zhang, X.; Zhang, J., *Org. Electron.* **2019**, *71*, 106.
197. Labban, A. E.; Chen, H.; Kirkus, M.; Barbe, J.; Del Gobbo, S.; Neophytou, M.; McCulloch, I.; Eid, J., *Adv. Energy Mater.* **2016**, *6* (11), 1502101.
198. Coropceanu, V.; Cornil, J.; da Silva Filho, D. A.; Olivier, Y.; Silbey, R.; Brédas, J.-L., *Chem. Rev.* **2007**, *107* (4), 926.
199. Smith, B. J.; Overholts, A. C.; Hwang, N.; Dichtel, W. R., *ChemComm.* **2016**, *52* (18), 3690.
200. Kim, Y.; Kim, G.; Jeon, N. J.; Lim, C.; Seo, J.; Kim, B. J., *ACS Energy Lett.* **2020**, *5* (10), 3304.

## 4 Summary

As perovskite solar cells have been developed for more than 10 years with increasing PCEs from 3 % to 25 %, a large amount of conjugated small molecules and polymers were explored as organic hole transport layers aiming to construct better performing perovskite solar cells with higher PCE and improved stability. Spiro-OMeTAD and PTAA are still most widely used as hole-transport materials providing high efficiencies. On the one hand, most small molecule HTMs for PSCs are triphenylamine (TPA)-based molecules, which suffer low charge carrier mobilities due to the propeller-like molecular structure of TPA and increased intermolecular distances due to the typical amorphous morphology. Therefore, dopants are introduced into HTM to modify the hole mobility, such as lithium bis(trifluoromethanesulfonyl)imide (LiTFSI) and *tert*-butylpyridine (*t*BP), which also reduce the stability of PSCs because of an increased hygroscopicity. On the other hand, polymers suffer from solubility problems, which would limit their use due to the non-solution-processability. Besides, different molecular weights of different batches can change thermal, morphological, and optoelectronic properties and subsequent photovoltaic performance, which may decrease feasibility in commercial PSCs. Impressive progress has been gained in designing new small molecules and polymers to achieved high performance PSC devices and understand the mechanism of PSCs, which include spiro-type, TPA based molecules, different carbazoles, porphyrins and phthalocyanines, substituted dithienopyrroles, substituted benzodithiophenes and substituted benzotrithiophenes, star-shaped molecules with truxene and triazatruxene cores. Even a large number of new small molecules and polymers with high photovoltaic performance were explored, but the structure-property-relations are still not clear. There are still no defined rules how structural features and optoelectronic and physicochemical properties contribute to better photovoltaic performances.

This thesis is designed to try to contribute to knowledge in facing these problems. COFs are porous crystalline frameworks with designable chemical structure. When COFs are applied as HTL in perovskite solar cells, its porous feature could be an improved better contact with the perovskite layer by increasing the hole transport ability. Crystallinity of COFs decreases the distance between neighboring COF layers which is expected to support the transport of holes. Structural diversity of COFs offers the opportunity to choose suitable building blocks to fit with specific perovskite layers.

At the same time, if the COF building reaction could be achieved on ITO directly, COF films would be formed on ITO, which would not be dissolved by solvents. The problems of solution-processability for most polymers would be overcome.

The thesis was started from applying small molecules as HTLs in *p-i-n* perovskite solar cells to figure out the relations between their structures and photovoltaic performances in PSC devices, meanwhile, also to find out suitable cores and linkers for COF film formation for a future applying as HTLs in PSCs. In chapter 2, the HTL molecules are designed by combining cores and terminals, which are trisphenylbenzene, trisphenylamine and tris thiophenebenzene as cores and di(4-methoxy-phenyl)amine and di(4-methoxy)carbazole as terminals. All model molecules show suitable HOMO, LUMO and band gap to achieve favorable energetic alignment with  $\text{FA}_{0.94}\text{Cs}_{0.06}\text{PbI}_3$  as perovskite active layer. However, the photovoltaic performance of all HTL small molecules was relatively low if compared to PTAA reference HTL. The possible reason may be that conditions of devices building are still not optimized since relative low shunt resistance and large series resistance are detected, which strongly related to the quality of the interface between HTL and perovskite layers. The work function difference between HTL and perovskite is used to describe the relation between interfacial dipole and device performance, via Kelvin probe measurement, but without clear trends. Besides that, the condition of plasma treatment may be another key issue for the undesirable photovoltaic performance. The PCEs are reduced obviously when going from plasma treated devices to non-plasma-treated devices. In chapter 3, different COF films with TPB, TPA, TTB cores and benzene, thiophene linkers were directly built on ITO substrates directly through C=N linkage formation via condensation reactions. The thickness can be controlled by tuning the concentration of the starting materials and the speed of spin-coating. The COF films built on ITO possess homogeneous and smooth surface. The crystallinity of COF films remains uncertain since no significant signal was detected in PXRD measurements. In PSCs, the COF films do not behave similar to other HTLs since unusual J-V curves with low  $J_{\text{SC}}$  and FF are detected. Besides, large  $R_s$  and  $R_{\text{sh}}$  demonstrate inferior interface qualities. These results may reflect a low hole mobility of the COF films. Especially the lack of crystallinity could reduce the hole mobility of these COF films. Similar to other common HTLs, dopants may be necessary to improve the hole mobility. Dopants could be introduced into COF films to overcome this issue.

## **List of Abbreviations**

AFM Atomic force microscopy

Ar Argon

BET Brunauer-Emmett-Teller

BT Bithiophene

CMP Conjugated microporous polymer

COF Covalent organic framework

CTF Covalent triazine frameworks

Cz Carbazole

DCM Dichloromethane

DSSCs Dye-sensitized solar cells

EDLC Electric double-layer capacitance

ETLs Electron transport layers

FA Formamidinium

FF Fill factor

FT-IR Fourier-transform infrared spectroscopy

GCD Galvanostatic charge–discharge

GID Grazing-incidence X-ray diffraction

HCP Hypercrosslinked polymers

HOF Hydrogen-bonded organic frameworks

HOMO Highest occupied molecular orbital

HRTEM High resolution transmission electron microscopy

HTL Hole transport layers

HV High vacuum

ITO Indium tin oxide

IUPAC International Union of Pure and Applied Chemistry

$J_{SC}$  Short circuit current density

LUMO Lowest unoccupied molecular orbital

MA Methylammonium

MALDI Matrix-assisted laser desorption

MOFs Metal-organic frameworks

OLED Organic light emitting diodes

OMe Methoxy

OPV Organic photovoltaics

OSC Organic solar cell

PAF Porous aromatic frameworks

PC Pseudo-capacitance

PCBM Phenyl-C61-butyric acid methyl ester

PCE Photoelectric conversion efficiency

PCP Porous coordination polymers

PESA/AC-2 Photoelectron spectroscopy in air

PIM Polymers of intrinsic microporosity

PL Photoluminescence

POC Porous organic cages

PPN Porous polymer network

PSC Perovskite solar cell

PV Photovoltaic

PXRD Powder X-ray diffraction

$R_s$  Series resistance

$R_{sh}$  Shunt resistance

SBU Secondary building units

ssNMR Solid-state nuclear magnetic resonance

T Thiophene

TAA Triarylamine

TEM Transmission electron microscopy

TGA Thermogravimetric analysis

TPA Triphenylamine

TPA Triphenylamine

TPB Triphenylbenzene

TTB tris(thiophen-2-yl)benzene

$V_{oc}$  open-circuit voltage

## **Acknowledgements**

I would like to thank Prof. Dr. Ullrich Scherf for offering opportunity to work in his working group, in which I learned much fantastic chemistry knowledge start from empty. Thank you for your patience, generously provided knowledge and valuable experience.

I would like to thank Prof. Dr. Thomas Riedl for offering his lab that I can finish devices building. Thank you for expertise supporting.

I would like to thank the daily help and measurements support from Kerstin Müller, Sylwia Adamczyk and Anke Helfer.

I would like to thank Kai Brinkmann, Dr. Ralf Heiderhoff, Tobias Haeger, Timo Maschwitz, Florian Zimmermann and Cedric Kreusel for teaching me devices building, different measurement technologies and sharing knowledge.

I would like to thank Dr. Edward Preis, Dr. Kim-Julia Kass, Dr. Sebnem Baysec, Robin Ammenhäuser, Dr. Florian Trilling and Dr. Isabell Geisler for teaching me all the chemistry knowledge and synthesis technologies.

I would like to thank my colleagues Marvin Unruh, Dr. Jannis Tent, Felix Niebisch, Tobias Mensak, Hauke Jötten and Christin Barron for offering pleasant working environment.

I would like to thank my dear friends Dr. Dario Wetterling, Dr. Markus Mühlinghaus and Dr. Patrick Klein, who make my hard time in Germany feel like home. I would like to thank Dr. Patrick Klein for correcting my thesis and the company in my dark days.

I would like to thank China Scholarship Council for supporting my PhD student study in Germany.

I would like to thank Prof. Dr. Yiwang Chen, thank you for your understanding.

I would like to thank the full supporting from my parents. Mama, I love you forever.